SPECTROSCOPY OF FISSION FRAGMENT EXCITED ATMOSPHERIC PRESSURE ARGON AND XENON PLASMAS

AIR FORCE INSTITUTE OF TECHNOLOGY

1975

SPECTROSCOPY OF FISSION FRAGMENT EXCITED ATMOSPHERIC PRESSURE ARGON AND XENON PLASMAS

By

ROBERT N. DAVIE, JR.

A DISSERTATION PRESENTED TO THE GRADUATE COUNCIL OF THE UNIVERSITY OF FLORIDA IN PARTIAL FULFILLMENT OF THE REQUIREMENTS FOR THE DEGREE OF DOCTOR OF PHILOSOPHY

UNIVERSITY OF FLORIDA

1975

UNCLASSIFIED

SECURITY CLASSIFICATION OF THIS PAGE (When Data Entered)

REPORT DOCUMENTATION PAGE

READ INSTRUCTIONS BEFORE COMPLETING FORM

1. REPORT NUMBER: CI-76-34	2. GOVT ACCESSION NO. / 3. RECIPIENT'S CATALOG NUMBER
4. TITLE (and Subtitle): Spectroscopy of Fission Fragment Excited Atmospheric Pressure Argon and Xenon Plasmas, 1975	5. TYPE OF REPORT & PERIOD COVERED: PhD Dissertation 6. PERFORMING ORG. REPORT NUMBER
7. AUTHOR(s): Robert N. Davie Jr. Capt, USAF	8. CONTRACT OR GRANT NUMBER(s)
9. PERFORMING ORGANIZATION NAME AND ADDRESS: AFIT student at the University of Florida, Gainesville, Florida	10. PROGRAM ELEMENT, PROJECT, TASK AREA & WORK UNIT NUMBERS
11. CONTROLLING OFFICE NAME AND ADDRESS: AFIT/CI Wright-Patterson AFB OH 45433	12. REPORT DATE: 1975 13. NUMBER OF PAGES: 312 pages
14. MONITORING AGENCY NAME & ADDRESS (if different from Controlling Office)	15. SECURITY CLASS. (of this report): Unclassified 15a. DECLASSIFICATION/DOWNGRADING SCHEDULE

16. DISTRIBUTION STATEMENT (of this Report)

Approved for Public Release; Distribution Unlimited

17. DISTRIBUTION STATEMENT (of the abstract entered in Block 20, if different from Report)

18. SUPPLEMENTARY NOTES

JERRY C. HIX, Captain, USAF
Director of Information, AFIT

APPROVED FOR PUBLIC RELEASE AFR 190-17.

19. KEY WORDS (Continue on reverse side if necessary and identify by block number)

20. ABSTRACT (Continue on reverse side if necessary and identify by block number)

DD FORM 1 JAN 73 1473 EDITION OF 1 NOV 65 IS OBSOLETE

UNCLASSIFIED

SECURITY CLASSIFICATION OF THIS PAGE (When Data Entered)

ACKNOWLEDGMENTS

I would like to begin by expressing my sincere thanks to the chairman of my supervisory committee, Dr. R. T. Schneider, and the other members, Dr. H. D. Campbell, Dr. E. E. Carroll, Dr. W. H. Ellis, Dr. M. J. Ohanian, and Dr. T. L. Bailey. Their numerous efforts on my behalf throughout my stay at the University of Florida are appreciated.

Execution of the research described herein required the support of nearly the entire Nuclear Engineering Sciences Department at one time or another from its chairman, Dr. M. J. Ohanian, on down. In spite of the number, I feel compelled to list the individual contributions. Administrative support was provided by Joan Boley, Barbara Davis, Lois Carroll, and Michey Kaselnak in funding. They were always willing to help me out "right now" when necessary. The reactor safety subcommittee was both patient and helpful in formulating an experimental approach consistent with safety guidelines. In particular Dr. Dalton, from whom I also learned a great deal in the classroom,

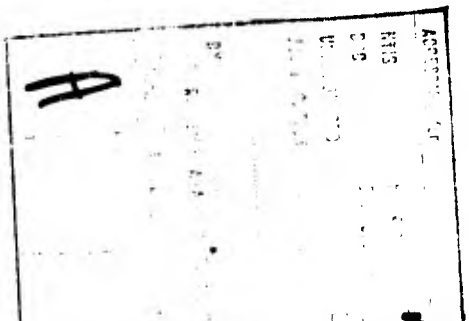

was extremely helpful in solving the various safety problems. With respect to the actual experimental work, most of the precision machining was done by Ralph Jones. Ernie Whitman did most of the heli-arc welding and gas filling. Joe Mueller must be credited with getting those big jobs done such as building the optical bench, beam trap and various shielding. The ideas of these three individuals had significant impact on every facet of the system design. The reactor staff under the direction of Dr. N. J. Diaz and Les Constable consistently made every effort possible to support this research. Henry Gogun and George Fogle provided numerous ideas and support, particularly during the initial setup and checkout of the system in the reactor. The swing shift operation of the reactor by Ed Donner was essential in getting that extra running time required to meet schedules. Ken Fawcett of the electronics shop saw plenty of action keeping the experimental equipment working. Willy Nelson supported this work through the timely procurement of various supplies and unglorified manual labor when I most needed it. An individual who always seemed available to help and put in many hours at the critical times was Dudley Carter; and he did almost anything from heli-arc welding to system alignment. Don Price, Harvey Norton, Gordon Renshaw, and Richard McGinley of Radiation Control were extremely helpful and always willing to do things immediately. I am indebted to all the

above individuals for their assistance; each played an important part.

Working with other students in the department was a pleasurable and educational experience for me. My closest association was with John Davis, for we used the same equipment for our research and worked together building most of it on a day-to-day basis. I consider this association my pleasure. Technical discussions with G. R. Shipman and Bruce Schnitzler, particularly during the early stages of my research, taught me a great deal. Other students to whom I am indebted for one reason or another are Jim Fuller, Bruce Kaiser, Eric Holtzclaw, Ken Sprague, and Dave Sterritt.

Support of the United States Air Force is acknowledged for paying my salary and providing me this unique educational opportunity. My research expenses were supported by NASA grant NGL-10-005-089.

Credit for the typing of this manuscript goes to Nancy McDavid and for the drafting to Robert Naranjo.

Finally, I express my deepest gratitude to my wife, Janet, and my two sons, Rob and Chris, for the sacrifices they made so that I might be able to pursue this educational goal. Their continual encouragement and support were also essential to its accomplishment.

TABLE OF CONTENTS

	Page
ACKNOWLEDGMENTS	ii
LIST OF TABLES	ix
LIST OF FIGURES	xi
ABSTRACT	xiv
CHAPTER	
1 INTRODUCTION	1
1.1 Interest in Fission Fragment Produced Plasmas	3
1.2 Summary of Past Related Work	5
1.2.1 Fission Fragment Excitation Experiments	5
1.2.2 Analytical Studies of Spatial Effects	8
1.2.3 Secondary Electron Energy Distributions	12
1.2.4 Experimental Studies of Plasmas Produced by Other Forms of High Energy Ionizing Radiation	15
1.3 Specific Objectives of This Research	19
2 THEORETICAL CONSIDERATIONS	21
2.1 Energy Loss of Fission Fragment in Gases	21
2.1.1 Primary Ionization and Excitation by Fission Fragments	22
2.1.2 Delta Rays and Secondary Electrons	23
2.1.3 Excited State Kinetics	26
2.2 Fission Fragment Plasma Characterization	27
2.2.1 The Corona Model	27
2.2.2 Recombination Regime	29
2.2.3 Trapping and Optical Thickness	38
2.2.4 Collisional Transfer of Excitation	39
2.2.5 Qualitative Summary Description of the Plasmas	40

TABLE OF CONTENTS (continued)

CHAPTER			Page
2 (cont.)	2.3	Energy Deposition Calculations and Spatial Effects	41
		2.3.1 Energy Deposition Calculation.	42
		2.3.2 Thermalized Electron Density Calculation.	52
		2.3.3 Fragment and Electron Energy Spectra.	53
	2.4	Discussion of Experimentally Measurable Parameters	68
		2.4.1 Spatial Variations	68
		2.4.2 Emission Intensity as a Function of Reactor Power Level.	69
		2.4.3 Pressure Effects	69
		2.4.4 Electric Field Amplification	70
		2.4.5 Temperature Effects.	70
3	EXPERIMENTAL SYSTEM DESCRIPTION.		71
	3.1	Design Considerations	71
	3.2	Overall System Concept.	73
	3.3	MCFIG Details	77
		3.3.1 Valve and Thermocouple Port.	79
		3.3.2 Sapphire Window.	80
		3.3.3 UO_2 Source	80
	3.4	Optical System.	84
	3.5	Instrumentation System.	88
		3.5.1 System Evolution	90
		3.5.2 Spectral Sensitivity	92
		3.5.3 Spectral Resolution.	92
	3.6	Reactor Environment	94
		3.6.1 Neutron Flux	94
		3.6.2 MCFIG Temperature.	96
	3.7	Test Procedures	98
		3.7.1 Gas Filling.	98
		3.7.2 Spatial Calibration and MCFIG Loading.	99
		3.7.3 Initial Reactor Startup.	100
		3.7.4 Data Acquisition	100
		3.7.5 Posttest Procedure	101
4	DATA ANALYSIS METHODS.		103
	4.1	Spectral Line Identification Techniques.	103
	4.2	System Absolute Calibration	105
		4.2.1 Relative Calibration Details	109
		4.2.2 Monochromator and Photomultiplier Absolute Calibration	115
		4.2.3 Relative Calibration Scaling	119
		4.2.4 Optical Collection Efficiency.	120
	4.3	Calculation of Excited State Populations	131

TABLE OF CONTENTS (continued)

CHAPTER		Page
5	ARGON RESULTS AND DISCUSSION	133
	5.1 Argon Spectra and Excited State Populations	134
	5.1.1 ArI.	136
	5.1.2 $ArII_o$.	144
	5.1.3 2250Å Continuum.	162
	5.1.4 Unidentified Lines	163
	5.2 Observed Spatial Effects.	166
	5.3 Emission Intensity Versus Reactor Power	175
	5.4 Temperature Effects	177
	5.5 Reassessment of Walters' Data . . .	178
	5.5.1 Pressure Effects	178
	5.5.2 Electric Field Amplification	180
	5.6 Discussion.	183 PT I
6	XENON RESULTS AND DISCUSSION	190 PT II
	6.1 Xenon Spectra and Excited State Populations	191
	6.1.1 XeI.	193
	6.1.2 XeII	197
	6.1.3 Visible Continuun.	204
	6.1.4 Unidentified Lines	208
	6.2 Observed Spatial Effects.	210
	6.3 Emission Intensity Versus Reactor Power	215
	6.4 Temperature Effects	217
	6.5 Discussion.	220
7	CONCLUDING REMARKS	222
	7.1 Summary of Significant Results and Conclusions	222
	7.1.1 Ar Data Base	222
	7.1.2 Xe Data Base	223
	7.1.3 Model of Fission Fragment Excited Plasmas.	223
	7.1.4 Implications for Nuclear Pumping.	224
	7.1.5 Spatial Effects.	226
	7.2 Implications for Future Research. .	226
	7.2.1 Gamma Excitation of Gases. .	227
	7.2.2 Radiation Effects.	227
	7.2.3 Source Geometry.	228
	7.2.4 Improvements of Experimental Setup.	228

TABLE OF CONTENTS (continued)

APPENDICES		Page
A	SOME OBSERVATIONS ON THE LUMINESCENCE OF ALPHA-Al_2O_3 (SYNTHETIC SAPPHIRE) IN A REACTOR ENVIRONMENT.	230
B	COMPLETE Ar SPECTRA.	243
C	TABULAR SUMMARY OF WATERS' DATA FOR ARGON. .	258
D	COMPLETE Xe SPECTRA.	266
BIBLIOGRAPHY		284
BIOGRAPHICAL SKETCH.		293

LIST OF TABLES

Table		Page
1.1	Summary of Past Spectral Investigations of Ar and Xe Excited by Ionizing Radiation . . .	16
5.1	ArI Excited State Population Densities. . . .	137
5.2	Comparison of ArI Relative Excited $2p_n$ State Populations with Those of Walters and with Electron Excitation Cross Sections.	142
5.3	ArII Excited State Population Densities . . .	145
5.4	List of Observed and Inferred ArII Laser Transitions	151
5.5	Comparison of ArII Relative Excited State Populations with Those of Walters, those of Rudko and Tang, and with Electron Excitation Cross Sections.	154
5.6	Analysis of Observed ArII Cascade Transitions	160
5.7	List of Unidentified Lines in the Ar Spectrum .	164
5.8	Tabulation of Selected ArI Spatial Measurements	168
5.9	Tabulation of Selected ArII Spatial Measurements	171
5.10	Relative Emission Intensity of Selected Portions of the Ar Spectrum at Various Reactor Power Levels.	176
5.11	Walters' Excited State Populations Multiplied by Total Transition Probability and Divided by the Excitation Cross Section	179
6.1	XeI Excited State Population Densities. . . .	194
6.2	XeII Excited State Population Densities . . .	198

LIST OF TABLES (continued)

Table		Page
6.3	List of Observed and Inferred XeII Laser Transitions	200
6.4	Analysis of Observed XeII Cascade Transitions	203
6.5	List of Unidentified Lines in the Xe Spectrum.	209
6.6	Tabulation of Selected Xe Spatial Measurements	213
6.7	Xe Emission Intensity as a Function of Power.	216
6.8	Summary of the Behavior of Observed Portions or the Xe Spectrum After Reactor Startup. . .	219

LIST OF FIGURES

Figure		Page
1.1	Effect of the Energy Dependence of the Excitation Cross Section.	10
1.2	Delta Ray Energy Spectrum Induced by Alpha Particles at the Centerline of a 2.5-cm-thick Helium Slab for Various Gas Pressures	11
1.3	Electron Energy Distribution in Fission Fragment Excited He and Ar as a Function of Pressure.	13
2.1	Ar_2^+ and Ar_2 Potential Energy Curves Showing Also ArI Levels and Important Transitions After	32
2.2	Geometry for Energy Deposition Calculations and Spatial Effects Evaluation.	43
2.3	Volumetric Energy Deposition Rate as a Function of Distance x from Source Where y = z = 0, $\phi = 2 \times 10^{12} n/cm^2$-sec, and t = 3μm.	50
2.4	Volumetric Energy Deposition Rate as a Function of Distance z from Center of Source Where y = 0 and x = $r_o/2$, $\phi = 2 \times 10^{12} n/cm^2$-sec, and t = 3μm	51
2.5	Electron Density as a Function of Distance x from Source Where y = z = 0, $\phi = 2 \times 10^{12} n/cm^2$-sec, t = 3μm.	54
2.6	Electron Density as a Function of Distance z from Center of Source Where y = 0 and x = $r_o/2$, $\phi = 2 \times 10^{12} n/cm^2$-sec, and t = 3μm. . . .	55
2.7	Geometry for Calculation of Fission Fragment Path Length Distribution Function	60
2.8	$r_o f(r)$ as a Function of x/r_o for n=1.	63
2.9	$r_o f(r)$ as a Function of x/r_o for n=2.	64

LIST OF FIGURES (continued)

Figure		Page
2.10	$E_o h(E)$ as a Function of x/r_o for n=2.	66
2.11	Average Relative Fragment Energy as a Function of x/r_o.	67
3.1	Overall Layout for MCFIG Gas Irradiation Studies	74
3.2	Test Tube End Cap Details and Gas Handling System.	75
3.3	Multipurpose Capsule for the Irradiation of Gases	78
3.4	Energy Distribution of Fission Fragments from a 2.53-Micron-Thick, 93% Enriched UO_2 Coating	81
3.5	Coating Effectiveness as a Function of Thickness	83
3.6	Optical Setup for MCFIG Gas Irradiation Studies	85
3.7	End on View of MCFIG Showing Spatial Sampling Region.	86
3.8	Instrumentation System for MCFIG Gas Irradiation Studies	89
3.9	Relative Spectral Sensitivity of Monochromator and Photomultiplier Compared to That for the Entire Instrumentation Systems Used in the Argon and Xenon Studies	93
3.10	Neutron Flux Distribution in the UFTR Horizontal Thruport	95
3.11	MCFIG Temperature as a Function of Time After Reaching Full Power	97
4.1	Schematic Showing Procedures to Effect an Absolute System Calibration	107
4.2	Optical Setup Used for Relative Calibration .	110

LIST OF FIGURES (continued)

Figure		Page
4.3	Optical Setup for the Absolute Calibration of the Monochromator, PM Tube, and Associated Instrumentation	116
4.4	Slit Image at Source and Lens Closest to Source.	122
4.5	Geometrical Layout for Calculation of $d\theta_y$ Showing the Four Regions for Which $d\theta_y$ is Non-zero.	124
4.6	Collection Efficiency for Region I.	125
4.7	Collection Efficiency for Region III.	127
4.8	Collection Efficiency for Region IV	128
5.1	ArI Level Diagram Showing the $2p_n$ Levels and Transitions Seen in This Study.	140
5.2	ArII Level Diagram Showing Lines Observed in This Study.	150
5.3	Comparison of Emissions Around 3093Å from this Study and from Walters' Data.	167
5.4	Scaled Ratio of the Intensity of the 4545Å ArII Line to That for the 6965Å ArI Line as a Function of Distance from the Source.	174
5.5	Flow Diagram Showing Important Processes in Fission Fragment Excited Ar	184
6.1	Xe Visible Continuum as Observed Close to and Far from the Source	205
6.2	True Intensity of Xe Visible Continuum 1.7mm from the Source	206
6.3	Variation of the Intensity of the 8280Å XeI Line and Continuum at 3300Å as a Function of Distance from the Source.	211
6.4	Ratio of 3300Å Continuous to 8280Å Line Emission as a Function of Distance from the Source.	212
6.5	Intensity of Continuum at 3300Å as a Function of Reactor Power.	218

Abstract of Dissertation Presented to the Graduate Council of the University of Florida in Partial Fulfillment of the Requirements for the Degree of Doctor of Philosophy

SPECTROSCOPY OF FISSION FRAGMENT EXCITED ATMOSPHERIC PRESSURE ARGON AND XENON PLASMAS

By

Robert N. Davie, Jr.

December, 1975

Chairman: Dr. Richard T. Schneider
Cochairman: Dr. Hugh D. Campbell
Major Department: Nuclear Engineering Sciences

Results of a spectroscopic investigation of atmospheric pressure Ar and Xe excited by fission fragments are reported. Spectra were taken at various distances from a planar fission fragment source, and a combined analytical and experimental absolute system calibration permitted estimation of excited state densities. The study was undertaken as part of an effort to develop new nuclear pumped laser systems, for which Ar and Xe are candidates.

A cylindrical gas containing chamber with a rectangular shaped planar 3 μm 93% enriched UO_2 fission fragment source mounted off center and parallel to the chamber axis was irradiated in the horizontal throughport of the University of Florida Training Reactor and subjected to a neutron flux of 1.6×10^{12} $n/cm^2 sec$. The optical emissions were monitored using a model 218 McPherson 0.3m scanning monochromator and EMI 9558QB (S-20) photomultiplier.

The spectral range sampled was 2000 to 8400Å, being limited by radiation damage to optical components in the UV and by the photomultiplier in the IR.

The most prominent spectral lines observed were from low lying atomic levels, $2p_2$ in Ar and $2p_5$ in Xe. Of significantly lower intensity are numerous ion lines which included 10 ArII and 4 XeII known laser transitions. Other transitions could be inferred from the data. Significant cascading into several upper levels was observed. A continuous emission was found in Ar around 2250Å and in Xe around 2500Å which extended at lower intensity to longer wavelengths. All emissions were found to vary linearly with reactor power, and ArII emissions were slightly enhanced relative to ArI close to the source. The spatial variation in the case of Xe was more complex.

These
The data are analyzed and compared with available information for other modes of excitation. The unpublished data of Walters for fission fragment excitation of Ar from 25 to 760 torr (with and without electric field amplification) were revaluated and tabulated. The spatial variation of volumetric energy deposition rates, electron densities, and fission fragment energy spectra are analytically treated for the source geometry used in the experiment.

Ionic lines are presumed to result from direct electron excitation from the atomic ground state and cascading. The ArII relative populations appear consistent with the coronal approximation and differ substantially from those typical in electrically pumped Ar ion lasers. Potential population inversions are approximately a factor of 10^4 below the estimated threshold for lasing; however, lasing should be possible at higher fluxes for both gases. Atomic emissions apparently result from dissociative recombination of the molecular ion with collisional redistribution of the energy among the atomic levels. While several atomic laser transitions were seen or inferred, they do not appear particularly promising for nuclear pumping. The Ar continuous emission was attributed to molecular recombination of excited atoms with ground state atoms. This process in Ar and associative ionization in both cases are considered responsible for depopulating the higher atomic levels not seen in this study. The observed Ar spatial variation is attributed to hardening of the electron energy spectrum near the source. Speculations are made as to the origin of the Xe continuum and the observed Xe spatial variation. The spectra in this study compare favorably with those for excitation by other ionizing radiations, suggesting excitation is due to secondary electrons and may be relatively independent of the primary ionizing particle type.

An appendix reports simultaneous optical transmission and luminescence measurements made during a reactor irradiation of α-Al_2O_3 (synthetic sapphire). Transmission decreased monotonically with irradiation time, being most degraded in the UV. The luminescence peak centered at 4100Å also decreased monotonically. The emission around 3300Å initially increased and appeared to saturate, remaining constant thereafter.

CHAPTER 1

INTRODUCTION

The scientific community has had a sustaining interest in the interaction of fission fragments with matter ever since the discovery of nuclear fission in 1939. Most of the early work in the field was empirical due to the inherent difficulties in treating the problem theoretically. Today, although fission fragment interactions are qualitatively better understood, a general theoretical solution to the problem does not exist, and we continue to rely on empirical relationships. Fission fragment interactions are one facet of the more general problem of ionizing radiation interactions; however, they constitute the most difficult and least understood aspect of the problem. Details on the fission process and fragment properties are presented elsewhere [1]. From an interaction standpoint fission fragments are distinguished from other charged particles by their higher mass (~97 for light fragments and ~138 for heavy fragments) and higher initial charge (~+20 e and +22 e, respectively). The fragments are born with energies of ~95 and ~67 MeV [2].

The slowing down or interaction of fission fragments with matter may be qualitatively described over two energy regions. For high energies the fission fragment is highly charged and loses energy primarily by inelastic collisions with orbital electrons of the target atoms; these produce ionization and excitation of the target medium. Delta rays produced in ionization reactions (and later generation secondary electrons) can cause additional ionization and excitation. As the fragment slows down below velocities on the order of its electron orbital velocities, it gradually approaches a neutral state by capturing electrons. In this region losses by elastic collisions with the target nucleus become increasingly important and eventually dominate. Ionization and excitation then occur primarily from secondary interactions of the recoiling target. In summary, the fission fragment bombardment results in ionization, excitation and heating of the medium, the ultimate distribution of which is highly complicated, particularly at higher pressures, because of the numerous secondary interactions and processes which follow the initial fragment interaction. The research described herein is directed at enhancing our understanding of the excitation produced in high pressure (760 torr) gases by fission fragment interactions, with specific emphasis on Ar and Xe.

1.1 Interest in Fission Fragment Produced Plasmas

Research efforts in this field are currently motivated by three major applications. The first, and primary motivation for this study, is the development of a direct nuclear (fission fragment) pumped laser. Such a system potentially offers operational advantages over conventional electrically pumped systems. The concept and review of past work are presented elsewhere [3-6]. Only recently has the feasibility of nuclear pumping been clearly established by the nearly simultaneous demonstration of nuclear pumping by University of Florida researchers using a He-Xe mixture [6-7] and by Sandia Corporation workers using CO [8]. Since these initial successes, nuclear pumping has also been achieved using a Ne-N_2 gas mixture at the University of Illinois [9]. Other nuclear pumping efforts are planned and some are perhaps underway at this time. So far, however, nuclear pumping has been demonstrated only at longer wavelengths and by using high flux pulsed reactors, even though some of the observed transitions should also operate in a CW mode. The immediate challenge now is to build a laser system which will operate in a CW mode. Since CW flux levels and corresponding input power densities to the gas will be orders of magnitude lower than for pulse systems, this task will be difficult. In addition it is desirable to develop nuclear pumped laser systems which operate at shorter wavelengths in the visible and in the UV

where higher inversions are required to overcome threshold. Because of the cost and difficulty involved in performing nuclear pumping experiments, other simpler methods (e.g., spectroscopy) to evaluate possible population inversions and better understand the fission fragment generated plasma are essential.

The second motivation for fission fragment generated plasma research is the development of a plasma core reactor system [7]. Such a plasma core or "nuclear light bulb" reactor, employing presumably some gas mixture containing UF_6, has some attractive features. Removal of the energy from the reacting volume in the form of optical radiation (perhaps even coherent) represents direct conversion of nuclear energy to light, and fission products could be retained on one side of an optically transparent barrier. Clearly an understanding of the radiative processes within such a plasma is an essential input to any system design.

The third area motivating fission fragment generated plasma research is the field of applied radiation chemistry. The relatively high energies of fission fragments and their availability in nuclear reactors make them attractive to promote chemical reactions. Such a concept has been of interest for some years and has been reviewed relatively recently [10].

1.2 Summary of Past Related Work

Although there exist a great many data on fission fragment stopping powers and ranges in gases, because of the complex nature of fission fragment interactions and experimental difficulties, excitation of gases by fission fragments has not been studied much until relatively recently, and most work has by necessity been experimental. The excitation data acquired for other charged particles, however, are of course useful in any study of fission fragments, particularly since it is generally accepted that most excitation from ionizing radiation is produced by secondary electrons. In fact the similarity of VUV spectra excited by 250 KeV electrons and 4 MeV protons has been clearly shown [11].

The most applicable analytical work have been efforts undertaken to characterize the secondary electron energy distribution. Past studies generally have given the most attention to He, with considerably less effort applied to the heavier noble gases owing to their complexity. However, from an engineering standpoint the heavier ones are more interesting.

1.2.1 Fission Fragment Excitation Experiments

Past experiments to study fission fragment excitation in gases have used two types of fission fragment sources.

The first type uses fragments from the spontaneous fission of ^{252}Cf which, while convenient, generally suffer the disadvantage of low light output and may also not realistically represent the kinetic effects seen in a plasma of larger volume excited by a large number of fragments (e.g., recombination may proceed by a different mechanism). Some early experiments conducted by Axtmann and Sears [12] of this type investigated excitation in N_2 at pressures from 28 to 266 torr. They used a PM tube to examine the excitation of the second positive group of the molecular N_2 spectrum by fission fragments and alphas and found they exhibited nearly the same efficiency for excitation. They concluded excitation must proceed by way of secondary electrons. In 1970 Pagano [13] studied several gases (e.g., CF_4, AR, N_2) and mixtures as scintillators for fission fragment kinetic energy spectrometry. He studied integrated light output as a function of pressure. Also in 1970, Calo [14] published results of luminosity as a function of pressure for ^{252}Cf fission fragments in N_2, CO_2, and CO. None of the above work with Cf provided any real spectral resolution. Ongoing ^{252}Cf experiments by Shipman [15] are designed to address this latter problem and may thus demonstrate the feasibility of acquiring spectral data on plasmas generated by ^{252}Cf fission fragments.

The second type of experiments used ^{235}U fissions and a reactor as a neutron source. In 1966 Morse,

Harteck, and Dondes [16] conducted in pile studies using ^{235}U glass fibers placed in a vessel containing 1 to 3 atmospheres of He, N_2, or Ar. The vessel was irradiated at flux levels of 10^{12} n/cm^2-sec. They used a quartz rod to get the light out of the reactor into the spectrograph and took photographic data which showed some line structure and numerous impurities.

The next series of in pile fission fragment experiments were performed by Walters and Schneider [17-18] at the University of Florida in 1972. Fission fragment excitation of He, Ar, and CF_4 was studied spectroscopically from 25 to 760 torr with and without electric field amplification. These experiments, although somewhat plagued by impurities, established the feasibility and desirability of conducting spectroscopy of in pile irradiated gases. The pressure data measured by Walters for Ar and CF_4 must be interpreted with care for two reasons. First, his optical system had a collection efficiency which was a function of location in his source region. Since at higher pressures this source region was larger than the fragment range, the collection efficiency is very important and could easily have caused his observed pressure variations about 100 torr (the relative spectra he presents for different pressures are still completely valid). The second reason for careful interpretation of pressure data is that close to the fission fragment source, the fragments (and

secondary electrons) will have a different energy distribution than far from the source, and also the volumetric energy deposition rate will vary, affecting secondary reactions. This in turn would be expected to affect excitation and produce a so-called "spatial variation" of the excitation depending on the distance from the source that the optical system is set up to sample at a given pressure. Resolution of some of these uncertainties in Walters' data was an important factor in the decision to initiate the research described herein.

1.2.2 Analytical Studies of Spatial Effects

Theiss and Miley in 1969 [19] and 1971 [20] specifically consider the problem of predicting the spatial distribution of primary excitation as well as ionization source rates in a medium being irradiated by a slab source of charged particles. The approach is to calculate the spatial dependence of the energy spectrum of charged particle currents in the media and use cross section information to calculate the primary ionization or excitation rates. Their work was motivated by the restriction imposed in preceding studies of spatial variation of ionization which did not take into account the energy dependence of the charged particle current in such a way they could make use of energy dependent cross sections. Miley and Theiss obtained cross sections for ionization and excitation by

using available data to normalize Bethe-Born cross sections. The effects of secondary electrons were taken into account by a pseudo cross section (i.e., all secondary effects were presumed to occur at the delta ray birth place). They present data for the excitation of helium by alpha particles in 1969 and by fission fragments in 1971. Although their data would change if excitation by recoiling neutrals and delta rays were included, they clearly show (see Figure 1.1) the importance of the energy dependence of the cross sections for He. This type of effect in heavier noble gases is a subject of the present experimental effort. Experimentally, however, one has the effects of delta rays and secondaries realistically included along with plasma kinetics effects.

In 1972 Guyot, Miley and Verdeyen [21] calculated the space dependent (in terms of data at a fixed point from the source but at different gas pressures) delta ray energy spectrum produced by alpha particles and lithium ions in helium at various pressures. Their approach was to calculate a spatially dependent energy flux of charged particles at a point using the previously discussed method of Theiss and Miley [20] and then employ Gryzenski classical cross sections (the Born approximation is not expected to give accurate results because of the low ion velocities). Some of their resulting calculations appear in Figure 1.2 and

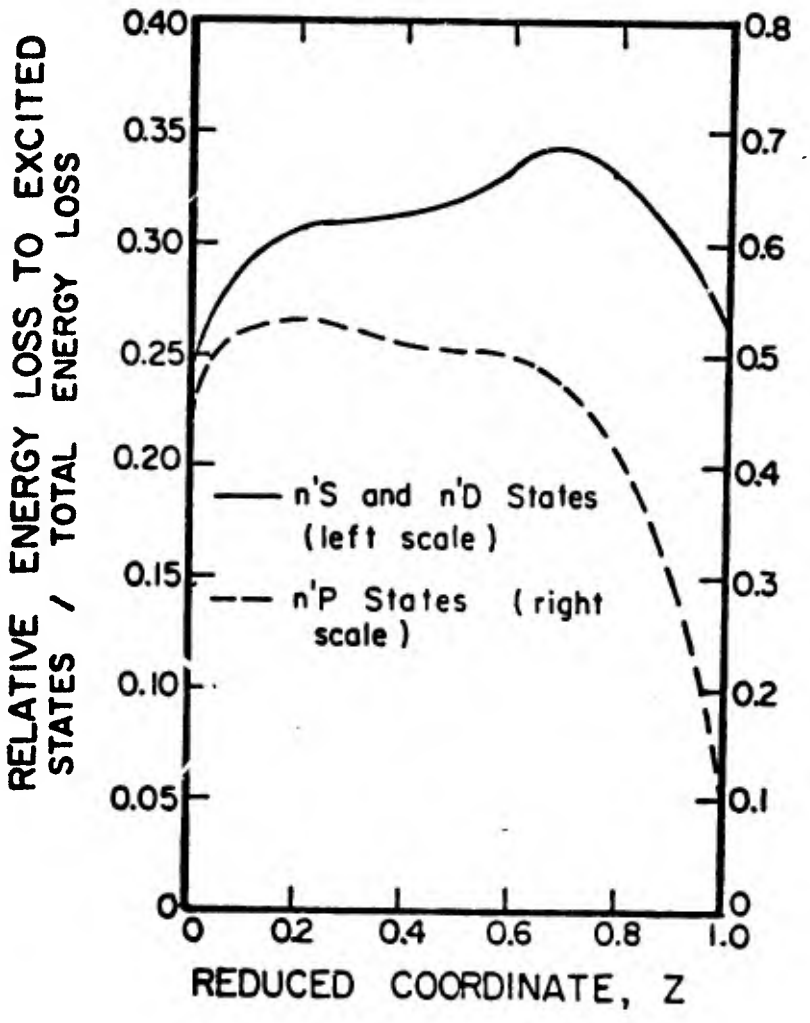

Figure 1.1: Effect of the Energy Dependence of the Excitation Cross Section

CURVE	P (TORR)
1	10
2	50
3	300
4	500
5	1000

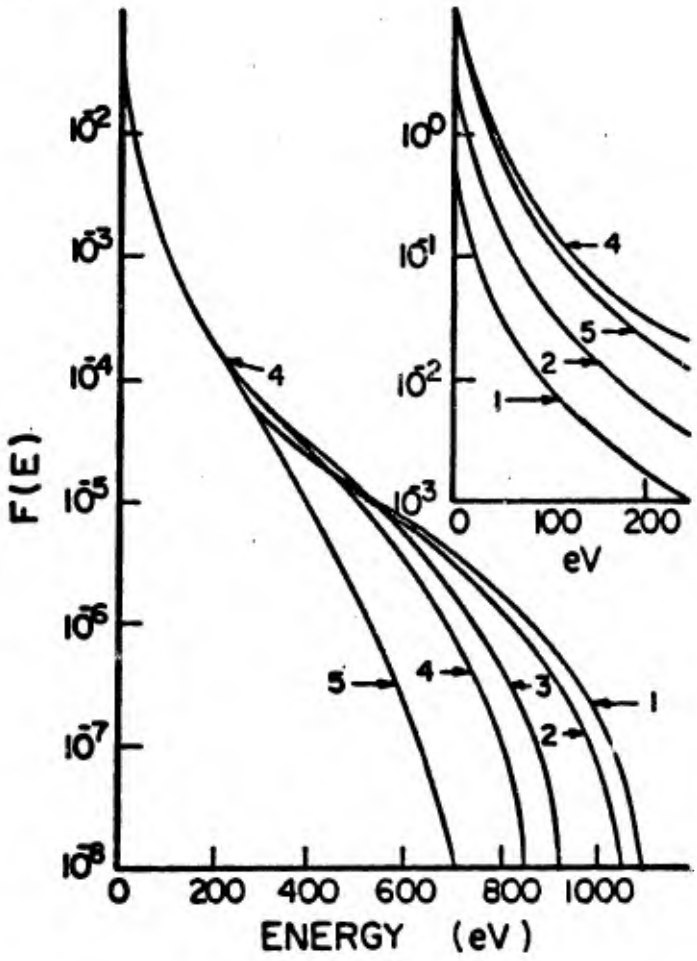

Figure 1.2: Delta Ray Energy Spectrum Induced by Alpha Particles at the Centerline of a 2.5-cm-thick Helium Slab for Various Gas Pressures [21]

show that the secondary electron energy spectrum will vary spatially. Unfortunately such calculations for fission fragments and heavier gases have not been made.

1.2.3 Secondary Electron Energy Distributions

Since most of the observed excitation in fission fragment generated plasmas has been attributed to the population of secondary electrons, several efforts have been undertaken to characterize their energy distribution. The only experimental data available were reported by Walters and Schneider for argon and helium as a function of pressure in 1973 [22]. This is shown in Figure 1.3.

The remaining analytical efforts worked the problem in terms of a given delta ray source energy. In 1972 Lo and Miley [23] reported calculations of the electron flux spectra as a function of initial delta ray energy for He, Ne, Ar, Kr, and Xe. One could then in principle represent the equilibrium electron spectrum from a real distributed source by a superposition of results for various delta ray energies, which for the case of alpha particles has been calculated [21] and agrees well with Walters' data for fission fragment excitation of He. Walters' results for fission fragments indicated an elevated population at high energies relative to Lo's calculations for alpha particles.

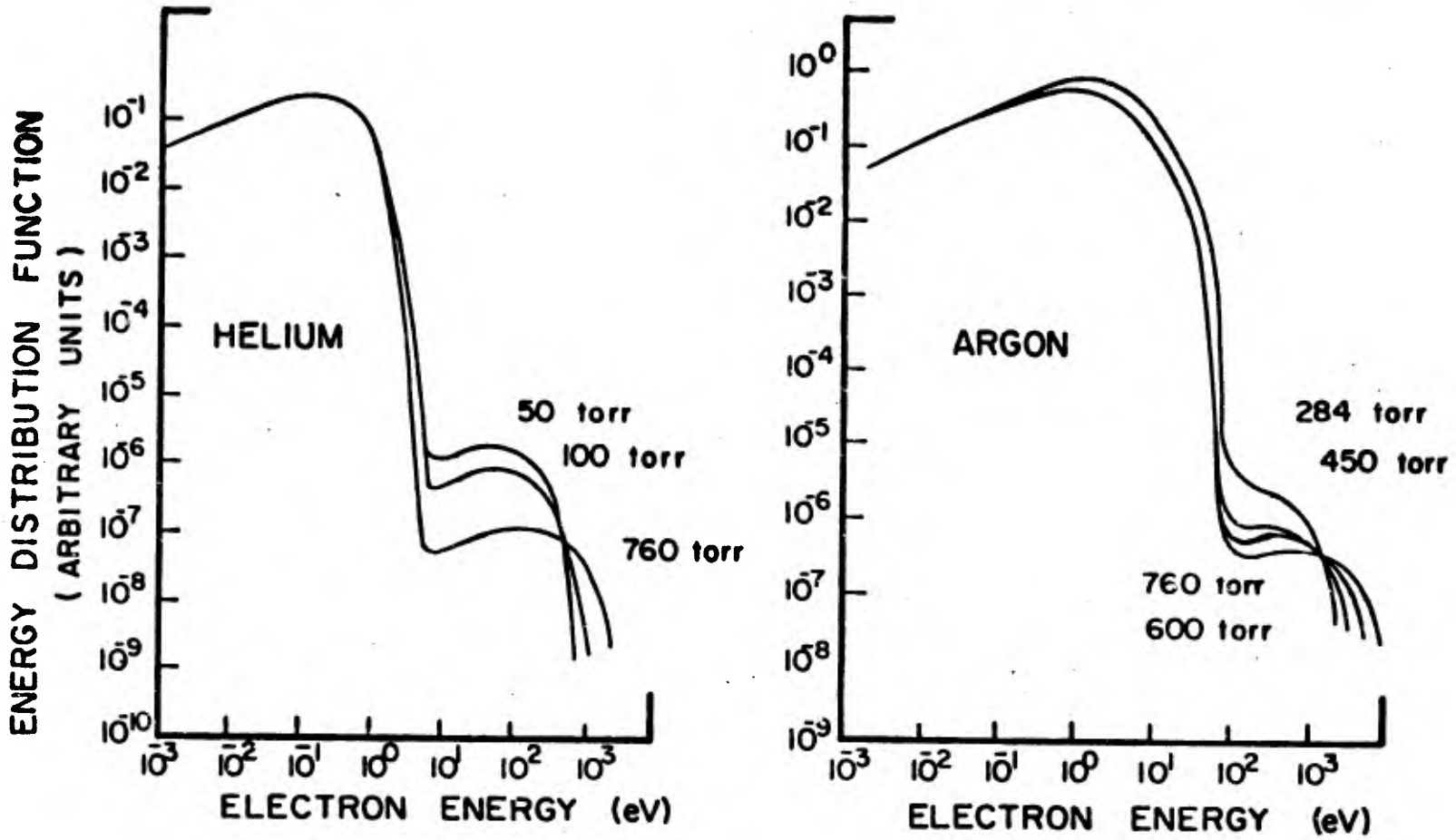

Figure 1.3: Electron Energy Distribution in Fission Fragment Excited He and Ar as a Function of Pressure [22]

Wang and Miley reported in 1973 [24] more extensive results from a Monte Carlo simulation of radiation induced plasma. They calculated the electron spectra resulting from a monoenergetic volume source of electrons in helium, including effects of an electric field. Their model included ionization, leakage, recombination, elastic scattering and inelastic scattering. Monte Carlo can simulate the physical processes involved as well as they are known; and in the present case this is the major limitation of the method, especially at high pressures where secondary effects are poorly understood.

Thus the basic analytical techniques to study electron energy distributions in fission fragment generated plasmas have been developed and applied to excitation of helium by alpha particles. What remains to be done is to apply these techniques to fission fragment excitation, a formidable problem, particularly in view of the fact we do not yet qualitatively understand the problem in most cases of practical interest. The results to date do, however, provide us insight into the problem.

1.2.4 Experimental Studies of Plasmas Produced by Other Forms of High Energy Ionizing Radiation

Experimental work has been done on alpha particle, proton and electron (primarily high energy electron beam) excitation of high pressure noble gases. Unfortunately most work has been qualitative in that complete spectral intensity information is not published in a form suitable for comparison with other data. Low light levels in the experiments have been an incessant problem limiting the spectral details subject to study. Also data over the visible spectral range have not been of much concern lately owing to the great interest in the VUV, stimulated by laser research. A brief summary of past studies of Ar and Xe at high pressures and over our range of spectral sensitivity is listed in Table 1.1. Included are the fission fragment experiments mentioned in a previous section. Not included are the numerous experiments concerned with gases or gas mixtures other than Ar and Xe and numerous studies solely concerned with the VUV. It is interesting that a complete optical emission spectrum giving relative line intensities and excited state populations has not been published to date in the open literature.

The experimental work using particles produced from the nuclear decay of various sources generally involves small volumetric energy deposition rates and plasmas of

TABLE 1.1: SUMMARY OF PAST SPECTRAL INVESTIGATIONS OF Ar AND Xe EXCITED BY IONIZING RADIATION

Researchers	Excitation Mechanism	Gases Studied	Pressure Range (Torr)	Spectral Range (Å)	Comments
W.R. Bennett [25] (1962)	5.1 MeV Alpha particles (^{239}Pu)	He, Ne, Ar, Kr, Xe	350	2400-6500 (PM Tube)	Ar: Detected only 2 lines (3083 & 3093) Xe: State rich spectral output obtained but report only very general features of it.
T.D. Strickler and E.T. Arakawa [26] (1964)	5.3 Alpha particles (^{210}Po)	Ar including mixtures	50-2000	1000-5400 (PM Tube)	Observed only a broad continuum centered at 2250Å and 3093Å line
V.W. Hanle, E. Kugler and A. Schmillen [27] (1964)	50 KeV Electron Beam Pulse	Ne, Ar, Kr, Xe	5-500	Unspecified but estimated to be 2600-7500 (photographic and PM tube with filters)	Present photographic spectra without relative intensity information. Studied time dependence of segments of spectrum using a PM tube and interference filters.
R. Henck and A. Coche [28] (1965)	5.3 MeV Alpha particles (^{210}Po)	He, Ne, Ar, Kr, Xe	350-4560	2000-5000 (PM Tube)	Observed only continuum centered around 2250-2575Å and N_2 emissions

Table 1.1 (continued)

Researchers	Excitation Mechanism	Gases Studied	Pressure Range (Torr)	Spectral Range (Å)	Comments
S. Dondes, P. Harteck, and C. Kunz [29] (1966)	5.3 MeV Alpha particles $^{210}P_o$	He, Ne, Ar, Kr, Xe and N_2 mixtures	780	2400-12000 (photographic)	Present photographic spectra without any line identification or quantitative intensity information. Studied electric field effects. Ar: Red ArI lines and noted continuum from 2600-2900Å when cell cooled Xe: A number of lines and continuum from 2600-5000Å
F. Morse, P. Harteck and S. Dondes [16] (1966)	Fission Fragments (Reactor)	He, Ar, and N_2 mixtures	760-2280	2400-12000 (photographic)	Observed photographically only 6965Å ArI line and mostly N_2 impurity emissions
R. Henck and R. Voltz [30] (1968)	5.3 MeV Alpha particles ($^{210}P_o$)	Ar	400-7600	2000-5000 (PM Tube)	Observed only continuum centered at 2250Å and N_2 emissions
G.S. Hurst and T.E. Bortner [31] (1969)	4 MeV protons	Ar	50-1400	1000-2300 (PM Tube)	Include study of continuum at 2100Å

Table 1.1 (continued)

Researchers	Excitation Mechanism	Gases Studied	Pressure Range (Torr)	Spectral Range (Å)	Comments
G.G. Dolgov-Savelev, V.A. Knyazev, V.V. Kuznetsov [32] (1969)	600 KeV Electron Beam Pulse	He, Ne, Ar	5-760	Unspecified (PM Tube)	Present intensity versus pressure for 7635, 9685, 7503, 8264, 8115, 8015Å ArI lines
S. Arai and R.F. Firestone [33] (1969)	500 KeV Electron Beam Pulse	Ne, Ar, Kr, Xe	200-1180	3500-1600 (PM Tube)	Measured time dependence of emission and absorption
P.E. Theiss and G.H. Miley [34-37] (1971-1975)	5.3. MeV Alpha particles ($^{210}P_o$)	He, Ne, Ar and various mixtures	1-760	3300-8500 (PM Tube)	Observed 6965, 7503, 7724, 7635Å ArI lines. Studied pressure and electric field effects
R.A. Walters [17] (1973)	Fission Fragments (Reactor)	He, Ar, CF_4	25-760	2000-8300 (PM Tube)	Presents complete spectra. Studied pressure and electric field effects
G.A. Carlson [38]	250-300 KeV Electron Beam Pulse	He, Ar, O_2 N_2, air	0.1-10	3500-6300 (photographic and image converter)	Present photographic spectra without line identification or intensity information. Studied time and pressure dependence of emissions.

commensurately low electron densities. The applicability of the resulting spectral data to more highly ionized plasmas is not established owing to the secondary kinetic processes involved. Electron beam and in pile fission fragment excited plasmas typically have involved electron densities on the order of 10^{10}-10^{11}/cc. These facts must be kept in mind when comparing different kinds of excitation data.

1.3 Specific Objectives of This Research

This research project was a part of the University of Florida fissioning plasma and nuclear pumped laser program. During the course of this research, the effort was guided by a number of objectives, not all of which were clear initially.

The major initial objective was to assess the importance of the aforementioned spatial variation, particularly with respect to nuclear pumped laser design and our basic understanding of fission fragment generated plasmas. This, of course, implied development of a method for acquiring in pile spectral data consistent with the most recent University of Florida training reactor (UFTR) safety philosophies.

Ar was selected as the initial gas to study because it would directly yield a checkpoint to confirm the validity of Walters' [17] measurements, and further is itself a potential candidate for nuclear pumping. In fact, nuclear pumping of Ar has been attempted [5, 17] but with inconclusive results. A fill pressure of 760 torr was selected partially because the range of a fission fragment in 760 torr Ar is about 1.3 cm, which enables taking data over the entire fragment path. While other pressures in this range could have been used, it was desired to maximize impurity effects for comparison with Walters' results. 760 torr was the highest pressure Walters used, so it was selected. The selection of Ar under these conditions also supported the planned work of Davis [39] on $Ar-N_2$ mixtures.

The next gas studied was 760 torr Xe which, because of its high stopping power and known laser potential, is of definite interest in nuclear pumped laser research. Xe data would further serve as a baseline for future mixture studies involving this gas.

Initially it was desired to quantify somehow the amount of light emitted from these fission fragment generated Ar and Xe plasmas. It later became apparent that an absolute system calibration was possible enabling calculation of approximate excited state densities. The potential rewards from such information motivated a combined analytical and experimental effort to effect this calibration.

CHAPTER 2

THEORETICAL CONSIDERATIONS

This chapter has two objectives. First, an attempt is made to present a basic theoretical description of the fission fragment produced plasmas investigated in this study. This is done by describing the basic processes thought to be important in the plasma, and indicating the current status of our knowledge with respect to Ar and Xe. Second, a theoretical or analytical description of the actual experiment is presented in terms of energy deposition calculations, spatial effects calculations (e.g., fission fragment spectra) and a discussion of experimentally measurable parameters. The correlation of these theoretical aspects and experimental results will be presented in the last three chapters.

2.1 Energy Loss of Fission Fragment in Gases

Prior to directing our attention to an analysis of the specific details of this experiment, a brief discussion of fission fragment energy loss in gases will be presented. Most of the early analytical work on fission fragment

interactions with gases had as its primary goal the establishment of reliable stopping power relations. A good review of both theoretical and experimental work on the passage of heavy ions through matter was conducted by Northcliffe in 1963 [40] and more recently by Miley [41]. Our interest, however, goes beyond this in that we would like to know the ultimate fate of the energy lost by fission fragments, and even more specifically how much of the energy results in excitation of the gas, or radiation.

2.1.1 Primary Ionization and Excitation by Fission Fragments

Qualitatively slowing down of fission fragments can be described in the following way. At high energies (E > 30 MeV) the highly charged fission fragments lose energy primarily by inelastic collisions with electrons of the stopping gas which directly produces ionization and excitation of the target gas. Because of their relatively large mass a fragment path is not expected to significantly deviate from a straight line in this region. However, while slowing down, a fission fragment has a finite probability of capturing or losing an electron during one of these collisions. When the fragment reaches a velocity lower than the orbital velocity of the first electron, the capture probability becomes very large relative to that for loss. As the fragment continues to slow

down, electrons are captured until the fragment becomes a neutral atom. At the lower energies (E > 30 MeV) the fragment may lose energy by elastic collisions with the screened nuclear field of the atom, and at sufficiently low energies this process is the dominant loss mechanism [14]. In this region the fission fragment direction may be changed appreciably. Although some electronic interaction may take place through the quasi-adiabatic interpenetration of the electron clouds of the fragment and target atom, most of the energy lost by the fragment at lower energies will appear initially as kinetic energy of the recoiling gas atoms [42]. Thus, primary fission fragment ionization and excitation of the gas is expected to be most significant at higher energies or during the first part of the fragment path.

2.1.2 Delta Rays and Secondary Electrons

High energy delta rays are electrons inelastically scattered during the electronic interaction of fission fragments and the target gas. They can have energies up to the KeV range. For electron energies exceeding the ionization potential, the ionization cross sections are much greater than those for excitation. Thus delta rays can result in numerous additional or secondary electrons. It is these secondary electrons that are the most important source of the excitation produced by fission fragments. This means information on gas excitation

by virtually all forms of high energy ionizing radiation is useful in interpreting and understanding fission fragment excitation and other forms of high energy ionizing radiation. Furthermore, as previously mentioned, their energy distribution function is highly important in determining the excitation that is observed. This quantity would be expected to vary according to the target gas, gas pressure, incident radiation and numerous secondary effects. Delta ray (and resulting secondary electron) excitation effects may be considered to take place at the delta ray birth point, since even the range of a 10 KeV electron in 760 torr Ar is only about 0.1 cm.

The relative ionization yield of a charged particle is usually expressed by w, which is defined as the energy of the charged particle divided by the number of ion pairs produced. This parameter, in principle embodying a number of complex physical processes, has been found very useful in practice and will be employed in later sections to calculate electron source rates. Following the analysis of Platzman [43], the energy balance for the energy loss of a high energy particle, T, may be written

$$T = N_i \bar{E}_i + N_e \bar{E}_e + N_i \bar{\varepsilon} \qquad 2.1$$

where N_i ions at an average energy expenditure of $\bar{E}_i$, N_e excited atoms at an average energy expenditure of $\bar{E}_e$ and

N_i subexcitation electrons having an average kinetic energy $\bar{\varepsilon}$ are produced in the slowing down process. The expression for w can then be written simply as:

$$w = \frac{T}{N_i} = \bar{E}_i + \frac{N_e}{N_i}\bar{E}_e + \bar{\varepsilon} \qquad 2.2$$

Note that $\bar{\varepsilon}$ will be eventually dissipated as heat to the gas. Platzman goes further and points out that for the noble gases $N_i/N_e \approx 2.5$ which is equal to the corresponding cross sections averaged over the degradation spectrum of particle energies. Clearly most of the initial particle energy produces ionization. For alpha and beta particles w has been found approximately constant for a given gas. A reasonably recent and detailed review of such w values for various gases is published elsewhere [44]. w values for fission fragments, however, show a complex variation with energy and gas type and in particular are higher (by approximately 7%) than values for alpha particles giving rise to a so-called "ionization defect." This is purportedly the result of the fragment having a variable charge as it slows and the importance of energy loss by elastic collisions [45]. However, as pointed out by Orvis, some of this defect may be due to columnar recombination affecting the experimental data [46]. Since the w correction is small and columnar recombination effects

will be corrected for in the recombination coefficient, the correction will not be made here and w values for alpha particles will be used.

2.1.3 Excited State Kinetics

The expected excited state sources and losses may be briefly summarized in the following steady state balance equation for a given state:

[excitation from recombination events]	+ [primary excitation by fission fragments]
+ [secondary excitation by electrons]	+ [secondary excitation by recoiling gas atoms]
+ [cascading from higher energy states]	+ [collisional transfer of excitation to the state]
= [radiative decay from the state]	+ [collisional transfer out of the state]

While the above balance can be easily stated it clearly represents a most difficult physical problem at high pressures such as in this study.

While primary excitation by fission fragments and secondary excitation by recoiling gas atoms can be neglected as noted above, to even get an estimate of secondary excitation by electrons requires knowledge of their energy distribution function, excited state densities, etc. Regarding collisional transfer of excitation, it can only

be qualitatively assessed. Cascading from higher energy states can be estimated only where knowledge of the higher state populations is available. When there are no radiation trapping effects, the radiative decay is straightforward to evaluate. Population of excited states through recombination events will be discussed in further detail in a later section on recombination.

2.2 Fission Fragment Plasma Characterization

The purpose of this section will be to roughly characterize the fission fragment plasmas examined experimentally in this study. The plasmas are typified by relatively low thermalized electron densities which are in the range of 10^{11}/cc as will be demonstrated in a later section and is also consistent with measurements by Walters [22]. The distinction between epithermal and thermal electrons is important because the density of the former will be a linear function of power input to the plasma (inversely proportional to the w value) while the latter will be proportional to the square root of the power because of recombination.

2.2.1 The Corona Model

At these low electron densities the plasmas in this study are far from local thermodynamic equilibrium

(LTE). The primary (electron induced) excitation and ionization in the plasma is described by the corona model. In effect this model assumes that only electron collisions with ground state atoms are important (i.e., recombination is ignored for the moment) [47]. Thus the distribution of ion and excited states is determined primarily by cross sections. For excited atomic states one can simply equate the electron excitation and radiative (or collisional) decay rates which yields

$$\frac{n(p)}{N(o)} = \frac{n_e K(p)}{A(p)} \qquad 2.3$$

where n(p) and n(o) are the excited and ground state atom densities, n_e is the electron density, A(p) is the total (including collisional losses) transition probability from the pth state and K(p) is an effective (including electron energy distribution effects) electron excitation cross section from the ground state. Collisional sources to the pth state have been neglected, and it is the collisional sources and losses that prevent the practical application of the model at high pressures. A similar relation can be written for ionic states. The electron ionization rate (including production of excited ionic species) is set equal to the ion loss rate by

collision and also radiation for excited ions. Recombination is not considered a loss because all ions are first converted to the molecular ion which undergoes dissociative recombination as will be described in the next section. This balance enables us to write

$$\frac{n_z(p)}{n_{z-1}} = \frac{n_e K'(p)}{A'(p)} \qquad 2.4$$

where $n_z(p)$ and n_{z-1} are the densities of the pth ionic and atomic ground states, and $K'(p)$ and $A'(p)$ are the appropriate effective cross sections and transition probability (including collisional effects) for the ionic states.

2.2.2 Recombination Regime

A recent (1974) in-depth review of the historical development of recombination to which the reader may wish to refer has recently been published by Bates [48]. It includes an excellent list of references on all facets of the problem. In addition Bardsley and Biondi [49] in 1970 published a detailed review of dissociative recombination from which much of the discussion to follow is extracted. A significant effort has been expended in recent years to

determine the recombination coefficients for the noble gases, and at the pressures and electron densities encountered in this study the controlling species are the molecular ions, Ar_2^+ and Xe_2^+. Recombination thus proceeds by way of the following dissociative recombination process (equations and discussions below will be specifically written for the case of Ar, but the situation is completely analogous for Xe):

$$Ar_2^+ + e \rightarrow Ar_2^* \text{ (unstable)} \qquad 2.5$$

where + and * indicate ionized and excited states respectively. The unstable Ar_2^* immediately dissociates into two Ar atoms, one of which will be excited as indicated below:

$$Ar_2^* \text{ (unstable)} \rightarrow Ar^* + Ar + K.E. \qquad 2.6$$

This process is known to give rise to atomic transitions observed in afterglows. It has been studied in most detail for Ne afterglows [50-51] and to a lesser extent for Ar [51]. The approach in these studies was to measure the Doppler broadening of the afterglow lines caused by the recoil motion of the excited dissociation product. Most afterglow line shapes were found broader than for the corresponding discharge lines, indicating that the $2p_n$

(Paschen notation will be used for ArI and NeI levels) excited levels of Ar and Ne are produced by dissociative recombination. Unfortunately only for Ne are the afterglow line intensities specified. The above process is illustrated using potential curves in Figure 2.1. Mention only will be made of one additional such study which investigated Kr afterglows [52] but which was inconclusive in establishing the dissociative recombination origin of the Kr afterglow lines. Analogous processes are, however, expected to occur in both Kr and Xe.

The radiative processes which follow dissociative recombination lead to production of $1s_n$ levels. These levels then collisionally give rise to the Ar_2^* dimer, the de-excitation of which is the basis of the recently developed VUV Ar [53] and Xe [54] lasers. The potential curves for this process are also shown in Figure 2.1

The relative contribution of dissociative recombination to the spectral lines (from the $2p_n$ states) observed in a steady state charged particle excitation situation is difficult to experimentally assess. Hanle, Kugler, and Schmillen [27] have studied the time dependence of portions of the spectra (using filters) of noble gases excited by a pulsed electron beam. The afterglow they found could be broken into a fast (representing higher energy electron effects) and a slow (representing an afterglow situation) decaying component. Ar and Xe at 100 and 200 torr

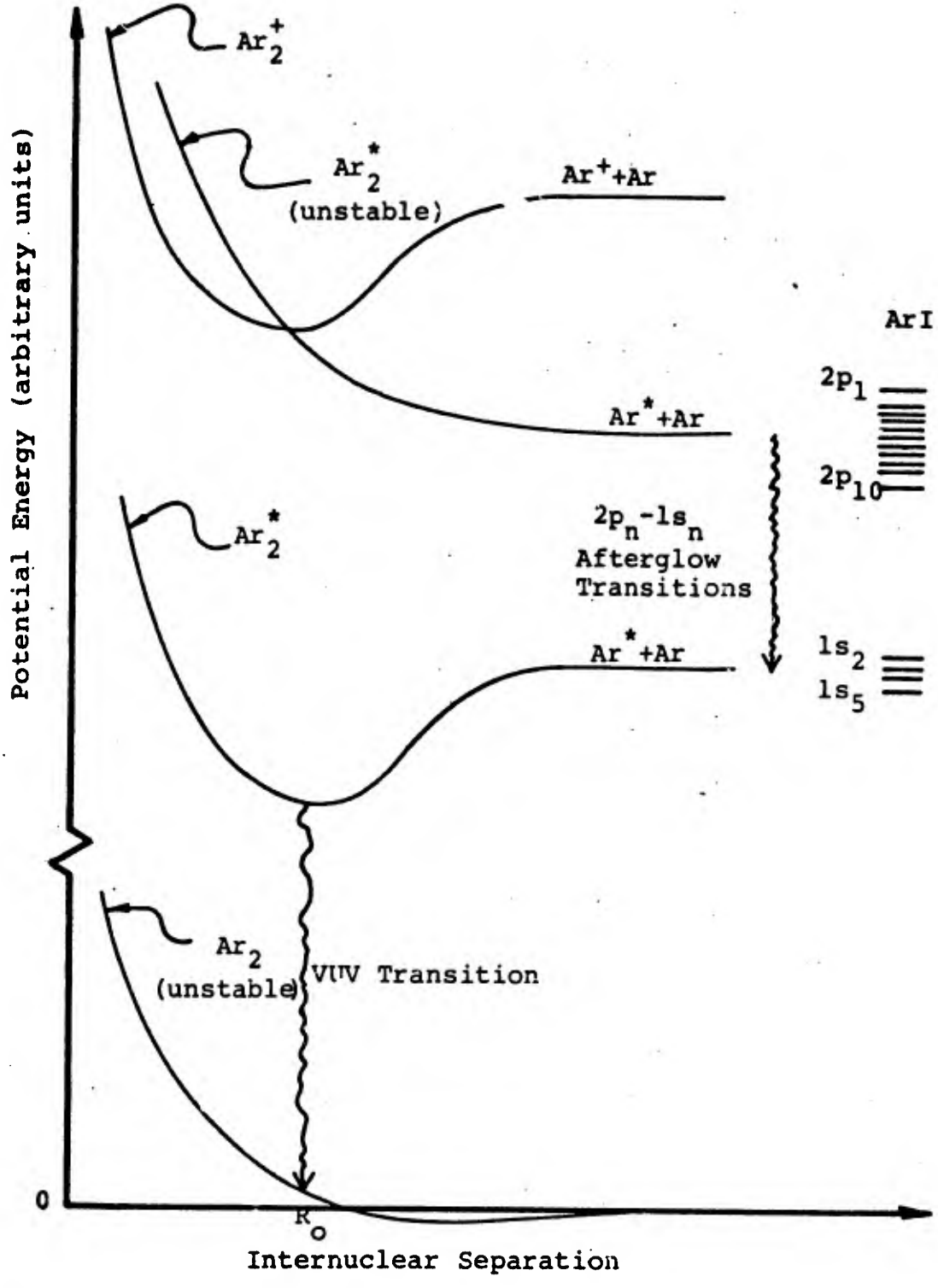

Figure 2.1: Ar_2^+ and Ar_2 Potential Energy Curves Showing Also ArI Levels and Important Transitions After [51]

respectively were reported in detail. In Ar the ratio of the amplitude of the slowly decaying component to the amplitude of the emission during the pulse over the region 7000-7200Å (includes 7067 and 7147Å ArI lines) was determined to be 10%. They conclude the afterglow emissions arise from either radiative recombination or electron excitation from metastable levels. In view of the more recent work on afterglows as already discussed, the former cause seems correct. In Xe the ratio for various spectral regions reaches as high as 95%. The large number of lines (XeI and II) in each spectral region make the data more difficult to interpret than in the Ar case. They do conclude, however, that the lines from Xe primarily result from dissociative recombination. More definitive information at higher pressures has not been published.

The bulk of the measurements of dissociative recombination coefficients have been made at low electron temperatures and also under conditions where the ion, electron and gas temperatures are approximately equal. The cause has been the convenience of working with afterglows. The recombination coefficient is known to be a function of electron temperature, T_e, and for the case of Ar has been found proportional to $T_e^{-.67}$ [55]. Xe has not been studied in this respect, but the temperature variation is probably not greatly different from the theoretical $T_e^{-.5}$ variation.

Experiments with Ne, Ar and N_2 lend support to this assumption [49]. More rigorous model results are available [56] but are not warranted for use here. The T_e dependence implies that one would expect to find the recombination coefficient for a gas excited by ionizing radiation to be dependent upon the electron (including of course all secondaries) energy distribution which may not be so simple to characterize by a single T_e value. Given a fixed radiation source incident upon a gas, this effect would be expected to manifest itself as a pressure dependence of the recombination coefficient.

When investigating recombination in plasma created by highly ionizing radiation, columnar recombination effects must be considered. When a charged particle slows down and creates ions and electrons along its path, a certain period of time exists (until the particles diffuse significantly away from the particle path) when the electron and ion densities will be quite large near the path. During this time, near the particle track recombination rates will be much higher than in the bulk of the ionized medium because of these higher local densities. If one measures the recombination coefficient for recombination over the entire volume based upon the average electron density, it will be higher than for a uniformly ionized medium such as that produced by gamma rays. This problem most recently has

been treated theoretically by Orvis [46] and Wilhelm [57]. Experimentally Ellis and Imani [58] investigated the effect by comparing the observed volume recombination coefficients for gamma and fission fragment generated plasmas. Coefficients for fission fragment plasmas were higher by a factor of 3 to 4. The enhancement due to columnar recombination effects agreed with that predicted by Wilhelm's theory to within 4%. For this reason Wilhelm's theory will be used here to estimate a recombination coefficient for the plasma in this study.

Following the approach of Ellis and Imani [58] the recombination coefficient for fission fragment ionization, α_{ff}, can be written as follows in terms of the coefficient for gamma ionization, α_λ,

$$\alpha_{ff} = \frac{\alpha_\lambda^2 N_o}{4\pi D_a \left[\ln\left(1+\frac{\alpha_\lambda N_o}{4\pi D_a}\right)\right]} \qquad 2.7$$

where N_o is the initial ionization density expressed in ion pairs per unit length and D_a is the ambipolar diffusion coefficient. A maximum N_o for Ar and Xe is 1.8×10^6 and 7.3×10^6 ion pairs per cm (as calculated in the section on energy deposition). D_a may be calculated from the following expression [59]

$$D_a \approx 2D_+ = \frac{2kT}{e}\mu = 4.8\times10^{-4}\,\frac{T^2}{P}\,\mu_0 \qquad 2.8$$

where k is the Boltzmann constant (8.62×10^{-5} eV/°K), P is the pressure in torr, T is the ion temperature in °K, e is the electronic charge, and μ and μ_0 are the ion mobility and reduced mobility in our case for Ar_2^+ and Xe_2^+. Reasonable values for μ_0 appear to be 1.9 for Ar_2^+ [60-61] and 0.79 cm^2/N sec for Xe_2^+ [62]. Corresponding values for D_a at a temperature 400°K (the actual temperature measured for the Xe case) are .192 and .080 cm^2/sec. For Ar at higher pressures α_λ has recently been measured by Kaiser [63] and for 760 torr is 3.0×10^{-6} cm^3/sec. The reason for the higher α value at high pressure is not known. This result compares well with those from an investigation of α in the noble gases from 5-150 torr excited by a beam of 600 KeV electrons [64]. In this latter study at 150 torr $\alpha(Ar) = 5.0\times10^{-6}$ and $\alpha(Xe) = 1\times10^{-6}$ cm^3/sec and their variation with pressure is asymptotic, suggesting these are also good values at 760 torr. Thus 3.0×10^{-6} and 1×10^{-6} cm^3/sec will be used here for Ar and Xe respectively. For Ar and Xe α_{ff} is calculated to be 5.7×10^{-6} and 3.4×10^{-6} cm^3/sec respectively. These values which will later be used to calculate the electron densities show that columnar recombination is important in the present situation. That the effect is not several orders of magnitude, however, is suggestive that

substantial recombination does not occur at extremely high local electron densities. Most recombination will still proceed by way of the molecular ions.

There are two sources of Ar_2^+ in the plasma, 3-body conversion of Ar^+ ions by the reaction

$$Ar^+ + Ar + Ar \xrightarrow{k_1} Ar_2^+ + e^- + Ar \qquad 2.9$$

and associative ionization by the reaction

$$Ar^* + Ar \xrightarrow{k_2} Ar_2^+ + e^- \qquad 2.10$$

where k_1 and k_2 are the appropriate rate coefficients. Typical values for k_1 at 300°K are 2.5×10^{-31} [65] and 3.6×10^{-31} cm^{-6} sec^{-1} [66] for Ar and Xe respectively. The corresponding lifetimes for the atomic ions from this process are 5.5 and 3.8 ns at 760 torr which are clearly shorter than the lifetime of the atomic ion to recombination (on the order of microseconds for our plasma). Recombination must proceed by way of the molecular ion as previously assumed.

Associative ionization has also been studied in Ar and Xe [67]. The thresholds for the process were found to be 14.71 and 11.16 eV for Ar and Xe, respectively. For the various Ar levels studied the ratios of de-exciting to

diatomic-ion-formation collisions ranged from 2.5 to .13. Values for τk_2 for various higher excited levels (the product of the effective radiative lifetime and diatomic-ion-formation rate constant) ranged from 3.6×10^{-18} to $1.28 \times 10^{-16} cm^3$. At 760 torr and 300°K the ratios of the radiative to collisional lifetime may be calculated from these values and are found to be in the range 96-3440. Radiation arising from levels above the threshold for associative ionization is not likely to be observed. Hanle et al. [27] invoked the process of associative ionization to explain why in their electron beam excitation studies the violet ArI lines were so weak compared to the red ArI lines. While this is probably valid for levels above the 14.71 eV threshold, it is unlikely the $3p_n$ levels would be affected since all but one of the levels is below this threshold. Detailed τk_2 data for Xe are not available, but it is probably a safe assumption to say that radiation from XeI levels above 11.16 eV is unlikely.

2.2.3 Trapping and Optical Thickness

At the high pressures employed in this study trapping of resonance radiation will enhance the branching rates for decay to lower excited states by preventing escape of radiation emanating from ground state transitions. The effective lifetime of the trapped states will show a corresponding

increase [68]. In the case of Ar and Xe this means that the $1s_2$ and $1s_4$ levels will have substantially longer lifetimes and higher steady state populations. This makes these levels along with the $1s_3$ and $1s_5$ metastable states potentially available for excitation by electrons to higher levels. For a metastable state this is written:

$$Ar^m + e^- \rightarrow Ar^* + e^- \qquad 2.11$$

Except for the above consideration the plasmas in this study may be considered optically transparent owing to the relatively low excited state densities expected.

2.2.4 Collisional Transfer of Excitation

Although a number of collisional processes are possible in a plasma, because in our case the plasma is weakly ionized and excited, only collisions with neutrals need to be considered. Two such reactions (2.9 and 2.10) have already been discussed. Of interest in this section are collisions of the type

$$Ar^{**} + Ar \rightleftarrows Ar^* + Ar + KE \qquad 2.12$$

between close-lying excited states (designated by ** and *).

Such collisions occur with a reasonable cross section for excited states lying closer than several kT of the gas apart. In the present case kT $\lesssim$ .05 eV. The cross sections would be negligible for states having separations of more than a few tenths of an eV [25]. The above reaction will have a tendency to cause populations to build up for states separated from the next lower state by a substantial energy difference. While the above reaction is almost certainly of importance in the high pressure plasmas studied, a quantitative assessment of the effects are beyond our present capability because of their complexity.

2.2.5 Qualitative Summary Description of the Plasmas

An attempt will now be made to put the above individual pieces of the picture together in a qualitative way. The fission fragments produce an electron population to which all the plasma effects may be attributed. The electron population will be roughly Maxwellian at low energies (with a temperature close to that of the gas) and have a high energy component corresponding to the electron slowing down spectrum. The higher energy electrons produce ionization (and excited ions) and excitation from the ground state according to the corona model. Superimposed on the distribution of ions and excited states as determined by the corona model are the following effects:

1) $2p_n$ excited state population from dissociative recombination of Ar_2^+ to which all Ar^+ is rapidly converted.

2) $2p_n$ excited state population by low energy electron excitation of the $1s_n$ long lived states.

3) higher (>14.710 eV) excited state losses by associative ionization.

4) a redistribution of close-lying states from collisional excitation transfer.

Xe is purely analogous to the Ar case, although the relative importance of the various effects may be appreciably different.

2.3 Energy Deposition Calculations and Spatial Effects

Previous fission fragment excitation experiments have used cylindrical fission fragment sources in order to enhance the volumetric energy deposition. In this study of paramount importance was the desire to obtain spectra at different distances from the fissioning source, reflecting excitation by different average fragment energies and different volumetric energy deposition rates (and resulting electron densities). Specifically it was desired to assess the importance of the fission fragment energy spectrum in determining the excitation character. As most excitation is attributed to secondary electrons, this can also be interpreted as an examination of delta ray energy spectrum effects. Each of these aspects of the problem will now be examined analytically.

2.3.1 Energy Deposition Calculation

The geometry for the problem is depicted in Figure 2.2. Essentially we have a finite rectangular plane source and desire to calculate the volumetric energy deposition at every point P(x,y,z) in our observation region (i.e., where the monochromator will be sampling during the spatial measurements). For a given P(x,y,z) any point on the source less than one fission fragment range away can contribute to the dE/dV for that point. The problem is clearly two dimensional owing to the lack of symmetry. More specifically this can be stated as follows:

$$\frac{dE}{dV}(x,y,z) = \int\int_{A_s} \frac{dE}{dV}(x,y,z;x_s,y_s)\,dx_s\,dy_s \qquad 2.13$$

where A_s is the area of the source and dE/dV is the volumetric energy deposition rate at P(x,y,z) per unit source area from a point (s_x,y_s) on the source.

The approach taken here to evaluate 2.13 is to divide up the source into small incremental areas and for each point P(x,y,z) sum the calculated contribution to dE/dV from fragments produced in each incremental area of the source (in effect a numerical integration). If the origin of the coordinate system is taken at the center of the

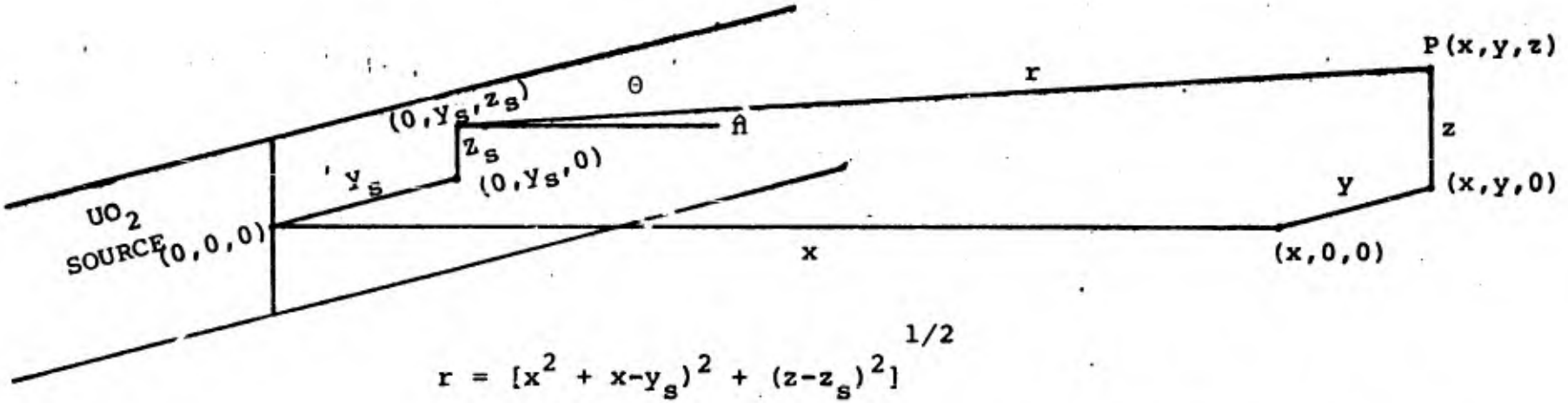

$$r = [x^2 + x\text{-}y_s)^2 + (z\text{-}z_s)^2]^{1/2}$$

$\cos\Theta = \frac{x}{r}$ where Θ is the angle r makes with the yz plane

$\hat{n}$ = vector normal to the source plane

Figure 2.2: Geometry for Energy Deposition Calculations and Spatial Effects Evaluation

rectangular source, dE/dV (x,y,z) need only be evaluated for positive y and z since by symmetry

$$\frac{dE}{dV}(x,y,z) = \frac{dE}{dV}(x, \pm y, \pm z) \qquad 2.14$$

The following factors must be taken into account in evaluating $dE/dV(x,y,z; x_s, y_s)$:

(1) Since fission fragments are not emitted isotropically from the source, the angular distribution function, $p(\Omega)$, is important. $p(\Omega)$ is the probability per unit solid angle that a fragment is emitted at an angle, θ, from the normal to the source. $p(\Omega)$ will be independent of θ, and it is further tacitly assumed here that the average fragment energy is independent of θ.

(2) dE/dr is a function of range (or fragment energy) along the fragment path.

(3) The effective length, Δr, over which the fragment deposits energy in an imaginary (and arbitrary) incremental volume, ΔV or $\Delta x \Delta y \Delta z$, with the point P(x,y,z) at its center depends on θ.(Note: This imaginary volume element is only a tool to better visualize what is happening.)

(4) The effective fragment source rate per unit area of source, S_A, must be related to the source volumetric fission rate and include the effect of self-absorption.

The energy, dE, deposited in ΔV by an incremental area, ΔA_s, of the source at (s_x, y_s) can be written

$$dE(x,y,z;\ x_s,y_s) = S_A\ \Delta A_s\ p(\Omega)\Delta\Omega\ \frac{dE}{dr}\ \Delta r \qquad 2.15$$

where $\Delta\Omega$ is the solid angle subtended by the imaginary incremental volume.

Based upon an experimental effort investigating the angular and energy dependence of fission fragments emitted from UO_2 coatings, $P(\Omega)$ is proportional to $\cos\theta$ [69]. The separation of energy and angular dependence was shown to be justified for thick coatings, which is true in the present case (i.e., the 3-micron coating is about one fission fragment range thick). Thus $P(\Omega)$ can be written as a normalized probability distribution function simply as

$$P(\Omega) = \frac{\cos\theta}{\pi} \qquad 2.16$$

where the normalization is such that

$$\int_0^{\pi/2} p(\Omega)\ \ d\Omega\ = 1 \qquad 2.17$$

The effective length, Θr, can be expressed as a function only of Δx, if we make Δy and Δz large enough with respect to Δx. Specifically, we want to insure

that Δr only intersects the sides of our imaginary volume at the two planes defining Δx. This is allowed because ΔV is completely arbitrary. Thus based on geometrical considerations one can write

$$\Delta r = \frac{\Delta x}{\cos\theta} \qquad 2.18$$

The $\Delta\Omega$ subtended by ΔV can simply be written in terms of steradians as

$$\Delta\Omega = \frac{\Delta y \Delta z}{r^2} \qquad 2.19$$

Upon direct substitution into the expression for dE and dividing by ΔV yields the following expression for the volumetric energy deposition rate at the point P(x,y,z) due to an incremental area of source, ΔA_s, located at (s_x, y_s),

$$\frac{dE}{dV}(x,y,z;\ x_s,y_s) = S_A \Delta A_s \frac{\cos\theta}{r^2} \frac{dt}{dr} \qquad 2.20$$

Incidentally, equation 2.13 reduces to a particularly simple form on the source surface (i.e., when x=0):

$$\frac{dE}{dV}(0,y,z) = S_A \frac{dE}{dx}\Big|_{x=0} = 2S_Z \frac{dE}{dr}\Big|_{r=0} \qquad 2.21$$

The factor of 2 in 2.21 arises because in the increment Δx next to the source, the average track length, $\Delta\hat{r}$, through the region defined by Δx is

$$r = \int_0^{2\pi} \int_0^{\pi/2} r\, p(\Omega)\, \sin\theta d\theta d\theta \qquad 2.22$$

$$= \int_0^{2\pi} \int_0^{\pi/2} \frac{\Delta x}{\cos\theta} \frac{\cos\theta}{\pi} \sin\theta d\theta d\theta = 2\Delta x$$

Thus we can write from conservation of energy that

$$\frac{dE}{dx} \Delta x = \frac{dE}{dr} \Delta\hat{r} = 2 \frac{dE}{dr} \Delta x \qquad 2.23$$

In order to effect a calculation from this point using either 2.13 or 2.21 one must select an expression for the specific energy loss of the fission fragments. Owing to the complexity of the problem a purely theoretical approach is generally considered impractical and the following simpler semi-empirical power law [41] for charged particle slowing is employed

$$\frac{E}{E_o} = \left(1 - \frac{r}{r_o}\right)^n \qquad 2.24$$

where E_o and r_o are the initial fragment energy and total range respectively and n is an exponent based on an empirical fit to experimental data. This expression does have a

theoretical basis (when n=2) but is limited in its applicability to fission fragment slowing because of the importance of nuclear elastic collisions at low fragment energies. The expression's simplicity and past success (when n is an empirically derived number) justify its use here. From this expression we can derive

$$\frac{dE}{dr} = - \frac{nE}{r_0} \left(1 - \frac{r}{r_o}\right)^{n-1} \qquad 2.25$$

where the negative sign signifies an energy loss. The experimental range energy data of Fulmer [70] for light and heavy fission fragments in Ar at 760 torr were fitted to determine the best average value of n. It was found to be 1.38. By interpolation of the data reported by Kahn, Harman and Forgue [71] for a 3-micron UO_2 source thickness the relative fragment escape energy, R, was found to be .56. Using 83 MeV for the average fission fragment initial (upon fissioning) energy, the escaping fragment will have an average energy of 46.5 MeV. Again using Fulmer's data [70], a corresponding average fission fragment range, r_o, was found to be 1.32 cm. For Xe, lack of experimental data necessitated selecting n=1.38 on the basis Xe and Ar would not be expected to have radically different slowing down mechanisms for fission fragments. The average range, r_o, for Xe was found to be .40 cm based on that for Ar and

the assumption that the range is inversely proportional to gas density [41].

Calculation of the effective fragment source rate, S_A, or average number of fragments per second per unit area is straightforward. It is simply written as

$$S_A = N\bar{\sigma}\phi t \qquad 2.26$$

where N = number of density of ^{235}U in the source (2.07×10^{22}/cc for 93% enriched UO_2)

$\bar{\sigma}$ = average ^{235}U fission cross section (330 b for a neutron temperature of 260°C)

ϕ = reactor thermal flux in UFTR (2×10^{12} n/cm^2-sec)

t = source thickness (3×10^{-4} cm)

S_A is thus calculated to be 4.1×10^9 cm^2 sec^{-1}. Also using 2.21 and 2.26 the volumetric energy deposition rates on the source surface (the maximum value anywhere in the volume) is 4.0×10^{17} and 1.3×10^{18} eV/cc-sec for Ar and Xe respectively. Assuming w values of 26.3 and 21.9 eV [44] the corresponding average initial ionization densities (calculated by dividing dE/dr by w) along the fragment tracks will be, using 2.25, 1.8×10^6 and 7.3×10^6 ion pairs/cm.

The volumetric energy deposition rates were numerically calculated using the procedures indicated above at various points in the volume. Figures 2.3 and 2.4 illustrate

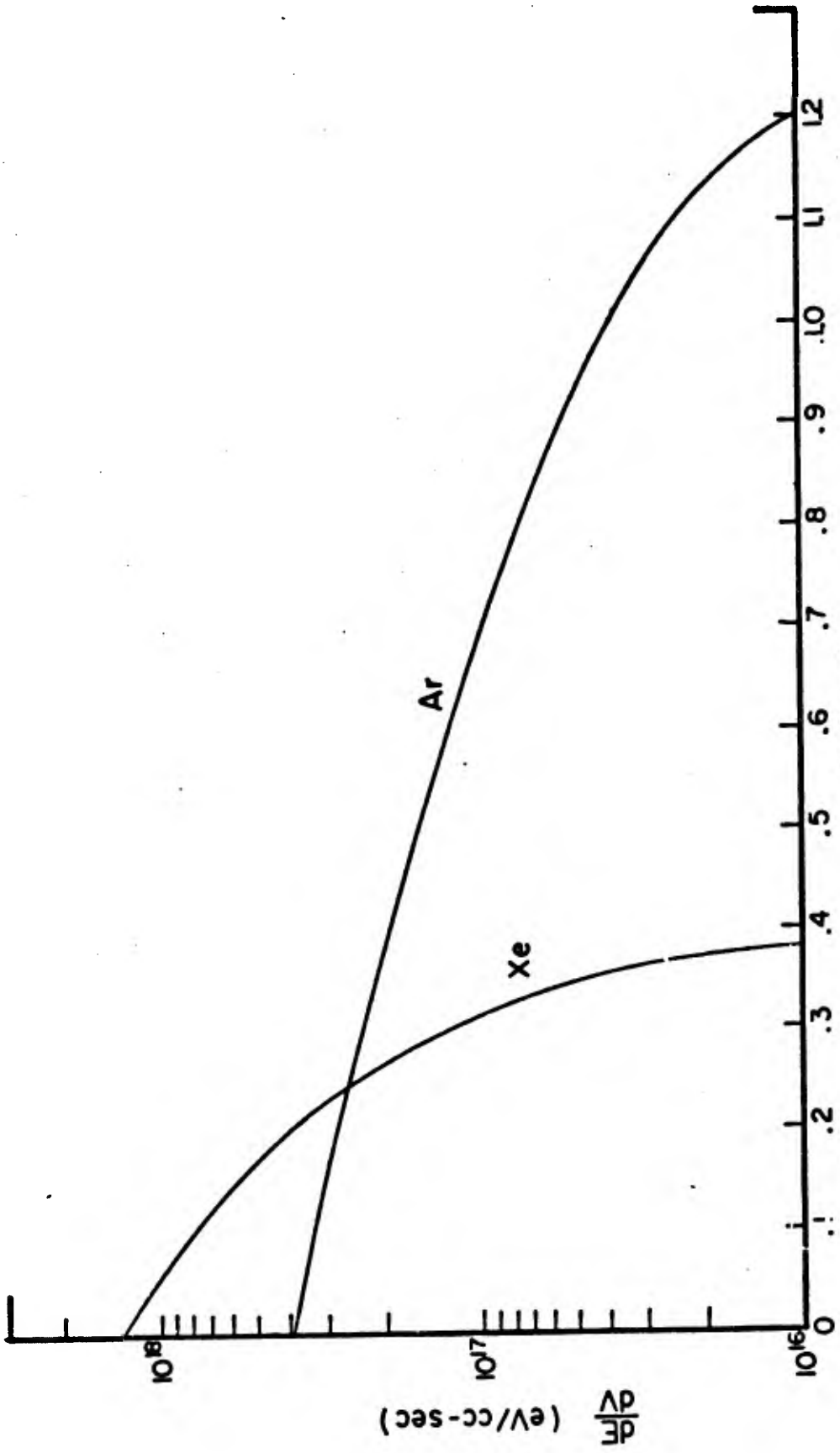

Figure 2.3: Volumetric Energy Deposition Rate as a Function of Distance x from Source Where y = z = 0, $\phi = 2 \times 10^{12} n/cm^2\text{-sec}$, and t = 3μm

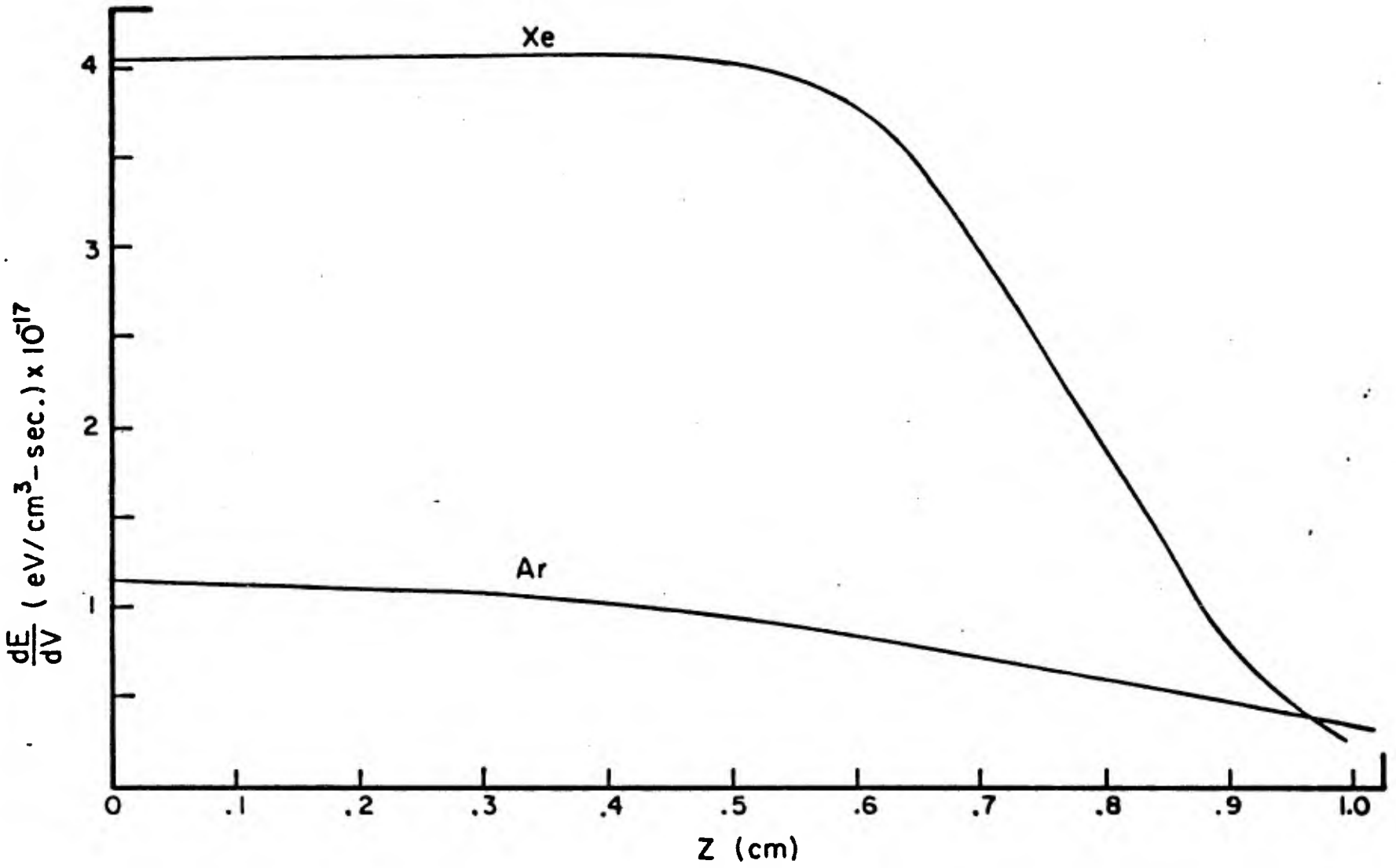

Figure 2.4: Volumetric Energy Deposition Rate as a Function of Distance z from Center of Source (Toward Edge) Where y = 0 and x = $r_o/2$, ϕ = 2×10^{12} n/cm^2-sec, and t = 3μm

the distribution in the x and z directions. Effectively dE/dV(x,y,z) is independent of y except within one fragment range of the end of the source. Also because the height of the monochromotor slit is roughly equal to the source width, the z variation in actual measurements will be small (i.e., in Figure 2.4 only z values less than .8 are sampled). The x variation is the controlling factor in the volumetric energy deposition rates sampled.

2.3.2 Thermalized Electron Density Calculation

Since diffusion losses to our recombination dominated plasma may be neglected the steady state balance equation for electrons may be written

$$\frac{dn}{dt} = 0 = S - \alpha_{ff} n_e^2 \qquad 2.27$$

where S is the electron source rate and n_e is the electron density. Solving for n_e and expressing S in terms of the volumetric energy deposition rate yields

$$n_e = \left(\frac{S}{\alpha_{ff}}\right)^{\frac{1}{2}} = \left(\frac{1}{\alpha_{ff} w}\right)\frac{dE}{dV}^{\frac{1}{2}} \qquad 2.28$$

This expression was evaluated at various points in the plasma volume. The value taken for α_{ff} was the average of the columnar recombination coefficient over the fragment

range (i.e., the average of the maximum and minimum α). To work the problem more rigorously would require treating each fragment for columnar recombination since fragments reaching a given point have different energies and thus N_o values. The values used were 4.4×10^{-6} for Ar and 2.2×10^{-6} for Xe. The variation of n_e with distance from the source is depicted in Figure 2.5. The variation of n_e as a function of z can be seen from Figure 2.6. Note that the effect in both cases is to reduce the apparent variation in terms of a percent of the maximum n_e.

It is interesting to note that the maximum value of n_e does not necessarily occur where dE/dV is largest, since α_{ff} will in actuality depend upon what parts of the individual fragment paths are contributing to the calculated dE/dV. They could have significant impact on the design of fission fragment excited systems at high pressures (where N_o is high) where maximizing n_e is important.

2.3.3 Fragment and Electron Energy Spectra

Every point in our volume has been characterized by a particular dE/dV and n_e value. In addition, the fission fragments and secondary electrons will have a particular energy distribution characteristic of the point. The significance of the secondary electron spectra has already been discussed. Of most importance here will be the high

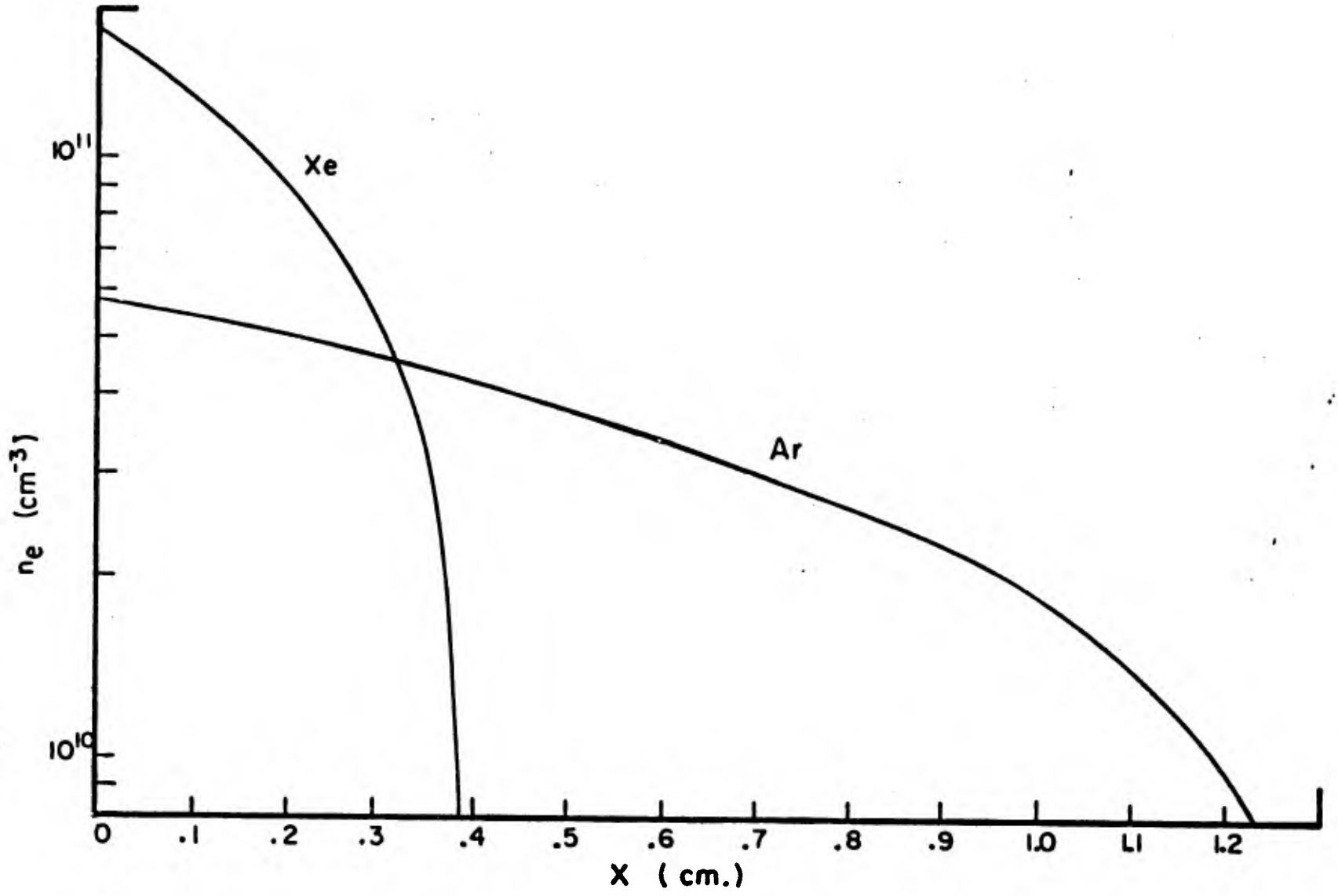

Figure 2.5: Electron Density as a Function of Distance x from Source Where y = z = 0, $\phi = 2 \times 10^{12} n/cm^2\text{-sec}$, $t = 3\mu m$

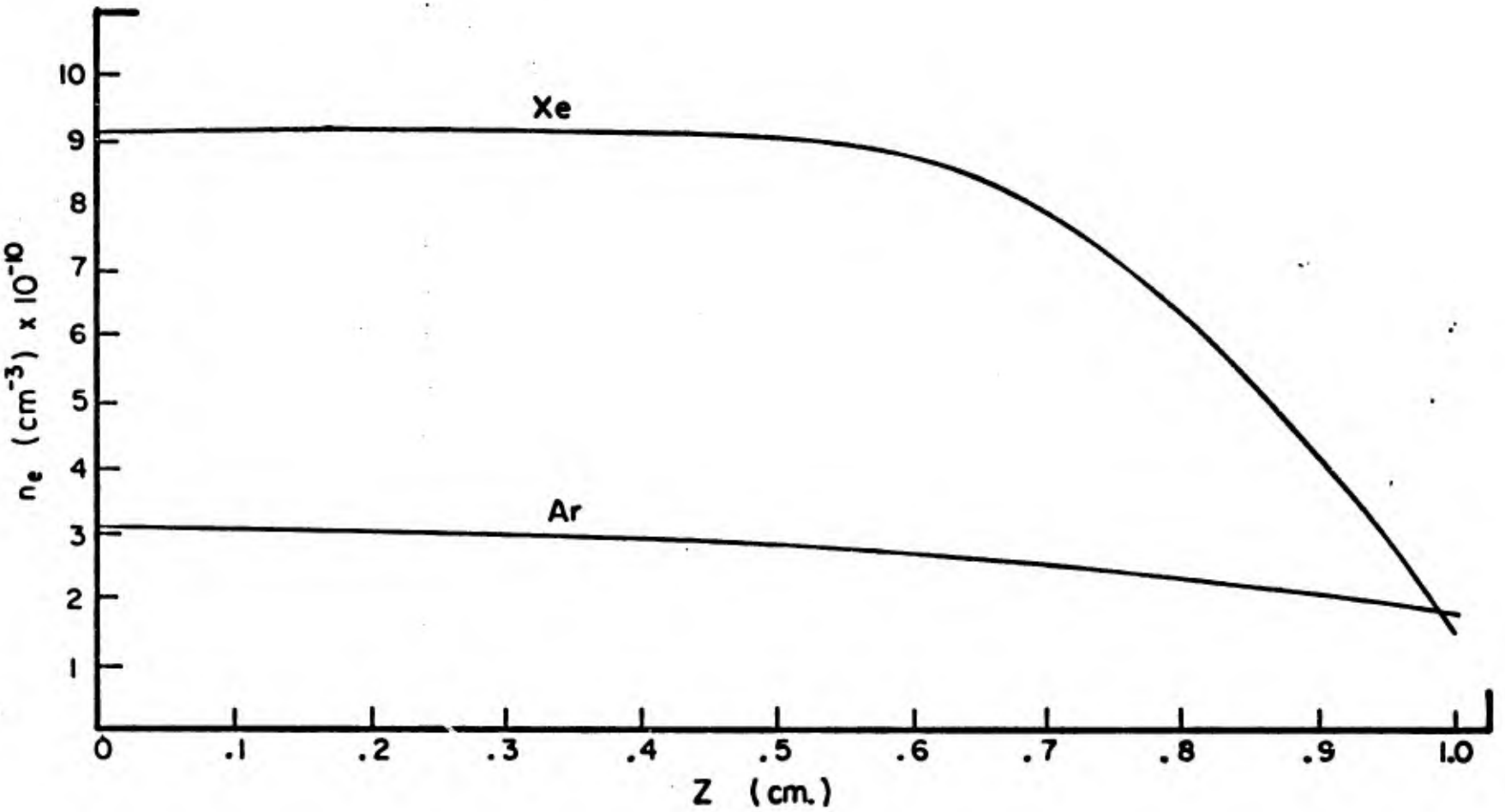

Figure 2.6: Electron Density as a Function of Distance z from Center of Source (Toward Edge) Where y = 0 and x = $r_o/2$, ϕ = $2x10^{12}$n/cm^2-sec, and t = 3μm

energy part of the electron spectrum (i.e., that from the slowing down of delta rays), since the Maxwellian part of the spectrum should be relatively unaffected by the initial delta ray energy spectrum. It was this sort of energy dependence which produced (through the energy dependence of the cross sections) the spatial variations analytically observed for primary alpha particle processes by Theiss and Miley [19-20].

Calculation of the energy of fission fragments losing energy at a particular point is relatively straightforward. The energy spectra of electrons ejected in the resulting ion-atom collisions, however, have not been studied for collisions between high energy ions having a mass typical of fission fragments and lighter atoms such as Ar and Xe. A review of available data was made by Ogurtsov in 1972 [72]. He presents some data for Ar^+-Ar collisions, and data for Xe^+-Xe collisions are also available [73]. These data would be applicable to a study of the ionization produced toward the end of the fragment path where ionization is produced by recoil gas atoms from nuclear elastic collisions between the fragment and gas atom. Unfortunately, it does not help solve the most important problem of primary interactions. This discussion is merely intended to point out that at the present time sufficient data do not exist to determine with any degree of confidence the delta

ray spectra arising from fission fragment interactions. Ogurtsov [72] points out that modeling of collisions between heavy atomic particles does appear promising, so solution of the problem may not be far off. Qualitatively we do know that delta rays will range from the eV to the KeV range. The distribution will always favor the lower energies, but for higher fragment energies the spectrum will be hardened considerably.

Since based upon the above discussion, one can only make qualitative observations based upon the fission fragment energy, this will be investigated in more detail. Instead of looking at an energy spectra we will look at the spectrum in terms of r/r_o which directly yields a fragment energy spectrum based upon a range energy relation such as 2.25, the semi-empirical power law. The problem can then be worked in general terms and apply to any stopping medium. Also to avoid specifying the exponent, n, in 1.21 the problem will be worked for n=1 and n=2 which bounds any practical problem one might expect to encounter. The objective of the remainder of the section will be to develop insight into the problem sufficient to enable interpretation of the experimental data. We wish only to know roughly how much the fragment energy spectrum varies as sampled different distances from the source.

At any given point, P, in our volume a distance x from the source, no fragment can reach P without having gone at least a distance x and no more than a distance r_o, the fragment range. Of interest is what the distribution is for r/r_o for the fragments which are losing energy at the point P. Furthermore it is desirable that the distribution function be weighted by dE/dr since we are interested in what the r/r_o (or energy) distribution for the fragments which deposit most of the energy at P, not those that just barely reach P. Also one must consider angular distribution of the emitted fragments, $p(\Omega)$, which is taken as before to be proportional to $\cos\theta$. The assumption is now made for simplicity that the source is an infinite plane. This assumption is considered justified for two reasons. First, experimentally we only sample the region directly in front of the source, so the calculated results (i.e., $\hat{r}/r_o$) will be worst case. Specifically $\hat{r}$ will actually be closer to x than what we calculate because for a finite source, the maximum distance from which a fragment may arrive at P can only be less than r_o. Secondly, only results for small x/r_o values will be affected since as x approaches r_o, only a small area of the source nearest P will contribute to the result. This effect is further amplified by weighting the distribution by dE/dr and $p(\Omega)$.

Assuming an infinite source, the only part of the source from which a fission fragment can reach x is a circle defined by a line which is a distance r_o from x. The geometry of the problem is depicted in Figure 2.7. In this figure r_o is the radius of the circle of the source from which fragments can reach P and r' is the distance from the center of the circle to the source point a distance r from P. The unnormalized distribution function, f(r'), which represents the relative number of fragments which reach P from a radius r' on the source weighted by $\cos\theta$ and dE/dr can be written by inspection as

$$f(r') = \frac{\cos\theta}{r^2}\left(\frac{dE}{dr}\right) r' \qquad 2.29$$

We are interested in f(r) which requires the following relation between dr' and dr':

$$\frac{dr'}{dr} = \frac{d}{dr}\left(\sqrt{r^2-x^2}\right) = \frac{r}{r'}, \qquad 2.30$$

The expression for f(r) is now found from the relation

$$f(r)dr = f(r')dr' \qquad 2.31$$

to be simply

$$f(r) = \frac{\cos\theta}{r}\frac{dE}{dr} = \frac{x}{r^2}\left(\frac{dE}{dr}\right) \qquad 2.32$$

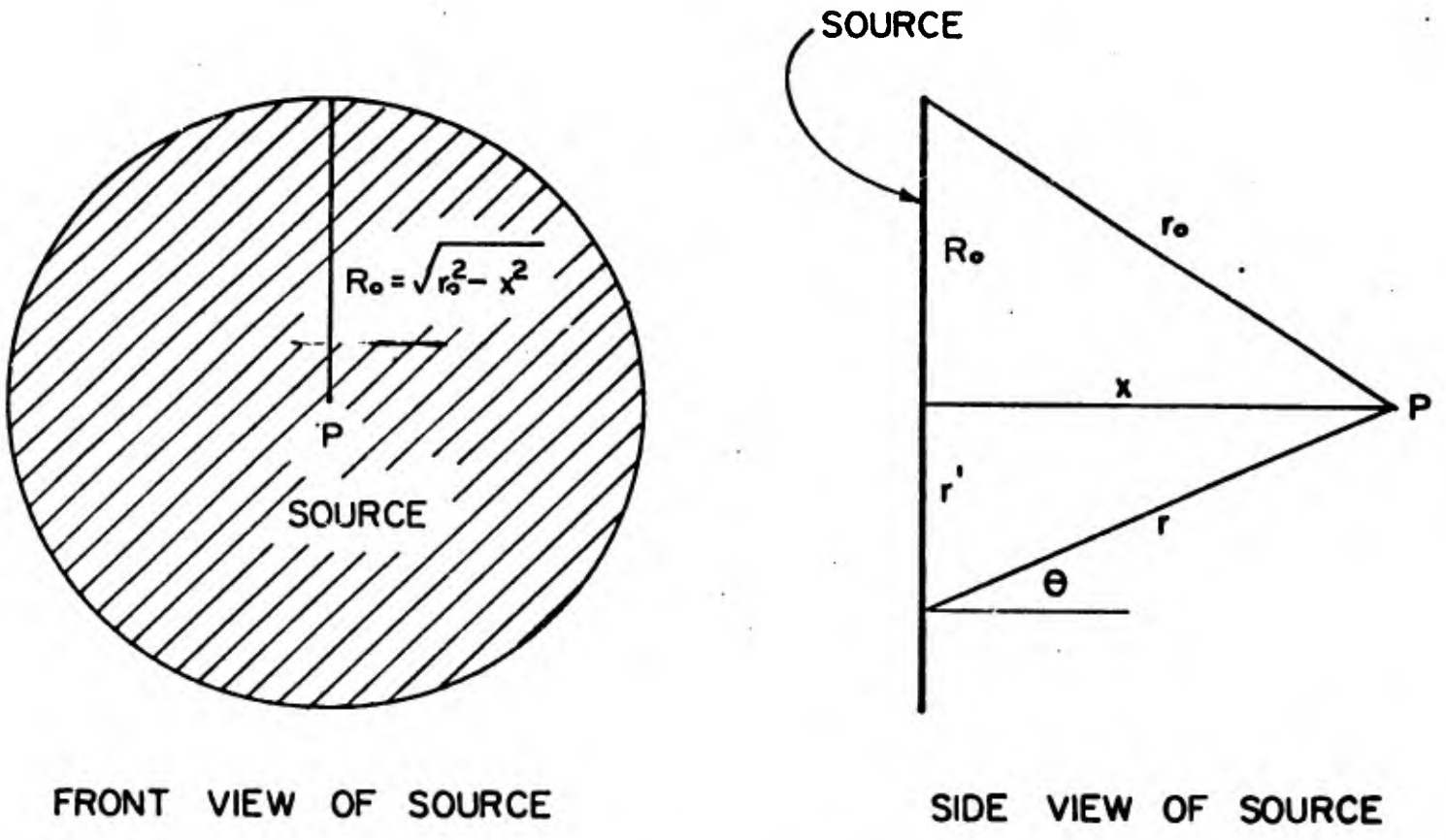

Figure 2.7: Geometry for Calculation of Fission Fragment Path Length Distribution Function

Dropping the x since it is not a function of r yields

$$f(r) = \frac{1}{r^2}\left(\frac{dE}{dr}\right) \qquad 2.33$$

Now using 2.25 with n=1 and 2 for dE/dr and retaining only the r dependence produces the following relations where it is understood that $x < r < r_o$

for n=1:

$$f(r) = \frac{1}{r^2} \qquad 2.34$$

for n=2:

$$f(r) = \frac{1}{r^2} - \frac{1}{rr_o} \qquad 2.35$$

These can be conveniently normalized by dividing the above expressions by their integral from x to r_o

for n=1:

$$f(r) = \frac{1}{r_o}\left(\frac{r_o}{r}\right)^2\left(\frac{r_o}{x} - 1\right)^{-1} \qquad 2.36$$

for n=2:

$$f(r) = \frac{1}{r_o}\left[\left(\frac{r_o}{r}\right)^2 - \left(\frac{r_o}{r}\right)\right]\left[\frac{r_o}{x} - \ln\frac{r_o}{x} - 1\right]^{-1} \qquad 2.37$$

It is convenient to rewrite these relations in the following form for computations where the range of validity is $b < a < 1$ for n=1:

$$r_o f(r) = \frac{a^2}{b-1} \qquad 2.38$$

for n=2:

$$r_o f(r) = \frac{a(a-1)}{b-1nb-1} \qquad 2.39$$

where

$$a = \frac{r_o}{r} \text{ and } b = \frac{r_o}{x}$$

The function $r_o f(r)$ for n=1 and 2 is plotted in Figures 2.8 and 2.9. The curves for n=1.38 would fall somewhere in between those shown.

The purpose in presenting these plots is to show (by examining the spectrum of path lengths traveled) roughly the energy spectrum resolution that was achieved in this experiment. It is quite good for small x because of the $\cos\theta$ term (discriminates against longer r values) and good for large x (i.e., as x approaches r_o) because all fragments reaching x must have gone a distance between x and r_o. For x values inbetween these extremes the

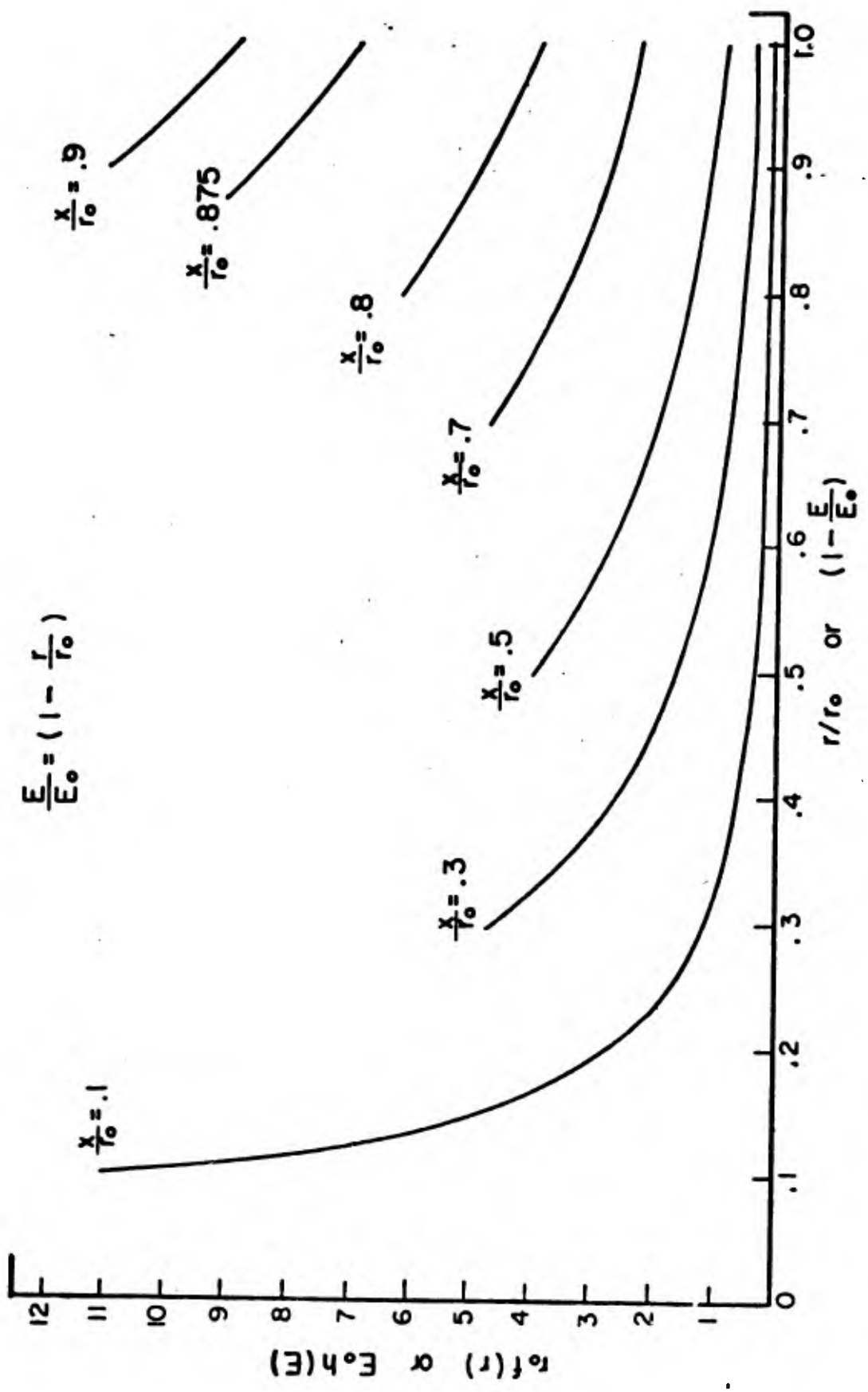

Figure 2.8: $r_o f(r)$ as a Function of x/r_o for n=1

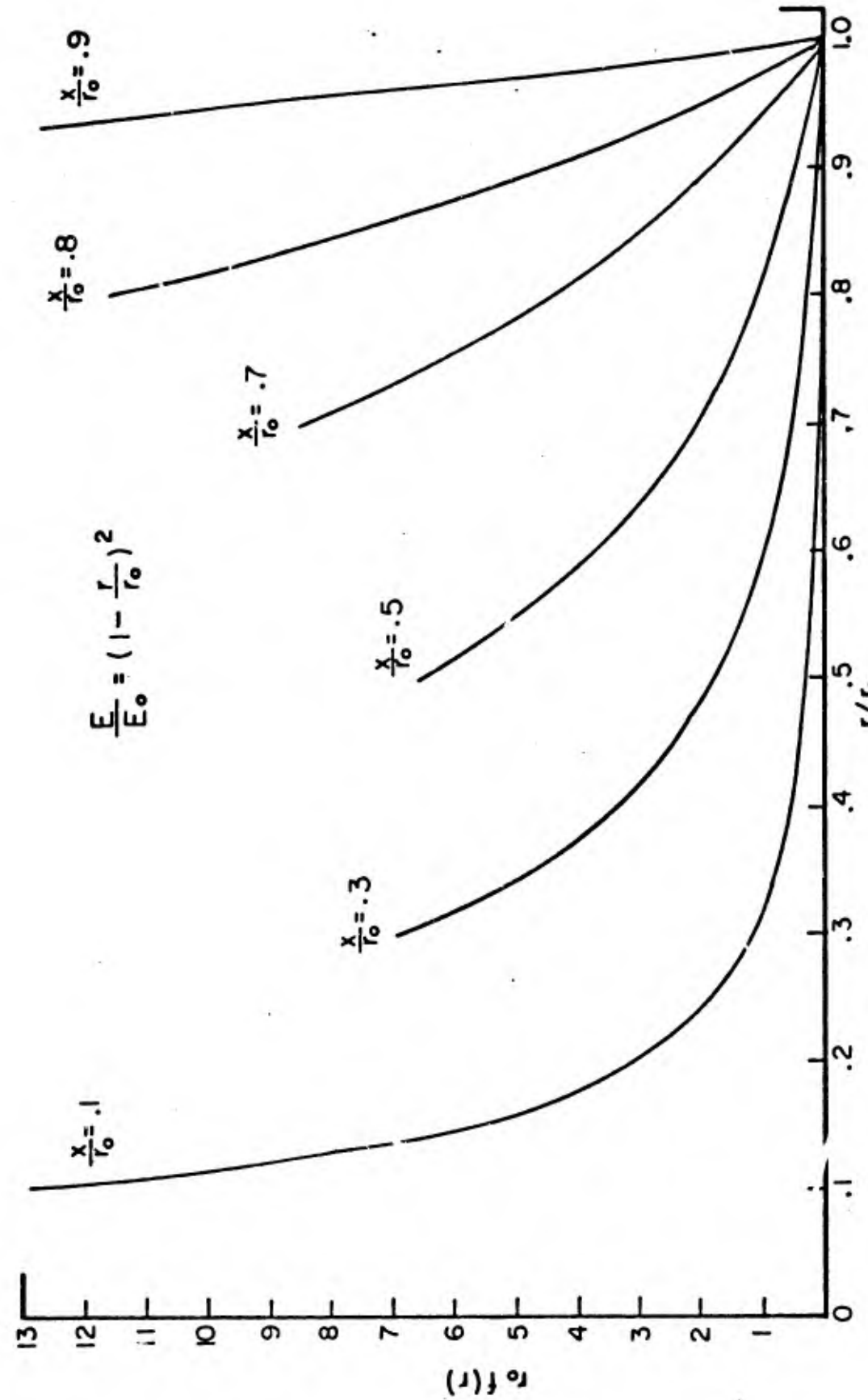

Figure 2.9: $r_o f(r)$ as a Function of x/r_o for n=2

resolution is not as good. The important point here is that it is possible to sample the beginning and end of the fragment paths.

Incidentally, the above expressions can be transformed into distribution functions in terms of the fission fragment energy, h(E).

For n=1:

$$h(E) = \frac{r_o f(r)}{E_o} \; ; \; E_o h(E) = r_o f(r) \qquad 2.40$$

For n=2:

$$h(E) = \frac{r_o f(r)}{2\sqrt{E_o E}} \; ; \; E_o h(E) = \frac{r_o f(r)}{2} \sqrt{\frac{E_o}{E}} \qquad 2.41$$

For the case where n=1 Figure 2.8 already directly shows the energy spectrum with the plot running from high to low energies. The case for n=2 is shown in Figure 2.10. The plots of $E_o h(E)$ in effect illustrate the same things as those for $r_o f(r)$. One can further calculate an average energy $\langle E \rangle / E_o$ as a function of x/r_o in the following way

$$\frac{E}{E_o} = \frac{1}{E_o} \int_x^{r_2} E f(r) dr \qquad 2.42$$

This information is plotted in Figure 2.11 for n=1 and 2 and results from straightforward application of the above equation.

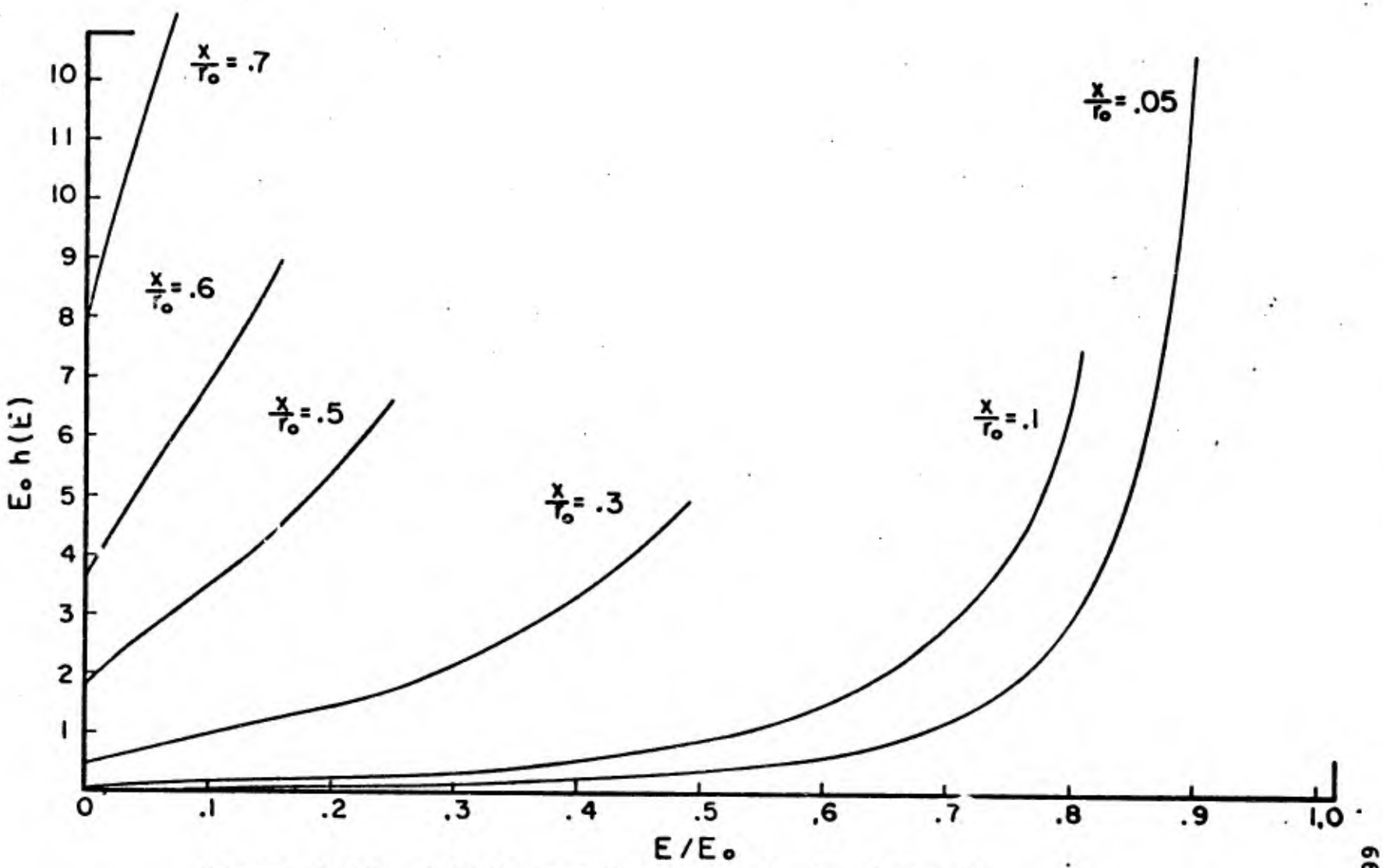

Figure 2.10: $E_o h(E)$ as a Function of x/r_o for n=2

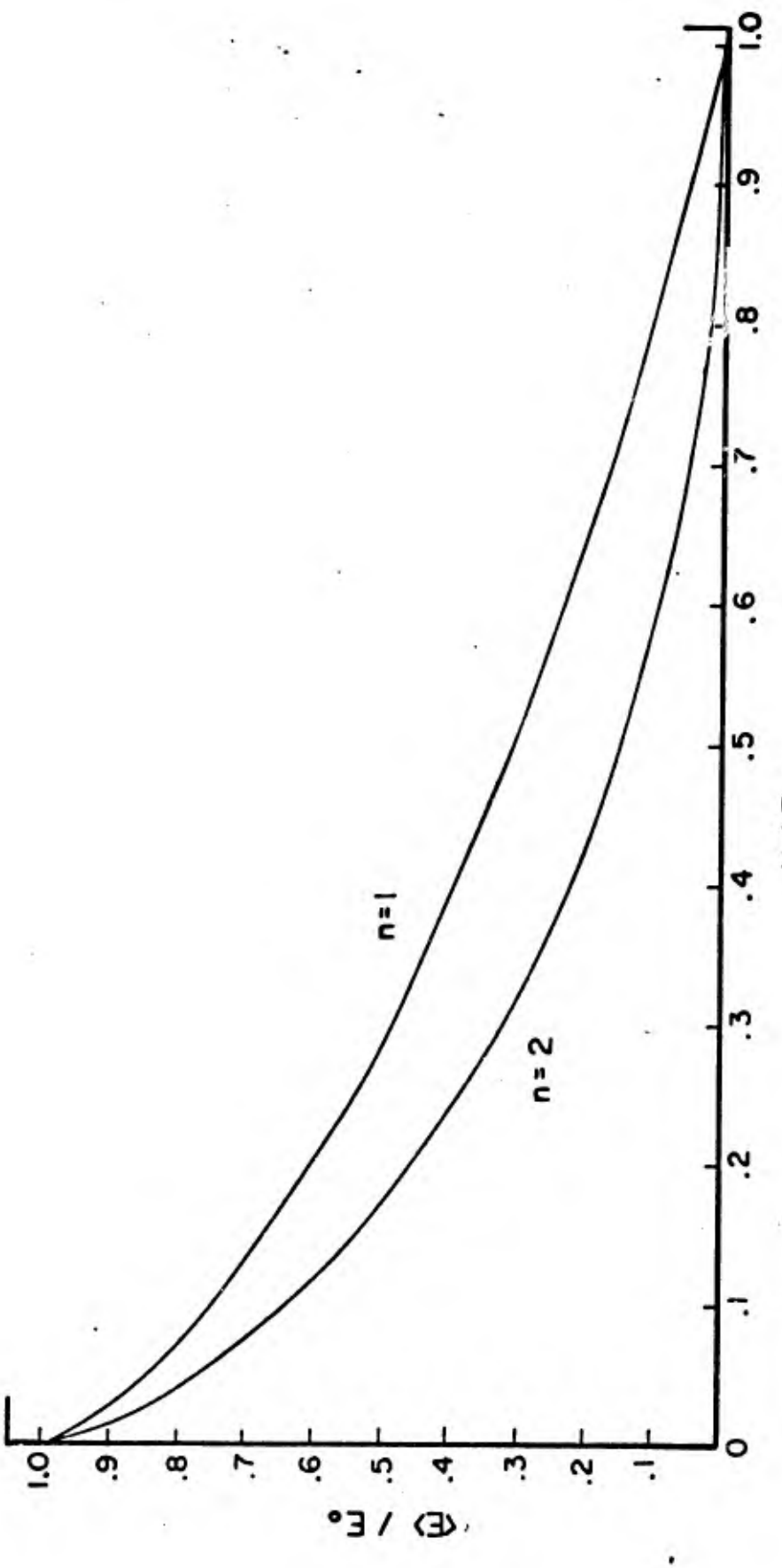

Figure 2.11: Average Relative Fragment Energy as a Function of x/r_o

2.4 Discussion of Experimentally Measurable Parameters

The purpose of this section will be to briefly relate the theory already presented to the parameters we can experimentally measure. Included also are short discussions on pressure dependence and electric field amplification as these were investigated in previous studies which have obvious impact on the interpretation of the data acquired in this study.

2.4.1 Spatial Variations

Sampling spectra at different distances from the source effectively samples different volumetric energy deposition rates, electron densities, fission fragment energy spectra, delta ray energy spectra, secondary electron energy spectra (particularly at intermediate and high energies), and columinar recombination effects (ionization per unit path length will be higher for fragments near the source). Interpretation of any spatial variations must rely upon assessing the importance of these several variables either by measuring some other plasma parameter or analysis.

2.4.2 Emission Intensity as a Function of Reactor Power Level

The volumetric energy deposition rate and square of the thermalized electron density are proportional to reactor power. Linearity with reactor power would be expected for recombination processes (i.e., dissociative recombination) and excited atomic and ionic lines if high energy electrons (before they are sufficiently thermalized to undergo recombination) directly excite them from the ground state. Essentially what this says is that the number of high energy electrons slowing down is proportional to power. For excitation from an excited state (e.g., metastable) whose population is linear with power, the upper excited state populations would be expected to be nonlinear unless these levels were in LTE with the lower excited state.

2.4.3 Pressure Effects

An increase in pressure will increase the recombination coefficient, columinar recombination, and collisional effects (e.g., collisional de-excitation) as well as reduce the volumetric energy deposition rate and electron densities. Experimentally in past studies these latter two effects have been difficult to assess owing to source geometry and stopping power effects.

2.4.4 Electric Field Amplification

The addition of an electric field is simple at least in that it will only influence electrons and harden their energy spectrum. This will in turn result in decreased dissociative recombination according to $T_e^{-.5}$ and increased excitation and ionization due to the increased relative population of higher energy electrons. The low energy part of the electron spectrum (the bulk of the electron population) will be affected and the important parameter is E/P.

2.4.5 Temperature Effects

In the reactor the irradiated gas will heat up by approximately 100°C and emission intensities can be monitored during heating. Heating will increase atomic collisional rates and also raise the thermalized electron temperature slightly.

CHAPTER 3

EXPERIMENTAL SYSTEM DESCRIPTION

3.1 Design Considerations

The system employed by Walters [17] to make his spectral measurements proved quite effective and had the advantage of simplicity. It also provided the capability of changing the pressure of the irradiated gas while in the reactor. This did, unfortunately, require a large system with long pumping distances, thus limiting his ability to control impurities. But by the time the present effort was initiated, new local safety requirements existed which negated use of Walters' basic design, so an entirely new system had to be designed and built anyway. Walters' work did, however, have significant impact on the entire system to be described below.

A primary objective of the experiment was to provide the capability to measure spectra at different distances from the fissioning source. This required a plannar source of fission fragments and an appropriate optical system to sample a well-defined region at a desired distance from the source. In addition it was desired to effect an absolute calibration of the system, so a simple optical system,

ammenable to analysis, was important. Since in all past studies the effects of impurities could not be eliminated, it was desired to maximize gas purity. This suggested a small gas volume in a capsule that could be carefully evacuated and filled under controlled laboratory conditions. The experimental system design also had to consider the following factors normally encountered in these types of studies: low expected light output, high noise level from gamma radiation around the reactor, radiation damage to in core components, possible system overheating from the fission source, and current UFTR safety philosophies. With respect to the last factor, of most importance is the requirement that the experiment provide double containment of fission products. This considerably limited design alternatives and practically eliminated any gas handling while the system was in the reactor.

The construction of a horizontal thruport (HTP) in the reactor on a timely basis to support this research proved of immense value. Besides the convenience of being able to work at waist level, experiment loading and unloading, radiation shielding, system calibration and optical alignment were all greatly simplified. Had this work been attempted in the UFTR center vertical port (CVP), the experiment would have been significantly more complex and time consuming, with some parts being impossible to carry out.

3.2 Overall System Concept

The final result of the above design considerations was the Multipurpose Capsule for Irradiation of Gases (MCFIG) system shown in Figure 3.1. The MCFIG system basically consists of a small capsule (the MCFIG) having a sapphire window mounted in the end and containing a UO_2 fission fragment source. The capsule is evacuated and filled prior to insertion in the test tube assembly. The test tube is an aluminum tube which extends through the HTP and is sealed at each end by use of end caps which have quartz windows for light transmission as shown in Figure 3.2. Two lenses which are part of the optical system are also mounted inside the test tube. After the MCFIG is loaded inside the test tube from the west end of the UFTR and the end cap replaced, the test tube is evacuated to a pressure of approximately 10^{-2} torr using a pump located at the west end and then isolated prior to reactor start-up. The test tube provides secondary containment should the MCFIG somehow leak, the test tube pressure being the primary diagnostic tool to detect it. When a thermocouple was located on the MCFIG it was monitored by instrumentation at the west end of the UFTR.

Once the test tube was isolated the reactor was brought up to power. The neutrons induced fissions in the planar UO_2 (aligned parallel to the monochromator slit)

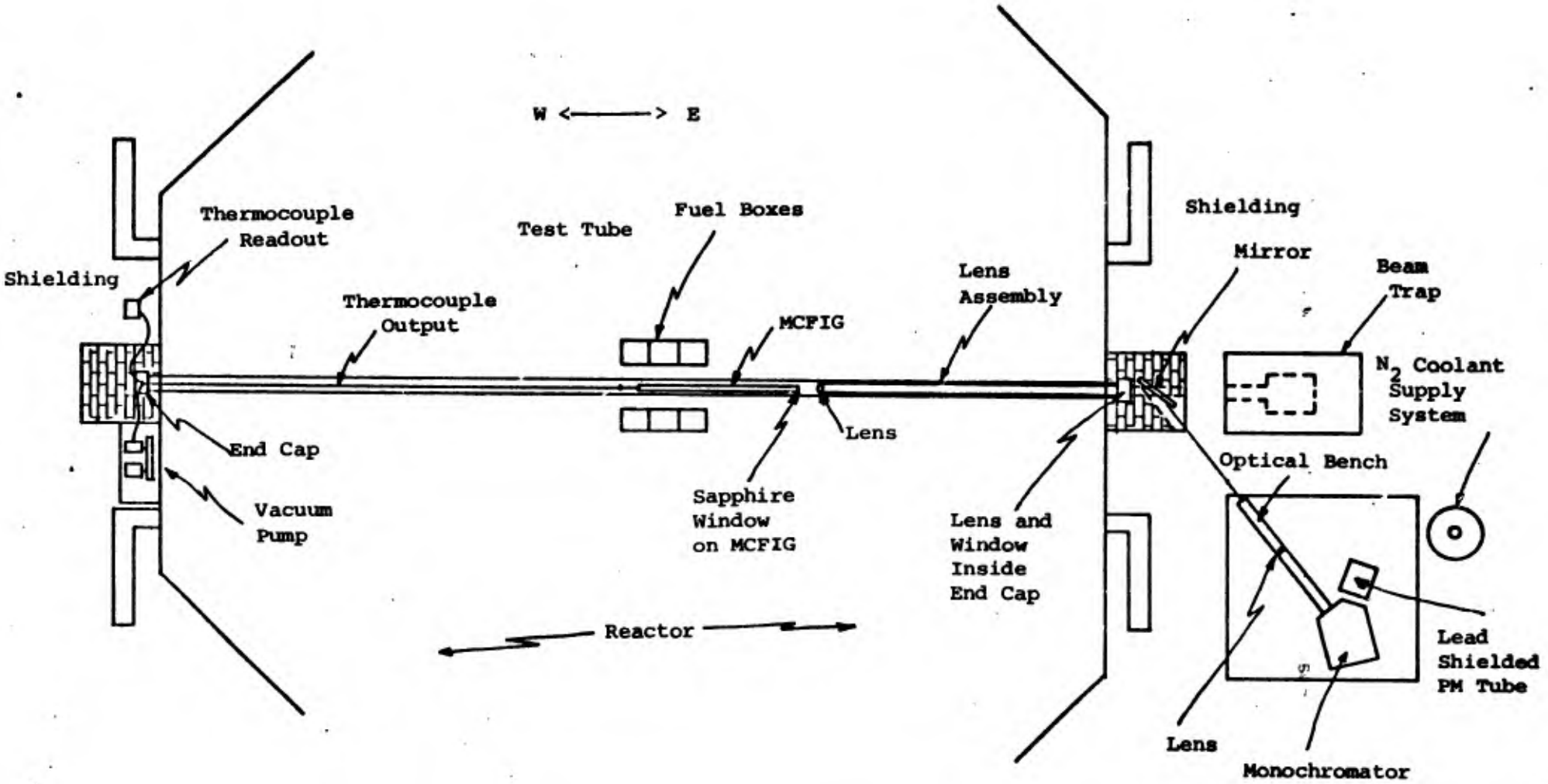

Figure 3.1: Overall Layout for MCFIG Gas Irradiation Studies

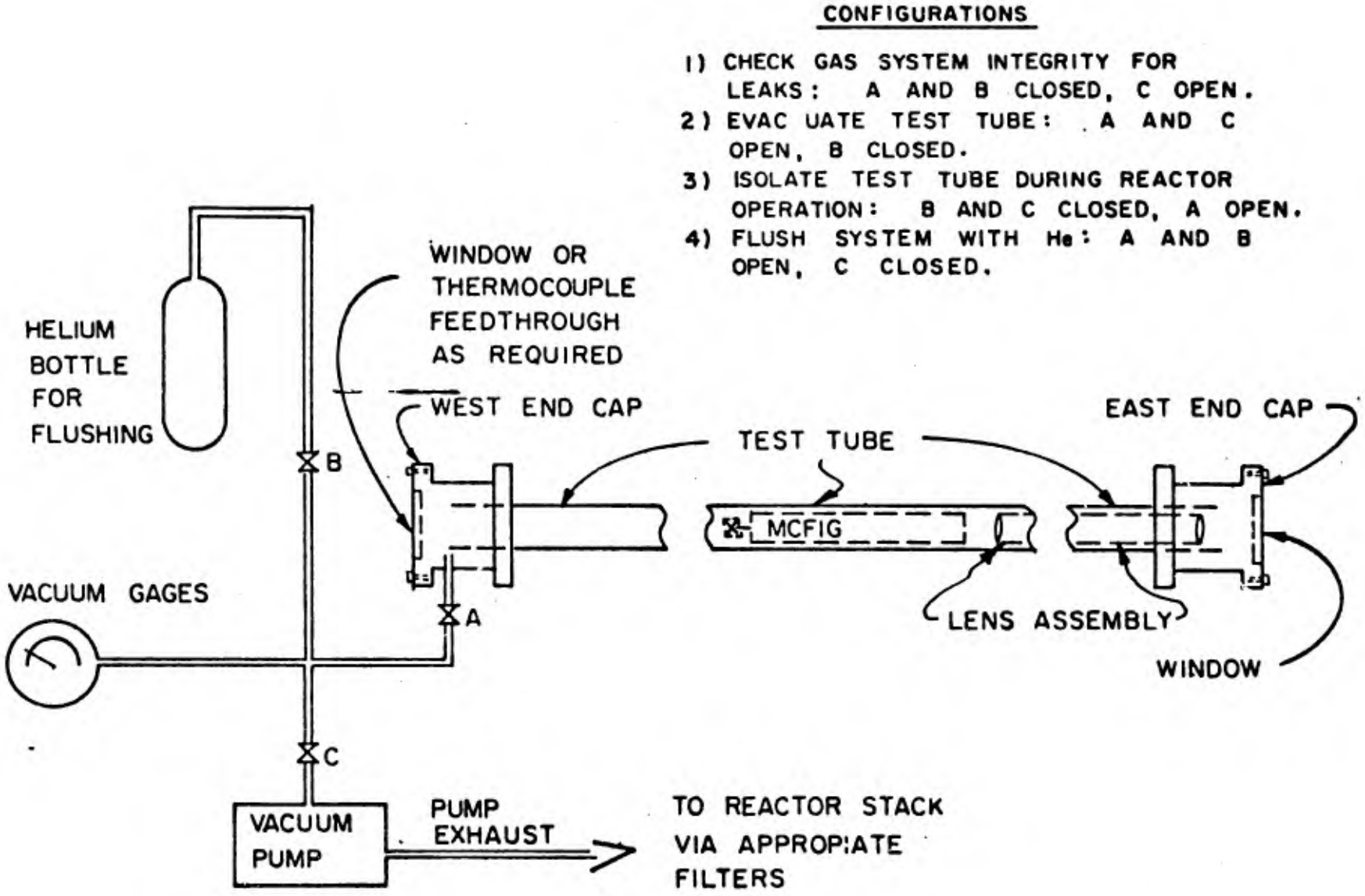

Figure 3.2: Test Tube End Cap Details and Gas Handling System

source which emitted fission fragments into the gas. As the fragments flow in the gas the light emitted passes through the MCFIG sapphire window and is collected by the optical system consisting of three lenses and a rotatable mirror (for looking different distances from the source). The light is focused on the monochromator slit where the spectrum is analyzed by measuring the output current of the photomultiplier and displaying it on an X-Y plotter.

Shielding or otherwise reducing the effects of reactor produced gamma radiation on the photomultiplier is a perpetual problem in experiments around reactors. A total system approach was taken here and may be of some future interest as a significant level of effort was applied to the problem. The approach consisted of the following measures: (1) by shielding, minimizing the general radiation level in critical areas; (2) positioning the photomultiplier as far as practical from the reactor and away from hot spots; (3) shielding the photomultiplier itself; and (4) using a low pass filter to discriminate out the gamma noise. Only (1) will be discussed here, postponing discussion of the other approaches until later sections.

With respect to area shielding, the west end of the UFTR proved a minor problem since little personnel activity takes place there. The only requirement was to reduce radiation levels outside the UFTR building to within allowable

limits. Borated paraffin blocks, steel bricks, and a large concrete block proved generally sufficient. At the east end the shielding had to reduce levels in the working areas (and the experimental instrumentation) to much lower limits as well as provide a reasonably large aperture for light to reach the monochromator. Several approaches failed, so a beam trap was constructed and efforts made to minimize placing material in the path of the beam emerging from the HTP and entering the trap. This approach was highly successful and also permitted easy access to the mirror and its rotation assembly.

3.3 MCFIG Details

The MCFIG is essentially a piece of stainless steel tubing with a commercially available sapphire window welded in one end, and a valve and thermocouple port in the other. This is shown in Figure 3.3 with the exception of the thermocouple port. A MCFIG costs about $150 to produce and can be reused several times depending on the degree of activation. Stainless steel was used primarily because of availability, machinability and cost; also it possesses good vacuum characteristics. Its main disadvantages are that it becomes highly activated when irradiated and has a high reactivity worth. A special MCFIG shielded transporter (MST) had to be constructed and procedures

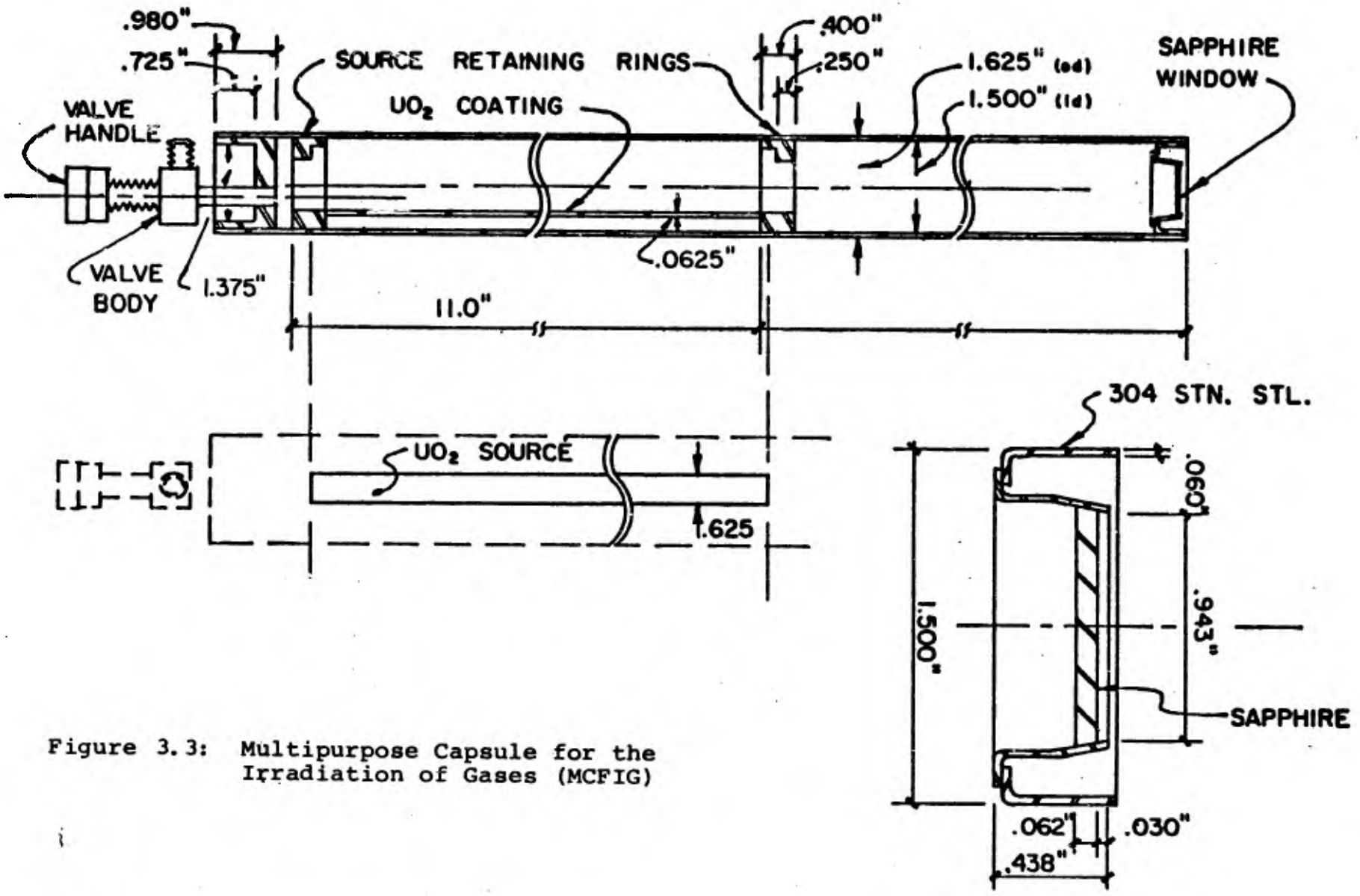

Figure 3.3: Multipurpose Capsule for the Irradiation of Gases (MCFIG)

developed to overcome the activation problem. Reactivity worth was not a problem in this experiment but should be evaluated for any future work to insure the reactor can achieve criticality with the system in place. The MCFIG radial dimension was determined essentially by the HTP dimensions. Two different lengths were used. The Ar data were taken with a short system which subjected the sapphire to the high flux region. Luminescence and damage (see Appendix A) to the sapphire resulted, consequently for Xe measurements the MCFIG was constructed in a way to keep the window out of the high flux region.

3.3.1 Valve and Thermocouple Port

The valve employed was a Nupro SS4H2 bellows type valve which was specially modified so that it would fit within the test tube inside dimension (1.709"). A valve was used instead of a pinch off seal to facilitate handling, particularly during recycle procedures when an irradiated capsule had to be evacuated and refilled. The thermocouple port was a small tube sealed on the inside of the MCFIG which served as a receptacle for a thermocouple. The tube was located just behind the UO_2 source so as not to interfere with the optical collection of light. The temperature was measured only on the Xe filled MCFIG and found to reach approximately 250°F, which is not significant from a MCFIG structural standpoint.

3.3.2 Sapphire Window

The sapphire window was selected primarily because sapphire is relatively resistant to radiation damage and commercially available in a mount weldable to stainless steel. Unfortunately the luminescence observed from this material (see Appendix A) came as a surprise and necessitated additional effort to quantify and understand the luminescence and absorption effects. However, now that these effects are well defined there have been additional benefits such as use of the MCFIG for UF_6 irradiation studies in which quartz windows would be unacceptable.

3.3.3 UO_2 Source

The fission fragment sources were 3-μm thick 93% enriched UO_2 coatings on zircaloy plates which were obtained courtesy of Los Alamos Scientific Laboratory. UO_2 was selected as the coating material because of the availability of information on it. The energy spectrum of fission fragments as a function of coating thickness was studied by Kahn, Harman, and Forgue [71] in 1965 and their data for a 2.53 μm coating appear in Figure 3.4. A 3-μm coating thickness was selected on the basis of their data for average fragment escape energy, E_{AVG}, and escape fraction, P_E, as a function of coating thickness. Specifically

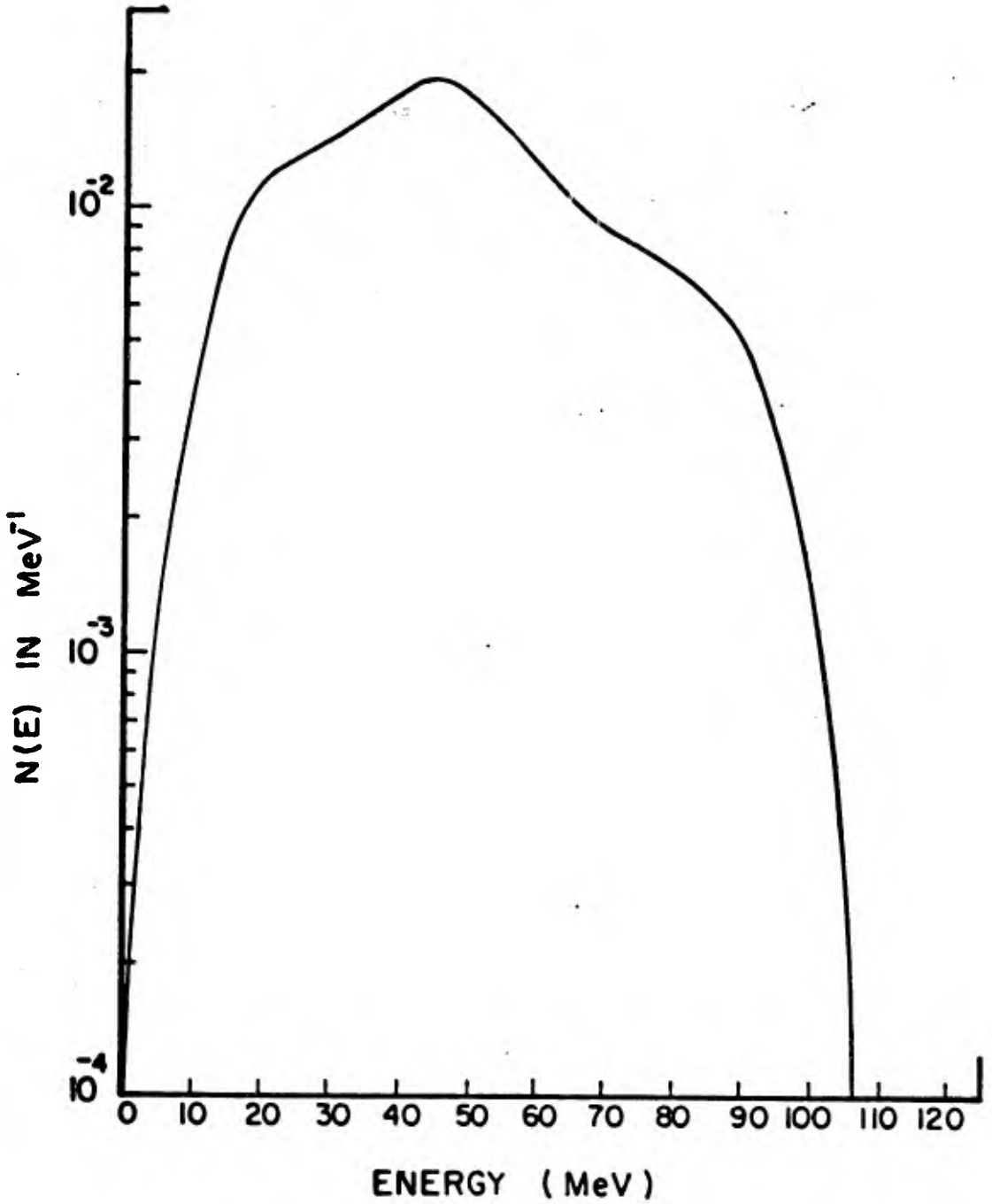

Figure 3.4: Energy Distribution of Fission Fragments from a 2.53-Micron-Thick, 93% Enriched UO_2 Coating [71]

assuming a constant flux, the total energy of fragments leaving the foil, E_T, is proportional to E_{AVG}, P_E, and the coating thickness, t.

$$E_T \propto E_{AVG}\ P_E\ t \qquad 3.1$$

A plot of this relation for their data yields Figure 3.5 where E_T has been normalized such that the maximum possible energy input to the system is unity, thus representing a coating effectiveness. The asymptotic behavior of the curve is the direct result of the fact that fragments born more than one fragment range in UO_2 from the coating surface do not leave the coating. Clearly not much of an increase (only 12%) can be obtained by going to coatings beyond 3 μm, and thicker coatings would increase the heat generation in the MCFIG and post irradiation fission product activity in direct proportion to the thickness. The secondary electron production from UO_2 coatings (created as the fragment passes through the coating) has also been studied by Anno [74]. He found an average of 300 electrons emitted from the coating surface per emitted fission fragment for a 3 μm coating thickness. As their average energy (~20eV) is low their effect is negligible relative to the energy of the fission fragments (~46.5MeV).

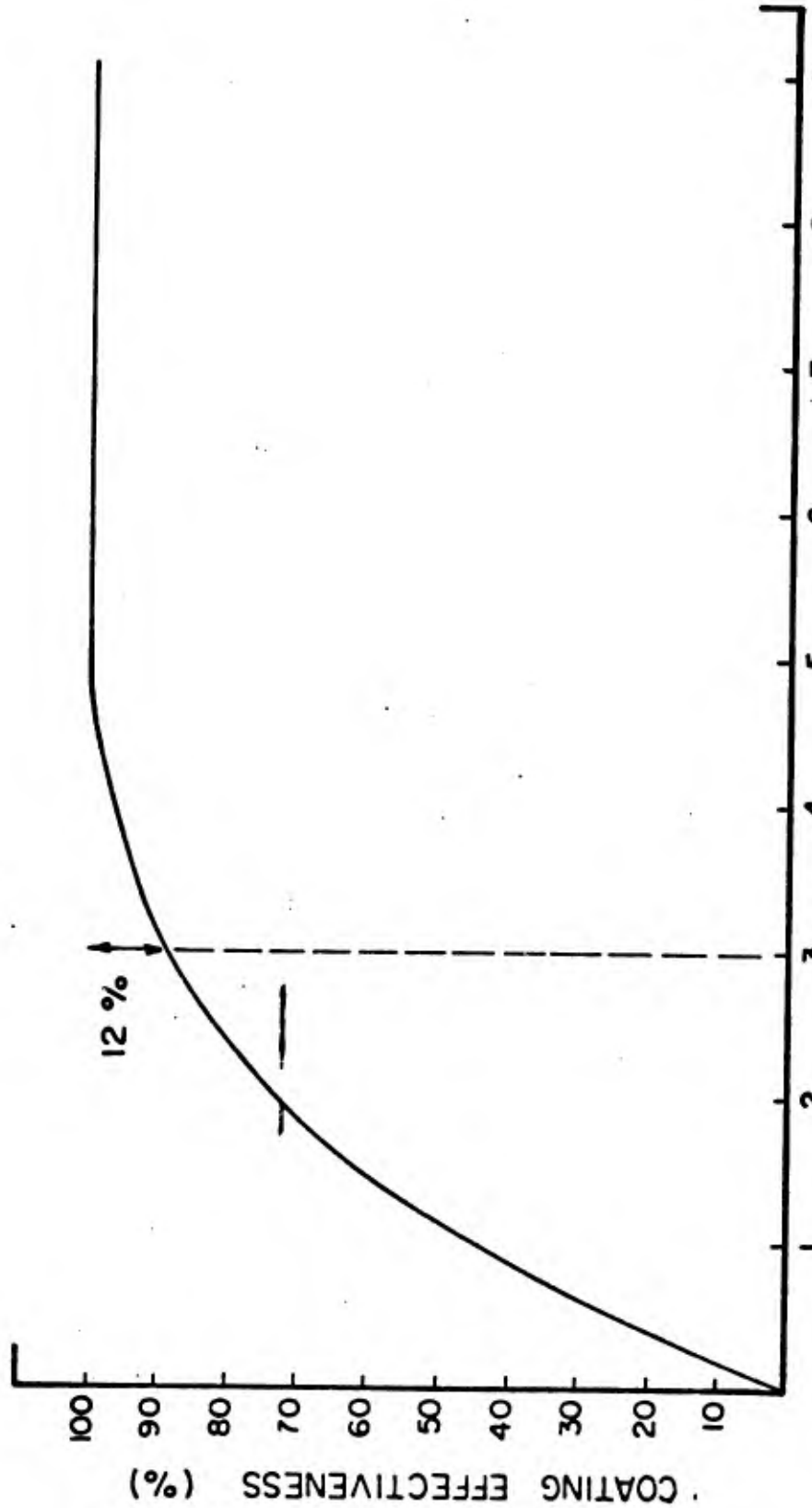

Figure 3.5: Coating Effectiveness as a Function of Thickness

3.4 Optical System

The optical system used in this research is shown in Figure 3.6. The lens system is focused for an image at the center of the UFTR core (corresponding also to the center of the source in the MCFIG). A 1:1 image is maintained throughout the system as a matter of convenience for analysis and because it represents the optimum in core system for light collection, if one assumes the lens diameters are fixed (this is our case because of a fixed HTP diameter). A front surface mirror was mounted on a precision rotation module which was modified to permit remote adjustments to be made (i.e., from outside the shielding). Mirror rotational adjustment permitted sampling different distances from the planar source. The 10-inch focal length lens served to permit moving the monochromator farther from the HTP and the correspondingly higher gamma radiation environment. A 2-inch lens diameter was selected so that when the mirror was rotated over the range of interest, the effective optical system aperature was not affected.

Although the actual spatial region sampled by the monochromator is quite complex (section 4.2.4), it is shown approximately in one dimension in Figure 3.7. The width of the region sampled is determined by the limiting f number, f#, of the optical system. Specifically ΔX is proportional to 1/f# while, as one would expect, the light

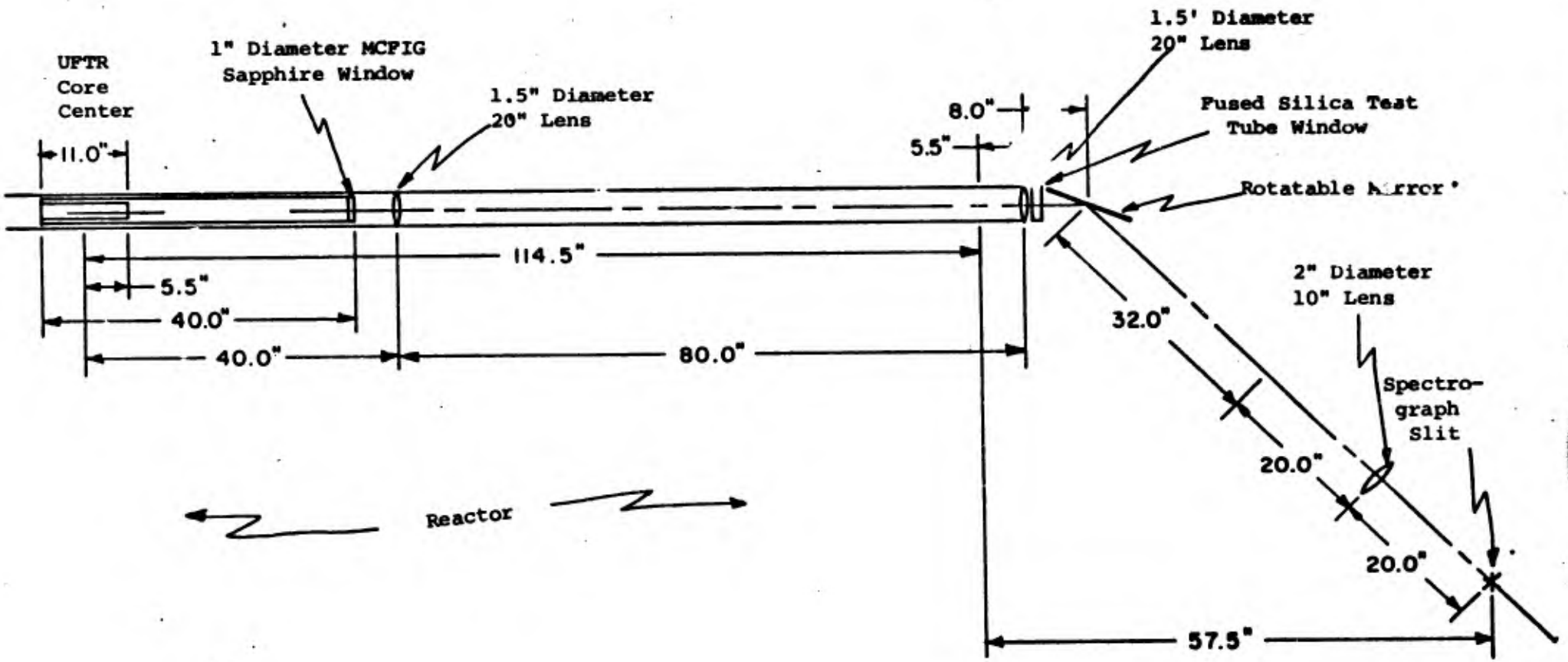

Figure 3.6: Optical Setup for MCFIG Gas Irradiation Studies (top view)

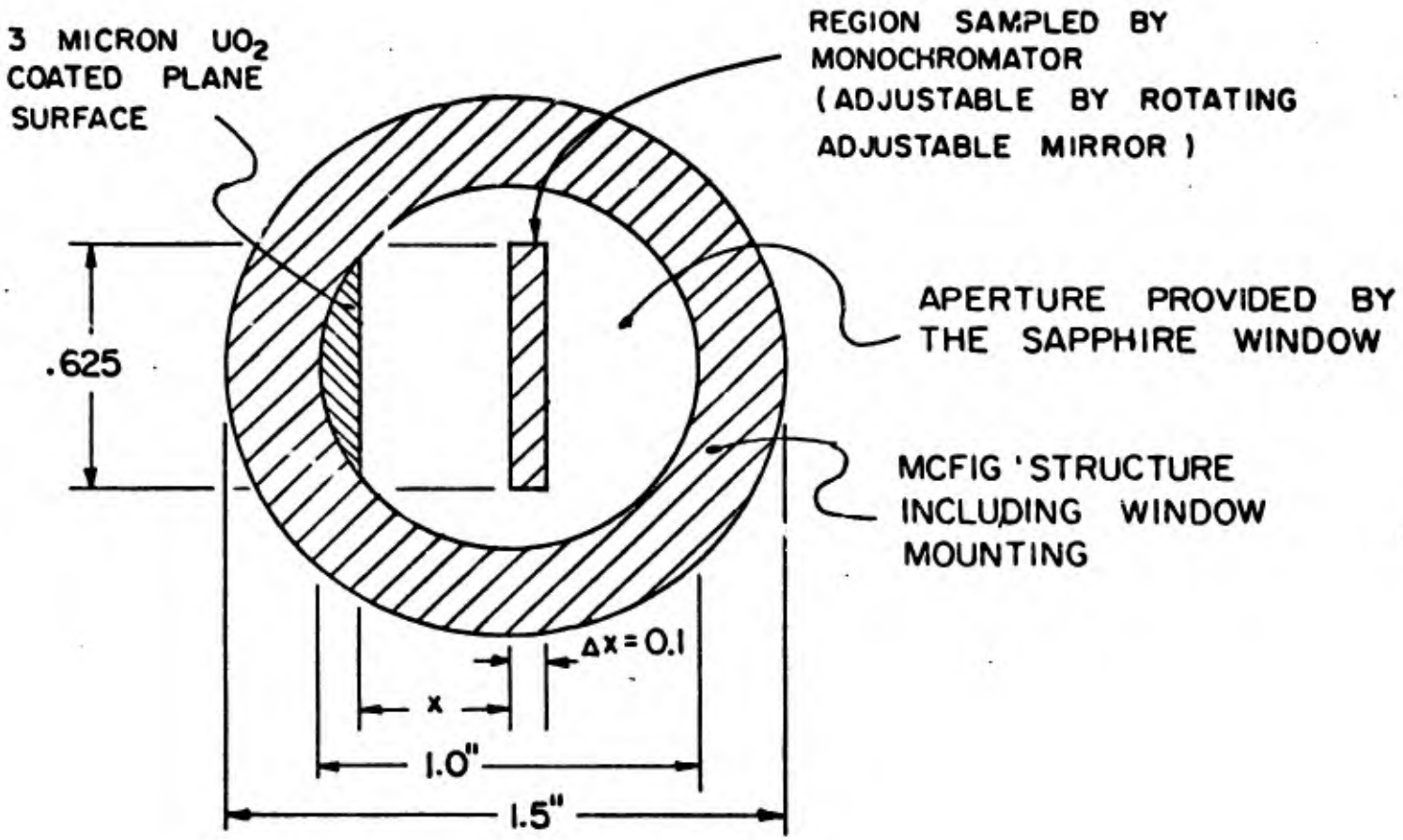

Figure 3.7: End on View of MCFIG Showing Spatial Sampling Region

entering the spectrograph varies as $1/f\#^2$, presenting an obvious design tradeoff. Another consideration is that if shorter focal length lenses (assuming the diameter is fixed) are used, more lenses (and complexity) are required to get the image to the monochromator slit. These considerations resulted in selection of 20-inch focal length lenses such that only two lenses were required to get the image out of the reactor. In addition this selection provided a spatial resolution of less than .25cm, which was considered acceptable. The two in core lenses were precisely mounted in a piece of machined tubing which fit into the HTP. The tubing between the two lenses was painted flat black to prevent any possible reflections from affecting the observed signal.

An alignment device was fabricated to insure proper operation of the optical system prior to each MCFIG irradiation. The alignment tool consisted of a light source encased in an aluminum tube (same diameter as MCFIG) with a ground glass window in the end which was masked by a pattern containing precisely positioned holes .1 in. apart and making a cross pattern. The tool was inserted into the HTP with a known pattern orientation (assured by a visible marking on the rear of the tool) such that the ground glass and pattern were precisely at the UFTR core center. A 1:1 image was verified and the rotatable mirror

set to center the pattern on the monochromator slit. Then using the actual photomultiplier (with the monochromator set on zero order) each of the pattern holes was located by rotating the mirror with the rotation module, yielding a calibration for the module (i.e., a relation between X in Figure 3.7 and the module micrometer reading). It was found that in practice the calibration was repeatable to easily within .01 in. X variation.

3.5 Instrumentation System

The instrumentation system, shown in Figure 3.8, consisted of a model 218 McPherson .3m scanning monochromator coupled with an EMI 9558QB (S20) photomultiplier. The output of the photomultiplier was input to a Keithley model 410 micro-micro ampmeter. The 0-5 volt Keithley output was routed through a low pass RC filter network and used to drive a Hewlett Packard model 7000AM x-y recorder and Keithley model 160 digital multimeter. The photomultiplier was located in a lead shield to reduce the gamma radiation level and was cooled by nitrogen gas to reduce dark current. The cooled gas was produced by immersing a variac controlled 500-800 watt heating element in a dewar containing liquid nitrogen and producing a desired gas flow rate by adjusting the amount of boiling. The signal to noise ratio of this system appears to be about 10 times that of Walters' [17]

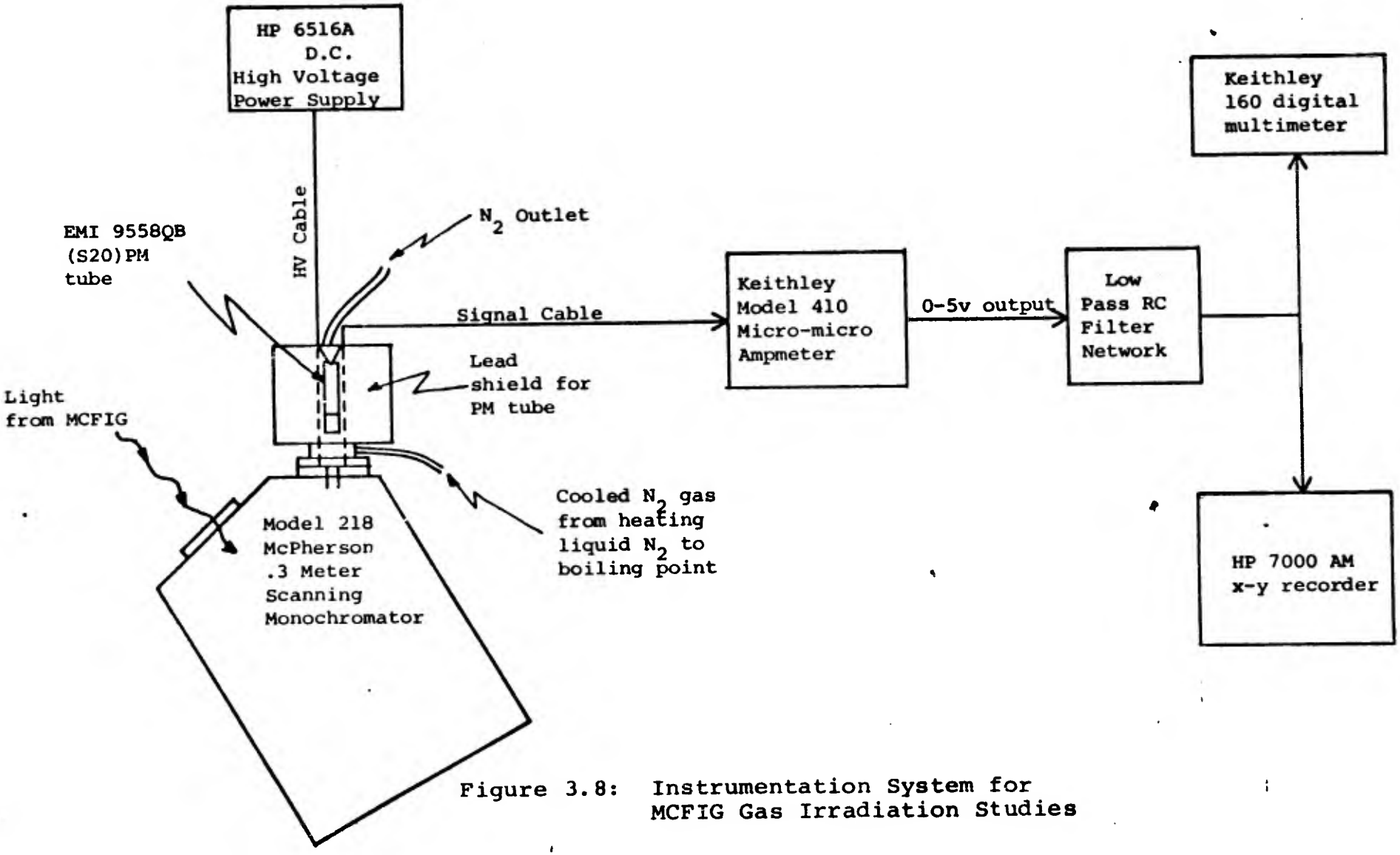

Figure 3.8: Instrumentation System for MCFIG Gas Irradiation Studies

system; however, the unknown optical effect on signal to noise makes it difficult to ascribe the improvement to any specific system differences.

3.5.1 System Evolution

The above instrumentation system evolved only after a number of other approaches had proved inferior, and some of this history will be documented here. It is clear that to remove gamma noise from the signal (assuming the shielding is as good as it can be practically made) one must resort to filtering the noise from the signal in some fashion. Initially a chopper was constructed which imparts a selected frequency to the signal by modulating the light beam so that it can be separated from the noise by using a bandpass filter. This system was tried but failed as the bandwidth of the noise was broad, and for all achievable chopping speeds enough noise made it through the filter to prevent any net gain in signal to noise. This occurred because the chopper speed could not be precisely maintained, requiring a relatively broad bandpass filter to prevent significant signal amplitude losses. Recording the data on magnetic tape for posttest data reduction (filtering, etc.) by computer was also attempted but insufficient instrumentation to adequately support this effort was available. In addition system reliability was poor for

such complex, homemade arrangements. A "brute force" technique was thus implemented. This consisted of using the monochromator sweep to control the signal bandwidth. Specifically by sweeping very slowly and using a low pass filter (time constant = 4 sec.), the signal, including spectral lines, was unaffected. This was verified experimentally when selecting the best sweep speed-filter combination. The gamma noise, however, would not be expected to vary greatly over 4 sec., so after filtering, it represented a steady state background level from which the signal could be distinguished. A noise level (fluctuations) did still exist primarily from reactor statistical power level variations. The significant reduction in noise permitted the system gain to be increased until the steady state background level became so large that the system dynamic range was unacceptable. The system was effectively dark current limited. Use of a log amplifier in the system was considered but discarded because a linear signal output was most desirable. The solution selected was to cool the photomultiplier, reducing the dark current by a factor of 12 and thus the steady state background level. The result was a system once again limited by gamma radiation levels.

The important disadvantage of the above approach to improve signal to noise is the long data acquisition times required because of the slow sweep speeds used (e.g.,

20Å/min). To collect data from 2000-9000Å required 5 hours' minimum time. This would appear to be a worthwhile problem for future work to address. Specifically, use of a phase lock amplifier or minicomputer synchronized with a light beam chopper could be the solution. The principle of using bandpass filter techniques is fundamentally sound but relies on having a very narrow bandwidth filter such as could be provided by these pieces of equipment.

3.5.2 Spectral Sensitivity

The spectral sensitivity of the system was limited by radiation damage to the optical system at short wavelengths and the photomultiplier in the infrared. This is illustrated in Figure 3.9 which shows the relative spectral response of the spectrograph and photomultiplier and that of the total system during typical data runs. Further details on system sensitivity and how it was determined appear later in the discussion of the system calibration and in Appendix A.

3.5.3 Spectral Resolution

The relatively low light levels being monitored in this experiment necessitated using relatively large monochromator entrance and exit slit settings. Usually

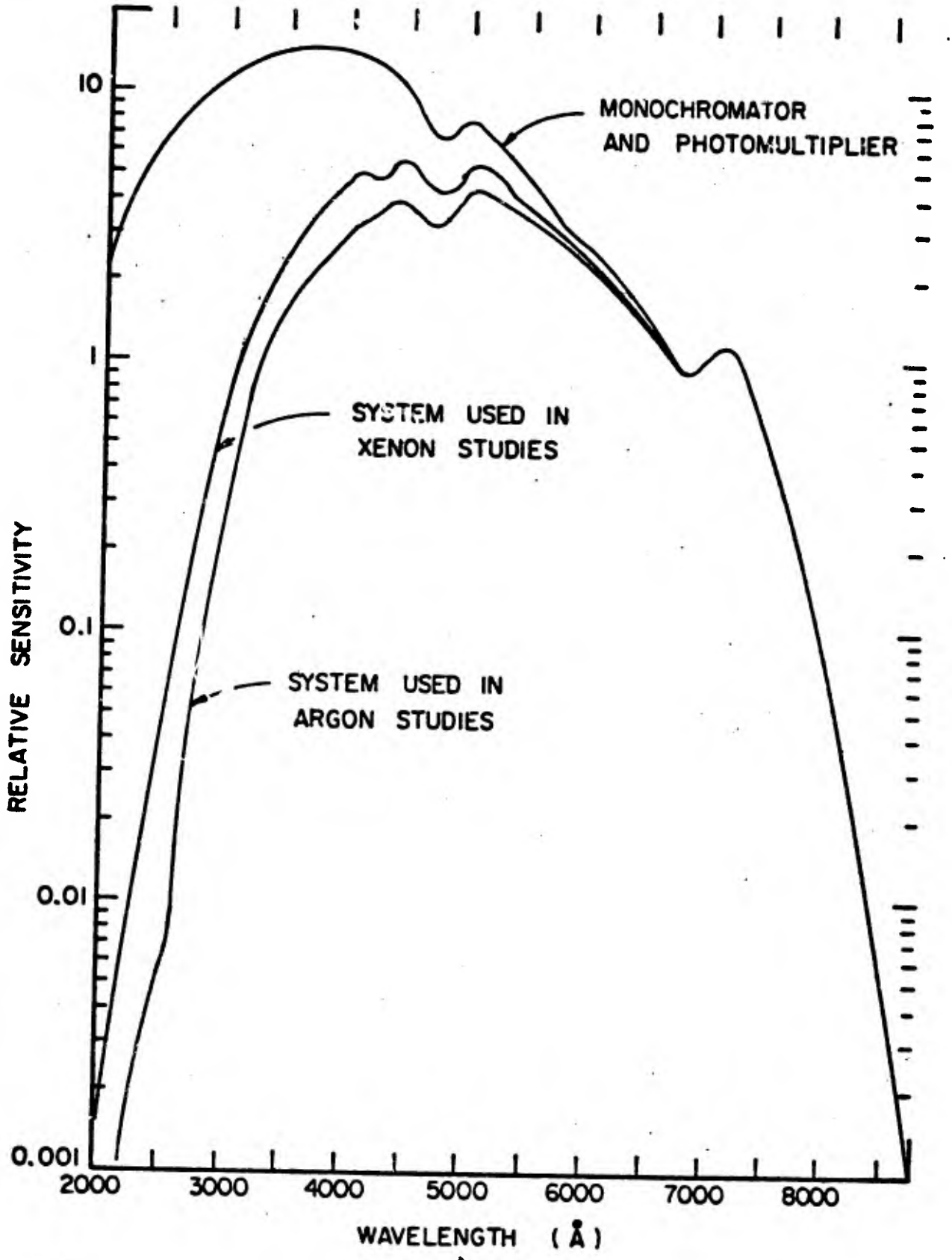

Figure 3.9: Relative Spectral Sensitivity of Monochromator and Photomultiplier Compared to That for the Entire Instrumentation Systems Used in the Argon and Xenon Studies

these ranged between 100 to 300 μm. To illustrate the tradeoff, at settings of 150 μm a linewidth of 3.5Å was experimentally determined. Reducing the settings to 100 μm reduced the linewidth to 2.7Å and the intensity by a factor of 2. Increasing the settings to 300 μm increased the linewidth to 7.6Å and the intensity by a factor of 2.7. Incidentally, the RC filter reduced the frequency response of the instrumentation system which affected the line heights and widths taken with slit settings less than 100 μm at scan rates of 20Å/min. The system response was too slow to follow the line, resulting in reduced line heights and increased widths.

3.6 Reactor Environment

3.6.1 Neutron Flux

The UFTR operational characteristics have recently been documented by Zuloaga [75]. Of particular interest to this study is the neutron flux distribution in the UFTR HTP. This is shown for the region around the CVP in Figure 3.10. The MCFIG was located for all experimental work directly below the CVP as it was previously thought this was the point of maximum thermal flux. Unfortunately the detailed mapping results presented in Figure 3.10

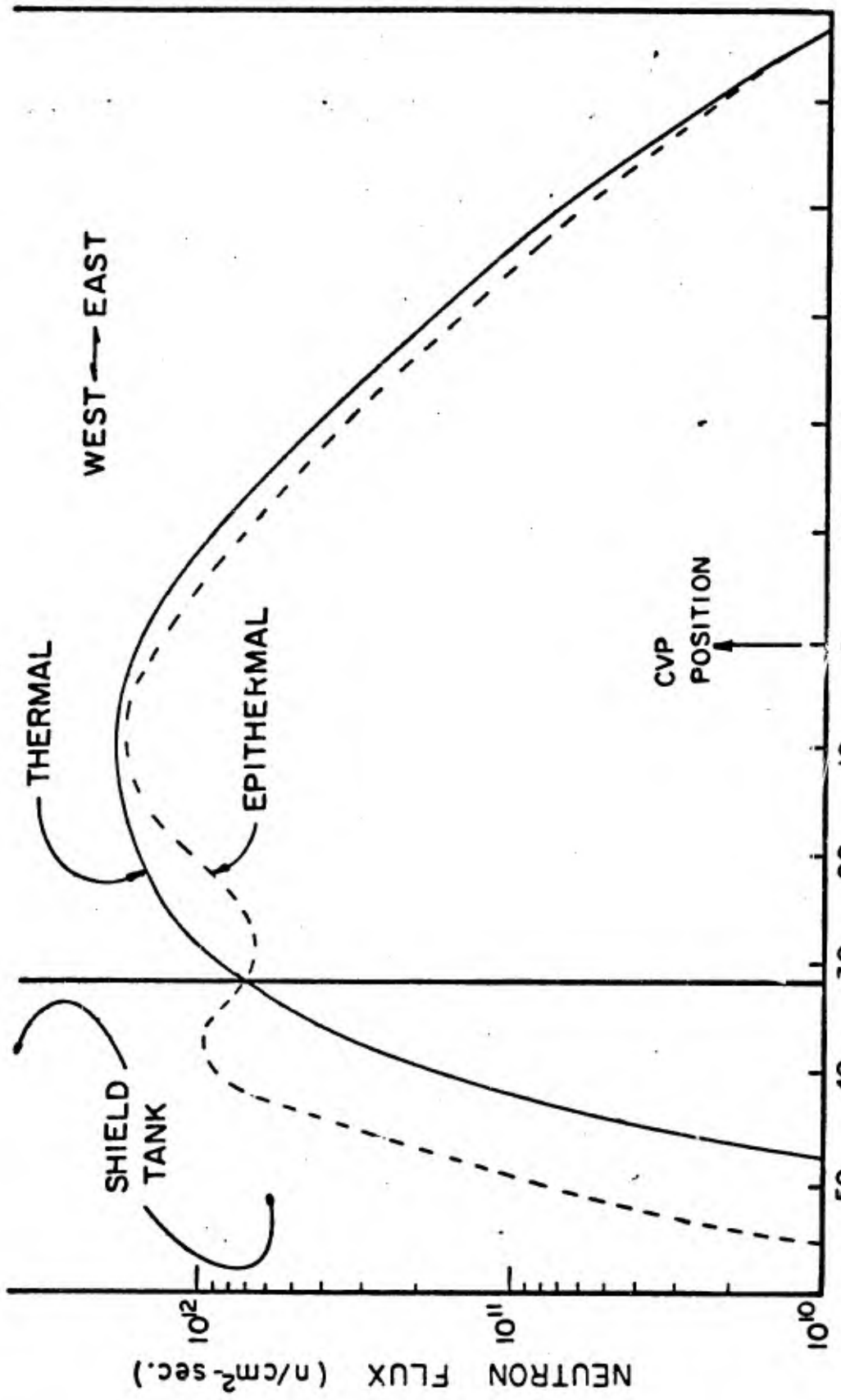

Figure 3.10: Neutron Flux Distribution in the UFTR Horizontal Thruport

were unavailable until after our experimental work with Ar and Xe was concluded. Thus in this experiment the MCFIG was exposed to a thermal flux of approximately 1.6×10^{12}. With appropriate repositioning of the lenses, etc. in the experiment the MCFIG position could be changed to the point of maximum flux which from Figure 3.10 is approximately 1.9×10^{12}. Even if these flux values are in error as to magnitude, the relative values should be very accurate, and they indicate we could gain about 20% in flux by this change.

3.6.2 MCFIG Temperature

Due to the MCFIG having a fissioning heat source in it and relatively poor heat transfer to dissipate it, the MCFIG will heat up during reactor operation. Poor heat transfer occurs because the test tube is evacuated and the only heat flow is by radiation or conduction to the test tube wall which supports the MCFIG. Safety considerations and interest in correlating MCFIG temperature changes to spectral intensity changes motivated us to instrument the Xe MCFIG with a thermocouple. The temperature as a function of time is plotted in Figure 3.11. The UFTR ambient operating temperature at the MCFIG

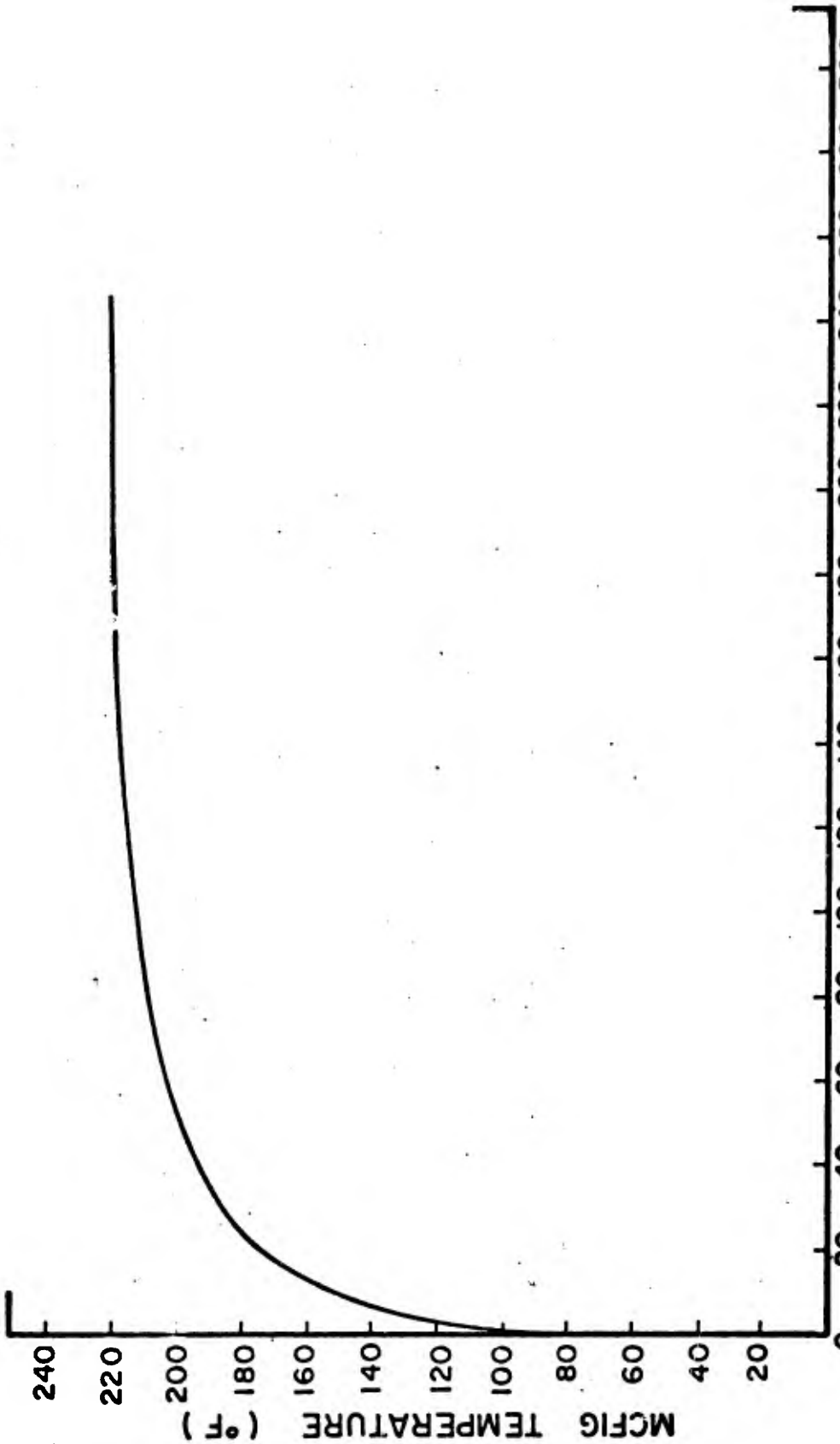

Figure 3.11: MCFIG Temperature as a Function of Time After Reaching Full Power

position based on reactor instrumentation is approximately 100°F. As it was experimentally determined that the MCFIG temperature affected the spectral data, an effort was made to only take spectral scans after the MCFIG had warmed up. Ideally this took more than 2 hours which because of the shortage of reactor time was not always satisfied in less critical cases. Twenty minutes, however, was considered an absolute minimum warmup time for virtually all data.

3.7 Test Procedures

This section briefly describes the basic test procedures employed during this experiment. Its objective is to provide the reader with some feel for how the experiment was conducted from a practical viewpoint. Additional safety related details are documented in the safety analysis of this experiment [76] which was prepared for the UFTR Safety Subcommittee in July 1973.

3.7.1 Gas Filling

The MCFIG capsules were evacuated on a pumping station for approximately two weeks to a final pressure on the order of 10^{-8} torr and helium leak tested prior

to filling. They were filled to 760 torr with the appropriate research grade gas at ambient temperature.

3.7.2 Spatial Calibration and MCFIG Loading

Prior to each MCFIG loading, the optical system alignment tool was inserted into the test tube and the micrometer on the adjustable mirror calibrated. Specifically, micrometer readings were correlated with the alignment tool test pattern position on the slit. Prior to insertion the MCFIG was cleaned on the outside with acetone to minimize potential activation of dirt, fingerprints, etc. A white mark was made on the valved end of the MCFIG to enable proper orientation of the planar source, and an aluminum wire was attached to the valve, so the MCFIG could be pulled back out of the HTP. The MCFIG was inserted into the HTP using a specially designed handling tool which enabled rotational adjustments to be made as necessary to align the planar source according to the visible mark on the MCFIG end. The test tube was then sealed and evacuated to a pressure of approximately 0.2 torr. Usually this required overnight due to the relatively large pumping volume. The test tube was then isolated and the pressure monitored to detect any leaking of the MCFIG.

3.7.3 Initial Reactor Startup

Just prior to reactor startup the N_2 cooling system was turned on to insure the photomultipler temperature had reached equilibrium prior to taking data. Of most importance during the actual reactor startup was the verification that radiation levels around the HTP ends did not exceed safe limits. The levels were found quite sensitive to how the shielding was positioned, and on no two runs was it ever stacked the same way. Minor adjustments were thus sometimes necessary to permit full power operation.

3.7.4 Data Acquisition

Upon reaching full power for the first time with a particular gas, the monochromator was put on zero order and adjusted for the maximum light signal. Then a few complete fast spectral scans were made from 2000-8500A at scanning rates of 200 or 1000Å/min with a large slit width to get a feel for the spectrum. After the MCFIG had warmed up a detailed scan of the entire spectrum was made at a scanning rate of 20Å/min and a slit width of 150 or 300 μm. At this point in the case of Ar, the first gas examined with the system, numerous system improvements and refinements had to be made over a period of several months to get the detailed scan to the quality desired. In the case of Xe, data

acquisition was straightforward. After obtaining a complete spectrum, selected spectral regions were investigated for spatial effects, and where effects were found detailed data were taken. Also representative lines were studied for linearity with power and temperature effects. Throughout the data acquisition process calibrated interference filters were used to insure no data contamination from second order effects and internal monochromator reflections. The data acquisition phase of the experiments required much more reactor time than was anticipated which coupled with various reactor schedule considerations, breakdowns, etc. was the limiting factor in only being able to study two gas fill conditions.

3.7.5 Posttest Procedure

After test termination and reactor shutdown, the MCFIGs were left to decay for several days. This minimized the fission product inventory subject to release in the event of an accident and reduced the radiation levels from the activated stainless steel MCFIG during the removal operation. The test tube atmosphere was sampled and analyzed for possible fission product presence prior to unsealing it. The Ar and Xe MCFIGs were pulled into a shielded transfer cask and subsequently placed in the UFTR spent fuel storage pit. In follow-on studies we removed the MCFIGs by

hand and placed them in the pit. While dose rates on the MCFIG surface approached 20R/hr, the short handling time required and inherent simplicity (and safety) make this approach the best. Also in follow-on studies it was shown that after a short decay period (1-2 weeks) a MCFIG could be evacuated and refilled for future use.

CHAPTER 4

DATA ANALYSIS METHODS

4.1 Spectral Line Identification Techniques

The identification of spectral lines making up the observed spectra was complicated by several factors. The relatively poor resolution resulting from the large slit widths employed (for example, linewidths of 3.5 and 7.6Å were experimentally determined for slit widths of 150 and 300 μm respectively) prevented identification of some unisolated lines. Variations in monochromator and plotter sweep speed made precise assignment of wavelengths based on known lines of limited value, except close to the known line. In addition the lines of lower intensity had poorly defined peaks as a result of a low signal to noise ratio.

The above factors made line identification dependent on more than just indicated wavelengths as calculated from the data. Specifically, the following information was evaluated prior to identifying any spectral line:

(1) the indicated wavelength based on the dispersion of the data and any known lines.

(2) the presence or absence of other transitions from the same excited level that should be detectable, and the consistency of excited state populations calculated from the different transitions.

(3) the presence or absence of detectable transitions from a lower level that is populated by a given transition, and the consistency of their intensities.

(4) the magnitude of the gA valve for a transition and known populations of nearby energy levels (i.e., one would not expect to see close lying energy levels having radically different populations).

The first three criteria are straightforward to use when they apply. When a transition is the only detectable one from a level only the first criterion and the last can be used. Still there are cases where a choice between several possible transitions cannot be made with certainty. The line identifications reported in this study are those which the author feels can be made with high confidence. Unidentified lines are listed along with their most likely identifications as an aid to future workers. It must be remembered, however, that judgment is obviously important in line identification, particularly when the fourth criterion is applied.

4.2 System Absolute Calibration

An objective of this research was to quantify the light emitted from a fission fragment produced plasma. During the course of this research, however, this was expanded to include estimating the population densities of excited atomic and ionic levels which requires some sort of absolute calibration. The primary difficulty in effecting such a calibration of our experimental setup is that we have a distributed light source over a relatively large spatial region with respect to the focal length of the system and diameter of the optical components. The problem was further complicated by the inaccessibility of the actual source region (in the core of the reactor) and time dependent radiation damage to optical components. With these problems in mind, the absolute calibration procedures described below were developed with the goal of obtaining an order of magnitude estimate of the population densities. The actual procedures as carried out are believed to have produced an absolute calibration accurate to within a factor of 3. Actual experimental considerations to be discussed later increase our uncertainty in calculated population densities, but they are still believed within a factor of 10.

An in situ experimental absolute calibration of the entire data acquisition system was considered impossible

in the limited time available for this research. Duplication of the system outside the reactor, while possible, was not considered practical, since the monochromator and PM tube would have had to be moved which would have affected accuracy. In addition, it was desired to have a calibration for various levels of radiation damage to the MCFIG sapphire window assembly so that spectra taken after different radiation exposures could be compared. This required an in situ calibration, avoiding the necessity of continually taking the window in and out of the reactor. Also any possible transmission changes that are known to occur after removal from the reactor are no longer of concern.

A calibration scheme outlined below was devised to overcome the above problems. It is shown schematically in Figure 4.1. The problem was broken into two parts: (1) the collection efficiency (based upon geometrical optics) of the optical system for the distributed source and (2) the relation between photomultiplier current and the energy collected by the optical system. The collection efficiency can be viewed physically in a number of ways; however, since we are interested in excited state densities we shall look at it as an effective volume. Given a uniform isotropically emitting distributed photon source filling a volume for which the efficiency of collection by our optical system is nonuniform, an equivalent volume

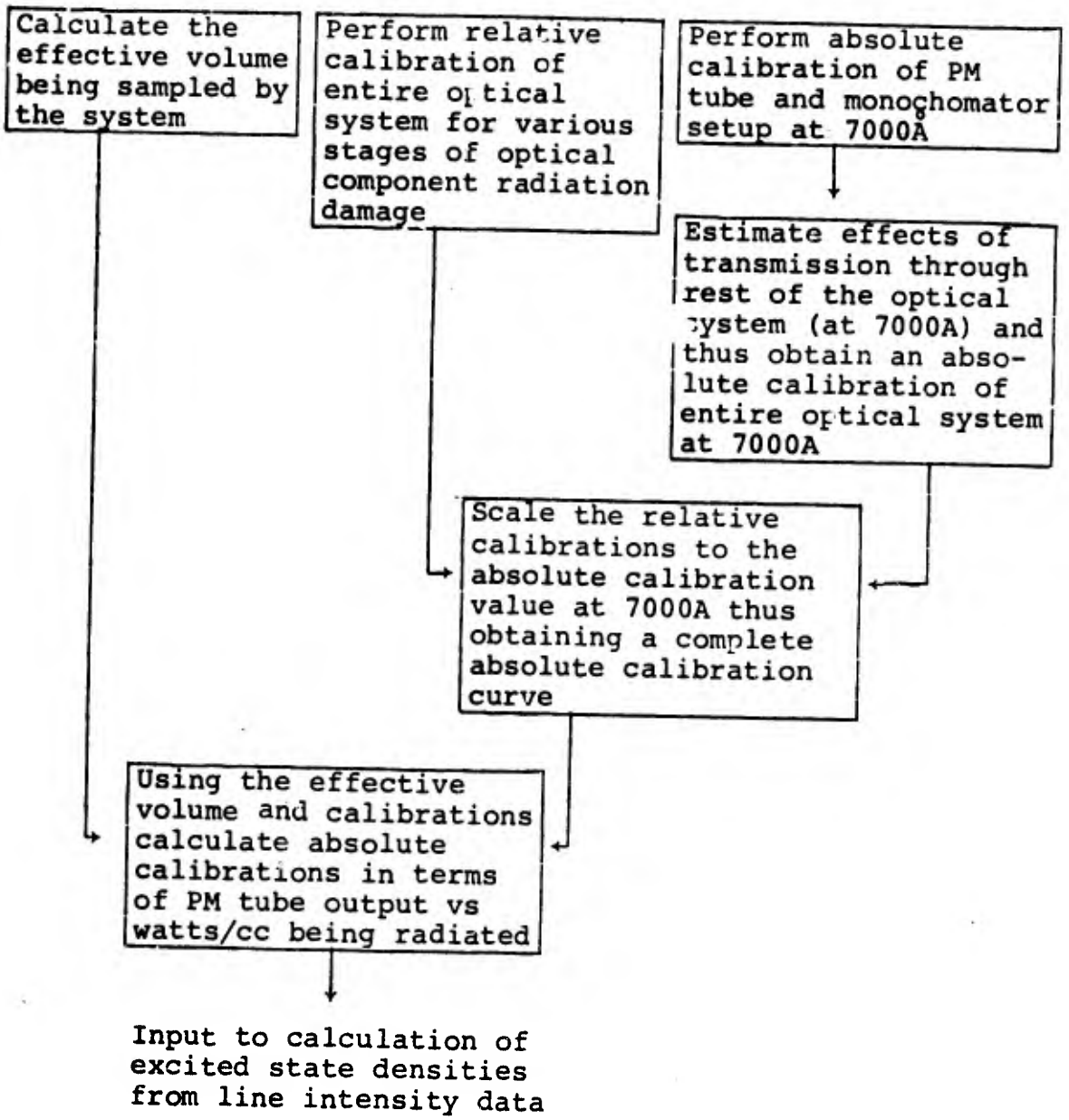

Figure 4.1: Schematic Showing Procedures to Effect an Absolute System Calibration

can be defined which is the smaller volume of source required to replace the original one, assuming every photon generated within that smaller volume is collected. Thus, if we can relate the total energy collected by the system to an observed photomultiplier current, the so determined energy divided by the equivalent volume yields the energy per unit volume radiated from the plasma. Excited state densities may then be directly calculated.

The collection efficiency of the optical system for the plasma source was evaluated analytically (and will later be described in detail). The relation between photomultiplier current and energy collected was experimentally obtained. This relation is defined to include reflective and transmission losses for all optical components. The approach taken was to obtain a relative calibration curve for the entire system under various conditions of radiation damage, and then scale this curve based on one wavelength (where no radiation damage is expected to occur) to an absolute calibration of the monochromator and photomultiplier. Lens, window, and mirror losses between the source and monochromator had to be estimated at this wavelength. This unusual approach was taken to reduce the precision required in carrying out the relative calibrations. Specifically, many such calibrations had to be made and over an extended time period. This way the working standard

could be operated at any current setting and the relative spectrum taken into account by measuring the filament temperature with a pyrometer. Otherwise, had the lamp been calibrated at a particular current (or temperature) this would have had to be repeatable. Due to warming up effects achieving a particular current was often found to be time consuming. It was easier to just turn on the lamp to approximately the usual operating conditions, let it warm up, measure the temperature and make a calibration run. Other approaches would certainly work just as well as the one used here; however, in view of the accuracy desired, the approach used is adequate.

4.2.1 Relative Calibration Details

The relative calibration was accomplished using the optical setup shown in Figure 4.2. A sapphire window mounted in a short aluminum tube was placed in the test tube to simulate the MCFIG window. The test tube was evacuated to simulate the operational configuration since it was experimentally found that for such a long path length, the transmission in the UV was sensitive to the presence of gas in the test tube. A tungsten and deuterium lamp provided the standard source below and above 3500Å respectively, and a 1:1 image of the lamp filament was focused on the monochromator slit. A removable mirror was used to permit

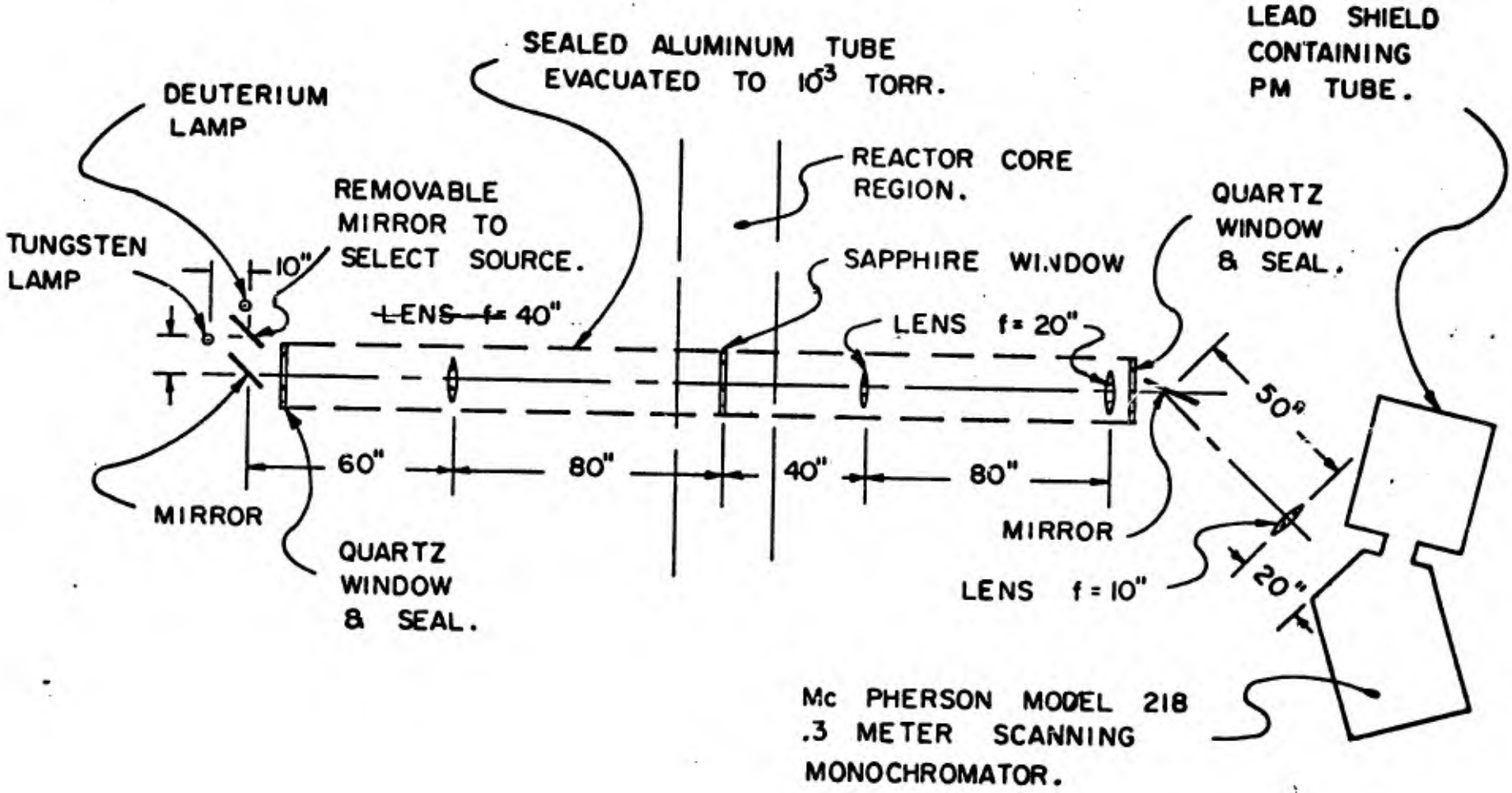

Figure 4.2: Optical Setup Used for Relative Calibration

easy selection of the standard source. The effects of the 40" quartz lens and window on the calibration were probably small because quartz has reasonably uniform transmission and radiation damage is negligible at their respective locations. The effect of the two mirrors is not negligible so the lenses, window, and mirrors were evaluated and their effects removed from the calibration data. This was done by mocking up their arrangement in a separate experiment to measure their transmission (and reflectivity) as a function of wavelength. Also, photomultiplier temperature was found to affect the relative calibration, so its effects were evaluated at the same time as those of the lens, window, mirrors. The deuterium data were used below 3500Å and normalized to the tungsten data at this point.

A standard tungsten lamp was used and operated at a temperature of about 3400°F. The temperature was measured with an optical pyrometer and was intentionally kept low to preserve lamp life over the extended periods of operation that were required. The pyrometer measures the brightness temperature, T_B, at 6350Å. To obtain the true temperature, T_T, we use the following expression for the observed emission intensity at 6350Å, $I_{\lambda*}$,

$$I_{\lambda*} = B_{\lambda*}(T_B) = \varepsilon_{\lambda*}(T_T)B_{\lambda*}(T_T) \qquad 4.1$$

where $B_\lambda(T)$ and $\varepsilon_\lambda(T)$ are the plank function and emissivity of tungsten and $\lambda^* = 6550\text{Å}$. We employ the following expression for $B_\lambda(T)$

$$B_\lambda(T) = \frac{2hc^2}{\lambda} \frac{1}{[e^{hc/\lambda kT} - 1]} \qquad 4.2$$

where symbols have their usual meaning. Putting this into equation 4.1 above yields

$$[e^{hc/\lambda^* kT_B} - 1]\ \varepsilon_{\lambda^*}(T_T) = [e^{hc/\lambda^* kT_T} - 1] \qquad 4.3$$

which is approximated by the following expression

$$T_T = \frac{22020}{\ln\varepsilon_{\lambda^*}(T_T) + \frac{22020}{T_B}} \qquad 4.4$$

where the temperatures are expressed in °K. Given a T_B, T_T may be calculated, and the relative output of the lamp as a function of wavelength I_λ is obtained from

$$I_\lambda = \varepsilon_\lambda(T_T) B_\lambda(T_T) \qquad 4.5$$

Then dividing the value of the lamp output into the photomultiplier output a calibration curve as a function of wavelength is obtained. Published empirical expressions for the emissivity of tungsten [77] were used.

To examine the errors in this calibration, the expression for I_λ was investigated.

$$I_\lambda \sim \frac{1}{e^{hc/\lambda kT}} \qquad 4.6$$

Taking the natural log of both sides and differentiating the result yields

$$\frac{dI\lambda}{I_\lambda} = \left(\frac{hc}{\lambda kT}\right) \frac{dT}{T} \qquad 4.7$$

Upon putting in some typical numbers and letting $\lambda = 5000\text{Å}$ yields

$$\frac{dI}{I} = 12.4 \frac{dT}{T} \qquad 4.8$$

This means a 1% relative error in T will cause an error of 12.4% in output intensity. T is probably repeatable to within 1% using the pyrometer and maintained within this 1% by the lamp power supply, assuming the lamp is adjusted after warming up completely. Also, a + 12.4% error at 5000Å means + 21% and + 4% at 3000Å and 9000Å respectively, so the relative calibrations from different runs will be affected, in this case 16%. Calibrated long wavelength pass filters were used to prevent second order

contributions to the signal and to assess the importance of internal monochromator reflections. Specifically, for a given cutoff filter, no wavelengths below the cutoff should contribute in the second order above cutoff. Likewise reflections from longer wavelengths can be the only contribution to any signal observed below cutoff. It was thus insured that the relative calibration was unaffected by these effects.

The deuterium lamp was operated at 315 ma current for which NBS calibration data were available. However, the absolute calibration is known to be dependent on lamp age, so only relative measurements were made. Repeatability of the deuterium lamp data seemed much better than that for the tungsten lamp. While the lamp intensity was found to be a strong function of current, the regulated power supply maintained this such that the intensity varied less than 2%. The relative intensity was found to exhibit negligible variations for even ±10% variations in current. Thus, it is concluded that the tunsten data were the limiting factor affecting the relative calibration errors. Of importance is the fact that the deuterium data were normalized to the tungsten data which were most sensitive to variations (i.e., that for short wavelengths).

A relative calibration was made several times during a typical reactor MCFIG irradiation scenario. In this way a calibration is available for those runs where the sapphire

window would have suffered some given amount of radiation damage. The system sensitivity is so low below 2700Å (due to radiation damage as explained in Appendix A) and above 8500Å (due to photomultiplier sensitivity) that the calibration should only be considered between these two limits. Outside of these, one can only say sensitivity is extremely low.

4.2.2 Monochromator and Photomultiplier Absolute Calibration

The objective of this part of the calibration procedure was to obtain a relationship between the photomultiplier current and energy entering the monochromator. The optical setup used is shown in Figure 4.3. A standard tungsten lamp (N.B.S. calibrated lamp no. EPUV-1148) was operated at a current of 35 amps (equivalent temperature of approximately 2600°K) which was monitored using a 200:1 current transformer and ammeter. Output data consisted of the photomultiplier current at several wavelengths where the spectral radiance of the standard was reported. The calculations to follow will only be carried out for the data obtained at 7000Å (the best normalization wavelength since radiation induced optical damage at this wavelength is negligible).

The spectral radiant power, P_λ, entering the monochromator slit in μ watts/mμ can be calculated from the following expression [78]:

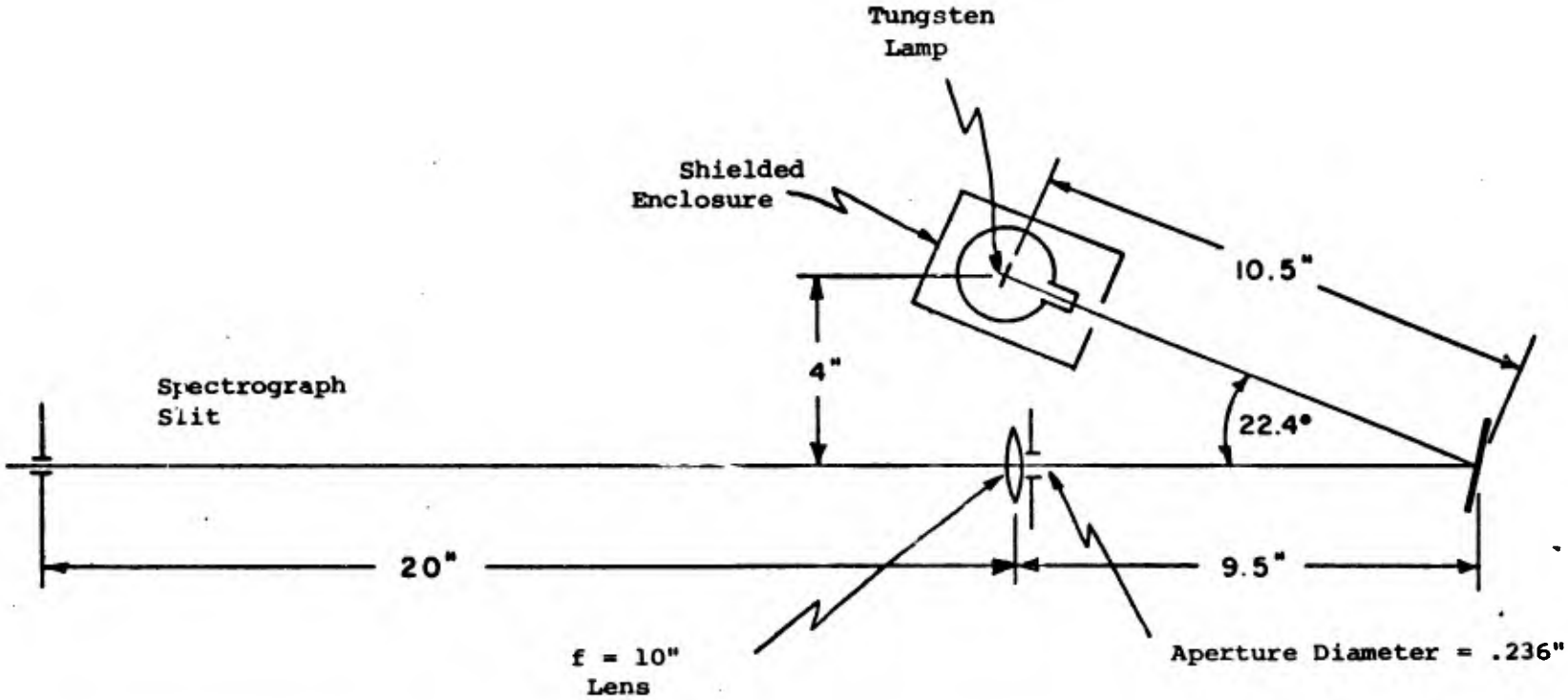

Figure 4.3: Optical Setup for the Absolute Calibration of the Monochromator, PM Tube, and Associated Instrumentation

$$P_\lambda = R_\lambda N_\lambda whA/D^2 \qquad 4.9$$

where R_λ = spectral reflectance of the mirror and transmission of the lens (using 1.05^{-2} for the lens and .96 for the mirror at 7000Å, R_λ = .87)

N_λ = reported spectral radiance of the standard lamp at 7000Å (from reference 1, N_λ = 10.7 watts/steradian-Å-m^2)

wh = area of the slit (for a slit width of 150 μm and height of 16 mm, wh = 2.4 x 10^{-6} m^2)

A = area of the limiting auxiliary optic (for aperature diameter of .236", A = 2.8x10^{-5})

D = distance of optic from slit (D = 20" or .51 m)

Putting in the indicated values for the variables into equation 4.9 yields,

$$P_\lambda = \frac{(.87)\ \dfrac{(10.7\ \text{watt})}{\text{steradian-Å-m}^2}\ (2.4\text{x}10^{-6}\ m^2)(2.8\text{x}10^{-5}\ m^2)}{(.51\ \text{m})^2}$$

$$= 2.4\text{x}10^{-9}\ \text{watts/Å}$$

Data were taken with both exit and entrance slit set at 150 microns so that the area under the slit function must be corrected. To obtain this correction factor, intensity versus exit slit measurements were made for a

constant entrance slit of 150 microns. The results for large (>300 microns) exit slits showed the expected linear behavior which when extrapolated to 150 microns indicated the measured value at 150 microns should be adjusted upward by a factor of 1.2. The slit function, S, thus becomes

$$S = 1.2\,\frac{W_e}{D} = (1.2)(150 \times 10^{-3}\text{mm})(26.5\text{Å/mm})$$

$$= 4.8\text{Å}$$

where W_e is the monochromator exit slit (150 microns) and D the monochromator dispersion (26.5Å/mm). Thus the effective power, P, input to the monochromator taking into consideration the slit function is

$$P = P_\lambda S = (2.4\text{x}10^{-9}\ \text{watts/Å})(4.8\text{Å}) = 1.2\text{x}10^{-8}\ \text{watts}$$

The measured photomultiplier current, i_{pm}, can now be used to obtain the desired relation between current and energy. Specifically

$$H = \frac{P}{i_{pm}} = \frac{1.2\text{x}10^{-8}\ \text{watts}}{9.1\text{x}10^{-5}\ \text{amp}} = 1.3\text{x}10^{-4}\ \text{watt/amp}$$

where H is the monochromator and photomultiplier transfer

function at 7000Å. Errors in this result are expected to be primarily from errors in lamp current and are estimated at less than 20%.

4.2.3 Relative Calibration Scaling

In order to scale the relative calibration curve, the absolute calibration at 7000Å must be corrected to include the effects of optical components between the source and monochromator. This is done by assuming only reflective losses are important since radiation induced absorption at this long a wavelength is negligible. The Al front surface mirror will be assumed to be 95% reflective at this wavelength and each optical surface (two for each window or lens) to reduce the intensity by 4.4% (reflectance calculated for an index of refraction of 1.53). Thus, for the mirror, three lenses and one window, the absolute calibration excluding these components must be adjusted upward by a factor of 1.48 prior to scaling the relative calibration. Also since data were taken with cooled photomultiplier the increased sensitivity at 7000Å requires H to be further adjusted upward by a factor of 1.2. The final value for H thus becomes 2.3×10^{-4} watt/amp. The relative calibration curves were thus scaled to have a value of 4.35×10^{3} amp/watt at 7000Å.

4.2.4 Optical Collection Efficiency

As already mentioned, the optical collection efficiency of the system will be evaluated in terms of an effective volume. This is analytically calculated below. The reason that an analytical ayproach was taken is that to experimentally work the problem one would have to place a point source at numerous points in the source volume (which is in the reactors) and map the collection efficiency throughout the volume. Such an approach would be a time consuming and nontrivial experiment even were the system not in the reactor. These considerations, along with the fact that the optical system was amenable to analysis, strongly support the analytical approach taken.

For an ideal optical system employing a 1:1 image throughout and with the limiting aperature being the lens closest to the source, the conditions for collection of a photon are quite simple based upon geometrical optics. While photon language is used in this analysis to make it more intuitive, it is tacitly assumed that diffraction effects are unimportant. Simply stated, the photon must hit the first lens and pass through the monochromator slit or its image at any image plane. Recall that reflections from the test tube are eliminated by the flat black paint between the lenses in the lens assembly and that reflection and absorption losses from the optical components

accounted for in the absolute calibration. This means the problem can be worked right at the source by using only the slit image at the image plane located in the distributed source and the first lens. This is shown in Figure 4.4. If the photon path (extended forward or backward as necessary) intersects both the slit and lens, it will be collected by the system of lenses. A mathematical formulation of this condition is all that is required to effect a calculation of the probability for collection of an isotropically emitting point source located at any specified coordinate (x,y,z) within the source volume.

Working this problem in two dimensions (x-y, x-z, or x-r) is most desirable, but this is complicated since the lens is circular and the slit rectangular. To circumvent this problem the lens is represented as a square having the same area as the lens. This assumption seems well justified in view of the overall accuracy desired. The problem then becomes separable in y and z and much easier to analytically attack. Specifically, at each source point it is desired to calculate a solid acceptance angle $\Delta\Omega$ from which the probability of collection is simply $\Delta\Omega/4\pi$. $\Delta\Omega$ is the product of $\Delta\theta z$ and $\Delta\theta y$ which are calculated considering the slit height and width respectively. The problem will now be set up for calculation of $\Delta\theta y$, and the $\Delta\theta z$ problem is completely analogous.

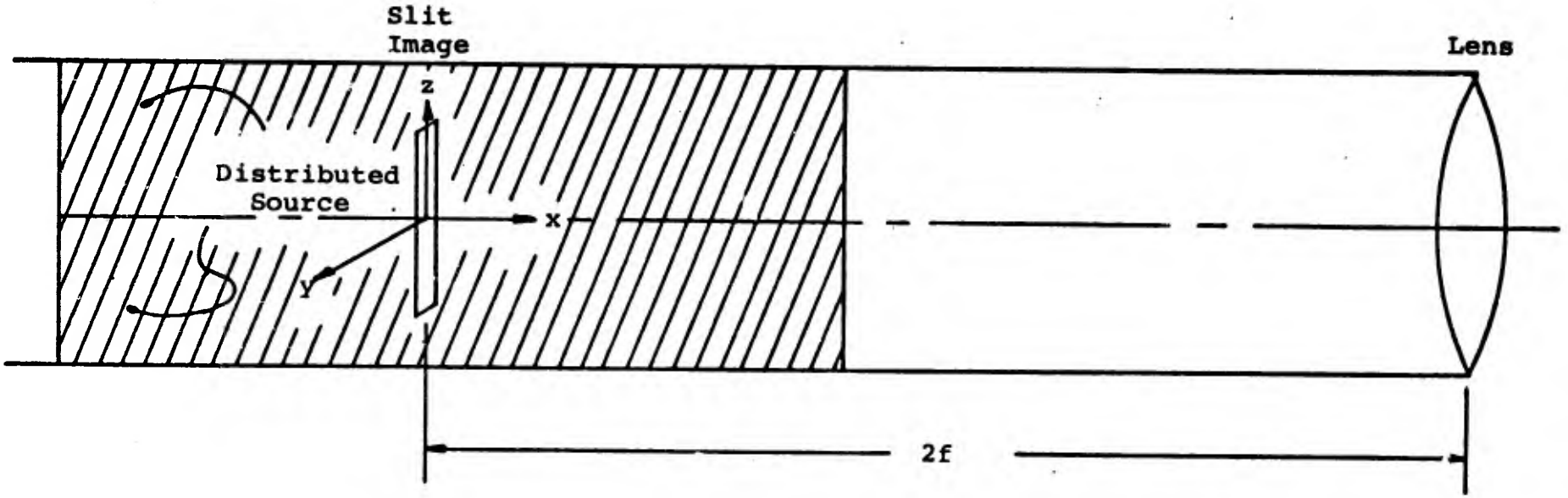

Figure 4.4: Slit Image at Source and Lens Closest to Source (dimensions exaggerated)

Figure 4.5 shows the detailed geometry to be used in the analysis. Only photons from the shaded regions in the figure can be collected by the optical system. The four regions indicated in the figure were selected as a convenience because within each the relation for the collection efficiency is unique. Any photon born in region I cannot hit the lens without passing through the slit image, so only the probability that it hits the lens need be considered. Likewise in region II only the probability that it hits the slit need be considered. In regions III and IV both slit and lens are important in determining the probability a photon is collected. The mathematical expressions for $\Delta\theta y$ in each of the regions will now be developed. Because of symmetry only positive y values of the source locations will be considered. Also indicated below in brackets are the lines (from Figure 4.5) limiting or defining the region.

Region I: The effective aperture is simply s, the lens dimension as shown in Figure 4.6. Also shown in the figure is the logic to obtain the $\Delta\theta y$ expression.

$$0 \leq x \leq X_1$$

$$\Delta\theta y = \tan^{-1}\left(\frac{s/2-y}{2f-x}\right) \qquad \frac{0 \leq y \leq w/2(1-x/X_1)\,[\text{line } EX_1]}{X_2 \leq x \leq 0}$$

$$+ \tan^{-2}\left(\frac{s/2-y}{2f=x}\right) \qquad 0 \leq y \leq w/2(1-x/X_2)\,[\text{line } EX_2 2$$

w = slit width
s = lens dimension (i.e., side of square)
f = focal length of lens

$$X_1 = \frac{2fw}{s+w} \qquad X_2 = \frac{-2fw}{s-w}$$

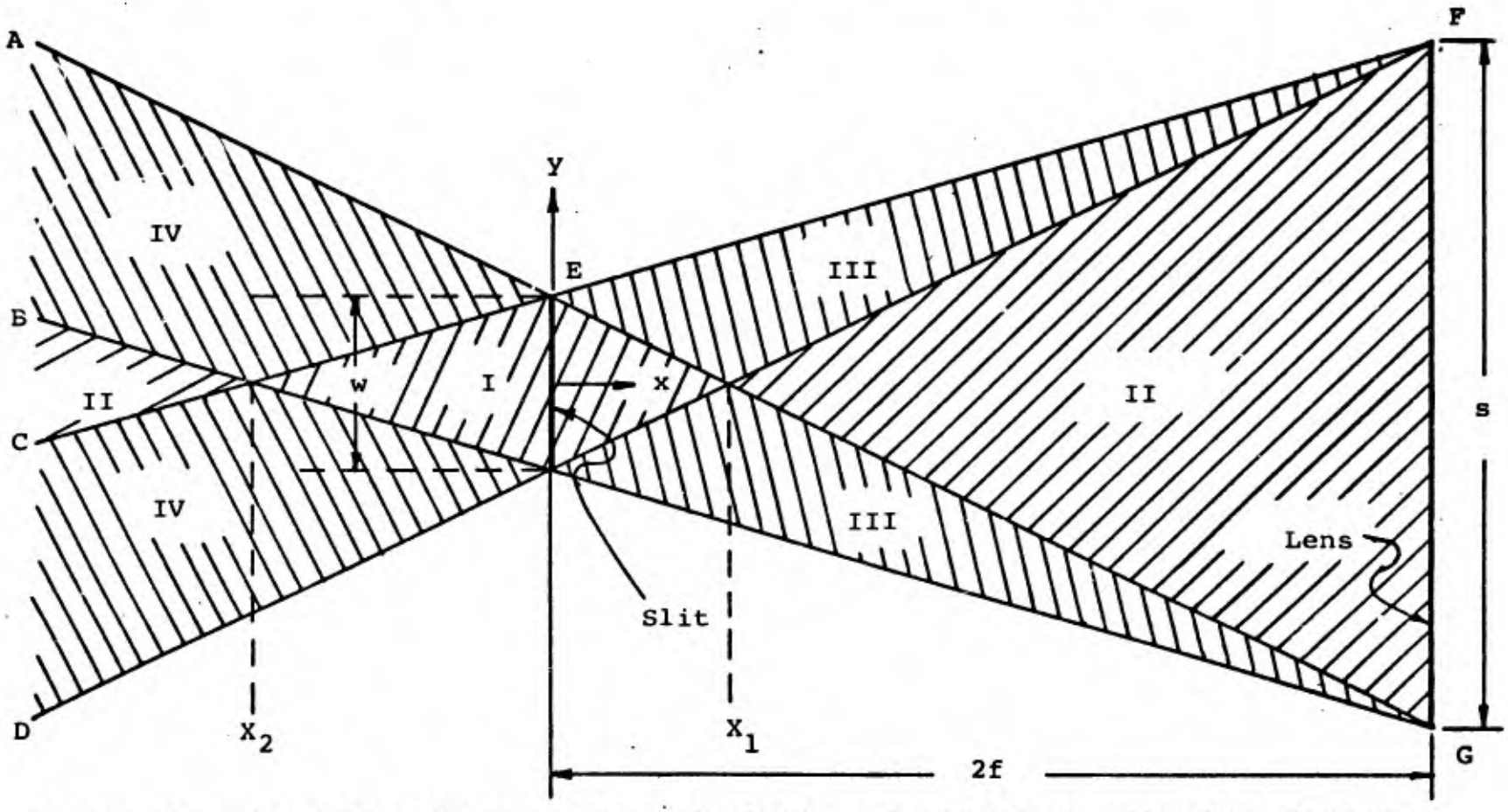

Figure 4.5: Geometrical Layout for Calculation of dθy Showing the Four Regions for Which dθy is Nonzero (dimensions exaggerated)

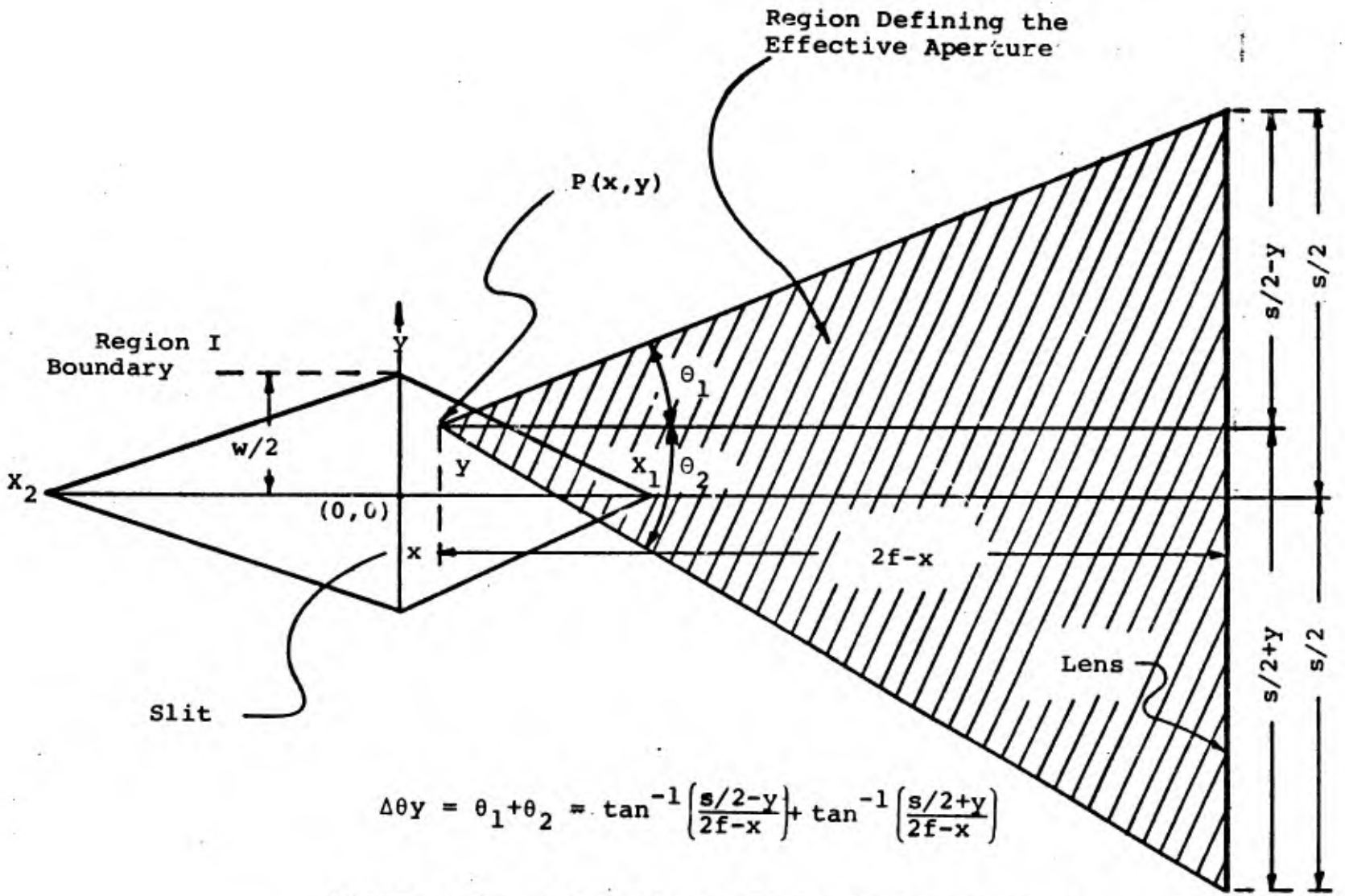

$$\Delta\theta y = \theta_1+\theta_2 = \tan^{-1}\left(\frac{s/2-y}{2f-x}\right)+\tan^{-1}\left(\frac{s/2+y}{2f-x}\right)$$

Figure 4.6: Collection Efficiency for Region I

Region II: The effective aperture is simply w, the slit width. $\Delta\theta y$ is determined in the same way as for region I.

$$X_1 \leq x$$

$$\Delta\theta y = \tan^{-1}\left(\frac{w/2-y}{|x|}\right) \quad 0 \leq y \leq w/2(x/X_1-1) \text{ [line } FX_1\text{]}$$

$$+ \tan^{-1}\left(\frac{w/2+y}{|x|}\right) \quad 0 \leq y^2 \leq w/2(x/X_2-1) \text{ [line } BX_2\text{]}$$

$$X \leq X_2$$

Region III: The effective aperture is jointly determined by the slit and lens as shown in Figure 4.7.

$$0 \leq x \leq X_1$$

$$\Delta\theta y = \tan^{-1}\left(\frac{s/2-y}{2f-x}\right) \quad w/2(1-x/X_1) \leq y \leq w/2(1-x/X_2) \text{ [lines } EX_1 \text{ and } EF\text{]}$$

$$+ \tan^{-1}\left(\frac{w/2-y}{x}\right) \quad w/2(x/X_1-1) \leq y \leq w/2(1-x/X_2) \text{ [lines } X_1F \text{ and } EF\text{]}$$

$$X_1 \leq x$$

Region IV: The effective aperture is again determined jointly by the slit and lens as shown in Figure 4.8.

$$X_2 \leq x \leq 0$$

$$\Delta\theta y = \tan^{-1}\left(\frac{w/2-y}{-x}\right) \quad w/2(1-x/X_2) \leq y \leq w/2(1-x/X_1) \text{ [lines } X_2E \text{ and } AE\text{]}$$

$$+ \tan^{-1}\left(\frac{s/2+y}{2f-x}\right) \quad w/2(x/X_2-1) \leq y \leq w/2(1-x/X_1) \text{ [lines } BX_2 \text{ and } AE\text{]}$$

$$x \leq X_2$$

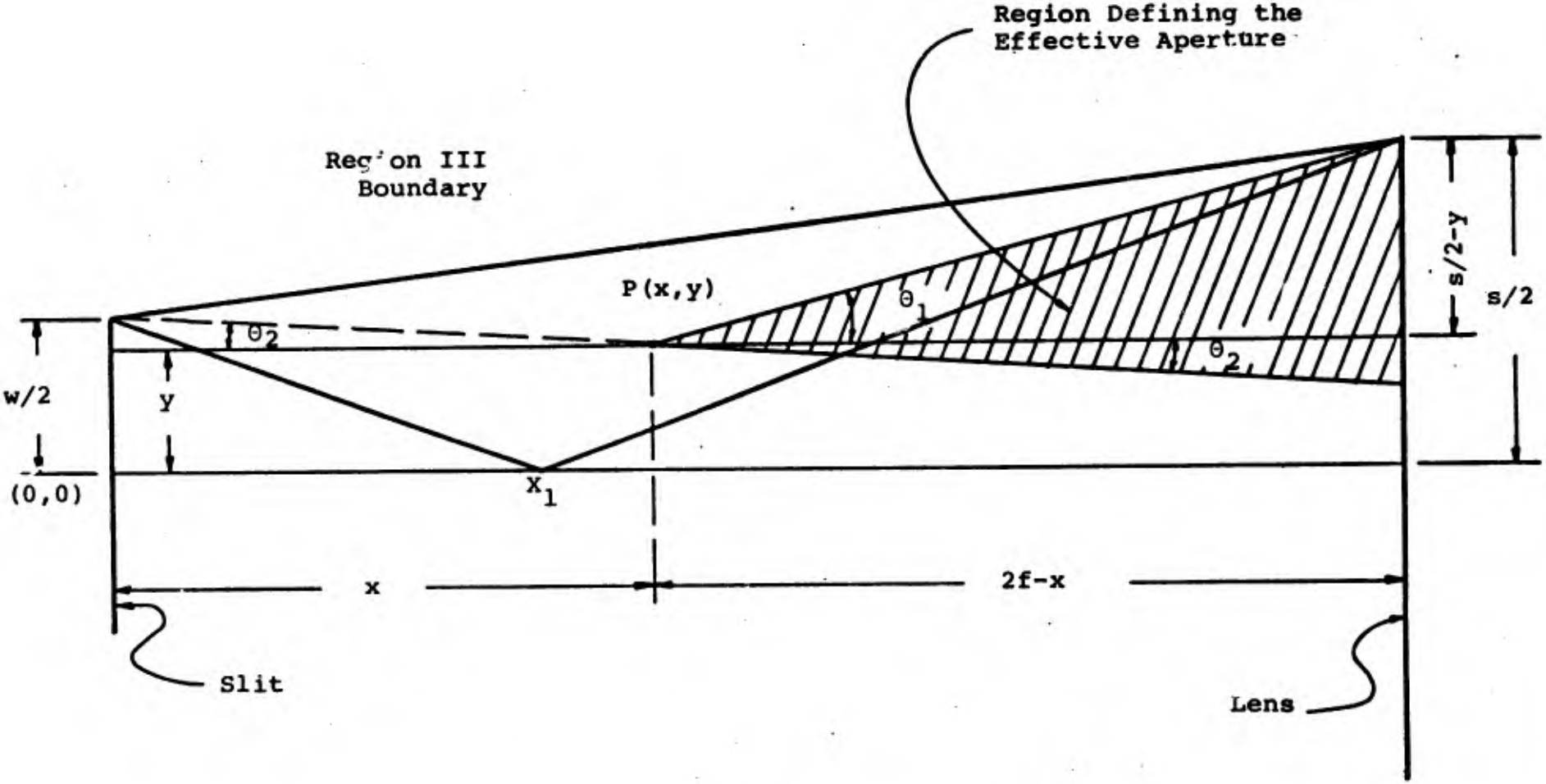

$$\Delta\theta y = \theta_1 + \theta_2 = \tan^{-1}\left(\frac{s/2-y}{2f-x}\right) + \tan^{-1}\left(\frac{w/2-y}{x}\right)$$

Figure 4.7: Collection Efficiency for Region III

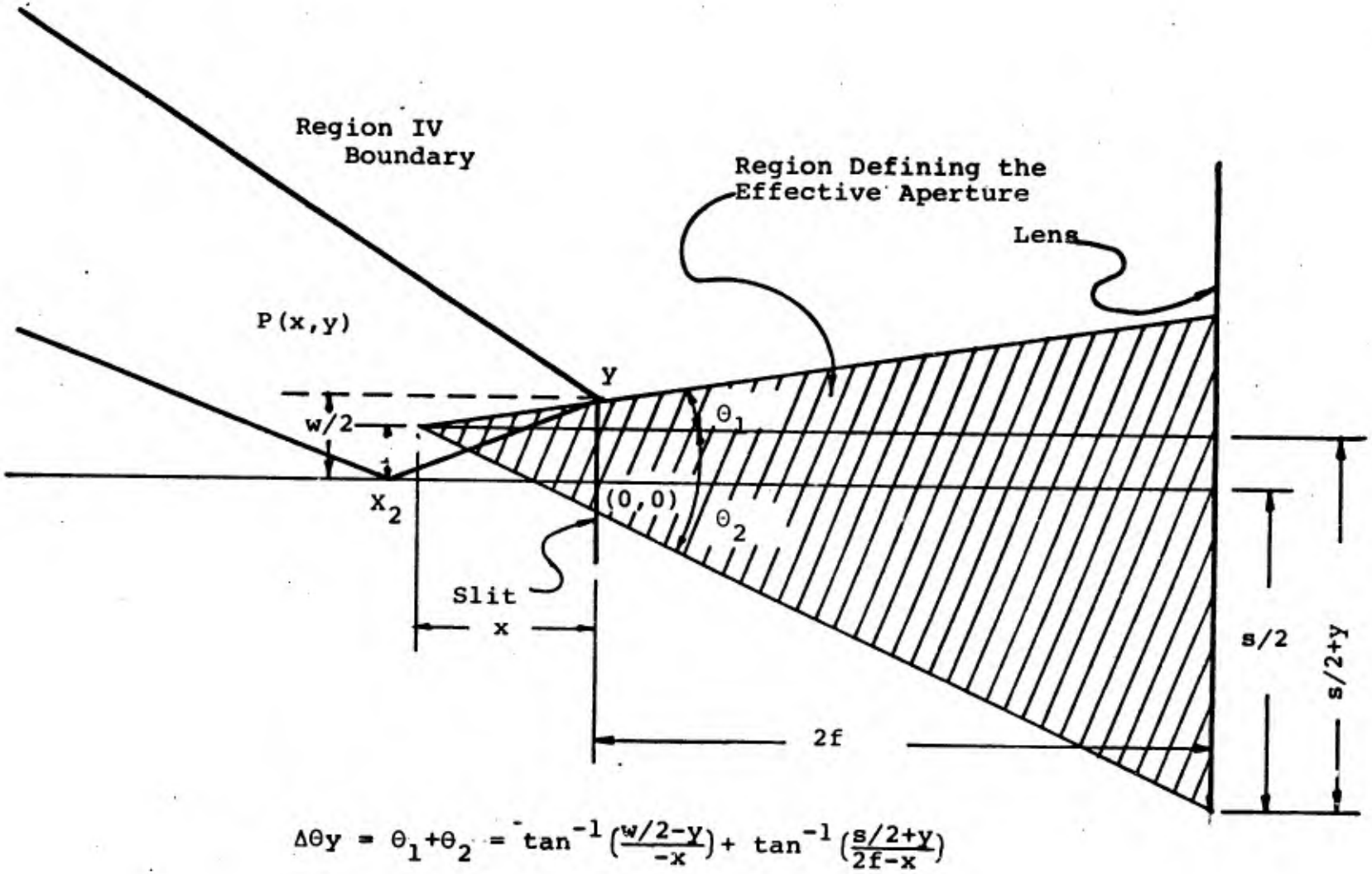

$$\Delta\theta y = \theta_1+\theta_2 = \tan^{-1}\left(\frac{w/2-y}{-x}\right) + \tan^{-1}\left(\frac{s/2+y}{2f-x}\right)$$

Figure 4.8: Collection Efficiency for Region IV

All expressions developed for the y direction are applicable to the z direction to get $\Delta\theta z$ by simply replacing y by z and w by h, the slit height. For any source point falling inside one of the regions of system sensitivity (they are now three dimensional and more than four in number, making them difficult to picture physically) one can calculate the probability, Ψ, an isotropically emitted photon is collected by the optical system and monochromator as follows

$$\Psi(x,y,z) = \frac{\Delta\Omega(x,y,z)}{4\pi} = \frac{\Delta\theta z(x,z)\,\Delta\theta y(x,y)}{4\pi}$$

The effective collection efficiency for the present experimental setup includes the effect of the source extent. It can further be expressed as an effective volume, V.

$$V = \iiint_{\substack{\text{All}\\ \text{Source}\\ \text{Volume}}} S_v(x,y,z)\Psi(x,y,z)\,dx\,dy\,dz$$

An evaluation of this integral for a unit uniform source was carried out numerically for the experimental setup used to make spectral measurements. Only 1/4 of the problem was actually worked, taking advantage of symmetry. The

following input parameters were used: slit width = .015cm, slit height = 1.6cm, s = 2.54cm, and f = 50.8cm. The integration was carried over a source region defined by following $-14 \leq x \leq +14$, $y \leq .25$, $z \leq 1.15$ (dimensions in cm). This region was selected sufficiently large to include all regions for which the collection efficiency is nonzero. The source region was divided into 2×10^5 incremental volume elements and the computer program required about four hours' running time on the IBM 1800 computer. The result was a value for the effective volume of 4.8×10^{-5}cc. The effective volume varies linearly with slit width so is simply twice this value when a 300 micron slit is used.

Errors arising from this analytical treatment are due to nonideal behavior of the optical system and the fact that the actual source is not uniform. Source nonuniformity is an important experimental problem and will later be discussed specifically for the cases of Ar and Xe. Nonideal behavior of the optical system is difficult to quantitatively assess; however, it seems unlikely that these would cause the results of the analysis to be in error by more than a factor of 2. In summary, the absolute calibration performed as indicated above is believed accurate to within a factor of 3 between 2700 and 8500Å, considering both errors from the experimental and analytical parts of the calibration.

4.3 Calculation of Excited State Populations

Line intensities as recorded on the plotter are easily converted to current as measured by the picoammeter, since it was found that the low pass filter employed to reduce gamma noise did not affect observed line heights measured with 150 μm slits providing the monochromator sweep was 20Å/min. or slower. Ideally for equal entrance and exit slit settings, the measured line intensity (in terms of current) represents the integrated effect of the line (i.e., includes all the photons in the line reaching the exit slit so that the lineshape is unimportant). Another way to view this is to consider the line formed on the exit slit of the monochromator to have the same width as the exit slit. In practice, however, when equal slits are used a correction must be made to account for the line being wider than the exit slit. Experimentally it was found by scanning a Hg line with a fixed entrance slit setting of 150 μm and various exit slit settings that the ratio of the true line intensity to that measured with equal 150 μm slit settings was 1.6. This relatively high value is apparently due to the monochromator being slightly out of focus. Thus, the following expression was used to calculate all excited state populations

$$n = \frac{1.6 I_\lambda \lambda}{hAVC_\lambda hc}$$

where I_λ = observed line height expressed in amps

C_λ = absolute calibration curve obtained by scaling the relative calibration curve to the absolute system sensitivity at 7000Å

V = effective volume in cm^3

λ = wavelength of the observed line in Å

hc = 1.99×10^{15} joule-Å

g = statistical weight of the excited level

A = transition probability of the observed transition in sec^{-1}

CHAPTER 5

ARGON RESULTS AND DISCUSSION

From 6 September to 21 November, 1974, 760 torr of research grade Argon was studied. The gas was supplied by Air Products and Chemicals with a minimum guaranteed purity of 99.999%. The impurity analysis (No. SG-6133-74) supplied with the gas was as follows:

Acetylene	<0.05ppm	Nitrogen	<2.0ppm
Carbon Dioxide	<0.5	Nitrous Oxide	<0.1
Carbon Monoxide	<1.0	Oxygen	<0.8
Hydrogen	<2.0	Hydrocarbons	<0.2
Methane	<0.5	Dew Point	-125°F
		Water	<0.15

In view of the high fill pressure of 760 torr and long evacuation to ~10^{-8} torr, this gas purity specification very likely holds for the MCFIG fill. This claim is further supported by the fact no N_2 emissionswere observed in the spectrum and even over the extended period of testing no increase in impurity emissions was observed.

5.1 Argon Spectra and Excited State Populations

The observed Argon spectrum consisted of a continuous emission around 2250Å, a large number of lines (mostly ArII) from 2900 to 5200Å and several large ArI lines from 6600 to the system cutoff around 8500Å. Also present was a continuous emission from 2500 to 5000Å from radiation induced luminescence of the sapphire window in the MCFIG. This sapphire emission was studied in detail and the results are presented in Appendix A. Its affect on the Ar data is small, however, as the only complicating factor is that lines falling on the sapphire continuum have a less well-defined baseline. This makes determination of line heights a bit more difficult at points where the continuum is rising or falling rapidly with wavelength, but the net effect on the determined height of any reasonably intense line is quite small considering already present baseline variations due to gamma noise. Reproductions of the actual spectra data obtained are included in Appendix B.

The Ar spectrum generally compares quite well with that taken by Walters at 760 torr except that the signal to noise ratio is much improved in this study and impurity emissions are virtually nonexistent. Of particular importance is the fact that no nitrogen emissions could be identified in the spectrum. Although the spectrum is consistent with that of Walters, the line identifications

made in this study are not. For example it is believed the ArIII lines reported by Walters are due to ArII. This problem is further discussed in Appendix C where Walters' data are tabulated for future reference.

Prior to presenting the excited state population data, the results must be qualified. In the discussion of absolution calibration errors the possible effects of the nonuniformity of the source were alluded to. The data used in the excited state population calculations were taken at a point 3.9mm from the source (where the spectral intensities were highest). Closer to the source one finds the effective source region diminished by the source itself (i.e., the approximately rectangular source region sampled becomes cut off by the source). Up close to the source there is a tradeoff between higher energy deposition rates and a smaller effective volume. From Figure 2.3 the energy deposition rate at 3.9mm is about one-half the maximum at the surface of the source. The measured population densities at 3.9mm consist of some contribution from near the surface of the source and some from farther away than 3.9mm, suggesting the factor of 2 be considered an additional uncertainty or error. When combined with the factor of 3 ascribed to the absolute calibration, the measured population densities are considered accurate to within an order of magnitude. Relative populations, however are probably accurate to within 30%.

5.1.1 ArI

The ArI lines observed and the corresponding excited state population densities are shown in Table 5.1. The more intense transitions observed were all from the $2p_n$ levels. A level diagram of the $2p_n$ levels is presented in Figure 5.1 and lines shown on the diagram are those observed in this study. In fact all the transitions originating from the $2p_n$ levels that fell within the sensitivity of the instrumentation were observed. These included the laser lines at 7067.22 and 7503.87Å [79]. Lasing on these lines requires short rise time pulses. They are probably unsuitable for nuclear pumping, except where short rise time pulses are available. Transitions were, however, observed from two additional upper laser levels. The $3p_6$ level has been lased at 2.82 and 2.88 μm and the $3p_9$ level at 2.55 and 3.10 μm [79]. CW laser action on these transitions was observed in .01 to .05 torr Ar. That they are at such long wavelengths is favorable to nuclear pumping since optical radiation damage would be negligible. Lack of knowledge of the lower level populations prevents a more indepth evaluation of the nuclear pumped laser potential of these levels.

The relative excited state populations are compared to those of Walters in Table 5.2 The agreement is quite good for all except four levels which differ by a factor

Table 5.1: ArI Excited State Population Densities

Upper Level (Paschen) [80]	Upper Level Racah [81]	Energy [80] cm^{-1}	Energy [80] eV	Lower Level (Paschen)	Transition Wavelength (A) [80]	Relative Intensity Observed	Relative Intensity True	Population Density (cm^{-3}) Based on Single Transition	Population Density (cm^{-3}) Weighted Average for State
$6d_5$	$6d[1/2]^0_1$	123468	15.32	$2p_{10}$	5162.29	17	1	6.4×10^2	6.4×10^2
$3p_3$	$5p'[3/2]_2$	118469	14.70	$1s_2$	4333.56	24	2	1.9×10^3	1.9×10^3
$3p_6$	$5p[3/2]_2$	117184	14.54	$1s_5$	4158.59	34	3	1.2×10^3	1.2×10^3
$3p_9$	$5p[5/2]_3$	116943	14.51	$1s_5$	4200.67	42	4	1.5×10^3	1.5×10^3
$2p_1$	$4p'[1/2]_0$	108723	13.49	$1s_2$	7503.87	965	525	$5/4x;-^4$	
				$1s_4$	6677.28	19	5	8.8×10^4	5.5×10^4
$2p_2$	$4p'[1/2]_1$	107496	13.34	$1s_2$	8264.51	119	1320	1.4×10^5	
				$1s_3$	7724.21	1667	1750	2.3×10^5	
				$1s_4$	7272.93	813	232	1.8×10^5	
				$1s_5$	6965.43	3253	1000	2.2×10^5	2.2×10^5

Table 5.1 (continued)

Upper Level (Paschen) [80]	Upper Level Racah [81]	Energy [80] cm^{-1}	Energy [80] eV	Lower Level (Paschen)	Transition Wavelength (Å) [80]	Relative Intensity Observed	Relative Intensity True	Population Density (cm^{-3}) Based on Single Transition	Population Density (cm^{-3}) Weighted Average for State
$2p_3$	$4p'[3/2]_2$	107290	13.31	$1s_2$	8408.21	11	296	1.3×10^4	
				$1s_4$	7383.98	439	168	1.9×10^4	
				$1s_5$	7067.22	360	99	2.3×10^4	2.1×10^4
$2p_4$	$4p'[3/2]_1$	107132	13.29	$1s_3$	7948.18	159	388	3.4×10^4	
				$1s_5$	7147.04	60	15	3.6×10^4	3.5×10^4
$2p_5$	$4p[1/2]_0$	107054	13.28	$1s_4$	7514.65	433	242	2.7×10^4	2.7×10^4
$2p_6$	$4p[3/2]_2$	106238	13.18	$1s_4$	8006.16	2527	2010	7.3×10^4	
				$1s_5$	7635.11	105	326	7.2×10^4	7.3×10^4
$2p_7$	$4p[3/2]_1$	106087	13.16	$1s_4$	8103.69	79	380	2.4×10^4	2.4×10^4

Table 5.1 (continued)

Upper Level (Paschen) [80]	Upper Level Racah [81]	Energy [80] cm^{-1}	Energy [80] eV	Lower Level (Paschen)	Transition Wavelength (Å) [80]	Relative Intensity Observed	Relative Intensity True	Population Density (cm^{-3}) Based on Single Transition	Population Density (cm^{-3}) Weighted Average for State
$2p_8$	$4p[5/2]_2$	105617	13.10	$1s_5$	8014.79	93	297	3.2×10^4	
				$1s_4$	8424.65	18	529	2.4×10^4	3.1×10^4
$2p_9$	$4p[5/2]_3$	105463	13.08	$1s_5$	8115.31	203	1020	2.1×10^4	2.1×10^4

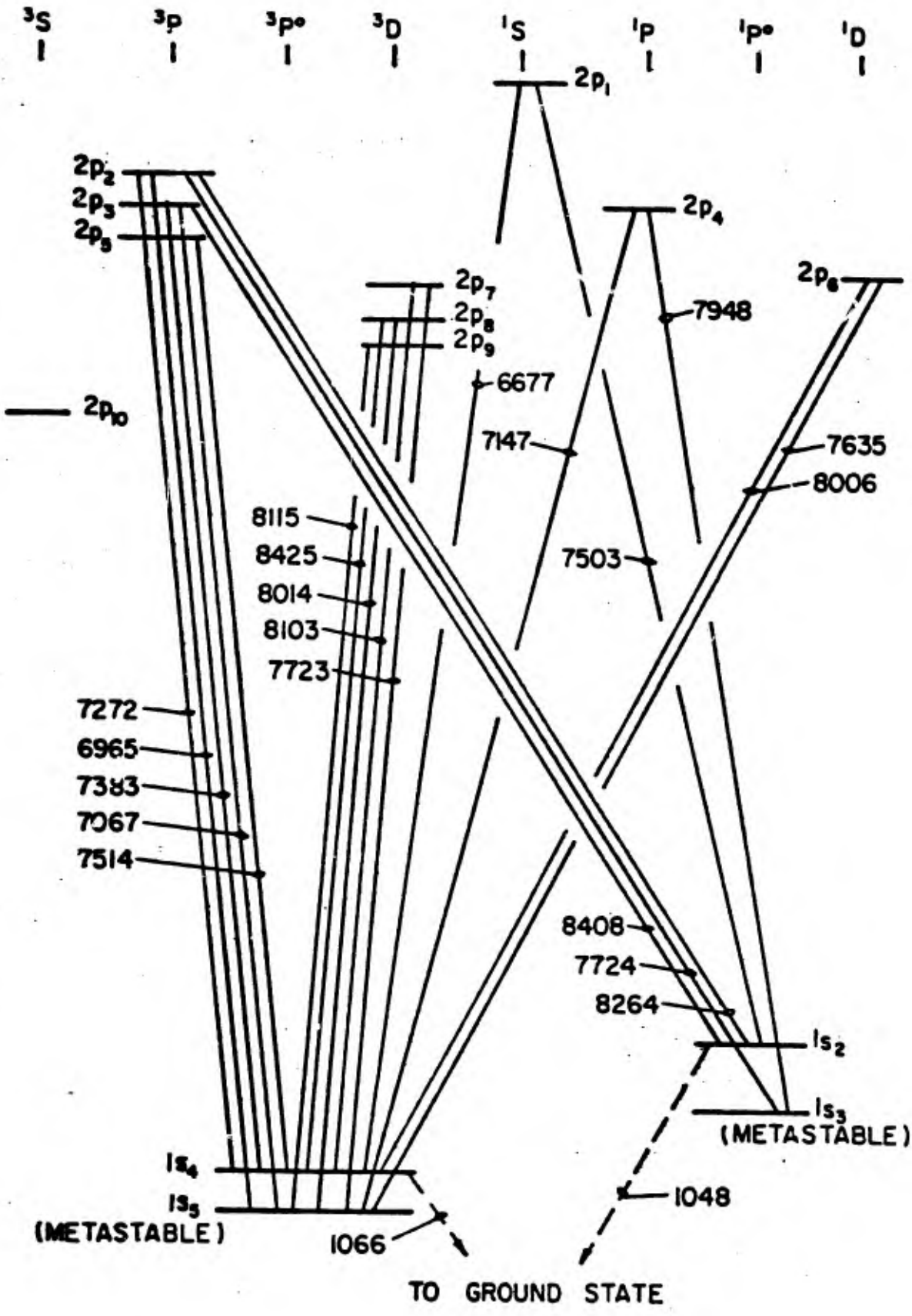

Figure 5.1: ArI Level Diagram Showing the $2p_n$ Levels and Transitions Seen in This Study

of 2. Since the four level populations are based on measured lines around 8000Å a calibration error seems likely. The $2p_6$ population is determined by using lines at 8006 and 7635Å, so this seems a reasonable test. In the present study the populations calculated from the two lines differ very little. Walters, however, calculated populations (see Appendix C) which differ by approximately a factor of 2, with that based on the 8006Å line being lower. The relative population of the $2p_6$ level he calculated from the 7635Å line is that shown in Table 5.2 which agrees well with the present results based on both lines. It is thus concluded that the populations reported in this study are more accurate. As to what might have caused such a calibration error in Walters' work, one can only say second order effects are important around 8000Å and long wavelength pass filters must be used when taking calibration data in this region.

Referring again to Table 5.1 several observations can be made. First of all the good agreement of populations calculated from different lines from the same level is encouraging. This also indicates there is no trapping of radiation from these transitions by metastable lower levels. Secondly, collisional transfer of energy between levels does not seem important in determining the relative populations. If it were important one would expect a

Table 5.2: Comparison of ArI Relative Excited $2p_n$ State Populations with Those of Walters and with Electron Excitation Cross Sections

Upper Level (Paschen)	Energy (eV)	Relative Populations		Electron Excitation Cross Sections ($cm^2 x 10^{19}$) [82]		$\Sigma g A_i$ (sec^{-1})	$\frac{N(p) g \Sigma A_i / K(p)}{\text{(Normalized)}}$	
		This Study	Walters[17]	Max.Value Including Cascades	at 100eV	[80]	Based on Max.Cross Section	Based on Value at 100eV
$2p_1$	13.49	.25	.26	110	62	.474	1.0	1.0
$2p_2$	13.34	1.0	1.0	57	27	1.15	19.	22.
$2p_3$	13.3[illegible]	.10	.10	84	35	1.85	2.0	2.8
$2p_4$	13 [illegible]9	.16	.09	96	25	1.05	1.6	3.5
$2p_5$	13.28	.12	.11	47	14	.430	1.0	1.9
$2p_6$	13.18	.33	.40	130	51	1.60	3.8	5.4
$2p_7$	13.16	.11	.05	78	38	1.12	1.5	1.7
$2p_8$	13.10	.14	.08	158	59	1.72	1.4	2.1
$2p_9$	13.08	.10	.04	136	20	2.56	1.7	6.7

buildup of the populations above large energy gaps between levels, and also reduced populations for levels a small energy (<kT) above the next lower level. Almost the opposite situation seems to prevail in this study. Lack of detailed information on collisional transfer of excitation between excited levels in Ar make this conclusion very tentative since the collision frequency is relatively high at this pressure. Finally, with the exception of the $6d_5$ level at 15.32 eV no transitions from levels above the 14.71 eV threshold for associative ionization were observed, consistent with our prediction. Excitation of the $6d_5$ level was indicated by the single line at 5162.29Å which is the only large line originating from this level. Thus, based upon the high energy of this level, its presence must be questioned.

The lack of detectable higher energy ArI levels and apparent collisional effects increases the possibility that the plasma might be modeled using the corona model. Equation 2.3 can be rewritten as follows

$$\frac{n(p)A(p)}{K(p)} = n_e n(0) = \text{constant} \qquad 5.1$$

The right hand side of 5.1 will be called the corona parameter whose constancy will serve as an indicator of

how well the level populations adhere to the corona model. A(p) is of course the total (including collisional losses) transition probability, but we are forced here to use simply $g\Sigma A_i$, or the optical transition probability. This parameter normalized to unity for the $2p_1$ level is presented for the $2p_n$ levels in Table 5.2. Considering the errors in the populations, cross sections and transition probabilities, agreement with the model is surprisingly good, with the exception of the $2p_2$ and $2p_6$ levels which are over populated relative to the others.

5.1.2 ArII

The ArII lines observed and the corresponding excited state population densities are shown in Table 5.3, and an ArII level diagram showing the observed transitions appears as Figure 5.2 A large number of known ArII laser lines [79, 83] were observed and a few more could be inferred. This information is summarized in Table 5.4. Of particular interest to nuclear pumping are the two near infrared transitions from the $(^3P)4p^2P^0_{3/2}$ level. This level has the highest measured ArII level population by a factor of 2, and radiation damage to optical components will be negligible at these long wavelengths. The gain for these transitions is considerably less than for the visible transitions, although the line at 10923Å was reported as

Table 5.3: ArII Excited State Population Densities

Upper Level [81]	Energy [80] cm^{-1}	Energy [80] eV	Lower Level	Transition Wavelength (Å) [80]	Relative Intensity Observed	Relative Intensity True	Population Density (cm^{-3}) Based on Single Transition	Population Density (cm^{-3}) Weighted Average for State
$(^1D)4d\,^2F_{5/2}$	200235	24.84	$(^1D)4p\,^2D^0_{3/2}$	3718.21	32	5	9.5	9.5
$(^1D)4d\,^2F_{7/2}$	200139	24.82	$(^1D)4p\,^2D^0_{5/2}$	3737.89	27	4	5.1	5.1
$(^1D)4d\,^2P_{3/2}$	199982	24.81	$(^1D)4p\,^2P^0_{1/2}$	3680.06	13	2	1.0x10	1.0x10
$(^1D)4d\,^2D_{5/2}$	199680	24.77	$(^1D)4p\,^2P^0_{3/2}$	3639.83	19	3	9.4	9.4
$(^1D)5s\,^2D_{3/2}$	195867	24.30	$(^1D)4p\,^2F^0_{5/2}$	3925.72	51	6	2.6x10	
			$(^1D)4p\,^2P_{1/2}$	4337.07	22	2	3.9x10	3.0x10
$(^1D)5s\,^2D_{5/2}$	195865	24.30	$(^1D)4p\,^2F^0_{7/2}$	3946.10	54	6	1.8x10	
			$(^1D)4p\,^2D^0_{5/2}$	4448.88	24	2	1.4x10	1.7x10
$(^1S)4p\,^2P^0_{3/2}$	191975	23.82	$(^1S)4s\,^2S_{1/2}$	4052.92	25	2	1.0x10	1.0x10

Table 5.3 (continued)

Upper Level [81]	Energy [80] cm^{-1}	Energy [80] eV	Lower Level	Transition Wavelength (Å) [80]	Relative Intensity Observed	Relative Intensity True	Population Density (cm^{-3}) Based on Single Transition	Population Density (cm^{-3}) Weighted Average for State
$(^3P)4d\,^2P_{3/2}$	190592	23.64	$(^3P)4p\,^2P^0_{3/2}$	3293.64	37	11	3.6x10	
			$(^3P)4p\,^2S^0_{1/2}$	3388.53	38	10	2.7x10	3.1x10
$(^3P)4d\,^2P_{1/2}$	189935	23.56	$(^3P)4p\,^2P^0_{1/2}$	3307.23	30	9	2.8x10	2.8x10
$(^3P)4d\,^4P_{5/2}$	186891	23.19	$(^3P)4p\,^4S^0_{3/2}$	3868.52	25	3	6.7	6.7
$(^3P)4d\,^4P_{1/2}$	18617.	23.10	$(^3P)4p\,^4S^0_{3/2}$	3979.36	23	2	2.4x10	2.4x10
$(^3P)4d\,^4F_{5/2}$	186074	23.08	$(^3P)4p\,^4D^0_{3/2}$	3582.36	40	8	8.4	8.4
$(^3P)4d\,^4F_{7/2}$	185625	23.03	$(^3P)4p\,^4D^0_{5/2}$	3576.61	39	8	8.3	8.3
$(^3P)4d\,^4F_{9/2}$	185093	22.96	$(^3P)4p\,^4D^0_{7/2}$	3588.45	50	10	6.9	6.9

Table 5.3 (continued)

Upper Level [81]	Energy [80] cm^{-1}	Energy [80] eV	Lower Level	Transition Wavelength (Å) [80]	Relative Intensity Observed	Relative Intensity True	Population Density (cm^{-3}) Based on Single Transition	Population Density (cm^{-3}) Weighted Average for State
$(^3P)4d\,^4D_{5/2}$	183797	22.80	$(^3P)4p\,^4P^0_{5/2}$	3476.75	59	13	3.8x10	3.8x10
$(^3P)4d\,^4D_{7/2}$	183676	22.79	$(^3P)4p\,^4P^0_{5/2}$	3491.54	54	12	1.1x10	
			$(^3P)4p\,^4D^0_{7/2}$	3780.84	22	3	9.8	1.1x10
$(^3P)5s\,^4P_{5/2}$	181594	22.53	$(^3P)4p\,^4D^0_{7/2}$	4103.91	51	5	1.7x10	
			$(^3P)4p\,^4P^0_{5/2}$	3765.27	27	4	1.6x10	1.7x10
$(^1D)4p\,^2D^0_{5/2}$	173393	21.51	$(^3P)3d\,^2D_{5/2}$	4481.81	33	3	2.6x10	2.6x10
$(^1D)4p\,^2P^0_{1/2}$	172816	21.44	$(^1D)4s\,^2D_{3/2}$	4131.73	69	6	6.0x10	6.0x10
$(^1D)4p\,^2P^0_{3/2}$	172214	21.36	$(^1D4s\,^2D_{5/2}$	4277.52	126	11	7.9x10	
			$(^1D4s\,^2D_{3/2}$	4237.22	20	2	6.1x10	7.7x10

Table 5.3 (continued)

Upper Level [81]	Energy [80] cm^{-1}	Energy [80] eV	Lower Level	Transition Wavelength (Å) [80]	Relative Intensity Observed	Relative Intensity True	Population Density (cm^{-3}) Based on Single Transition	Population Density (cm^{-3}) Weighted Average for State
$(^1D)4p\,^2F^0_{7/2}$	170530	21.15	$(^1D)4s\,^2D_{5/2}$	4609.56	67	6	2.4x10	2.4x10
$(^1D)4p\,^2F^0_{5/2}$	170401	21.14	$(^1D)4s\,^2D_{3/2}$	4589.90	37	3	1.9x10	
			$(^3P)3d\,^2D_{3/2}$	5017.16	13	1	2.1x10	2.0x10
$(^3P)4p\,^2P^0_{3/2}$	160239	19.88	$(^3P)4s\,^2P_{3/2}$	4545.04	102	9	$1.5x10^2$	
			$(^3P)4s\,^2P_{1/2}$	4764.86	101	8	$1.3x10^2$	$1.4x10^2$
$(^3P)4p\,^2P^0_{1/2}$	159706	19.81	$(^3P)4s\,^2P_{3/2}$	4657.89	44	1	9.1x10	
			$(^3P)4s\,^2P_{1/2}$	4889.03	11	4	7.4x10	8.8x10
$(^3P)4p\,^2D^0_{3/2}$	159393	19.77	$(^3P)4s\,^2P_{1/2}$	4965.07	21	2	3.6x10	
			$(^3P)4s\,^2P_{3/2}$	4726.86	30	3	4.3x10	4.0x10

Table 5.3 (continued)

Upper Level [81]	Energy [80] cm^{-1}	Energy [80] eV	Lower Level	Transition Wavelength (Å) [80]	Relative Intensity Observed	Relative Intensity True	Population Density (cm^{-3}) Based on Single Transition	Population Density (cm^{-3}) Weighted Average for State
$(^3P)4p\ ^2D^0_{5/2}$	158730	19.69	$(^3P)4s\ ^2P_{3/2}$	4879.86	59	5	3.3x10	3.3x10
$(^3P)4p\ ^4D^0_{1/2}$	158428	19.65	$(^3P)4s\ ^4P_{1/2}$	4379.67	37	3	4.1x10	4.1x10
$(^3P)4p\ ^4D^0_{5/2}$	157673	19.56	$(^3P)4s\ ^4P_{3/2}$	4426.01	40	3	1.8x10	1.8x10
$(^3P)4p\ ^4D^0_{7/2}$	157234	19.51	$(^3P)4s\ ^4P_{5/2}$	4348.06	48	4	1.1x10	1.1x10
$(^3P)4p\ ^4P^0_{1/2}$	155708	19.32	$(^3P)4s\ ^4P_{3/2}$	4847.82	11	10	1.8x10	1.8x10
$(^3P)4p\ ^4P^0_{3/2}$	155354	19.27	$(^3P)4s\ ^4P_{1/2}$	5062.04	8	1	2.0x10	
			$(^3P)4s\ ^4P_{5/2}$	4735.91	16	2	2.0x10	2.0x10
$(^3P)4p\ ^4P^0_{5/2}$	155043	19.23	$(^3P)4s\ ^4P_{5/2}$	4806.02	20	2	1.2x10	
			$(^3P)3d\ ^4D_{7/2}$	4400.99	13	1	1.5x10	1.3x10

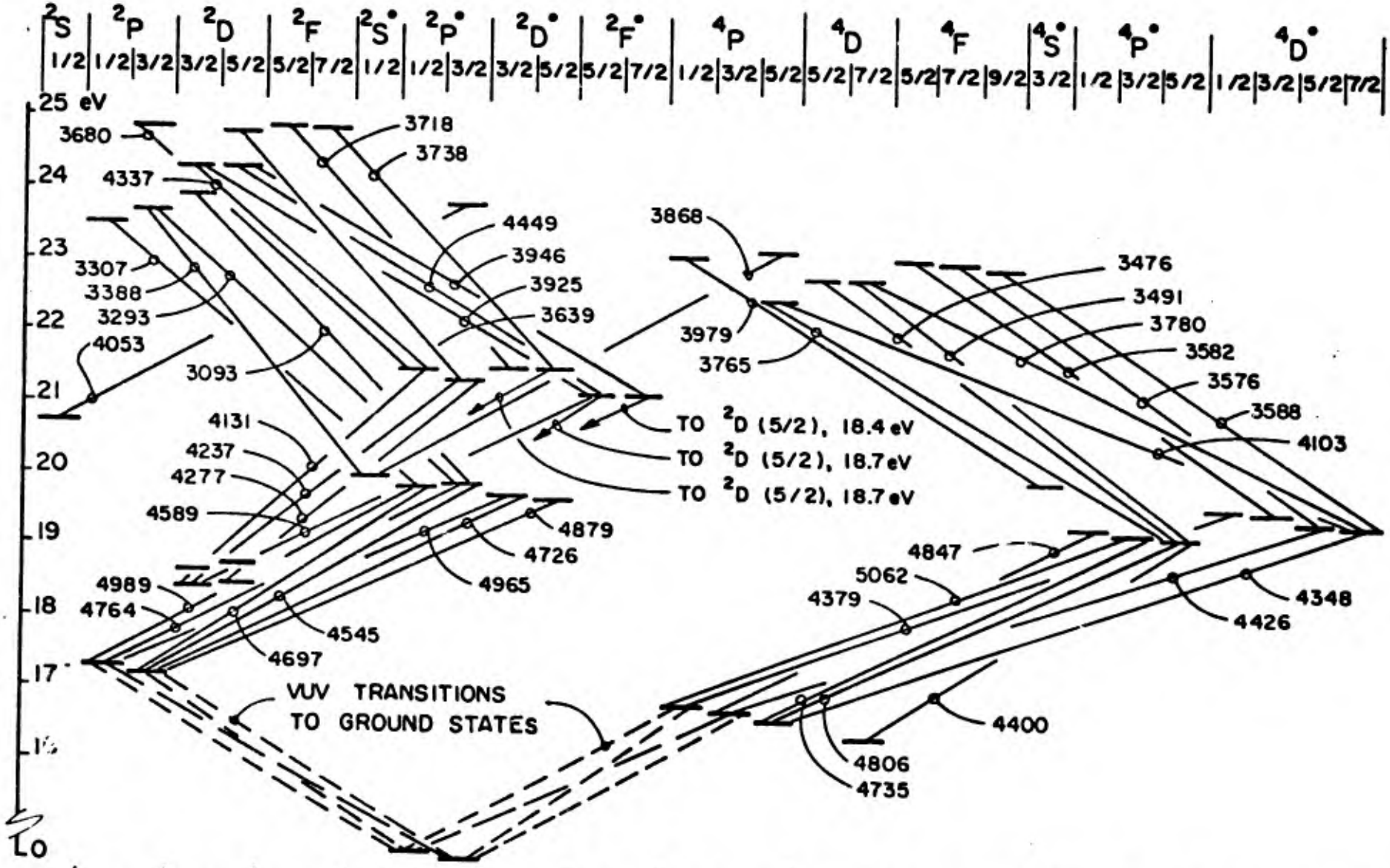

Figure 5.2: ArII Level Diagram Showing Lines Observed in This Study

Table 5.4: List of Observed and Inferred ArII Laser Transitions

Wavelength (Å)	Upper Level	Lower Level	Remarks
3576.61	$(^3P)4d\,^4F_{7/2}$	$(^3P)4p\,^4D^0_{5/2}$	no inversion
4370.75	$(^1D)4p\,^2D^0_{3/2}$	$(^3P)3d\,^2D_{3/2}$	inferred from 3718.21Å line which populates upper level
4481.81	$(^1D)4p\,^2D^0_{5/2}$	$(^3P)3d\,^2D_{5/2}$	observed
4545.05	$(^3P)4p\,^2P^0_{3/2}$	$(^3P)4s\,^2P_{3/2}$	observed
4579.35	$(^3P)4p\,^2S^0_{1/2}$	$(^3P)4s\,^2P_{1/2}$	inferred from 3388.53Å line which populates upper level
4609.56	$(^1D)4p\,^2F^0_{7/2}$	$(^1D)4s\,^2D_{5/2}$	observed
4657.89	$(^3P)4p\,^2P^0_{1/2}$	$(^3P)4s\,^2P_{3/2}$	observed
4726.86	$(^3P)4p\,^2D^0_{3/2}$	$(^3P)4s\,^2P_{3/2}$	observed
4764.86	$(^3P)4p\,^2P^0_{3/2}$	$(^3P)4s\,^2P_{1/2}$	observed
4879.86	$(^3P)4p\,^2D^0_{5/2}$	$(^3P)4s\,^2P_{3/2}$	observed
4889.09	$(^3P)4p\,^2P^0_{1/2}$	$(^3P)4s\,^2P_{1/2}$	observed
4965.07	$(^3P)4p\,^2D^0_{3/2}$	$(^3P)4s\,^2P_{1/2}$	observed
5017.16	$(^1D)4p\,^2F^0_{5/2}$	$(^3P)3d\,^2D_{3/2}$	observed
5141.79	$(^1D)4p\,^2F^0_{7/2}$	$(^3P)3d\,^2D_{5/2}$	inferred from other lines from upper level

Table 5.4 (continued)

Wavelength (Å)	Upper Level	Lower Level	Remarks
4145.32	$(^3P)4p\,^4D^0_{3/2}$	$(^3P)4s\,^2P_{3/2}$	inferred from other lines from upper level
5286.90	$(^3P)4p\,^4D^0_{3/2}$	$(^3P)4s\,^2P_{1/2}$	inferred from 3582.36Å line which populates upper level
8771.19	$(^3P)4p\,^2P^0_{3/2}$	$(^1D)4s\,^2D_{5/2}$	inferred from other lines from upper level
10923.44	$(^3P)4p\,^2P^0_{3/2}$	$(^3P)3d^2\ _{5/2}$	inferred from other lines from upper level

being quite strong [84]. High power operation on these lines is considered unlikely because of the unfavorable branching ratios [85].

In Table 5.5 the measured relative populations are compared with those of Walters at 760 torr and those reported by Rudko and Tang [86] for an operating Ar ion laser at 0.3 torr. While the agreement between Walters' data and the one taken in this study is quite good for populations based on the more intense lines, the spectrum for an electrically excited plasmas is clearly different. Fission fragment excitation seems to strongly favor excitation of the $(^3P)4p\,^2P^0_{3/2}$ upper laser level relative to electrical excitation.

With respect to the population densities presented in Table 5.3, the magnitudes of potential inversions are several orders of magnitude below those required to exceed the threshold for lasing. For example, in the case of the 4880Å laser line a reasonable mininum population inversion threshold to exceed lasing is no less than 10^7/cc and probably closer to 10^8. Because the measured population densities seemed so low, the following calculation was carried out to at least prove that the potential inversions in the plasma are one order of magnitude or more from threshold. The approach is to calculate the energy radiated from the $2p_2$ ArI level assuming a population of

Table 5.5: Comparison of ArII Relative Excited State Populations with Those of Walters, those of Rudko and Tang, and with Electron Excitation Cross Sections

Level	Energy (eV)	Relative Populations of Excited States (760 torr) This Study	(160 torr) Walters [17]	(0.3 torr) Rudgo & Tang [86]	Effective Electron Excitation Cross Sections ($cm^{-2} x10^{19}$) [87]	$g\Sigma A_i$ (sec^{-1}) [80]	$\frac{N'(p) g\Sigma A_i}{K'(p)}$ (Normalized)
$(^1D)4d^2F_{5/2}$	24.84	.068	---	---	---	---	---
$(^1D)4d^2F_{7/2}$	24.82	.036	---	---	---	---	---
$(^1D)4d^2P_{3/2}$	24.81	.071	---	---	---	---	---
$(^1D)4d^2D_{5/2}$	24.77	.067	---	---	---	---	---
$(^1D)5s^2D_{3/2}$	24.30	.21	---	.011	---	---	---
$(^1D)5s^2D_{5/2}$	24.30	.12	.10	.025	---	---	---
$(^1S)4p^2P^0_{3/2}$	23.82	.071	.10	---	---	---	---
$(^3P)4d^2P_{3/2}$	23.64	.22	---	---	---	---	---

Table 5.5 (continued)

Level	Energy (eV)	Relative Populations of Excited States (760 torr) This Study	(160 torr) Walters [17]	(0.3 torr) Rudko & Tang [86]	Effective Electron Excitation Cross Sections ($cm^{-2} \times 10^{19}$) [87]	$g\Sigma A_i$ (sec^{-1}) [80]	$N'(p) g\Sigma A_i / K'(p)$ (Normalized)
$(^3P)4d\,^2P_{1/2}$	23.56	.20	---	---	---	---	---
$(^3P)4d\,^4P_{5/2}$	23.19	.048	.051	---	---	---	---
$(^3P)4d\,^4P_{1/2}$	23.10	.17	.33	---	---	---	---
$(^3P)4d\,^4F_{5/2}$	23.08	.060	.11	---	---	---	---
$(^3P)4d\,^4F_{7/2}$	23.03	.060	---	---	---	---	---
$(^3P)4d\,^4F_{9/2}$	22.96	.049	.11	---	---	---	---
$(^3P)4d\,^4D_{5/2}$	22.80	.27	---	---	---	---	---
$(^3P)4d\,^4D_{7/2}$	22.79	.079	.14	---	---	---	---

Table 5.5 (continued)

Level	Energy (eV)	Relative Populations of Excited States (760 torr This Study)	(160 torr, Walters [17])	(0.3 torr) Rudko & Tang [86]	Effective Electron Excitation Cross Sections ($cm^{-2} \times 10^{19}$) [87]	$g\Sigma A_i$ (sec^{-1}) [80]	$\frac{N'(p) g\Sigma A_i}{K'(p)}$ (Normalized)
$(^3P)5s^4P_{5/2}$	22.53	.12	.084	.19	---	---	---
$(^1D)4p^2D^0_{5/2}$	21.51	.19	.23	.15	---	---	---
$(^1D)4p^2P^0_{1/2}$	21.44	.43	.50	.051	---	---	---
$(^1D)4p^2P^0_{3/2}$	21.36	.55	.47	.14	9.0	4.84	3.0
$(^1D)4p^2F^0_{7/2}$	21.15	.17	.21	1.0	---	---	---
$(^1D)4p^2F^0_{5/2}$	21.14	.14	.19	.80	---	---	---
$(^3P)4p^2P^0_{3/2}$	19.88	1.0	1.0	1.0	10.2	4.13	1.0
$(^3P)4p^2P^0_{1/2}$	19.81	.63	.56	.48	3.6	2.09	.90

Table 5.5 (continued)

Level	Energy (eV)	Relative Populations of Excited States (760 torr) This Study	(760 torr) Walters [17]	(0.3 torr) Rudko & Tang [86]	Effective Electron Excitation Cross Sections ($cm^{-2} \times 10^{19}$) [87]	$g\Sigma A_i$ (sec^{-1}) [80]	$\frac{N'(p) g\Sigma A_i}{K'(p)}$ (Normalized)
$(^3P)4p\,^2D^0_{3/2}$	19.77	.29	.37	.60	6.8	3.68	.39
$(^3P)4p\,^2D^0_{5/2}$	19.69	.24	.20	1.6	11.5	5.98	.31
$(^3P)4p\,^4D^0_{1/2}$	19.65	.29	.19	.55	---	---	---
$(^3P)4p\,^4D^0_{5/2}$	19.56	.13	.16	1.7	4.6	7.92	.55
$(^3P)4p\,^4D^0_{7/2}$	19.51	.079	.080	2.2	---	---	---
$(^3P)4p\,^4P^0_{1/2}$	19.32	.13	---	.72	---	---	---
$(^3P)4p\,^4P^0_{3/2}$	19.27	.14	---	1.9	4.2	3.78	.31
$(^3P)4p\,^4P^0_{5/2}$	19.23	.093	---	2.9	2.3	8.3	.83

10^7/cc for the 4880Å line upper level. The relative populations of the two levels as determined spectroscopically should be very accurate and the results of this study and of Walters agree well. The ratio, R, the $2p_2$ to $(^3P)4p^2D^0_{5/2}$ used is $7x10^3$. The energy radiated, E_r, is then calculated as follows:

$$E_r = R\, N[(^3P)4p^2D^0_{5/2}]g\Sigma A_i\, h\nu \qquad 5.2$$

$$= (7x10^3)(10^7/cc)(1.15x10^8 sec^{-1})(1.8eV)$$

$$= 1.45x10^{19} eV/cc$$

Based upon the results of Chapter 2, E_r exceeds by a factor of 36 the maximum total volumetric energy deposition rate in the plasma. These results apply also to the other ArII laser lines and throughout the pressure range examined by Walters (25-760 torr). Although these results are pessimistic from the standpoint of achieving nuclear pumping of Ar at flux levels of the UFTR, they add credibility to the absolute population densities reported herein.

Returning now to Table 5.5 and Figure 5.2, one can make several observations. As in the case of ArI, collisional effects also seem unimportant in affecting

level populations. Populations above and below large energy gaps are opposite from those one would expect for collisional transfer. Cascades, however, are very important in populating lower levels. Upon calculating the total cascade rates into various levels, they are found to represent up to 100% of the source rate for some levels. This is shown in Table 5.6. The 3 transitions marked with an asterisk appear to contribute more than 100%. Two factors must be considered. First, there are 4 error sources in each case: the 2 populations and 2 transition probabilities. Second, each of the 3 transitions represent the only one observed from that particular level and in addition for the 3588Å line the measured line height was to a great extent dependent on judgment. Thus about the only conclusion one can confidently substantiate is that cascading is very important in populating the ArII levels.

Also indicated in Table 5.5 is the corona parameter as a test of the applicability of the corona model as was done for ArI. The cross sections used [87] include the contribution of cascading, making them perhaps more realistic for application here. The agreement is surprisingly good. Were this approach applied to the data of Rudko and Tang [86] factors of 10 variation in the corona parameter would be observed.

Table 5.6: Analysis of Observed ArII Cascade Transitions

Level	Total Radiative Decay Rate ($cm^{-3} sec^{-1}$)	Cascade Transition			
		Wavelength (Å)	Rate ($cm^{-3} sec^{-1}$)	Contribution to Level Population (%)	Total Cascade Contribution (%)
$(^1D)4p\ ^2D^0_{5/2}$	191	4448.88	56	35	
		3737.89	94	49	84
$(^1D)4p\ ^2P^0_{1/2}$	168	3680.06	48	29	
		4337.07	41	24	53
$(^1D)4p\ ^2P^0_{3/2}$	373	3639.83	79	21	21
$(^1D)4p\ ^2F^0_{7/2}$	202	3946.10	143	71	71
$(^1D)4p\ ^2F^0_{5/2}$	137	3925.72	168	122	100
$(^3P)4p\ ^2P^0_{3/2}$	578	3293.64	211	37	37
$(^2P)4p\ ^2P^0_{1/2}$	184	3307.23	190	103	100

Table 5.6 (continued)

Level	Total Radiative Decay Rate (cm^{-3} sec^{-1})	Cascade Transition			Total Cascade Contribution (%)
		Wavelength (Å)	Rate (cm^{-3} sec^{-1})	Contribution to Level Population (%)	
$(^3P)4p\,^4D^0_{5/2}$	143	3576.61	184	129	100
$(^3P)4p\,^4D^0_{7/2}$	135	4103.91	122	90	
		3780.84	83	61	
		3588.45	234	173*	100
$(^3P)4p\,^4P^0_{5/2}$	108	3765.27	100	93	
		3476.75	306	283*	
		3491.54	264	244*	100

5.1.3 2250Å Continuum

A broad continuous emission was observed which had a peak around 2250Å. Fixing its shape and location precisely is impossible because of the low sensitivity of the instrumentation at this short a wavelength and lack of calibration information. While this continuum appeared quite small in the data (see Appendix B) it would be very large if corrected for the low sensitivity. This continuum has been reported by numerous researchers under a variety of conditions [17, 26, 28-30, 88, 89] although its location has been reported from 2100 to 2300Å. The location and intensity have also been reported to be a function of pressure [26] and Hill [89] points out that in electron beam excitation studies it is over very fast (10-20 nsec). Hurst and Bortner [31] have proposed that this continuum represents a recombination spectra as classified by Herzberg [90]. Specifically as an excited atom collides with a ground state atom, at the classical turning point they separate again or emission takes place caused by a transition from this unbound state into a bound molecular state. ArI levels having energies from 14.2 to 14.5 eV are considered likely candidates to produce the recombination spectrum around 2250Å by this reaction. Tanaka and Yoshino [91] in their investigation of the Ar molecule mention the presence of the continuum and the above explanation

without comment, implying no theoretical difficulties with the explanation. This explanation would also help explain the relative absence of ArI emission from levels above the $2p_1$ and below the 14.7eV threshold for associative ionization.

5.1.4 Unidentified Lines

A list of all unidentified lines in the observed Ar spectra is presented in Table 5.7. Also included under the comments column are the lines suspected, where it was simply a case that one line could not be singled out from two or more likely lines based on our identification criteria. Because of the large number of Ar spectral lines, virtually every line could (if one stretches the identification criteria a bit) be ascribed to some Ar transition, however, it was felt little would be gained by doing this. A few particular items of interest will now be discussed.

The emission around 3093Å is relatively broad and consists of at least 3 lines and has a rather gradual degradation toward longer wavelengths. This is suggestive of some sort of band structure. Emissions around 3093Å have been previously observed in Ar excited by ionizing radiation [17,25-26] and attributed to OH arising from the presence of water. Relative to the rest of his spectrum

Table 5.7: List of Unidentified Lines in the Ar Spectrum

Approximate Wavelength (Å)	Comments
2949	unknown
3032	unknown but perhaps OH
3072	unknown but perhaps OH
3084	unknown but perhaps OH
3093	unknown but perhaps OH
3464	unknown
3509-3521 (2 lines)	ArII at 3509.78, 3520.00, 3521.26, 3514.39, and 3517.89
3545	ArII at 3545.60 and 3545.84
3560	ArII at 3559.51 and 3561.03
3529	unknown
3849	unknown
3889	unknown
4032	ArII at 4033.40 and 4033.82
4042	ArI at 4044.42 and ArII at 4042.90
4071 (broad)	ArII at 4072.01 and 4076.94
4079	ArII at 4076.94, 4076.64, 4079.58
4226	ArII at 4225.00 and 4226.99
4298	unknown
4312	unknown

Table 5.7 (continued)

Approximate Wavelength (Å)	Comments
4372	ArII at 4370.75 and 4371.33
4427-4440 (several lines)	unknown
4474	unknown
4579	unknown
8553	unknown
8623	perhaps ArI at 8620.46

Walters' emission around 3093Å was orders of magnitude greater than in this study strongly suggesting perhaps an impurity. In fact it dominated his entire spectrum at 760 torr with the 3371Å N_2 band being next highest in intensity at almost an order of magnitude lower intensity. It was also a strong function of pressure. Because the emission was so large, he was able to scan it at high resolution and low gain to get good detail. A trace of his plot of this spectral region is shown along with that taken in this study in Figure 5.3. The data for this study fall right on the rise of the sapphire continuum, however, the two spectra compare almost perfectly. This suggests all 4 lines (3028, 3072, 3083, and 3093Å) have the same origin and further this must be related to an impurity, probably OH.

Another curiosity is the line at 4312Å. It was one of the more intense lines seen and no strong Ar or expected impurity lines fall very close by.

5.2 Observed Spatial Effects

All the $2p_n$ ArI transitions were studied for possible spatial variations but none were observed for the relative ArI spectrum. The spatial data for 3 selected transitions which were studied in detail are tabulated in Table 5.8. The first two lines have the same upper level,

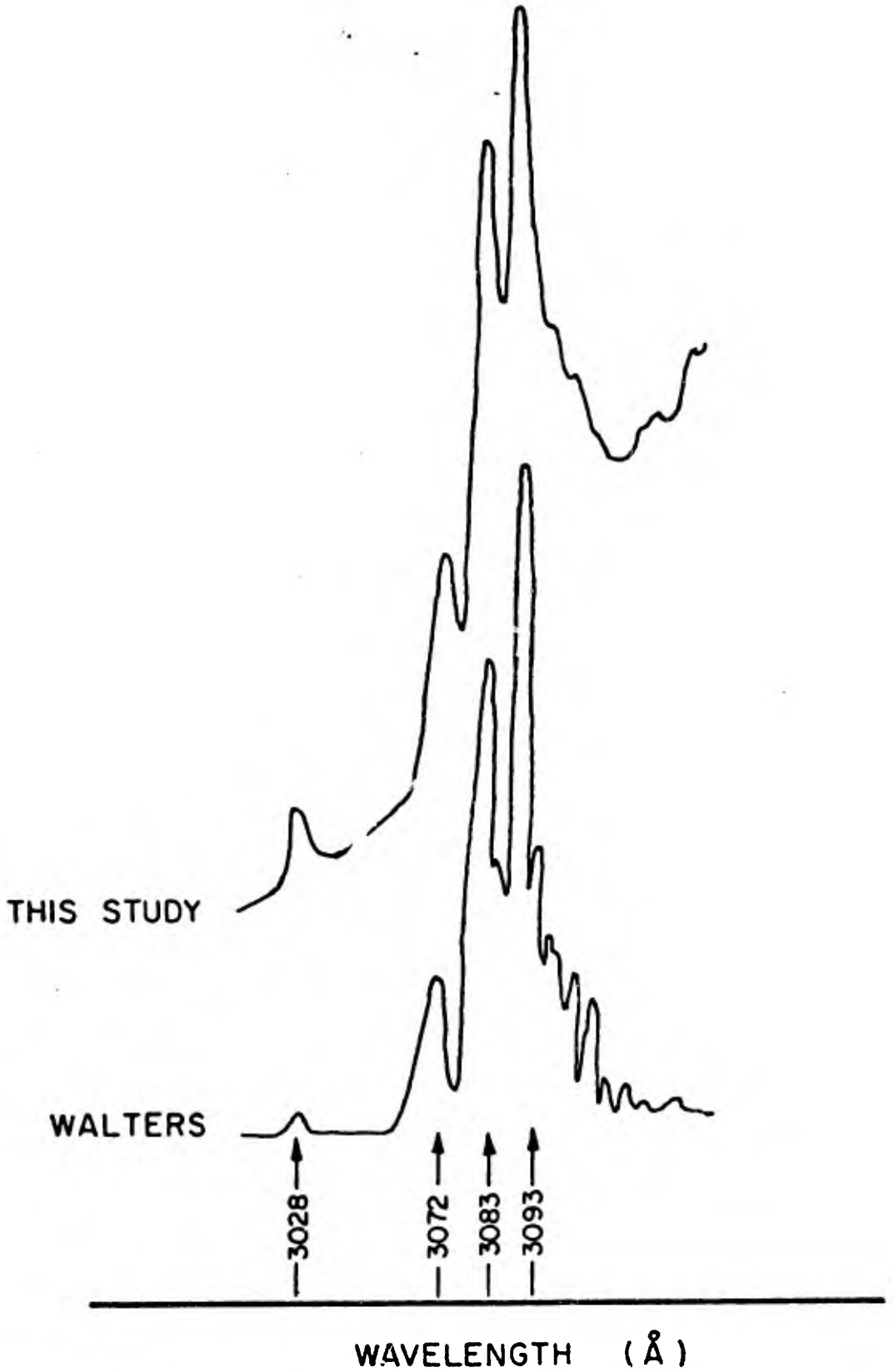

Figure 5.3: Comparison of Emissions Around 3093Å from this Study and from Walters' Data

Table 5.8: Tabulation of Selected ArI Spatial Measurements

Distance from Source x(mm)	Line Intensity Relative to 6965Å Line and Scaled Such That It Is Equal to Unity at x = 3.9mm		
	$2p_2$ 6965Å	$2p_2$ 7272Å	$2p_3$ 7383Å
13.0	1.00	1.01	.99
12.5	1.00	1.04	.94
12.0	1.00	1.02	.92
11.5	1.00	1.02	.90
11.0	1.00	.98	.92
10.5	1.00	1.01	.89
10.0	1.00	1.04	.90
9.4	1.00	1.05	.96
8.9	1.00	1.03	.94
8.4	1.00	1.02	.96
7.9	1.00	1.01	.94
7.4	1.00	1.01	.93
6.9	1.00	1.03	.96
6.4	1.00	1.01	.94
5.9	1.00	1.01	.94
5.4	1.00	1.00	.96
4.9	1.00	1.00	.97
4.4	1.00	1.00	.96
3.9	1.00	1.00	1.00
3.3	1.00	1.00	.98
2.8	1.00	1.03	1.02

Table 5.8 (continued)

Distance from Source x (mm)	Line Intensity Relative to 6965Å Line and Scaled Such That It Is Equal to Unity at x = 3.9mm		
	$2p_2$ 6965Å	$2p_2$ 7272Å	$2p_3$ 7383Å
2.3	1.00	1.01	1.01
1.8	1.00	1.00	1.01
1.3	1.00	1.00	1.04
.8	1.00	1.04	1.02
.3	1.00	1.01	1.00
-.2	1.00	.99	1.00
-.7	1.00	.96	1.00
-1.2	1.00	1.04	.99
-1.7	1.00	1.02	1.03
-2.2	1.00	.90	.96

so are indicative of the experimental errors involved. ArI levels other than $2p_n$ could not be accurately studied because the line intensities were too low. That the distance from the source in Table 5.8 is sometimes negative arises from the fact that the measurement was made with the system set to sample a region centered behind the centerpoint of the planar source. This means the sample region is partially reduced by the source itself, however, at these positions photon collection is at points very close to the source. Of course the observed intensities are lower and it is this reduction in the effective volume that in this experiment prevents measurement of the absolute intensities close to the source.

Because most of the ArII lines were superimposed on the sapphire continuum, a segment of the ArII spectrum was scanned at different spatial points. This was a time consuming process so efforts had to be made to minimize the number of lines studied. The segment selected contained all of the ArII laser lines having intensities large enough to be studied. The data on these five lines appear in Table 5.9. Again the first two lines are indicative of the experimental errors. Based on these data it seems reasonably well established that there is no significant spatial variation of the relative ArII spectra, at least as represented by the investigated levels.

Table 5.9: Tabulation of Selected ArII Spatial Measurements

Distance from Source x(mm)	Line Intensity Relative to 4545Å Line and Scaled Such That It Is Equal to Unity at x = 3.9mm				
	$(^3P)4p\,^2P^0_{3/2}$ 4545Å	$(^3P)4p\,^2P^0_{3/2}$ 4764Å	$(^1D)4p\,^2F^0_{7/2}$ 4609Å	$(^3P)4p\,^2P^0_{1/2}$ 4657Å	$(^3P)4p\,^4D^0_{1/2}$ 4880Å
11.0	1.00	1.15	1.21	1.30	1.24
10.0	1.00	.90	1.16	1.14	1.05
8.9	1.00	1.01	1.19	1.17	1.07
7.9	1.00	.99	1.09	1.17	1.07
6.9	1.00	.99	1.13	1.01	.99
5.9	1.00	.95	.95	.97	.90
5.4	1.00	.98	1.01	.99	.99
4.9	1.00	1.00	1.00	1.00	1.01
4.4	1.00	1.05	1.04	1.03	.99
3.9	1.00	1.00	1.00	1.00	1.00
3.3	1.00	1.00	1.04	1.07	.97

Table 5.9 (continued)

Distance from Source x (mm)	Line Intensity Relative to 4545Å Line and Scaled Such That It Is Equal to Unity at x = 3.9mm				
	$(^3P)4p\,^2P^0_{3/2}$ 4545Å	$(^3P)4p\,^2P^0_{3/2}$ 4764Å	$(^1D)4p\,^2F^0_{7/2}$ 4609Å	$(^3P)4p\,^2P^0_{1/2}$ 4657Å	$(^3P)4p\,^4D^0_{1/2}$ 4880Å
2.8	1.00	1.00	.95	1.06	.96
2.3	1.00	1.03	1.01	1.09	.98
1.8	1.00	1.01	.97	1.01	1.01
1.3	1.00	1.04	.98	1.11	.97
.8	1.00	.99	.96	1.04	.98
.3	1.00	.97	1.00	1.04	.90
-.2	1.00	.99	.98	1.05	.91
-.7	1.00	.98	1.00	1.04	.99
-1.2	1.00	1.01	1.06	1.06	1.01
-1.7	1.00	.99	.98	1.10	1.06
-2.2	1.00	.97	.95	1.11	1.14

A spatial variation of the relative ArI to ArII line intensities was found. This variation of the ratio of the largest ArI and ArII lines is shown in Figure 5.4. The ArII emission is enhanced about 30% relative to ArI as one approaches the source. Because the data are based on two intensities having perhaps 20% relative errors, the experiment was performed on two occasions to insure the results were statistically significant. The close agreement of the two independent measurements suggests the effect is real.

The above results suggest that columnar recombination and fission fragment energy spectra are not important in determining the ArI and ArII spectra, and even the ratio of ArII to ArI cannot be too greatly affected. Walters' pressure dependent data (see Appendix C) show that the ArII to ArI intensity ratio (depends on the ArI line chosen since the relative ArI spectra is pressure dependent) as based on the 7383Å ArI line increases by a factor of 2.5 in going from 760 to 25 torr. The present data suggest part of this enhancement is due to spatial effects since in effect Walters had better spatial resolution than in this study. For example, at 25 torr Walters was sampling only about the first 1/30 of the fragment total path length. It is doubtful in this study that less than the first 1/10 of the total path can be sampled. Since in the present measurement the ratio increased with

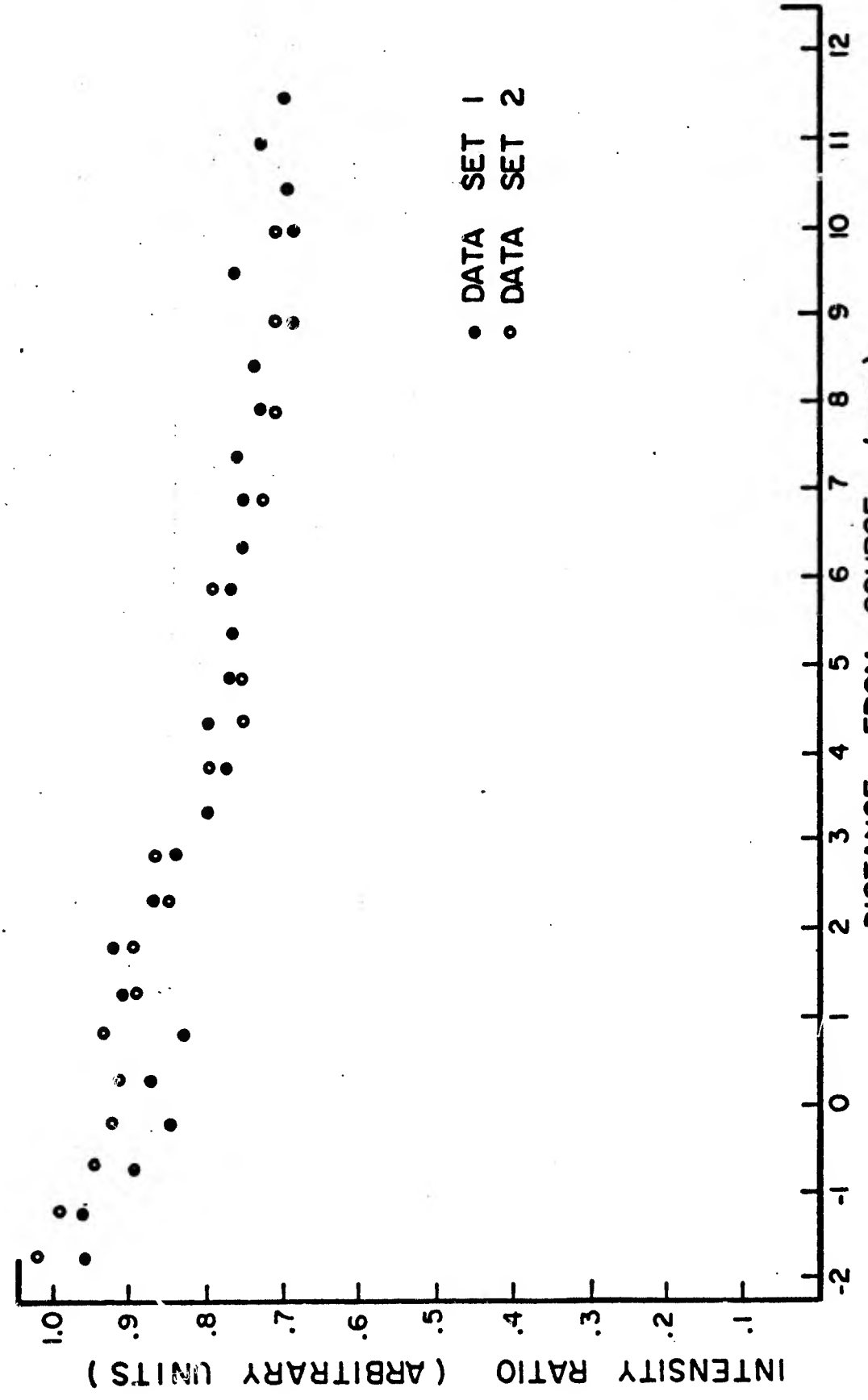

Figure 5.4: Scaled Ratio of the Intensity of the 4545Å ArII Line to That for the 6965Å ArI Line as a Function of Distance from the Source

higher ionization density and Walters' dependence went the other way, columnar recombination and volumetric energy deposition must not be important in causing the observed effects, suggesting the effects are related to the fragment or secondary electron energy spectra.

5.3 Emission Intensity versus Reactor Power

The relative emission intensity of selected portions of the Ar spectrum is shown in Table 5.10 as a function of power. The intensities are considered to vary linearly with power to within experimental error. That all the emissions were found linear with power rules out the possibility that a significant number of excited states are indirectly excited from lower excited states by low energy electrons.

On the larger emissions, the effect of gamma excitation could be roughly evaluated by shutting down the reactor and monitoring the emission after shutdown. The number of neutrons decay rapidly by several orders of magnitude, while the gamma level only drops to 5 or 10% of its operational level and decays more slowly according to the usual decay heat relations used in reactor calculations. The contribution by gammas to excitation was found to be less than 1%, not a surprising result considering relative energy deposition rates. In the case of the sapphire luminescence,

Table 5.10: Relative Emission Intensity of Selected Portions of the Ar Spectrum at Various Reactor Power Levels

Reactor Power Level (kW)	Relative Intensity Expressed as a % of the Intensity at a Power of 100kW		
	6965Å (ArI Line)	4545Å (ArII Line)	2250Å (on Continuum)
100	100	100	100
95	95	89	95
90	89	87	89
85	84	79	83
80	79	76	79
75	73	68	74
70	68	63	68
65	63	61	63
60	58	55	58
55	53	50	54
50	48	45	48
45	43	39	43
40	38	37	40
35	33	29	35
30	28	26	33
25	24	21	25
20	19	18	20
15	14	14	15
10	10	intensity	10
5	5.0	too low for	5.6
1	1.2	measurement	1.0

however, all the emission could be attributed to gammas (see Appendix A).

5.4 Temperature Effects

Temperature effects were monitored by observing emissions as a function of time after reactor startup. The sapphire luminescence was observed to increase while the 2200Å continuum and 6965Å ArI line decreased by about 10-15% within 15 minutes after startup. Unfortunately further investigations of other lines was not made primarily because of preoccupation with the sapphire effect. Efforts were made to insure that these observations were not due to the reactor. One possibility investigated was flux tilting. The flux was tilted in virtually all directions while at full power, but the observed intensities remained constant. The effects of gammas on the Ar emissions must be negligible as discussed in the preceding section. This leaves kinetic effects to explain the data barring some undiscovered reactor effect. Were the effects due to atomic collisions, one would expect collisional rates to vary roughly as $T^{1/2}$. Assuming a 100°C rise in temperature of the gas, one would expect collisional rates to increase by 16%. This number is in line with the decreases observed, suggesting collisional depopulation of levels may be causing the observed effects.

5.5 Reassessment of Walters' Data

Walters in his investigation of the fission fragment excitation of Ar was able to evaluate two effects not investigated in the present study. In order to make maximum use of his data it were revaluated in light of the results of this study. Of particular interest were his data on pressure effects and electric field amplification.

5.5.1 Pressure Effects

Walters' relative level populations and some comments appear in Appendix C. Only a summary of the key trends will be presented here. First, the ArII level relative populations do not appear to be a function of pressure. This suggests they are produced by direct electron excitation of the ground state. Second, the ArI relative populations change strongly as a function of pressure. While most levels remain constant the relative $2p_1$ level population decreases by a factor of 2 while the $2p_2$ and $2p_6$ levels increase by factors of 6 and 2 respectively. Finally, the ArI / ArII ratio is enhanced at high pressures as already discussed.

To investigate the second observation the corona parameter was applied to Walters' ArI levels with the results indicated in Table 5.11. Normalization of the

Table 5.11: Walters' Excited State Populations Multiplied by Total Transition Probability and Divided by the Excitation Cross Section

Upper Level Paschen	$\frac{N(p)g\Sigma A_i}{K(p)}$ Normalized						
	Pressure (torr)						
	25	75	150	284	450	600	760
$2p_1$	1.0	1.0	1.0	1.0	1.0	1.0	1.0
$2p_2$	2.3	4.0	7.0	6.7	15.	16.	21.
$2p_3$	1.7	1.0	2.0	1.7	2.5	2.5	2.7
$2p_4$	1.0	1.3	1.2	1.0	1.6	1.5	1.8
$2p_5$	1.3	1.3	1.4	.95	1.4	1.4	1.5
$2p_6$	1.5	2.1	2.1	2.7	4.3	4.6	6.7
$2p_7$	.40	.36	.37	.28	.45	.48	.68
$2p_8$	.73	.80	.75	.61	1.4	1.1	1.1
$2p_9$	1.6	1.2	1.6	1.2	1.9	1.9	2.6

data relative to that for the $2p_1$ level is arbitrary. The same increasing and decreasing trends would be evident in this table if the data were normalized to the $2p_3$ level. At 25 torr it would appear the relative populations agree reasonably well with the corona model. At 760 torr, however, the $2p_2$ and $2p_6$ level populations are strongly enhanced. This suggests the populating or quenching mechanisms for these levels are changing with pressure.

5.5.2 Electric Field Amplification

Walters presents his electric field amplification data in the form of semilog plots of amplification (fractional enhancement or enhancement divided by the original intensity) versus voltage. The parameter of interest is E/P, and the E/P ranges he reported at each pressure were as follows:

Pressure (torr)	E/P (V/cm-torr)
25	.131-.459
75	.043-.175
150	.022-.109
284	.012-.058
450	.007-.066
760	.004-.035

In Ar the average energy of electrons begins a rapid increase from thermal energies at E/P = 10^{-3} and reaches approximately 1eV for E/P = 10^{-2} and 2eV for E/P = 10^{-1} V/cm-torr [92]. These are considerable energies and will significantly reduce the recombination coefficient. In addition, based upon his measured current of $3x10^{-3}$ amp at 900V, his power output to the cavity was 2.7 watts. This is quite large compared to only about .24 watts input by fission fragments (based on his reported value of $1.5x10^{18}$ eV/sec as the maximum input for Ar).

Walters' observations will now be summarized. He studied the 6965 ($2p_2$), 7272 ($2p_2$), 7724 ($2p_2$) and 7503 ($2p_1$) ArI lines and the 4277Å ArII line (at 150, 284 and 450 torr only) and noted increases in output intensity with applied electric field. A maximum enhancement of 100% was obtained at 25 torr for E/P = .459. At 760 torr the maximum enhancement was about 8% for an E/P = .035. ArII amplification was generally a bit lower than that for the ArI lines which as a group exhibited roughly the same amplification behavior. The only complete spectrum he took with an applied field was taken at 600 torr and an E/P = .032. The spectrum closely resembled that without the field, showing no enhancement effects. It is unfortunate that no spectra are available under conditions where the enhancement was significant.

If one assumes that upon applying the electric field a significant portion or even all recombination is stopped then the production rate of the $2p_n$ and $1s_n$ (including trapped and metastable levels) by recombination will also decrease. Since virtually all optical decay goes through the $1s_n$ levels, the population rate of these levels should decrease by 60% according to Platzman's figures [43]. The observed amplification of the $2p_n$ to $1s_n$ transitions must result from either a significant increase in electrons with energies exceeding the threshold for excitation of the $2p_n$ levels (~13eV) from the ground state or an increase in the lower energy electrons (~1.8eV) which excite $2p_n$ from $1s_n$ levels. In addition this increase must be sufficient to overcome the loss of the recombination contribution. There are two reasons to suspect that the high energy electrons are responsible. First the enhancement of any ArII lines is evidence that high energy electrons are affected for the applied fields studied. Second, were the steady state $1s_n$ level populations sufficiently large to support significant excitation, then the $2p_n$ to $1s_n$ transitions would be a very effective pathway for extraction of the energy inthe applied electric field, since the $1s_n$ levels would not be destroyed. The $1s_n$ levels would represent a near constant population of excitable atoms, meaning the excitation role would be

solely dependent on the density of electrons having the appropriate energy for excitation. Application of the electric field would be expected to result in order of magnitude increases in the observed intensities.

Based upon these facts, nothing can be said about the dissociative recombination contribution to the $2p_n$ levels. The data do support the argument that indirect excitation from the $1s_n$ levels is insignificant even without the electric field.

5.6 Discussion

After a detailed evaluation of Walters' data and a comparison of them with the present results, it is concluded that Walters' data are generally valid. The close agreement of the two independent measurements at 760 torr along with the fact no real anomalies have been found in his data lend confidence to the use of his data at other pressures.

The elimination of the possibility of indirect excitation of excited levels by low energy electrons simplifies things considerably. The important processes are summarized in flow chart form in Figure 5.5. Not shown in the chart are cascades from levels slightly above the $2p_1$ level (few were observed) and collisional deexcitation. This latter item will be discussed later. Of importance in population of the $2p_n$ levels are dissociative

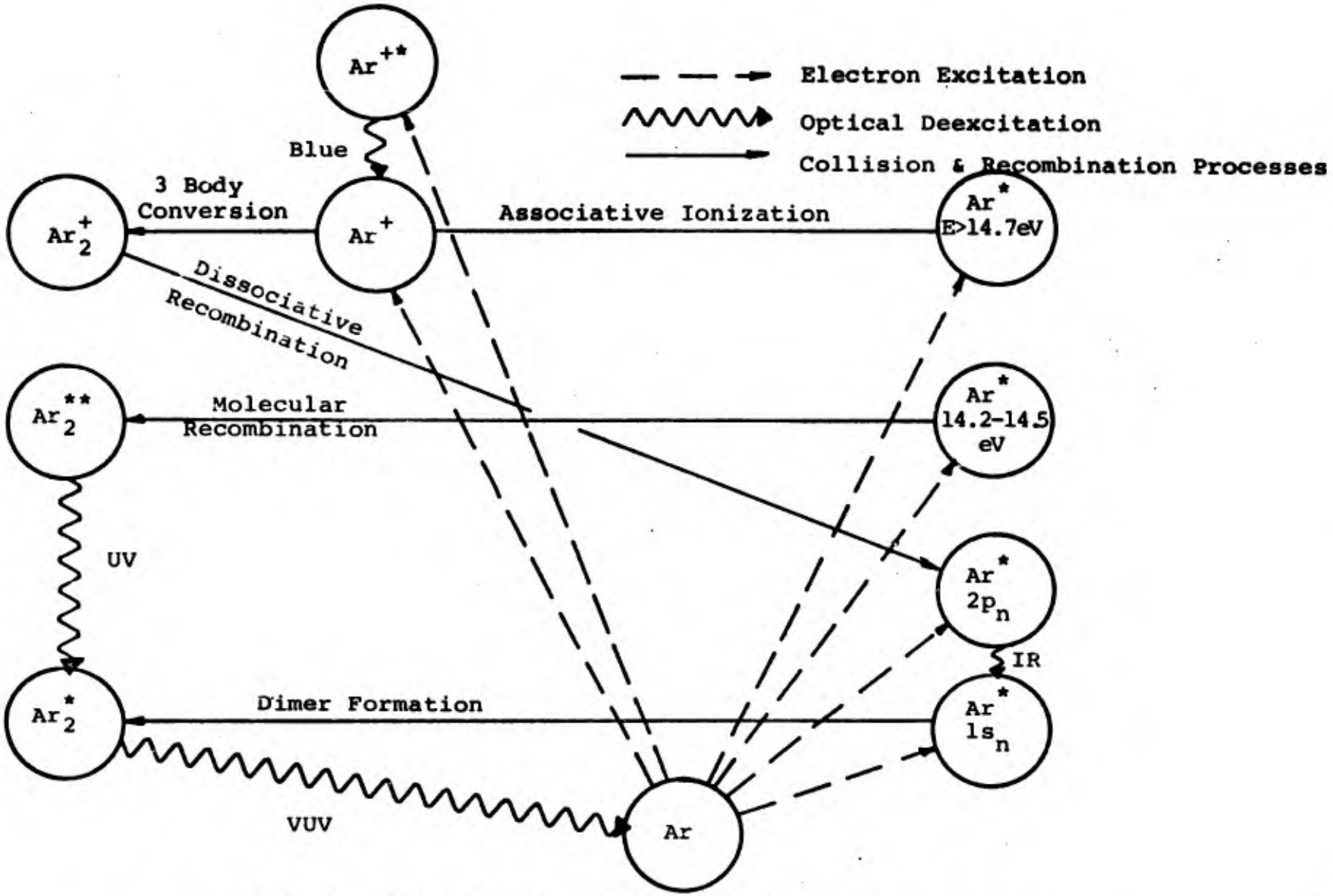

Figure 5.5: Flow Diagram Showing Important Processes in Fission Fragment Excited Ar

recombination and direct electron excitation. It is well known, however, that more ions than excited atomic levels are produced by slowing charged particles in the noble gases, the ratio of 2.5 being derived by Platzman [43]. This can be seen qualitatively by noting that Ar has a w value of 26.7 eV/ion pair and an ionization potential of 15.8 eV. This implies 60% of the energy goes into formation of ions leaving a maximum 10.9 eV for excitation of the medium and for the kinetic energy of the electron population. Since the $2p_n$ levels reside around 13 eV only one level could be created for each 2 ions formed, assuming 100% efficiency. Of course this tacitly assumes no indirect excitation. It is thus contended that at least 80% (based on an ion to excited atomic level ratio of 2.5) of the $2p_n$ population rate is due to dissociative recombination.

The above contention should also be true at all the pressures studied by Walters. The three body conversion process would be slower at lower pressures but still far exceed recombination rates. The recombination of the molecular ion will also be slower because of the lower recombination coefficients and electron densities. Using Walters' data at 25 torr, $\alpha n_e = 3.3 \times 10^3$ sec^{-1} which corresponds to an ion lifetime, τ, of 3×10^{-4} sec. Using a value of $2.9 cm^2/sec$ for D^+ for Ar_2^+ (see section 2.2.2) one can calculate the radius of a sphere, r_D, corresponding to the distance traveled by the ion during its lifetime based upon

diffusion theory as follows [93]

$$r_D = \pi\sqrt{D^{+}\tau} = .093\text{cm}$$

Since the dimensions of Walters' container are much greater than r_D the diffusion loss at the pressures he investigated should be negligible and thus an unimportant loss mechanism.

If the significant population mechanism forthe $2p_n$ levels (i.e., dissociative recombination) is a constant as a function of pressure the question still remains as to why Walters observed pressure dependent ArI spectra. The only other logical variable dependent on pressure could be collisional excitation transfer. Taking as a first approximation the gas kinetic cross section for Ar [93] of 1.0x 10^{15}cm^2 and assuming a gas temperature of 400°K (.034 eV) the collision frequency is calculated to be $3.6\text{x}10^7$ and $1.1\text{x}10^9$ sec^{-1} for 25 and 760 torr respectively. Since the optical transition probabilities are on the order of 10^{-8}, Walters' measurements are going from low pressures where collisions must be unimportant to high pressures where they should be important. Thus the distribution of levels at higher pressures must be determined by collisional transfer between the various nearby levels. The temperature effects observed for the 6965Å ArI transition lend further support to this conclusion. At lower pressures, however, it would appear the corona model is useful in describing the excited state populations. It may be that dissociative recombination

populates the $2p_n$ levels roughly according to their electron excitation cross sections as assumed in the corona model. It is interesting that in Walters' data the ArII to ArI ratio only changes by a factor of 2.5. If collisions are actually effective in depopulating the $2p_n$ levels one might expect the ratio to change drastically with pressure, assuming ArII excitation rates do not change.

Since collisional effects in this study were held constant, the observed spatial variation is most likely due to changes in the electron energy spectrum various distances from the source. This undoubtedly also contributed to Walters' observed pressure effects, along with the collisional effects just discussed.

The energy emitted per unit volume by the $2p_n$ levels (excepting level $2p_{10}$ because of lack of knowledge of its population) can be calculated based upon the absolute excited state densities measured in this study and is found to represent .075% of the total estimated energy deposition rate in the gas by fission fragments. The rate of ion production (and recombination) is a factor of 1.5×10^2 higher than the calculated $2p_n$ transition rates. Presumably they should be about the same order of magnitude. This discrepancy could result from collisional de-excitation and/or experimental error (which is estimated to be less than an order of magnitude). If all the recombination resulted in optical $2p_n$ to $1s_n$ transitions, nearly 6% of the total energy deposited in the gas would be emitted in the infrared from the $2p_n$ levels.

Regarding the possibility of a nuclear pumped Ar ion laser, the only requirement seems to be higher fluxes. There is no mechanism or characteristic that would inherently prevent the concept from working based upon the results of this study. The strongest line, however, might not be at 4880Å, for the distribution of ArII excited states is quite different than for a typical Ar ion laser. For calculational purposes the corona model can be used to estimate the relative populations, based on the results of this study.

Optimistically if the present results are in error and the recombination rates and $2p_n$ transition rates actually are equal this would imply that the $(^3P)4p\,^2D^0_{5/2}$ level would, based upon its relation with the $2p_n$ level population, have a population of 4.0×10^3/cc. This would mean that at fluxes of 10^{16} lasing of ArII might be possible. It seems assured at fluxes greater than 10^{18} n/cm^2sec.

Although the literature has abounded with recent work on electron beam excitation of gases, no detailed work on excitation of the noble gases has yet been published except with respect to the VUV. Workers at SRI [94] did make measurements on Ar and Xe in the visible and infrared regions of the spectrum in an effort to determine the atomic levels populated by dissociative

recombination. Their data were never reduced because of the intense interest in other phenomenon. Hill [89] verbally described that in Ar 3 large lines were seen. The largest was the 8264Å ($2p_2$) line with the 7723Å ($2p_2$) and 7635Å ($2p_6$) of lower and approximately equal intensity. Neglecting grating effects and considering the response of their photomultiplier, an RCA 7102(S-1), the 7723 and 7635Å emissions being equal in their case is consistent with the present results. The 8264Å emission would also be largest. No ArII emissions were observed, however, this was probably due to their sensitivity being too low. The ArII emissions observed in this study were down in intensity from the strong ArI lines by nearly three orders of magnitude, and the RCA 7102 tube is not very sensitive. They did see the 2250Å continuum as previously discussed. This limited, somewhat qualitative comparison of the spectra produced by the two excitation mechanisms at least produces no discrepancies. It is interesting that at four atmospheres pressure Hill noted that the ArI lines decreased in intensity by several orders of magnitude even with an increased energy deposition rate.

CHAPTER 6

XENON RESULTS AND DISCUSSION

From 7 March to 20 March, 1975, 760 torr of research grade Xenon was studied. The gas was furnished courtesy of Los Alamos Scientific Laboratory without an impurity analysis. Prior to filling the MCFIG the gas was checked by mass analysis to insure it was of research quality. Although not verified in detail, a typical impurity analysis for research grade Xe will be assumed as follows:

Carbon dioxide	<5.0ppm	Nitrogen	<10
Carbon monoxide	<1.0	Nitrous oxide	<.1
Helium and hydrogen	<5.0	Oxygen	<5.0
Krypton	<25	Hydrocarbons	<5.0
Methane	<5.0	Dew Point	-105°F
		Water	<1.0

Purity in the case of Xe is not expected to be as important as with Ar which is extremely sensitive to N_2. That the Xe used in this study was of high purity is supported by the fact that no impurity emissions were found in the fission fragment excited spectrum.

6.1 Xenon Spectra and Excited State Populations

The observed Xe spectrum contained a sizable continuous emission from the UV cutoff of the instrumentation system, at slightly above 2000Å, to about 6000Å. A lower level emission extended from this point out to about 8000Å. The continuum may have extended further but the system sensitivity begins dropping off rather rapidly beyond 7000Å. Also observed were a number of XeI and II lines from 3900 to 8350Å. As in the case of Ar all the XeI lines observed were from the lower energy levels ($2p_n$ and $3p_n$). Several XeII laser lines also were detected. The complete Xe spectrum is presented in Appendix D.

The sapphire continuum was not detectable except where extremely high gains were used so it contributes insignificantly to the observed spectra. This was easy to demonstrate by simply shutting the reactor down and measuring the spectral intensity at the point of known sapphire maximum emission. Based upon the detailed study of the sapphire emission (see Appendix A) ten times the intensity after shutdown should roughly approximate the full power emission intensity. These results confirmed that lengthening the MCFIG to get the sapphire out of the high flux region was successful in eliminating the sapphire luminescence observed in the Ar spectra. It is fortunate

this was done since Xe does have a continuous emission in the same spectral region as sapphire.

The number of lines observed in Xe were much less than in the case of Ar as one would expect. This made line identification much easier. The lack of knowledge of the Xe atom was a limitation, particularly with respect to transition probabilities. Experimental values were not available for all the transitions observed, and theoretical calculations for such a complex atom as Xe are inherently unreliable. It was fortunate that a 1973 study [95], motivated by Xe laser work, measured most of those needed, and all those used in this research are from this work. Prior to this 1973 study there were no experimental values available for the leading visible arrays of XeI or XeII.

As with the case of Ar, before presenting the excited state population data the errors arising from source nonuniformity will be discussed. The effect is the same as that for Ar except more severe for two reasons. The data were taken 1.7mm from the source or at the point of maximum intensity. This reduces the effective volume. Also by examining Figure 2.3 one can see that the volumetric energy deposition rate is highly variable, introducing an additional uncertainty. The combination of these two effects is believed to make the population densities reported here too low by an estimated factor of 10. It is probably safe to say that the reported population densities are accurate

to within a factor of 100 and probably are low if anything.

6.1.1 XeI

The XeI lines observed and the corresponding excited state population densities are shown in Table 6.1. For comparison purposes only the data conveyed to the author by Hill [89] were available. It was taken for 2 atmospheres of Xe excited by an electron beam with the following results:

Line (Å)	Upper Level (Racah)	Relative Intensity as Observed with RCA 7102 Photomultiplier
8231	$6p[3/2]_2$	160
8280	$6p[1/2]_0$	300
8819	$6p[5/2]_3$	170
9045	$6p[5/2]_2$	120
9800	$6p[1/2]_1$	120

Because the relative spectral sensitivity of the systems was different, the only lines seen in both studies were at 8280($2p_5$) and 8231Å($2p_6$). The closeness of the 2 lines in wavelength enables the system responses to be neglected, so the line ratios can be directly compared. The ratios of the 8280 to 8231Å were 1.87 and 1.89. Although the transition probabilities are not known for the other 3 transitions, it is probably a reasonable assumption

Table 6.1: XeI Excited State Population Densities

Upper Level (Paschen) [96]	Upper Level (Racah) [81]	Energy cm^{-1} [96]	Energy eV	Lower Level (Racah)	Transition Wavelength (Å)	Relative Intensity Observed	Relative Intensity True	Population Density (cm^{-3}) Based on Single Transition	Population Density (cm^{-3}) Weighted Average for State
$2p_1$	$6p'[1/2]_0$	89861	11.14	$6s'[1/2]^0_1$	7887.40	Very small	--	---	---
$2p_2$	$6p'[1/2]_1$	89279	11.07	$6s'[1/2]^0_0$	7642.03	8	49	3.2x10	
				$6s[3/2]^0_2$	4500.97	22	8	5.9x10	5.1x10
$2p_3$	$6p'[3/2]_2$	89163	11.05	$6s[3/2]^0_1$	4734.15	18	9	$1.7x10^2$	
				$6s'[1/2]^0_1$	8346.82	Very small	--	---	---
$3p_5$	$7p[1/2]_0$	88842	11.01	$7p[1/2]_0$	4807.02	15	7	4.2x10	4.2x10
$3p_7$	$7p[3/2]_1$	88745	11.00	$6s[3/2]^0_1$	4829.71	11	5	8.0x10	8.0x10
$3p_6$	$7p[3/2]_2$	88687	10.99	$6s[3/2]^0_2$	4624.28	33	14	5.7x10	5.7x10

Table 6.1 (continued)

Upper Level (Paschen) [96]	Upper Level (Racah) [81]	Energy cm^{-1} [96]	Energy eV	Lower Level (Racah)	Transition Wavelength (Å)	Relative Intensity Observed	Relative Intensity True	Population Density (cm^{-3}) Based on Single Transition	Population Density (cm^{-3}) Weighted Average for State
$3p_8$	$7p[5/2]_3$	88469	10.97	$6s[3/2]^0_2$	4671.23	74	34	$6.8x10$	$6.8x10$
$3p_9$	$7p[5/2]_2$	88352	10.95	$6s[3/2]^0_2$	4697.02	14	7	A unavailable	---
$2p_5$	$6p[1/2]_0$	80119	9.93	$6s[3/2]^0_1$	8280.12	89	8235	$1.3x10^4$	$1.3x10^4$
$2p_6$	$6p[3/2]_2$	79213	9.82	$6s[3/2]^0_2$	8231.63	47	3254	$2.6x10^3$	$2.6x10^3$

to conclude that the 3 additional levels Hill saw are highly populated in his case and the present one. Two of these lines, at 9045 and 9800Å are laser lines, but as in the case Ar they require short rise time pulses.

Transitions from 2 other known upper laser levels were observed. The $2p_5$ level has been successfully lased at 75.6 μm in a 100:1 He-Xe mixture at 35m torr of Xe and a 3:1 Kr-Xe mixture at 15-20m torr of Xe. The $2p_9$ level has been lased at 3.43 μm in 1 torr of He containing .01 to .04 torr of Xe [79]. Both transitions were lased CW and are interesting from a nuclear pumping viewpoint because these longer wavelengths require lower threshold inversions and are not affected by optical component radiation damage. The lower level for the transition at 75.6 μm is a level decaying by a resonant transition. The lower level for the 3.43 um transition has several nonresonant decay paths and in this respect is promising as a nuclear pumping possibility. Further evaluation of these transitions cannot be made for a lack of knowledge of upper and lower level populations and loss mechanisms.

All but one of the indicated population densities in Table 6.1 were based on the observation of a single

transition, giving little feel for the possible errors involved. The one level having 2 observed transitions exhibits a relative error of 50%; however, one of the transitions was very weak and had a low signal to noise ratio. Again as in the case of Ar, one observed level seems much more populated than the others, and no obvious explanation for this observation can be given. That no levels at energies greater than 11.16eV were observed is suggestive that associative ionization is effective in quenching radiation from these levels. The lack of excitation cross section and transition probability data prevents calculation of the corona parameter for the XeI levels observed. Collisional redistribution of the excited levels is expected on the basis that the gas kinetic cross section for Xe is $1.8 \times 10^{-15} cm^2$ and at a gas temperature of 400°K and pressure of 760 torr this implies a collision frequency of $6.8 \times 10^{9} sec^{-1}$, considerably greater than typical transition probabilities.

6.1.2 XeII

The XeII lines observed and the corresponding excited state population densities are shown in Table 6.2 A number of known XeII laser lines [79 , 83] were observed and several others could be inferred. This information is summarized in Table 6.3. As in the case of Ar the gains

Table 6.2: XeII Excited State Population Densities

Upper Level [81]	Energy cm^{-1} [96]	Energy eV [81]	Lower Level	Transition Wavelength (A)	Relative Intensity Observed	Relative Intensity True	Population Density (cm^{-3}) Based on Single Transition	Population Density (cm^{-3}) Weighted Average for State
$(^3P)6d\,^2D_{5/2}$	144385	17.90	$(^3P)6p\,^4S^0_{3/2}$	4393.20	18	7	5.7	5.7
$(^3P)6d\,^4F_{5/2}$	139094	17.24	$(^3P6p\,^4D^0_{5/2}$	3907.91	10	5	A unavailable	
			$(^3P)6p\,^4D^0_{3/2}$	4480.86	17	6	6.6	6.6
$(^3P)20_{1/2}$	138726	17.20	$(^3P)6p\,^4P^0_{1/2}$	3990.33	20	9	8.6x10	
			$(^3P)6p\,^4D^0_{3/2}$	4555.94	11	4	3.2x10	6.3
$(^3P)18_{1/2}$	136554	16.93	$(^3P)6p\,^4P^0_{1/2}$	4369.20	15	6	2.3x10	2.3x10
$(^3P)6d\,^4F_{7/2}$	136598	16.93	$(^3P)6p\,^4D^0_{5/2}$	4330.52	16	6	4.9	4.9
$(^3P)6d\,^4D_{3/2}$	135708	16.82	$(^3P)6p\,^4P^0_{3/2}$	4180.10	16	7	3.1x10	3.1x10
$(^3P)7s\,^4P_{1/2}$	135061	16.74	$(^3P)6p\,^4P^0_{3/2}$	4296.40	28	11	6.3x10	6.3x10

Table 6.2 (continued)

Upper Level [81]	Energy cm^{-1} [96]	Energy eV [81]	Lower Level	Transition Wavelength (Å)	Relative Intensity Observed	Relative Intensity True	Population Density (cm^{-3}) Based on Single Transition	Population Density (cm^{-3}) Weighted Average for State
$(^1D)6p'\,^2P^0_{1/2}$	132741	16.46	$(^1D)6s'\,^2D_{3/2}$	5044.92	11	4	A unavailable	----
$(^1D)6p'\,^2D_{3/2}$	131924	16.36	$(^1D)6s'\,^2D_{3/2}$	5261.95	8	3	1.5	1.5
$(^3P)6p\,^4D^0_{3/2}$	116783	14.48	$(^3P)6s\,^4P_{3/2}$	4603.03	28	12	3.6x10	3.6x10
$(^3P)6p\,^4D^0_{7/2}$	113705	14.10	$(^3P)5d\,^4D_{5/2}$	5460.39	6	3	1.5x10	1.5x10
$(^3P)6p\,^4P^0_{1/2}$	113673	14.09	$(^3P)6s\,^4P_{3/2}$	5372.39	5	2	4.3	4.3
$(^3P)6p\,^4D^0_{5/2}$	113513	14.07	$(^3P)6s\,^4P_{3/2}$	5419.15	6	3	2.4	2.4
$(^3P)6p\,^4P^0_{5/2}$	111959	13.89	$(^3P)6s\,^4P_{5/2}$	5292.22	9	4	2.8	2.8
$(^3P)6p\,^4P^0_{3/2}$	111792	13.86	$(^3P)6s\,^4P_{5/2}$	5339.38	6	3	3.6	3.6
unclassified				4462.19	15	6	A unavailable	----
unclassified				4448.13	12	5	a unavailable	----

Table 6.3: List of Observed and Inferred XeII Laser Transitions

Wavelength (Å)	Upper Level	Lower Level	Remarks
4296.39	$(^3P)7s\,^4P_{1/2}$	$(^3P)6p\,^4P^0_{3/2}$	observed
4603.03	$(^3F)6p\,^4D^0_{3/2}$	$(^3P)6s\,^4P_{3/2}$	inferred from 4393.20Å line which populates upper level
5044.92	$(^1D)6p\,^2P^0_{1/2}$	$(^1D)6s\,^2D_{3/2}$	observed
5261.95	$(^1D)6p\,^2D^0_{3/2}$	$(^1D)6s\,^2D_{3/2}$	observed
5419.15	$(^3P)6p\,^4D^0_{5/2}$	$(^3P)6s\,^4P_{3/2}$	observed
6694.31	$(^3P)6p\,^4P^0_{3/2}$	$(^3P)5d\,^4D_{1/2}$	inferred from other lines from upper level
7149.03	$(^3P)6p\,^4D^0_{3/2}$	$(^3P)6s\,^2P_{3/2}$	inferred from other lines from upper level
7988.00	$(^3P)6p\,^4P^0_{1/2}$	$(^3P)6s\,^4P_{1/2}$	inferred from other lines from upper level
8716.17	$(^3P)6p\,^4D^0_{3/2}$	$(3P)5d\,^2P_{3/2}$	inferred from other lines from upper level

Table 6.3 (continued)

Wavelength (Å)	Upper Level	Lower Level	Remarks
9698.59	$(^3P)6p\,^4D^0_{3/2}$	$(^3P)4d\,^4P_{5/2}$	inferred from other lines from upper level
10633.85	$(^3P)6p\,^4D^0_{3/2}$	$(^3P)5d\,^4P_{3/2}$	inferred from other lines from upper level

for the inferred red lines have been found considerably lower than for the visible transitions from the same levels [84]. Unfavorable branching ratios would also likely prevent high power operation.

With respect to the population densities presented in Table 6.2, the magnitudes of potential inversions are several orders of magnitude below those required to exceed the threshold for lasing, which should approximate those required in Ar. Although the reported values are suspected to be too low this does not affect this conclusion.

It is interesting that in the Xe data some XeI level populations exceed those of XeII by factors of 10^4 while others are about equal. In Ar the ratio of the ArI to ArII populations is perhaps a factor of 10 higher. This might mean in Xe for a given energy input to the system more energy goes into XeII; however, based upon the population densities measured less total excitation results. Collisional effects may also be greatly reducing ArI populations, thus masking perhaps the opposite effect.

Cascade effects are analyzed in Table 6.4 The results must be interpreted with care because of the lack of transition probabilities. As indicated in the table data were not available for one cascade transition. The more significant problem was estimating the total transition rate from a level when transition probabilities were

Table 6.4: Analysis of Observed XeII Cascade Transitions

Level	Total Radiative Decay Rate ($10^8 cm^{-3} sec^{-1}$)	Cascade Transition			
		Wavelength (Å)	Rate ($cm^{-3} sec^{-1}$)	Contribution to Level Population (%)	Total Cascade Contribution (%)
$(^3P)6p\,^4D^0_{3/2}$	211	4480.86	53	25	
		4555.94	7.2	3.4	28
$(^3P)6p\,^4P^0_{1/2}$	79	3990.33	5.0	6.3	
		4369.20	46	58	64
$(^3P)6p\,^4D^0_{5/2}$	48	3907.91*	44	92	
		4330.52	51	106	198
$(^3P)6p\,^4P^0_{3/2}$	73	4180.10	53	72	
		4296.40	91	124	196

*Transition probability not available so cascade rate was calculated using the 4480Å transition rate and the true intensity ratios.

published only for one or two lines. This was the case for each of the 4 levels shown. The approach taken was to sum the available transition probabilities [95] and scale this number up according to the ratio of the total radiated intensity reported for all transitions from the level to the radiated intensity of transitions whose transition probabilities were summed. The intensity data of Striganov and Sventitski [81] were used. Discounting the contributions exceeding 100% as probably being the result of errors in the above procedure, it is clear that cascades play an important role in the population of XeII levels as in the case of ArII. Note that in the Xe case the 4 levels having a detectable cascade source are XeII laser levels.

6.1.3 Visible Continuum

A visible continuous emission was observed in Xe from about 2000 to 8000Å. The continuum was highly dependent on how far the region being sampled was from the source. This spatial effect is shown in Figure 6.1 and will be discussed more later. The true intensity of the continuum obtained by correcting the data for system sensitivity is shown in Figure 6.2. The curve in Figure 6.2 represents a location between the two curves in Figure 6.1. The structure below 2900Å in Figure 6.1 is obscured in Figure 6.2 because the applied calibration curve is

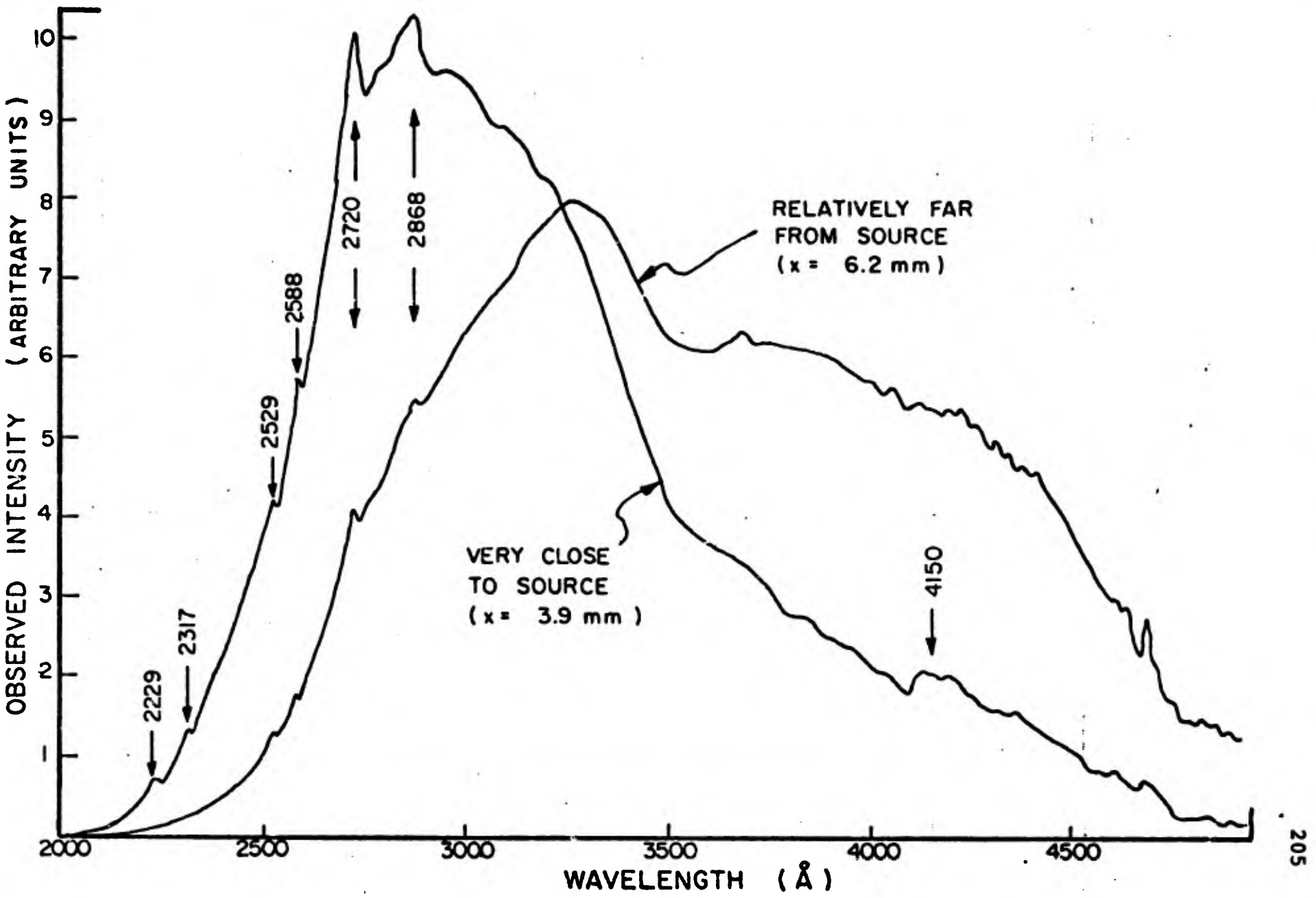

Figure 6.1: Xe Visible Continuum as Observed Close to and Far from the Source

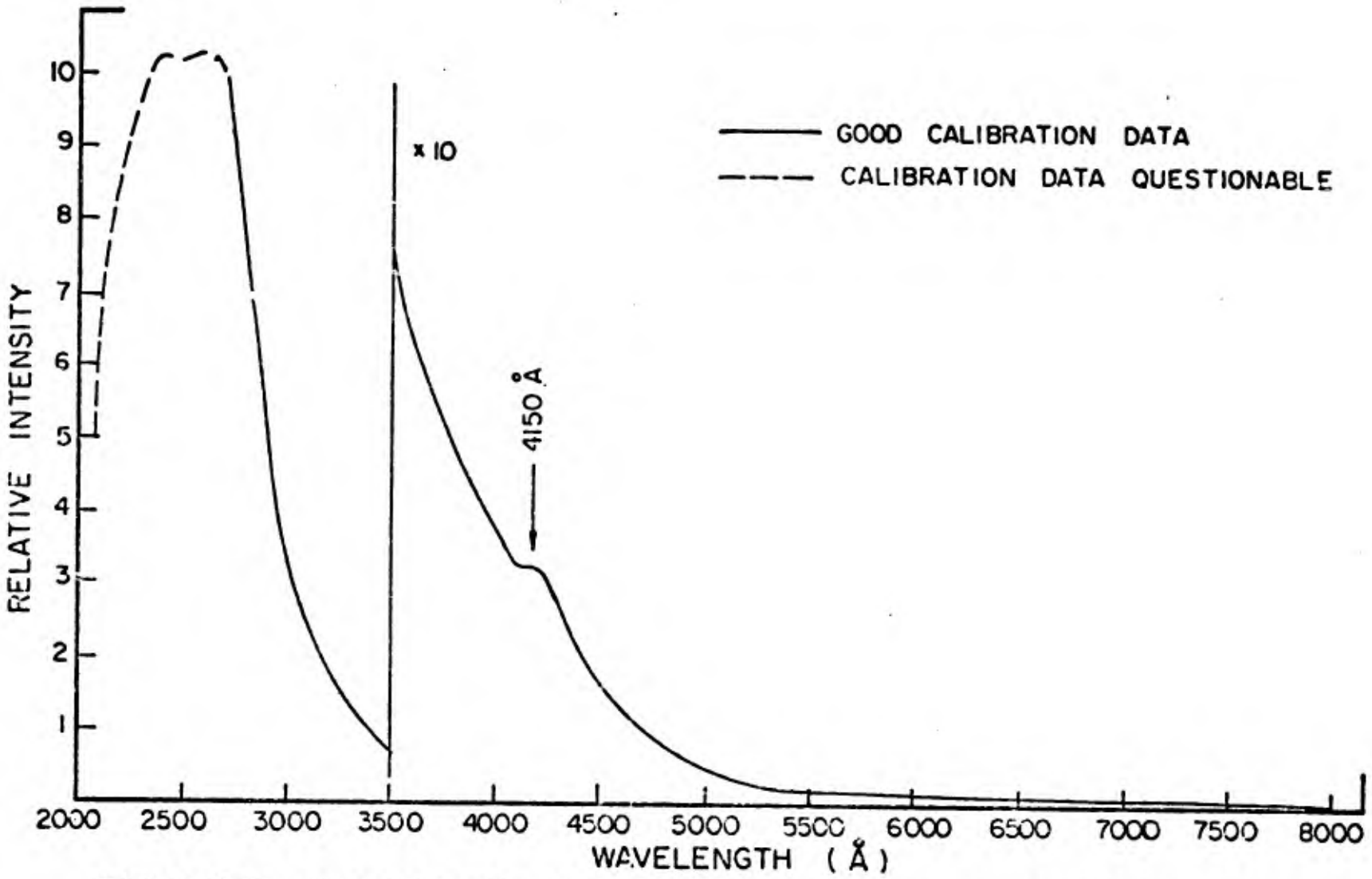

Figure 6.2: True Intensity of Xe Visible Continuum 1.7mm from the Source

noisy. The 6 small peaks below 2900Å in Figure 6.1 are real and too broad to be single lines. This was determined by scanning them at a slit setting of 100 μm. The locations must be considered accurate only to within ±3Å. Another small maximum was observed around 4150Å and this does show up in Figure 6.2. A slight maximum visible only in Figure 6.2 also occurs around 7300Å. This is believed real as the entire continuum was carefully scanned using long wavelength pass filters (see Appendix D).

That the noble gases emit visible continuua is well established. The Xe continuum observed in this study qualitatively agrees with that reported by Prince and Robertson [97] for emissions from a Xe positive column, Henck and Coche [28] for alpha particle excitation of Xe, and Hill [89] for electron beam excitation of Xe at 2 atmospheres' pressure. The origin of these visible continuua, except for the case of He, is not so well defined. Prince and Robertson [97] experimentally show that the continuua do not arise from free-bound or free-free transitions, indicating they are of molecular origin. Unfortunately, as pointed out by Mulliken [98], nothing experimentally is known about the excited molecular states of the heavier rare gases except the approximate location of the lowest. Some possibilities will now be discussed.

Mulliken [98] suggests that recombination of Xe_2^+ to form excited Xe_2^* states which cascade down by emission

in the visible and UV to lower states would help explain why the 1650Å Xe continuum is favored in a condensed discharge. However, he points out the lack of discrete bands in the visible and near UV raise doubts about whether this is possible. In contrast dissociative recombination seems quite probable.

Prince and Robertson [97] as well as others have ascribed the continuum to electron excitation of metastable molecules formed by 3 body conversion of metastable atoms. Mulliken [98] points out that while the molecular origin of the continuum is still an open question, their proposed excitation mechanism is probably incorrect owing to the lack of Xe_2 states having lifetimes long enough to be considered metastable.

Based upon the available data one is forced at this point in time to tentatively attribute the Xe continuum observed in this study to Xe_2^* transitions.

6.1.4 Unidentified Lines

Table 6.5 contains a list of all the unidentified lines observed in the Xe spectrum. All the lines could be logically attributed to Xe.

Table 6.5: List of Unidentified Lines in the Xe Spectrum

Approximate Wavelength (Å)	Comments
4037	XeII at 4037.29 or 4037.59
4193	XeII at 4193.15 or 4191.01
4214	XeII at 4213.72, 4214.69, or 4215.60
4239-4253 (3 poorly defined peaks)	probably 3 of the following XeII lines at 4238.25, 4243.88, 4244.41, 4245.38
4357	XeII at 4357.66 is only nearby Xe line
4523	XeI at 4524.68 or XeII at 4524.21
4844	XeI at 4843.29 and XeII at 4844.33
4916-4922 (2 close lines)	probably XeI at 4916.51 and XeII at 4921.48
4971	XeII at 4971.71 or 4972.71

6.2 Observed Spatial Effects

Along with Figure 6.1 the spatial variations observed in this study are summarized in Table 6.6. Two distinct trends are evident. First, the lines and continuous emissions in Table 6.6 exhibit generally the same spatial variation with the exception of the 8280 and 8231Å lines which together exhibit the same variation. Second, from Figure 6.1 it is evident that the short wavelength part of the continuum is enhanced relative to longer wavelengths (tabulated in Table 6.6) close to the source.

The first trend suggests that the short wavelength part of the continuum and the 4 XeI and XeII lines are produced close to the source while the XeI levels decaying by the 8280 and 8231Å lines are produced farther away. This effect is illustrated in Figures 6.3 and 6.4 and suggests the levels producing the 8280 and 8231Å lines are produced roughly 1mm farther from the source. One explanation might be that these two levels are populated by dissociative recombination and that the ions diffuse outward 1mm prior to recombination. The other emissions presumably arise from direct excitation of the ground state or fast secondary kinetic processes. This is difficult to reconcile with the fact that the diffusion coefficient for Xe_2^+ is small (.08cm^2/sec), the Xe^+ lifetime to conversion is short (~nsec), and the liftime of Xe_2^+ to recombination

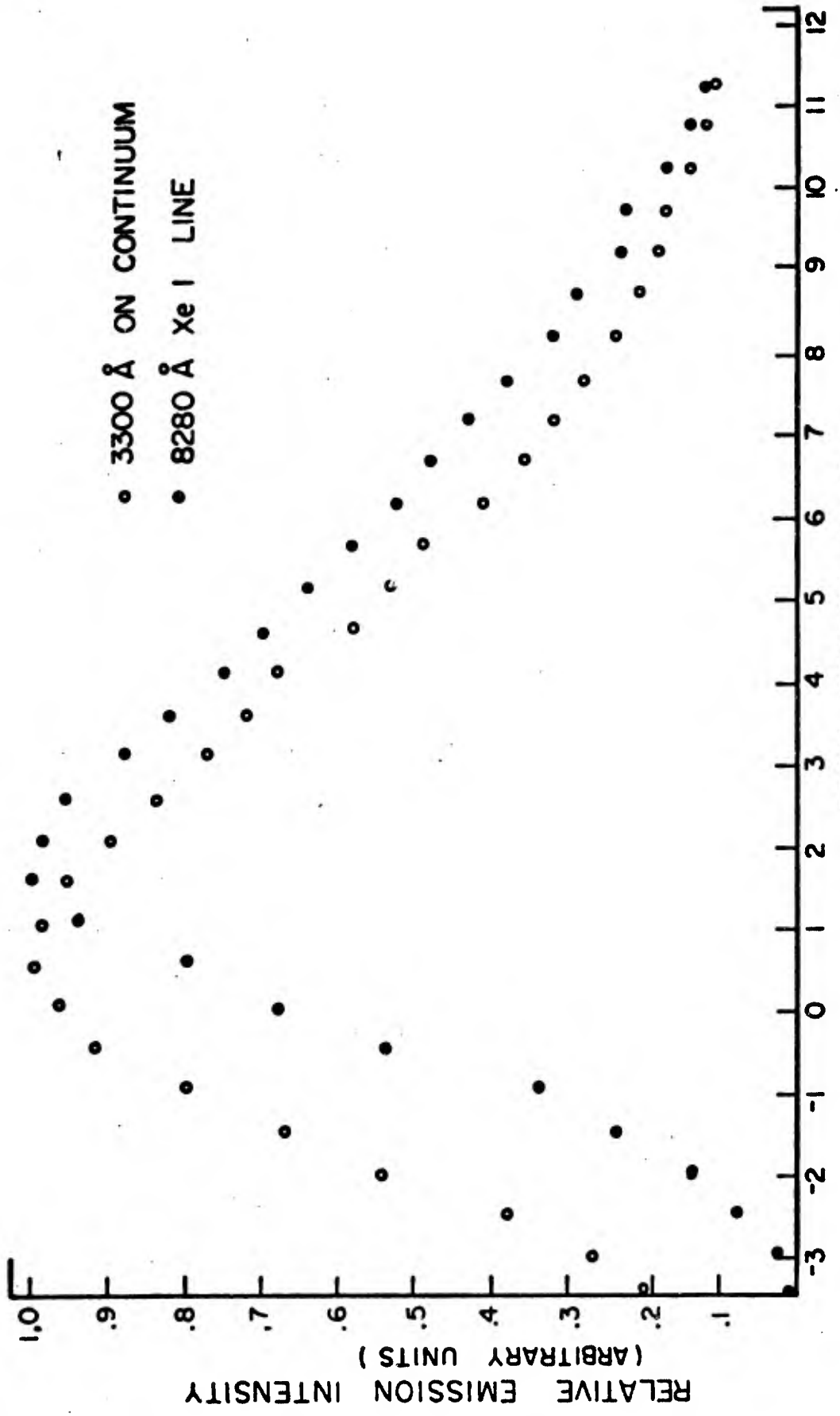

Figure 6.3: Variation of the Intensity of the 8280Å XeI Line and Continuum at 3300Å as a Function of Distance from the Source

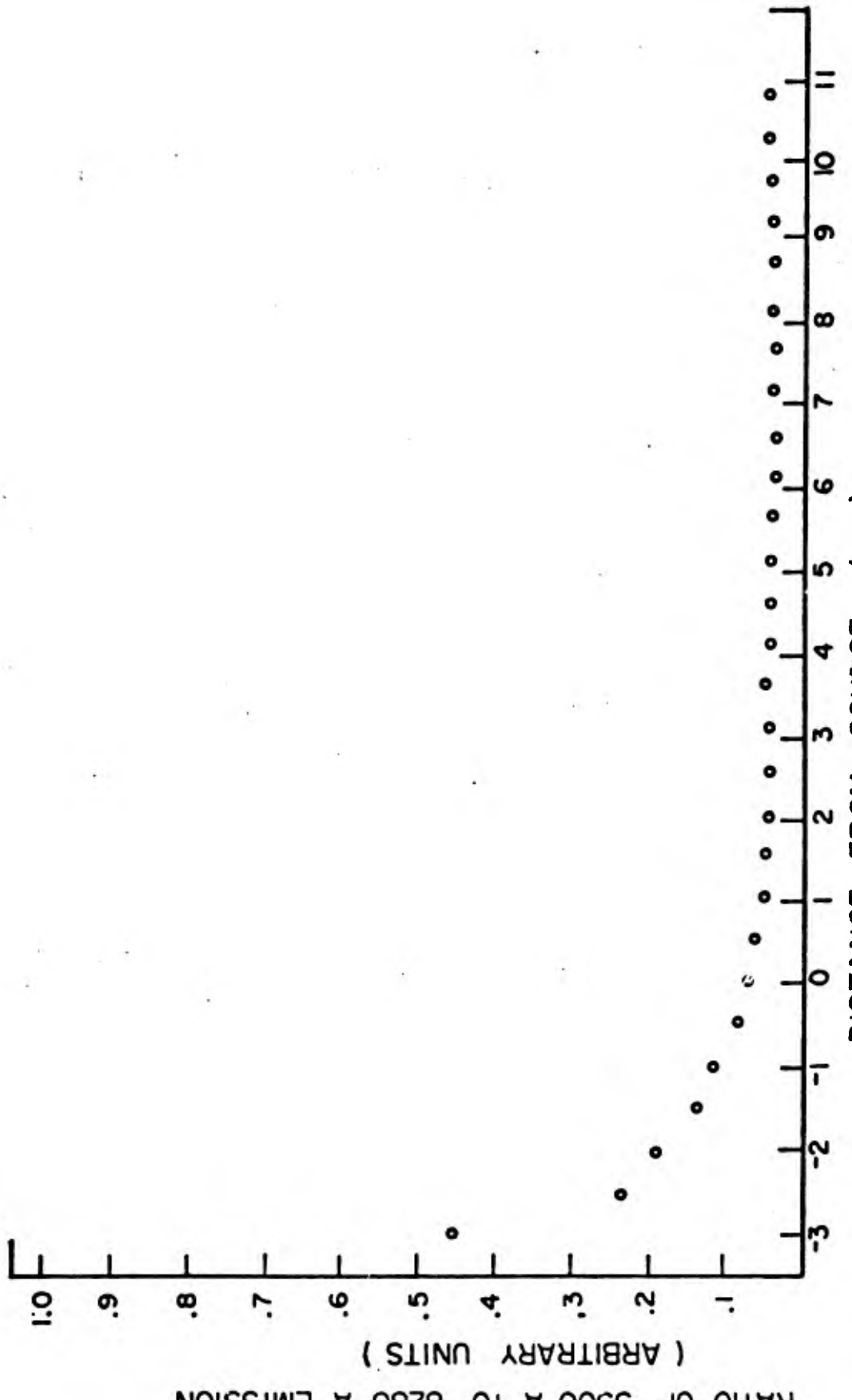

Figure 6.4: Ratio of 3300Å Continuous to 8280Å Line Emission as a Function of Distance from the Source

Table 6.6: Tabulation of Selected Xe Spatial Measurements

Distance from Source x (mm)	Line on Continuum Intensity Relative to 8280Å Line and Scaled Such That It Is Equal to Unity at x = 1.7mm							
	8280Å XeI	8231Å XeI	4671Å XeI	4624Å XeI	4603Å XeII	4296Å XeII	4250Å on Continuum	3300Å on Continuum
-1.4	1.00	1.05	1.72	1.78	2.00	2.11	2.11	2.91
- .9	1.00	.97	1.62	1.66	1.55	1.69	1.76	2.45
- .4	1.00	1.04	1.44	1.46	1.22	1.44	1.47	1.77
.1	1.00	.96	1.47	1.51	1.32	1.47	1.47	1.49
1.2	1.00	1.02	1.13	1.04	1.09	1.00	1.10	1.09
1.7	1.00	1.00	1.00	1.00	1.00	1.00	1.00	1.00
3.7	1.00	.97	.74	.71	.82	.93	.88	.92

is short ($<10^{-5}$sec). These numbers imply recombination occurs within 2.8×10^{-3}cm of the point of initial ionization, assuming an electron density of 10^{11}/cc. Associative ionization processes would also be very fast. Likewise the thermalization of secondary electrons would be expected to occur over very short distances and have no effect on where recombination occurs.

Turner and Riccius [99] in afterglow studies in Kr suggest that Kr_2^+ may be created in a highly excited state $(Kr_2^+)^*$, which is unfavorable to recombination. The effective recombination rate will then be controlled by 2-body collisional de-excitation of $(Kr_2^+)^*$. At pressures of 760 torr, however, the collisional deexcitation process is more rapid than recombination based on their number for Kr. This process is probably not important for Xe at 760 torr for the same reason.

That the electron energy spectrum is harder near the source might account for the XeII levels being enhanced relative to those of XeI, but ionization (reflected ultimately by recombination and production of the 8280 and 8231Å lines) would be favored over excitation of lower XeI levels such as that giving rise to the 4671Å line. This is not evident in the data.

Collisional redistribution of excitation so as to favor these levels would also not be expected to take

times long enough for the atoms to diffuse more than about 10^{-5}cm.

Consider now the second trend as indicated in Figure 6.1. It would appear that the emission close to the source does have some band structure to it. Perhaps this is indicative that near the source the process of radiative decay of Xe_2^* competes with dissociative recombination as suggested by Mulliken [98]. This would account for both observed trends, but there is no reason apparent to the author why the radiative process would occur with higher frequency near the source.

Again with respect to the second trend, Henck and Coche [28] observed that the maximum of the Xe continuum is a function of pressure for alpha particle excitation of Xe. Their data indicate it varies from 2600 to 3400Å, shifting towards the blue at lower pressures. This effect and the spatial effect observed in this study may be somehow related.

6.3 Emission Intensity versus Reactor Power

The relative emission intensity of selected portions of the Xe spectrum is shown in Table 6.7 as a function of power. The intensities are considered to vary linearly with power to within experimental error. However, since all the relative intensities showed a systematic variation in

Table 6.7: Xe Emission Intensity as a Function of Power

Power (KW)	Intensity Relative to that at 100 KW (%)						
	Continuum				XeI		XeII
	2900Å	3300Å	4000Å	4100Å	8280Å	467Å	4296Å
100	100	100	100	100	100	100	100
90	88	88	89	87	89		
80	76	77	78	75	76		
75		71				73	74
70	65	66	66	64	64		
60	54	55	56	52	54		
50	44	46	46	43	44	43	48
40	34	37	36	34	34		
30	25	27	27	25	23		
25						18	23
20	17	17	18	16	14		
10	9	8	10	8	8		

being consistently low, the intensity of the continuum at 3300Å was plotted as shown in Figure 6.5 Plotted for comparison purposes are the variations expected if the intensity varies linearly with power, P, and as $P^{3/2}$. The data most closely approach the linear curve, but do show a systematic deviation from it. This deviation cannot be explained, although reactor instrumentation deviations from linearity and the reduction of emission intensity with MCFIG heating are possible sources of error.

In any case that the emissions nearly linear suggests excited states (atomic, ionic, and molecular) are not excited by low energy electrons from lower excited (Metastable) states as was proposed by Prince and Robertson [97].

The contribution of post-shutdown gammas to the observed excitation was found negligible as in the case of Ar.

6.4 Temperature Effects

The observed temperature effects as reflected by the behavior of the emission intensity after reactor startup and heating of the MCFIG are summarized in Table 6.8. The data are very confusing, but do seem to indicate that if the MCFIG temperature is the only variable important here, temperature effects are not negligible and collisions must be important.

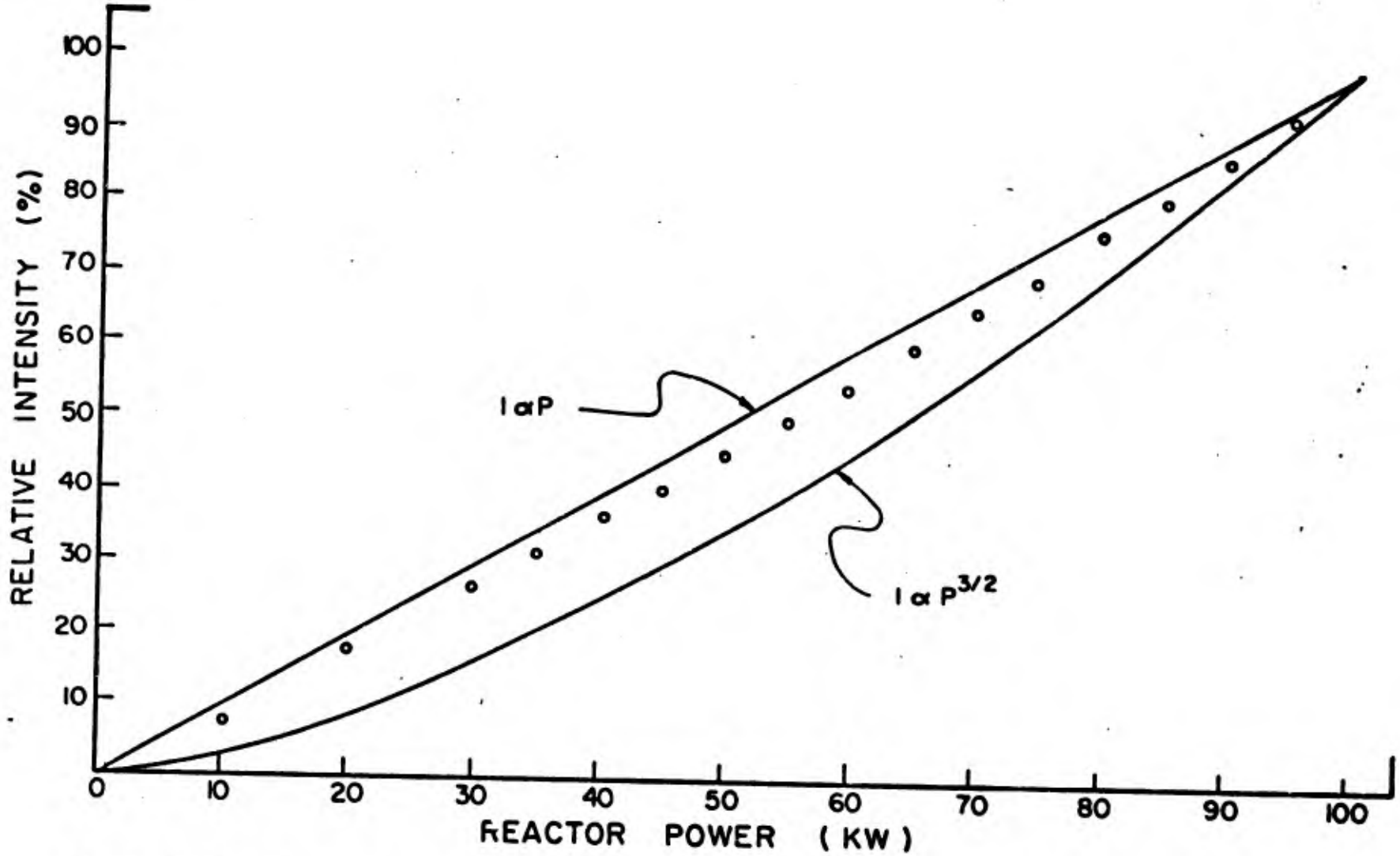

Figure 6.5: Intensity of Continuum at 3300Å as a Function of Reactor Power

Table 6.8: Summary of the Behavior of Observed Portions or the Xe Spectrum After Reactor Startup

4671Å (ArI):	perhaps slight increase (<10%) in 22 min.
8280Å (ArI):	definite 7% increase in 6 min.
4296Å (ArII:	perhaps slight increase (<10%) in 15 min.
2900Å (on continuum):	definite 5% increase in 9 min.
3300Å (on continuum):	increases perhaps 2% in 2 min then decreases about 7% in the next 6 min.
4000Å (on continuum):	negligible change in 6 min.
4100Å (on continuum):	initially constant but decreases about 6% over one hour.

6.5 Discussion

The data obtained in this study on the Xe continuum (particularly the spatial effects) only create more questions as to its origin, etc. Hopefully the data from this study will ultimately aid in clarifying this generally unknown phenomenon. One additional speculation or observation will be made at this point. Since all the emissions vary linearly with power in this study and yet other researchers consider indirect excitation important, columnar recombination becomes suspect. Columnar recombination effects are independent of power and only dependent on effects within the column itself. Thus any indirect or nonlinear processes going on in the column would still macroscopically exhibit linear behavior. Exactly how columnar recombination might cause the observed effects in this study is not known.

The good agreement between electron beam excitation of Xe and that observed in this study with fission fragments adds even more support to the case for the excitation being essentially by the same mechanisms in both cases.

The energy emitted per unit volume by the $2p_5$ and $2p_6$ levels based upon the absolute densities measured in this study, only the 8280 and 8231Å transitions (for lack of the other transition probabilities), and an average energy deposition rate of 5×10^{17} eV/cc-sec. is found to represent .0046% the total estimated volumetric energy

deposition rate. The rate of ion production (and recombination) is a factor of 1.3×10^3 higher than the number of transitions from the $2p_5$ and $2p_6$ levels as calculated above. These numbers are down from those for Ar by about a factor of 10 which is what the author estimates the densities are too low by in section 6.1. The same possible reasons for the above discrepancy between ion production and optical transition rates stated for Ar apply here.

It would appear that except for the observed continuous emissions, the Ar and Xe data are quite similar. It is suspected that the processes indicated in Figure 5.5 for Ar apply equally well in the case of Xe with the above noted exception.

Although the XeI populations are nearly a factor of 10, lower than those for ArI, the XeII levels are lower by only about a factor of 2 from those of ArII. Thus, particularly in the case that the Xe data are low by a factor of 10, a nuclear pumped XeII laser might be attainable at lower fluxes than one based on ArII, perhaps by as much as a factor of 5 or 10. In particular the 4296.40Å transition would seem a prime candidate for nuclear pumping.

CHAPTER 7

CONCLUDING REMARKS

7.1 Summary of Significant Results and Conclusions

In this section the important results from this study will be summarized and general conclusions presented.

7.1.1 Ar Data Base

This study has produced fission fragment excited spectra from 2000 to 8500Å at 760 torr having a much greater signal to noise ratio and lower impurity emissions than in past studies. Of particular significance is that no N_2 emissions were detected. In addition order of magnitude population densities of excited states were obtained, providing the first direct experimental information on the energy pathways in fission fragment excited Ar. Spatial data and variations with reactor power at 760 torr were also acquired. The relatively good agreement of the results of this study with those of Walters [17] at 760 torr suggest Walters' data at other pressures are valid (for relative intensities) and not sensitive to low levels of impurities.

7.1.2 Xe Data Base

This study reports the first spectral observations of Xe excited by fission fragments. The data taken from 2000 to 8500Å and at a pressure of 760 torr yield estimates of the excited state population densities accurate to within a factor of 100 (this could probably be reduced to a factor of 10 if the reported values are increased by a factor of 10 for the reasons explained in paragraph 6.1). This study has also produced measurements of spatial effects and the variation of intensity with power.

7.1.3 Model of Fission Fragment Excited Plasmas

With the exception of the Xe continuum and associated effects the basic processes in fission fragment excited plasmas appear at least partially understood. Fission fragment spectra are clearly different from those typically observed in electrical excitation situations, although the atomic spectrum is probably similar to that in a recombining afterglow. Excited ionic states are directly excited by high energy electrons from the atomic ground state and cascading. This is evidenced by the good agreement between relative ArII populations and those predicted on the basis of the corona model where an effective cross section (including cascades) was used. It seems likely that the corona model is applicable to the

XeII populations as well. Cascading is certainly important for both cases. The observed atomic levels for Ar arise from dissociative recombination of Ar_2^+ and this is also likely the case for Xe. The importance of collisions in determining the distribution of atomic levels would seem established from Walters' pressure data for Ar as well as by estimates of collision frequencies for both gases. Should high energy electrons from fission fragments actually be the primary excitation mechanism and the line radiation be determined by direct excitation, recombination, and collisions, only the electron energy is important in determining excitation for a given set of gas conditions. And even then the input energy of electrons to the system is probably not too important if well above the ionization threshold. This means the excitation observed in a gas excited by alpha particles, electron beams, gamma rays, and fission fragments, etc. should in a given gaseous medium produce the same excited levels. This is supported by the comparison of electron beam data to that taken in this study. Unfortunately, complete detailed spectral measurements over the visible part of the spectrum for these other forms of excitation have not been published.

7.1.4 Implications for Nuclear Pumping

High energy electrons most probably do all the excitation, and ArII and XeII laser levels appear preferentially

populated which is very encouraging. A nuclear pumped laser based on this concept would appear feasible. Relatively high flux levels ($>10^{16}$ n/cm^{2}sec) will, however, probably be required to exceed threshold. Nuclear pumping is far more efficient in producing ionization than excited ionic levels. In fact the majority of the energy deposited inthe medium results in ionization, and tapping this energy resource would seem highly desirable for any nuclear pumping approach. While dissociative recombination populates excited atomic levels, most transitions from these levels are to lower metastable or trapped levels which are not conducive to CW operation. One exception, the 3.43 μm XeI line would appear to have some promise, but this study was unable to obtain a population for the upper level for lack of a transition probability. This implies that collisional transfer of energy from the trapped and metastable levels might be a very efficient means to extract the energy, and this is the basis of the VUV molecular lasers. It would seem possible to also use another gas to collisionally depopulate these levels. For example, N_2 is known to be very effective in this respect [100] and is presently being investigated for possible nuclear pumping applications [39].

7.1.5 Spatial Effects

In Ar the lack of any significant spatial effects is encouraging. It indicates that calculation of excited state populations, evaluation of inversions, etc. are simplified from an engineering standpoint. The most important parameter would seem to be simply the volumetric energy deposition rate, essentially an easy number to reliably estimate even for complex geometries. In Xe the situation is more difficult to assess. It would appear that spatial effects must be considered in the engineering of a nuclear pumped Xe laser. XeII populations do seem to follow the volumetric energy deposition rates, so an XeII laser design can neglect these effects. This study has shown that measurement of spatial effects is both feasible and desirable in the cases studied. Spatial measurements also proved useful as a practical diagnostic tool during the experiment. For example, by measuring the emissions as a function of distance from the source, it was possible to separate the true Ar spectrum (asymmetric, being most intense near the source) from that due to sapphire (symmetric across the sampled region).

7.2 Implications for Future Research

This section includes some results, so far not discussed, which may be of some interest to future researchers.

7.2.1 Gamma Excitation of Gases

During the course of this study the test tube was filled with several gases (air, N_2, and H_e) and spectra taken with only the reactor gamma level acting as a source. Making measurements of this kind are completely feasible. While the observed intensities are reduced compared to the fission fragment case, so are the safety complications. Thus to study high pressure gases excited by ionizing radiation, reactor gammas might be an easy approach. Higher pressures would increase the gamma energy deposition. In fact high pressures are a complication in the fission fragment case owing to the extremely short range of fission fragments and the fact that still no more total energy is deposited in the gas.

7.2.2 Radiation Effects

Although it was well known that radiation damage to optical components could be expected, the extent of the experimental problems arising in this study from the effects came as a surprise to the author. While radiation effects are generally minor in the infrared part of the spectrum, in the visible and UV they are not. The author would recommend paying careful attention to these effects in any future nuclear pumped laser or spectroscopy work in the visible and UV. Brewster windows, dielectric coating, etc. are all susceptible to radiation damage.

7.2.3 Source Geometry

In future spectroscopy of fission fragment excited gases at high pressures, a planar fragment source should be used since it deposits the energy over a region that can efficiently be sampled by the monochromator. In fact it was found that in the case of UF_6 at 760 torr, approximately the same volumetric energy deposition rate over the spatial region sampled by the monochromator was achieved using a planar UO_2 source as would have been obtained with 93% enriched UF_6, assuming equal fluxes. While the enriched UF_6 would deposit orders of magnitude more total energy in the MCFIG, most of it cannot be observed spectroscopically. It will be uniformly distributed with a volumetric energy deposition rate over the effective volume sampled spectroscopically roughly equal to that for the case of a planar source. A cylindrical source is still desirable to maximize the volumetric energy deposition rate over the effectively sampled region when low gas pressures are used such that the range of fragments exceeds the diameter of the cylinder.

7.2.4 Improvements of the Experimental Setup

Since the basic experimental system described in Chapter 3 has already been used by other experimentors and future use is anticipated, some suggested improvements will be listed here.

(1) Reduction of noise by filtering either with a minicomputer or phase lock amplifier has already been discussed in section 3.5.1.

(2) The lead shield around the photomultiplier could be modified to incorporate a commercially produced cooled photomultiplier housing. This would reduce the inconvenience and cost of liquid N_2 required presently to cool the system.

(3) If the lead shield were also modified to permit easy changing of detectors, perhaps future work could include monitoring emissions in the infrared, beyond the cutoff of the present system.

APPENDIX A

SOME OBSERVATIONS ON THE LUMINESCENCE OF ALPHA-Al_2O_3 (SYNTHETIC SAPPHIRE) IN A REACTOR ENVIRONMENT

During the spectral measurements of fission fragment excited Ar, a visible continuous emission which changed with irradiation time was observed. As this had not been observed in previous Ar studies using entirely quartz optical components, it was suspected that luminescence of the sapphire window used in the MCFIG, coupled with a loss of transmission, were observed. Because the luminescence output seemed surprisingly high and exhibited what appeared to be an unusual spectral variation over the irradiation period, an experiment was set up to examine this in more detail by making simultaneous optical absorption and luminescence measurements. The results of this study are presented here.

Radiation damage to the optical properties of sapphire was most recently extensively investigated by Levy [101]. He reported results for both reactor (gamma and neutron) and gamma only irradiations, identified and characterized a number of induced color centers, and related these observations to theory. In addition, the thermoluminescence of the aluminum oxides has been investigated by Rieke and Daniels [102]. This study does not mention, however, the wavelength spectrum of the thermoluminescent output. The

thermoluminescent applications of Al_2O_3 have not received great attention because of its insufficient sensitivity for most purposes [103] and little recent work has been reported in the literature. The effects of high pressure on the thermoluminescence of gamma irradiated single crystal α-Al_2O_3 was later investigated [104] but the report also did not present any spectral (wavelength) data. Other studies of radiation damage to α-Al_2O_3 have involved measurement of long wavelength neutron scattering cross sections, thermal conductivity lattice expansion and electron-spin resonance. The only published luminescence spectrum for Al_2O_3 known to the author is shown in Figure A.1 and was taken some years ago for excitation by 12.4 KeV X-rays at a sample temperature of 1600°C [105].

A.1 Experiment

The α-Al_2O_3 specimen employed was a standard 1 inch sapphire window assembly manufactured by Ceramaseal, Inc. (New Lebanon Center, N.Y. 12126) as shown in Figure A.2. The sapphire was synthetic and of hexagonal single-crystal structure [106]. The window assembly was located in the HTP of the UFTR with the optical set up shown in Figure 4.2. The HTP was sealed and evacuated to a pressure of 10^{-3} torr. A McPherson Model 218 3m scanning monochromator in combination with a EMI 9558QB(S20) photomultiplier were used to

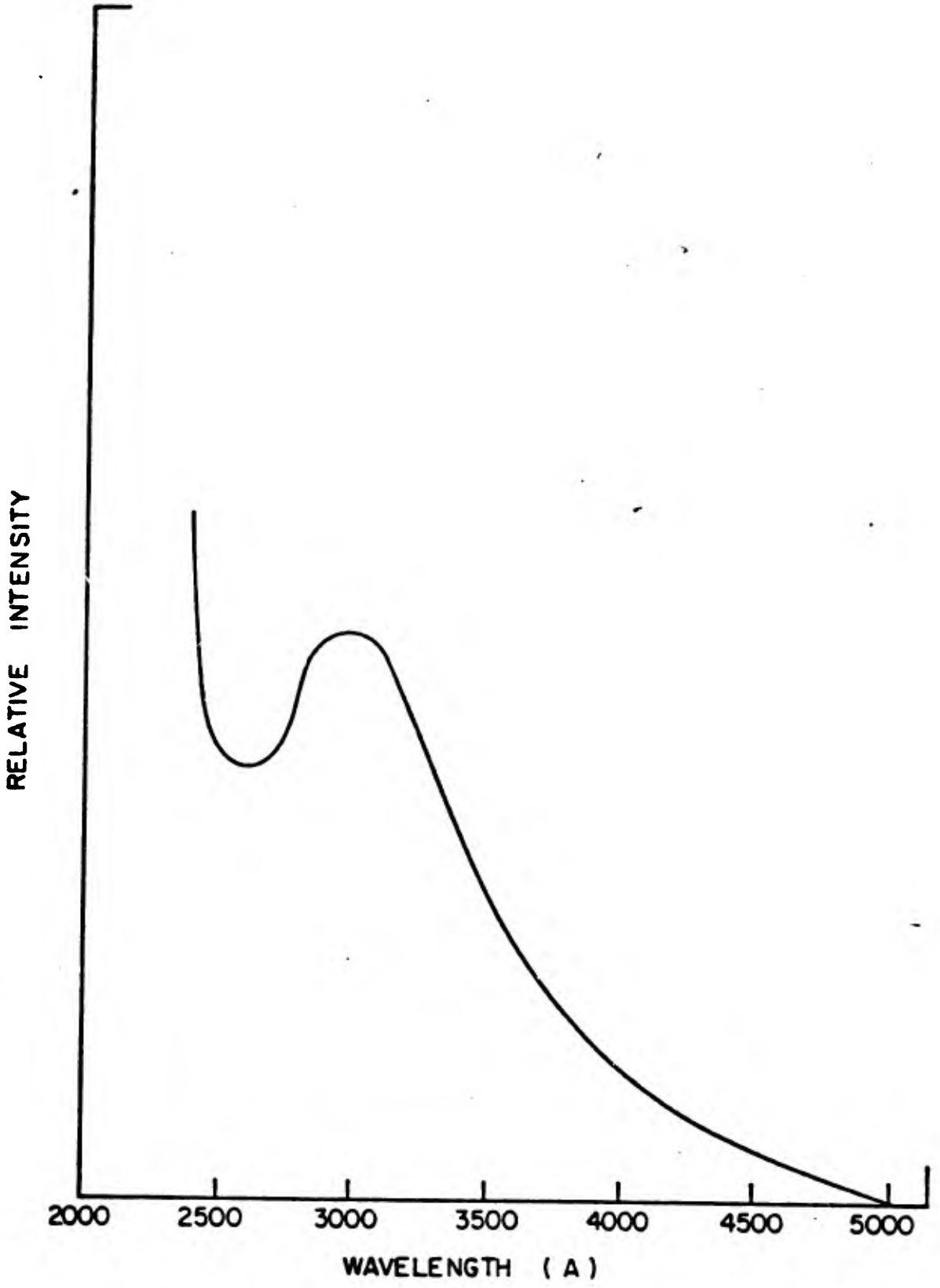

Figure A.1: Luminescence Spectrum for Al_2O_3 Excited by 12.4 KeV Photons [105]

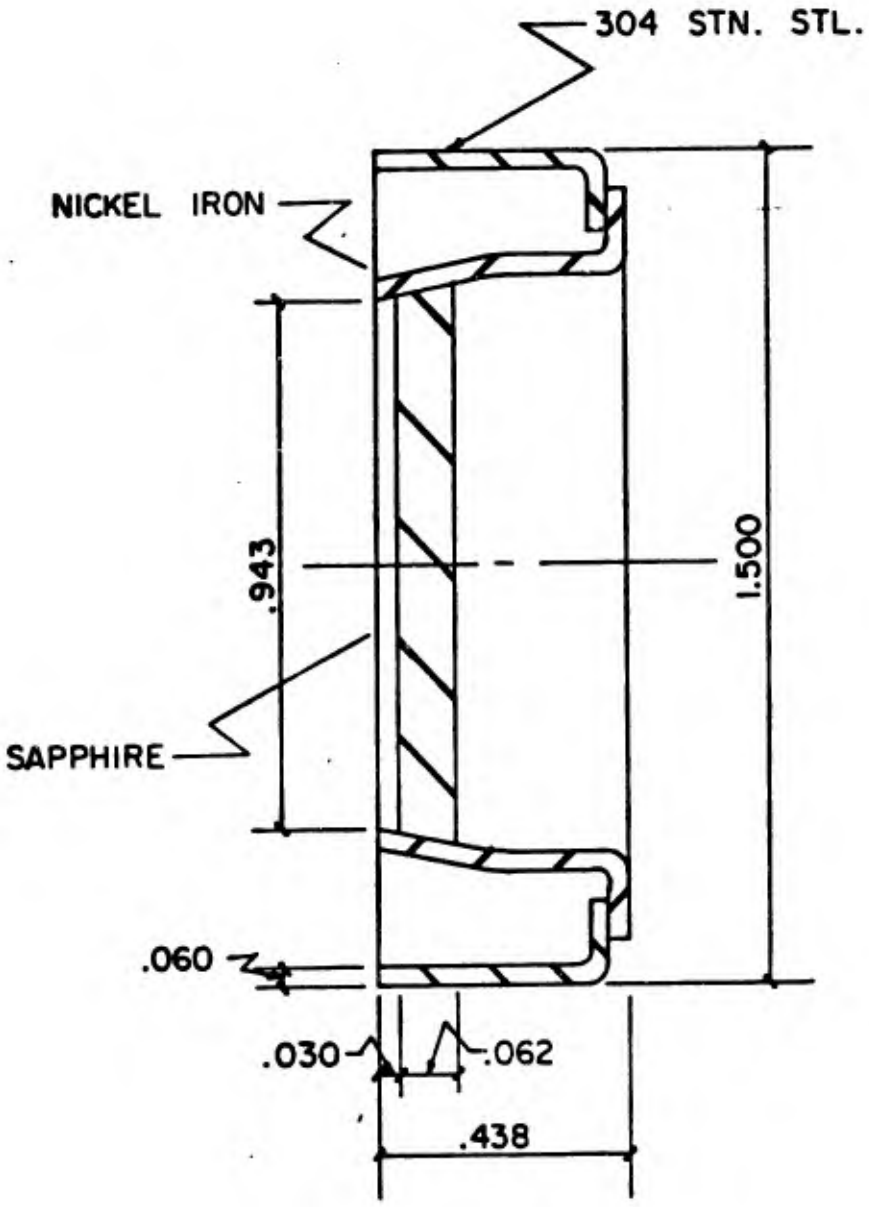

Figure A.2: Sapphire Window Assembly Used in Irradiation Studies

make the spectral measurements. Deuterium and tungsten lamps provided the standard source for the absorption measurements. The lenses used in HTP were UV grade quartz and had been found to be relatively resistant to large radiation induced damage at locations from the core typical of the ones used here and for transmission at wavelengths longer than 3000Å. Thus, changes in the system transmission after irradiation can be attributed to changes induced in the sapphire.

Prior to reactor operation a baseline relative transmission measurement was made from which reactor induced transmission loss could be evaluated. Residual gamma activity in the reactor core brought gamma induced coloring in the sample to saturation (requires a dose of around $5x410^{4}_{r}$) [101] prior to this calibration. Reactor operation was then begun which subjected the sample to a gamma dose of $\sim 10^{8}$R/hr, a thermal neutron flux of $\sim 1.8x10^{12}$ $n/cm^{2}sec$ and an epithermal neutron flux of $\sim 2.0x10^{12} n/cm^{2}sec$. The core ambient temperature and thus that of the sample was approximately 110°F. The reactor was operated intermittently over the period 28 January-17 February, 1975, with a cumulative total exposure equal to 69 hours at full power (100kW), corresponding to a $\sim 7x10^{9}$R gamma dose and $5x10^{17} n/cm^{2}$ fast neutron fluence. The sapphire emission spectrum was measured 28 times while the reactor was operating during this period, and the system transmission was measured 7 times when the reactor was shut down.

A.2 Results

The luminescent output of the sapphire sample as a function of irradiation times is shown in Figure A.3. These data have not been corrected for system sensitivity. Figure A.4 shows the corrected data for scans S1 and S25 which reflect the true output spectrum at the beginning and end of irradiation. These spectra are clearly different from that shown in Figure A.1. Of particular interest here is the fact that the emission intensity around 3300Å increases while that around 4100 decreases which is seen best in Figure A.3. A plot of these peak intensities as a function of reactor operating time is shown in Figure A.5. The 3300Å peak appears to saturate after 30 hours exposure while that at 4100Å monotonically decreases. The luminescent output in this test was a factor of 2 or more lower than that previously observed from windows used in the actual Ar studies. In the Ar studies, the windows were actually subjected to somewhat lower radiation levels; however, the gas capsule contained a fission source and reached temperatures on the order of 300°F. Thus, it appears that the luminescent output is a strong function of temperature. The actual output spectrum and its variation observed during the course of the gas studies was the same as that found in the present sapphire study. The luminescent output from the sapphire did exhibit an afterglow following reactor

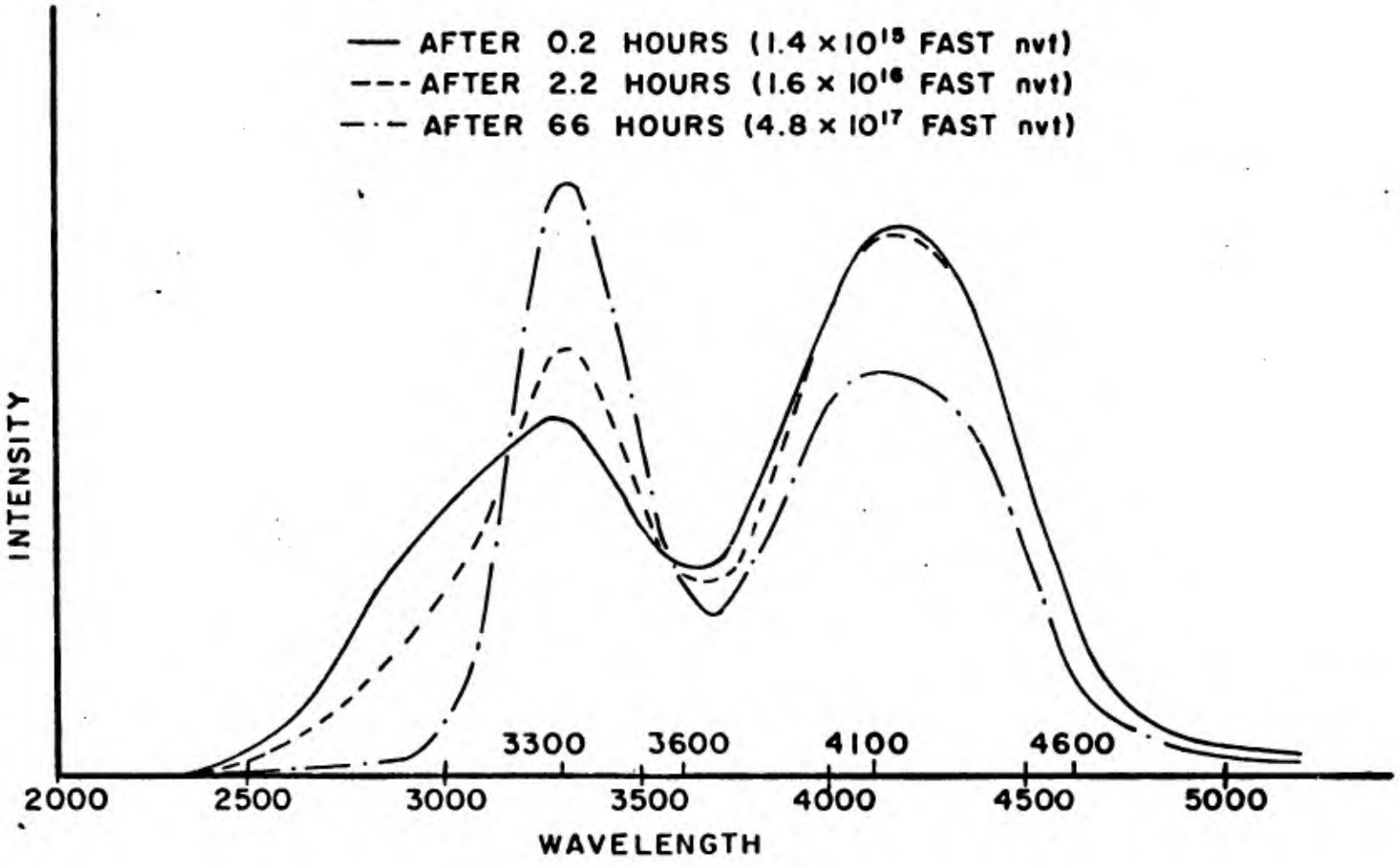

Figure A.3 : Sapphire Luminescent Output Spectrum as a Function of Irradiation Time

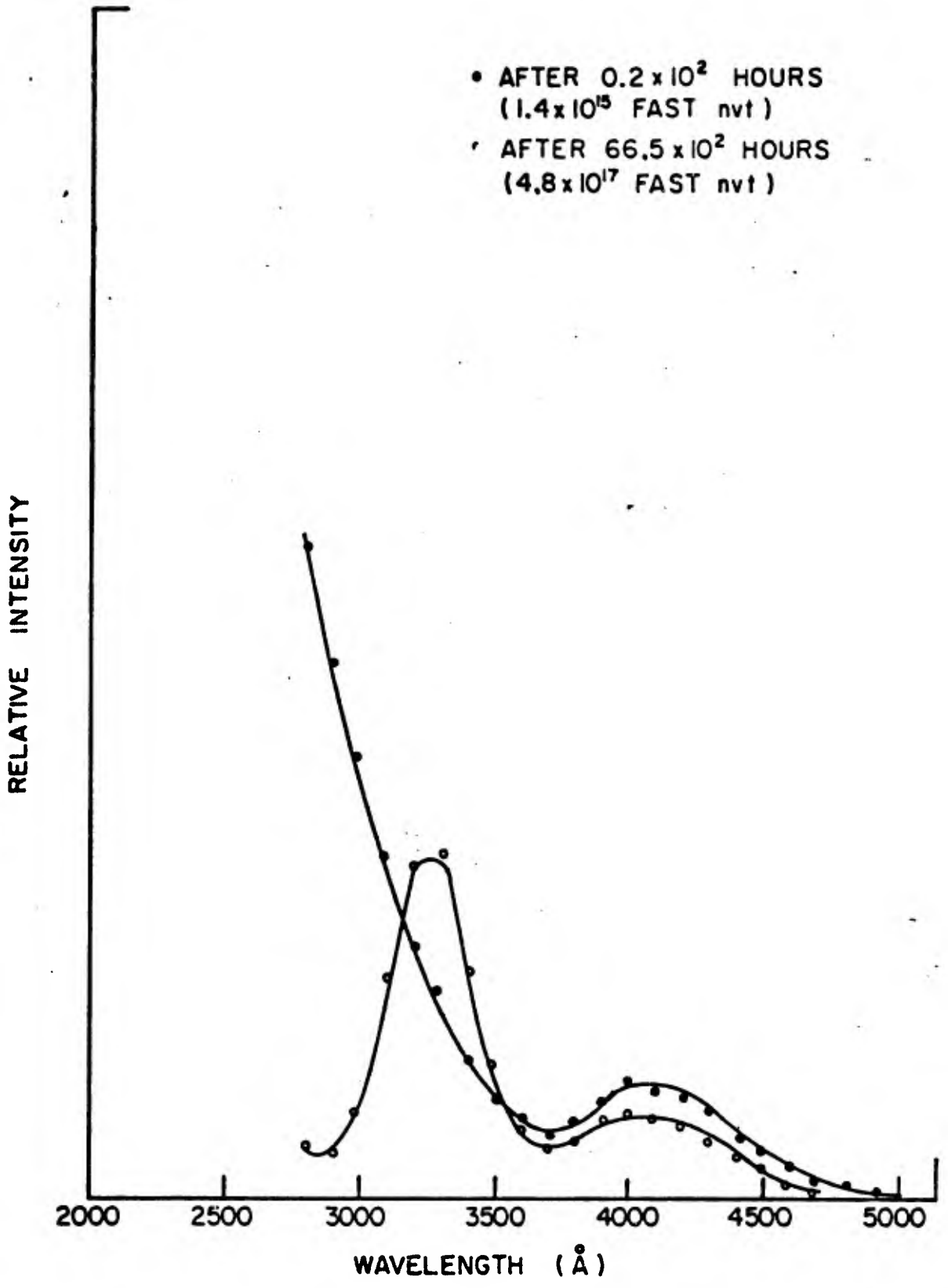

Figure A.4: True Luminescence Spectrum at Beginning and End of Reactor Irradiation

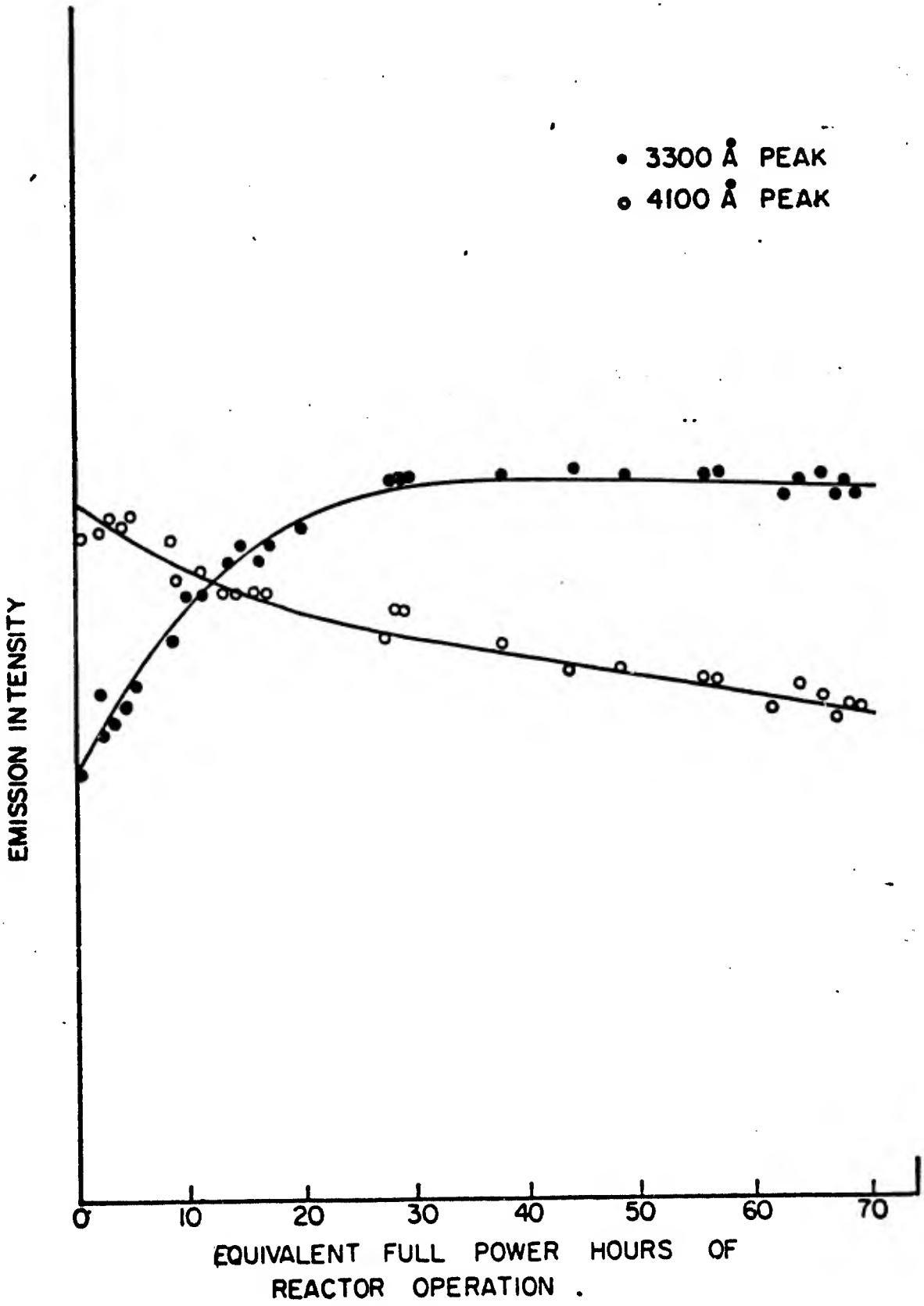

Figure A.5: Sapphire Luminescence Intensity at 3300 and 4100Å as a Function of Irradiation Time

shutdown. The luminescence intensity immediately following reactor shutdown was about 10% that observed at full power operation and is postulated to be due to post shutdown gamma decay. Otherwise the emission appears to linearly follow all power changes.

The measured absorption coefficient for the sample at the end of the 69-hour exposure is shown in Figure A.6. While these data are inherently prone to some error (estimated to be in the range of 20%) due to the detailed experimental procedures (e.g., setting the tungsten lamp temperature by using an optical pyrometer, continually removing and replacing mirrors, not taking into account surface reflections, etc.) they do qualitatively compare with those from the more refined measurements by Levy [101]. The absorption also appears to increase linearly with dose as Levy observed. In magnitude, however, our absorption coefficient is consistently higher than that we estimated from Levy's data for our conditions, suggesting perhaps a difference in sample compositions or that we saw some degradation of the quartz components in our system. The key point here is that absorption is increasing throughout the spectral region of luminescent output.

A.3 Discussion

The surprising behavior of the Al_2O_3 luminescence spectrum as a function of radiation dose is similar to some

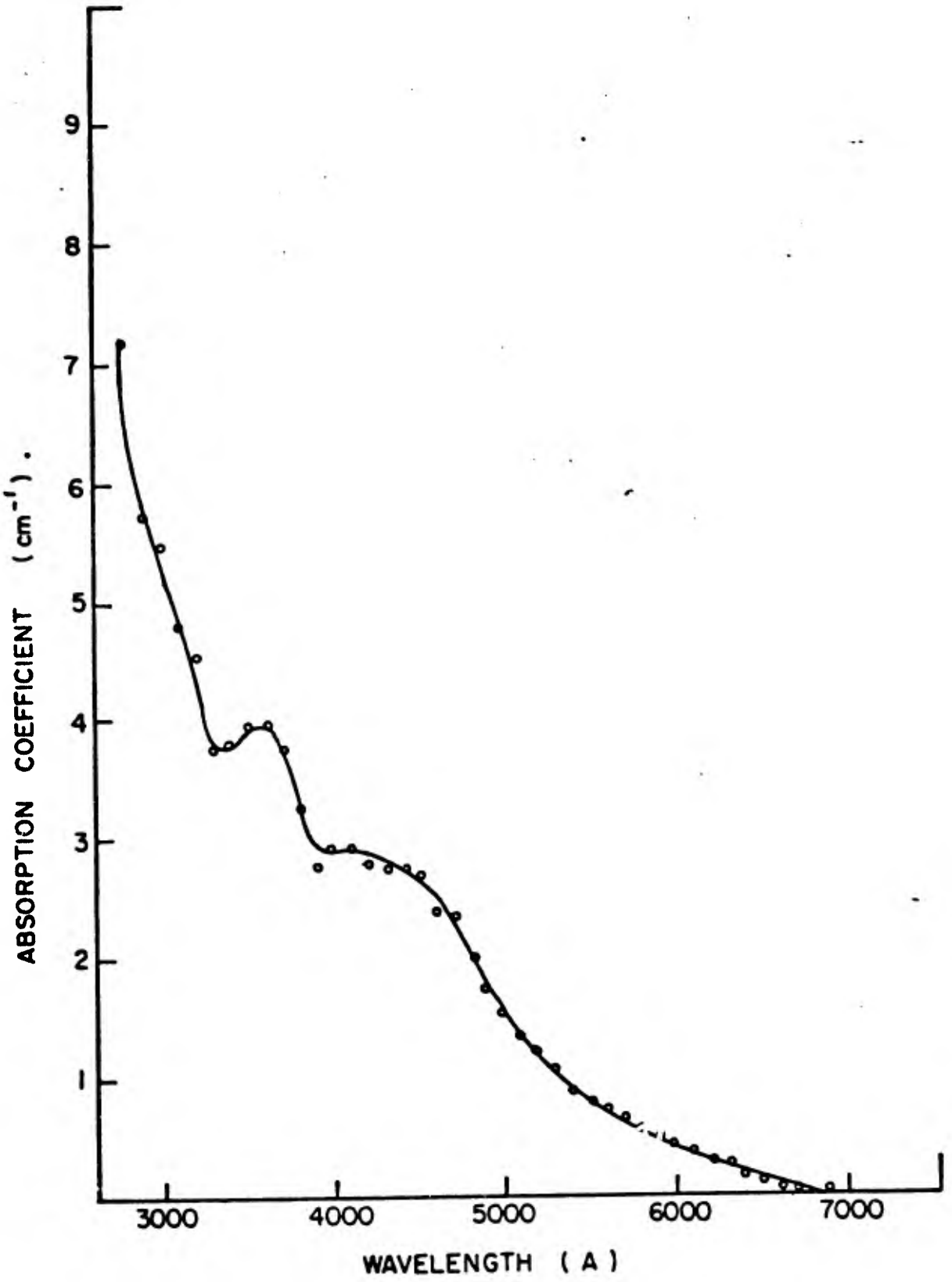

Figure A.6: Sapphire Absorption Coefficient at the End of 69 Hours of Full Power Reactor Operation

recently reported data for LiF under continuous electron bombardment in which the luminescent output also increased with dose [107]. This effect was attributed by these authors to complex F-center growth kinetics in LiF. As for an explanation of the present results, the simultaneous effects of neutrons and gamma rays must be considered. This clearly represents a difficult problem and will not be attempted here.

Assuming that the 3300Å luminescence peak does saturate at the fluences encountered in this study (~2×10^{17} nvt fast neutron) and exhibits a linear response to power variations, an in core power monitor might be based on this phenomenon. The temperature dependence of the luminescence would have to be studied; however, it might be possible to place the sapphire at points where the temperature remains relatively constant. Such a detection system could be very small and resist high temperatures. Instrumentation would be very simple consisting only of a light transmission tube, a filter to select the 3300Å emission and a photomultiplier.

To speculate a little, the ratio of the 3300Å to 4100Å luminescence peaks may possibly be a good indicator of total neutron fluence. This parameter appears sensitive over fluences which one would expect in the core of typical power reactors operated for several hours. Thus, one might be able to take advantage of the thermoluminescence properties of Al_2O_3 combined with the peak ratio variation and

devise a scheme to use Al_2O_3 to simultaneously measure neutron and gamma doses. From a thermoluminescence standpoint it may be that the energy in the two peaks would be released at different temperatures, providing a convenient way to measure the peak ratio.

APPENDIX B

COMPLETE Ar SPECTRUM

The data presented in this appendix are that used to calculate the excited state densities presented in Chapter 5. The data in Figures B.1 through B.11 were taken under the following conditions:

Slit setting: 150 μm
Monochromator scan rate: 20Å/min
Photomultiplier high voltage: 1250V
Picoampmeter full scale: 3×10^{-8} amp
Plotter sweep speed: 50 sec/cm
Plotter gain: .05V/cm

The data from Figures B.12 and B.13 were taken with a 100 μm slit setting to better resolve close-lying lines and at reduced gain to get all the large ArI lines on scale. The relationship between these two figures and those taken at higher gain was established by comparing on scale lines under both conditions.

No filters were used in taking these data as second order and reflective effects were found negligible for the Ar spectrum during earlier runs made with filters while getting the system checked out. Also the plotting paper ruling should be ignored. The indicated wavelength scale is that based on measured dispersion and the monochromator wavelength indicator. Line identificationsare those reported in Chapter 5. Use of different type paper resulted

from a local paper shortage. The 2250Å continuum appears to be located at nearly 2400Å in Figure B.1. This is because radiation damage to optical components caused the continuum to shift towards the red as UV transmission is reduced.

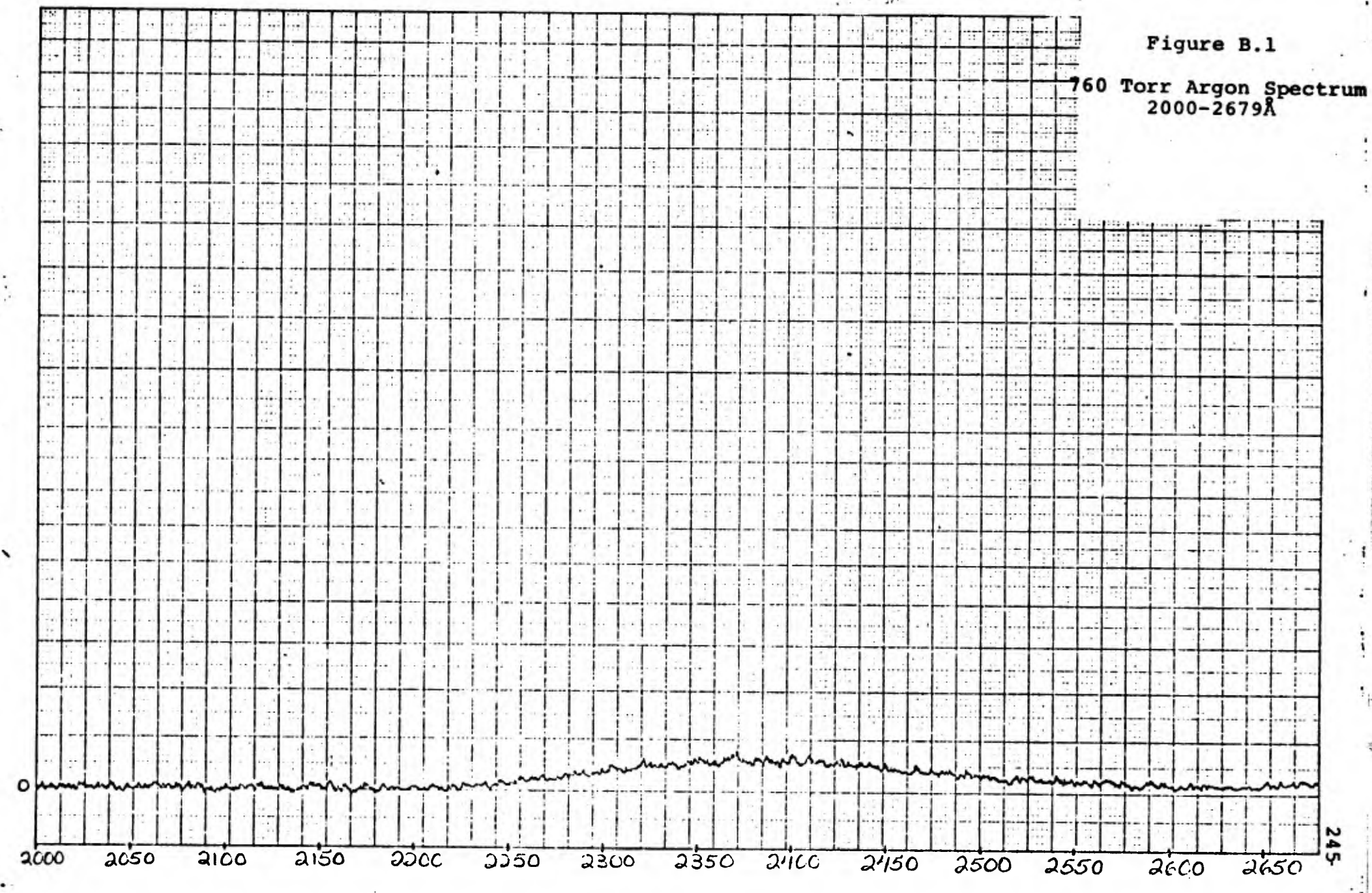

Figure B.1

760 Torr Argon Spectrum
2000-2679Å

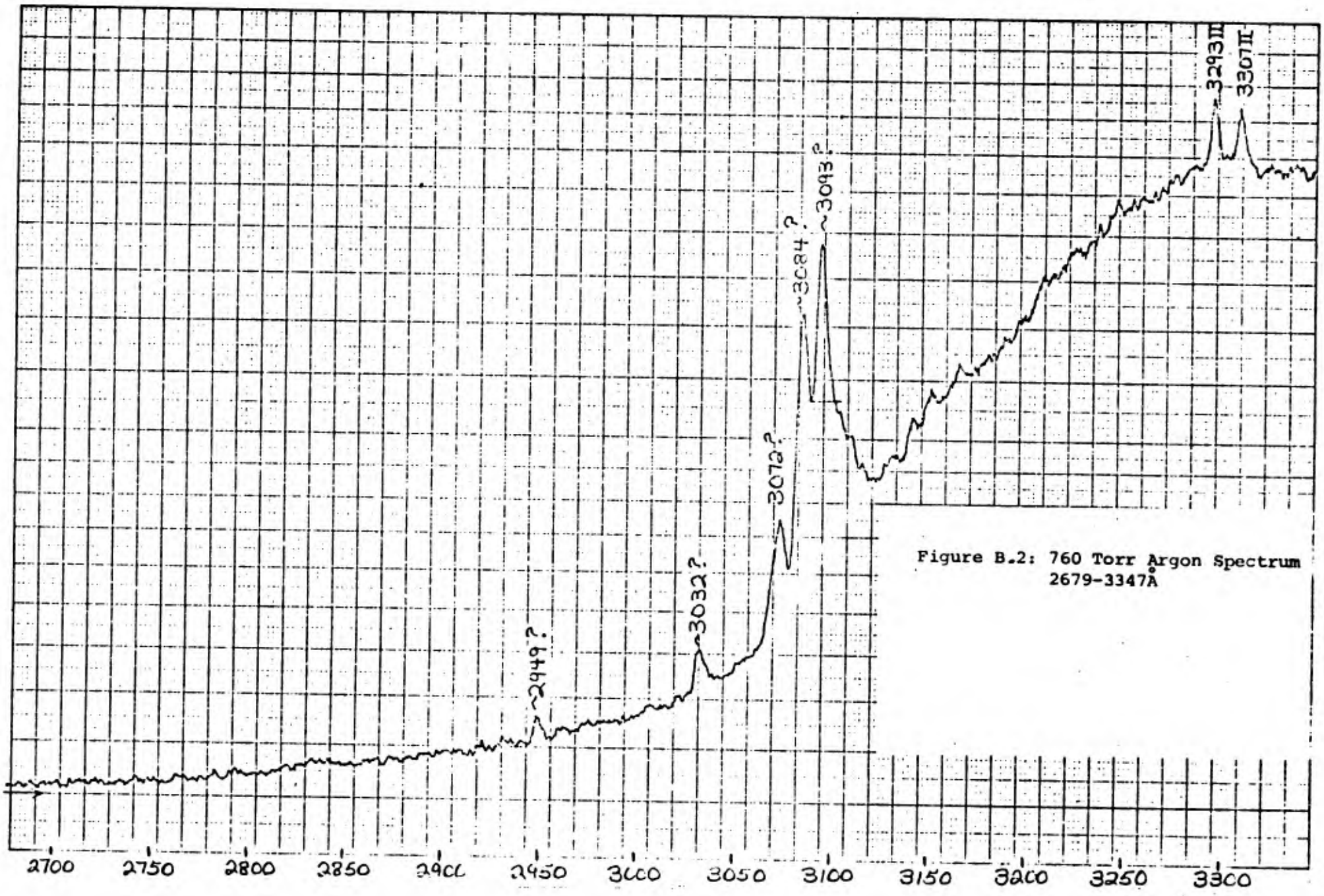

Figure B.2: 760 Torr Argon Spectrum
2679-3347Å

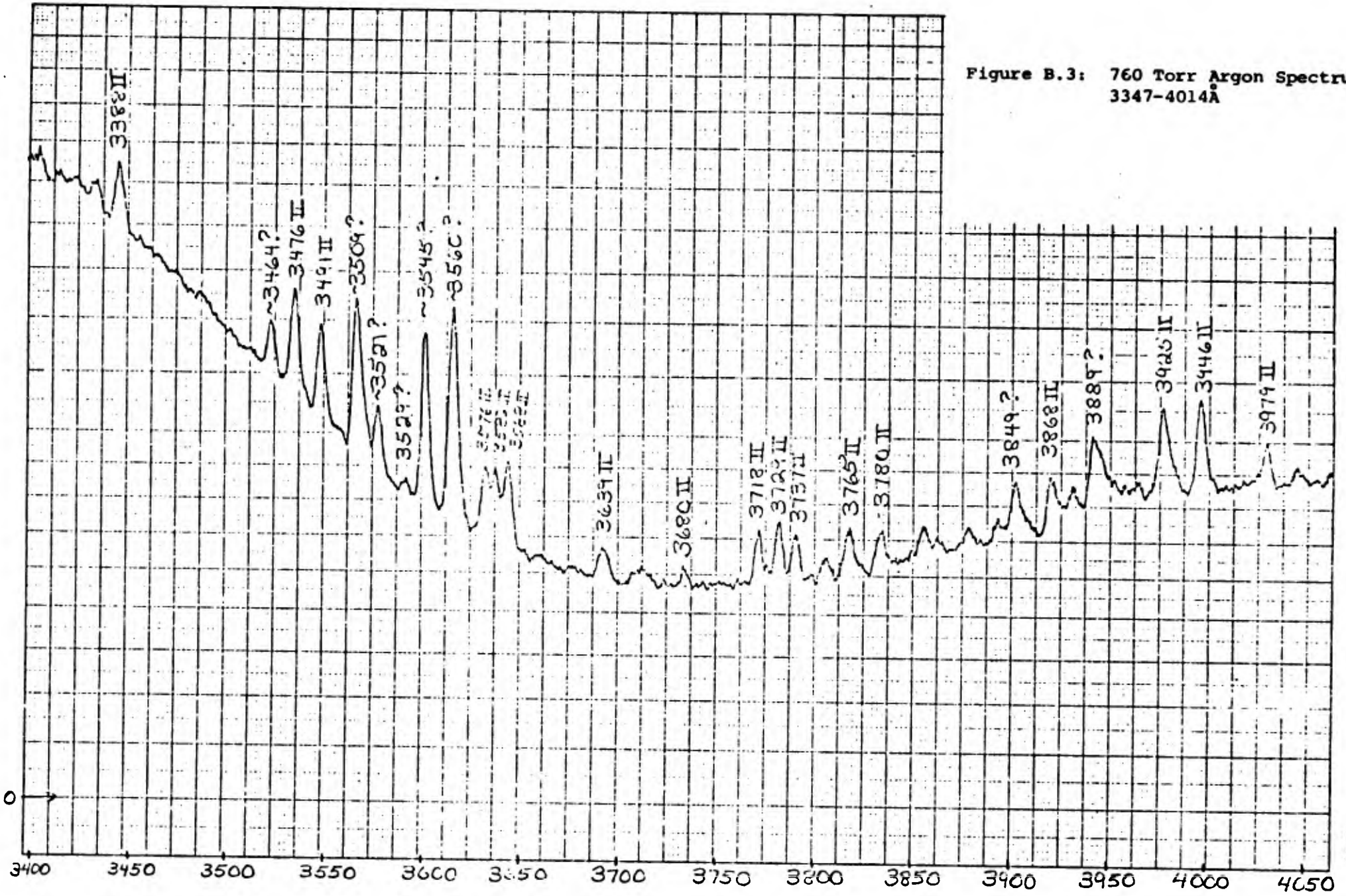

Figure B.3: 760 Torr Argon Spectrum 3347-4014Å

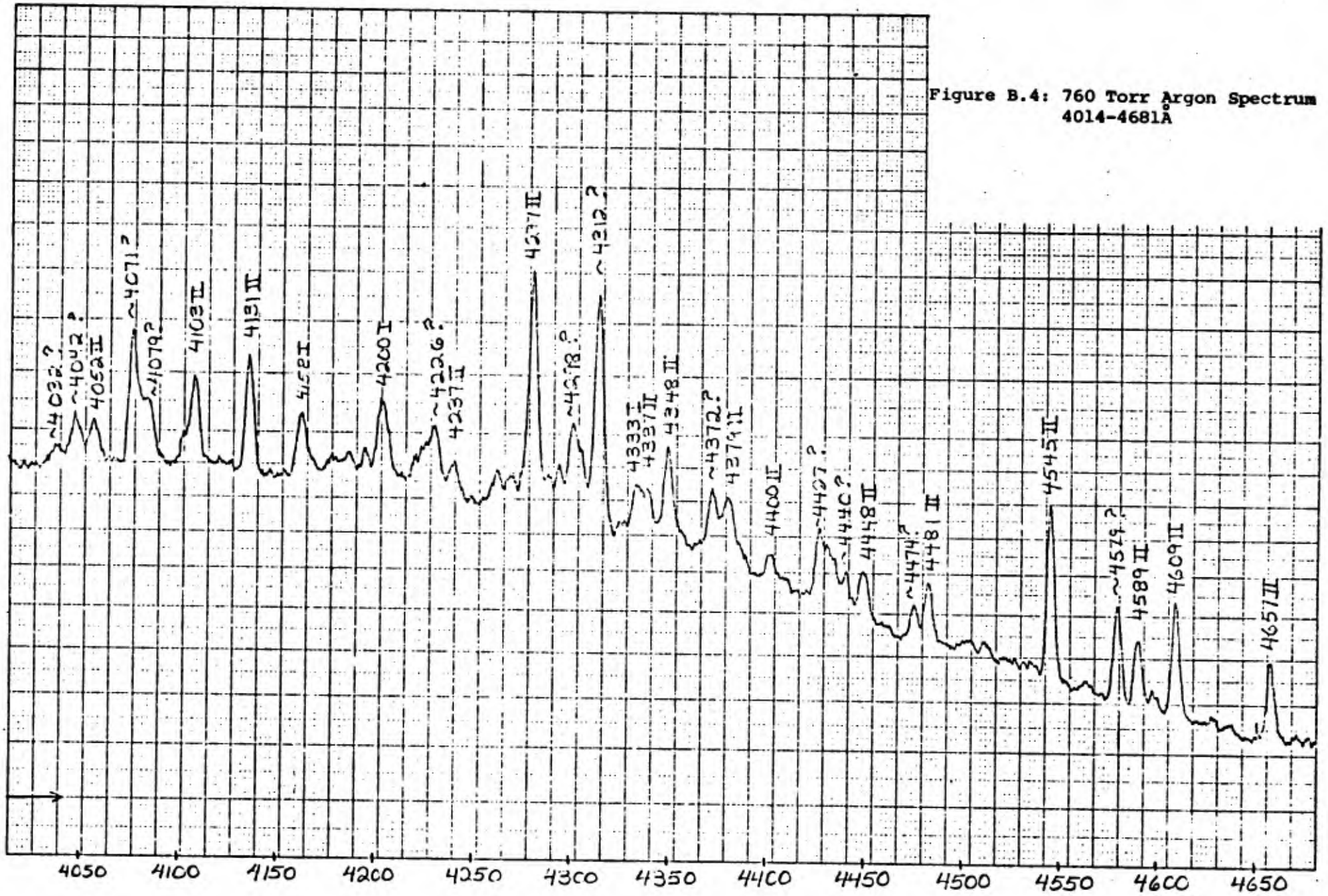

Figure B.4: 760 Torr Argon Spectrum
4014-4681Å

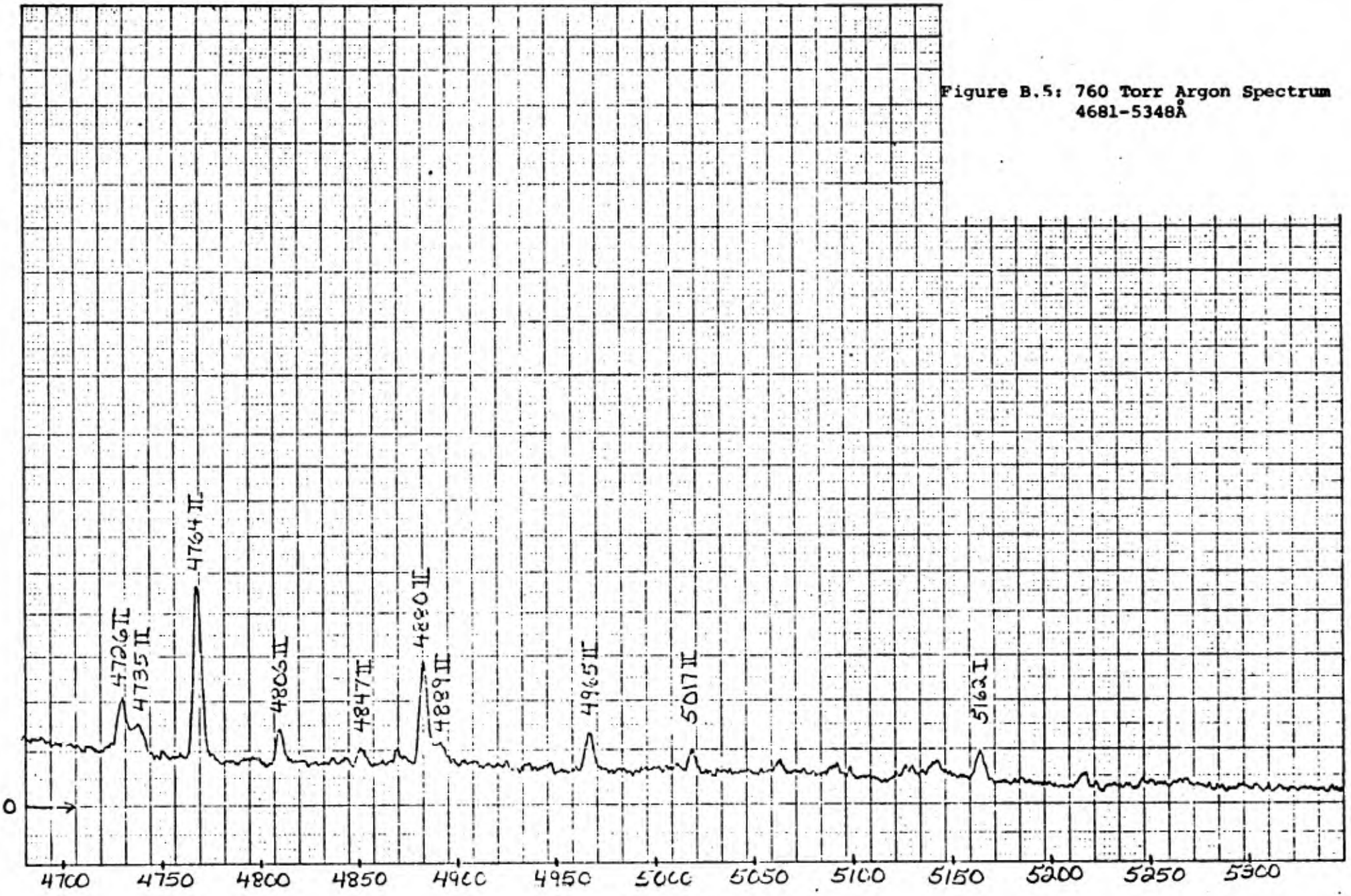

Figure B.5: 760 Torr Argon Spectrum
4681-5348Å

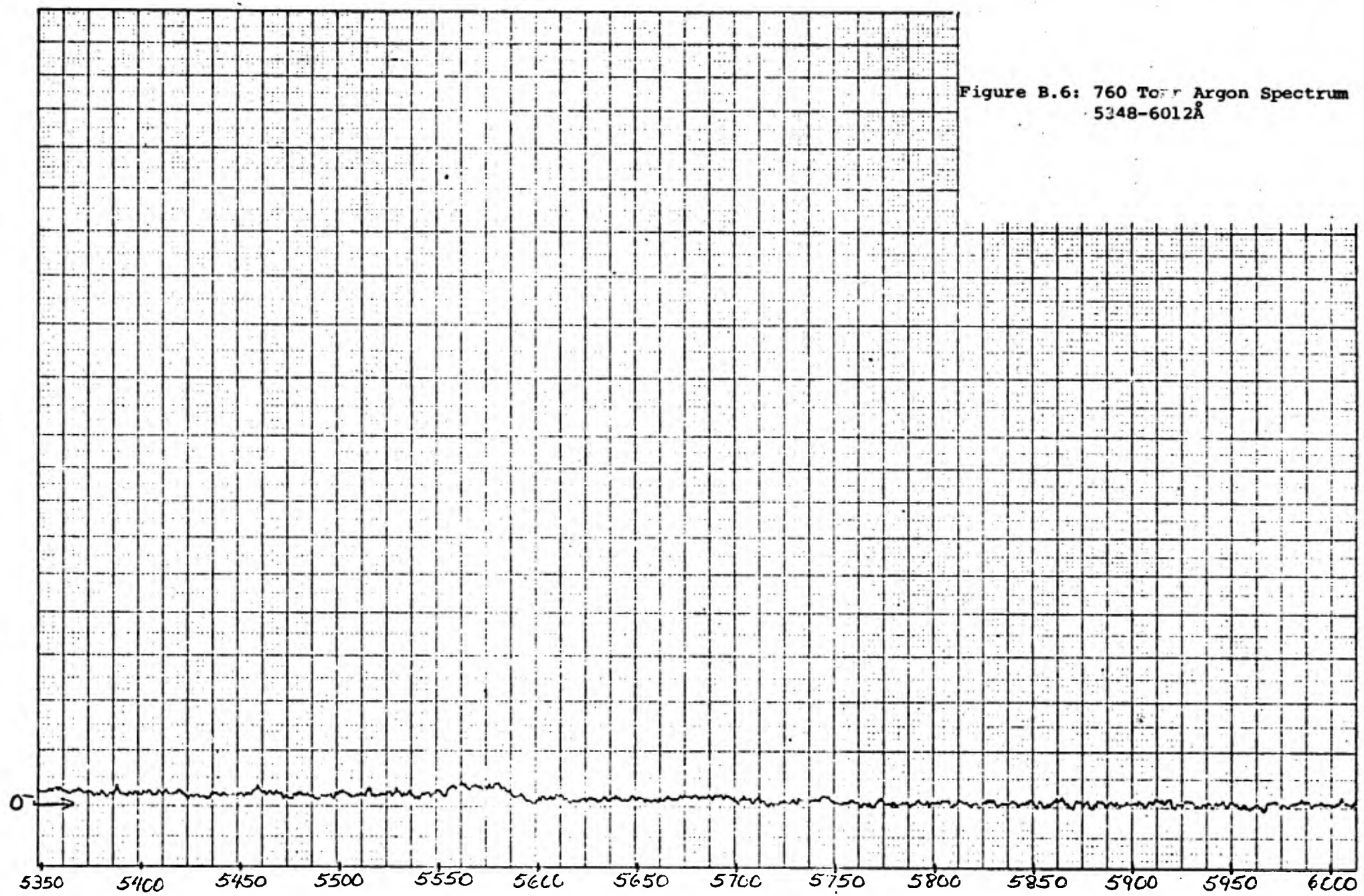

Figure B.6: 760 Torr Argon Spectrum
5348-6012Å

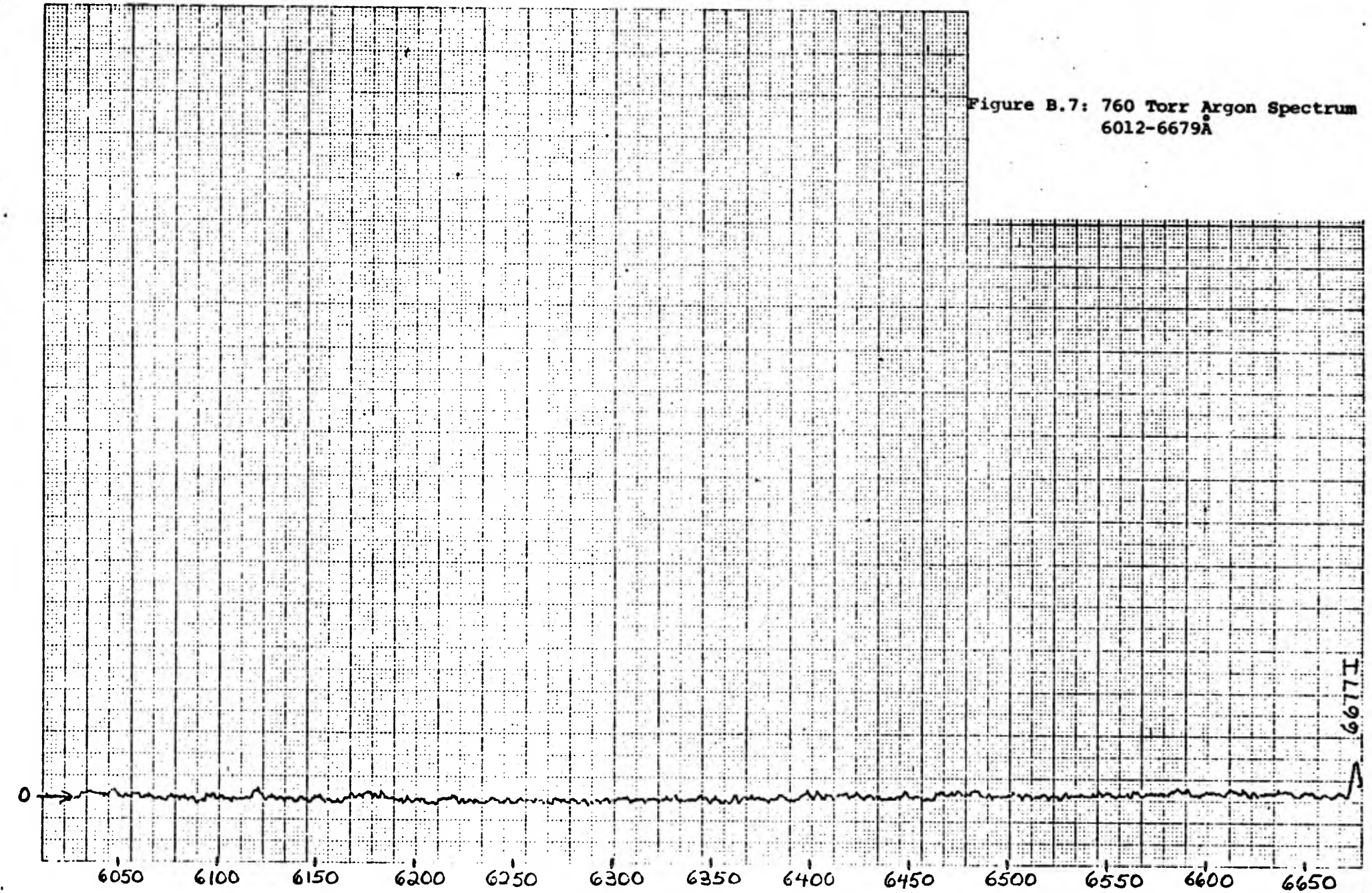

Figure B.7: 760 Torr Argon Spectrum
6012-6679Å

Figure B.8: 760 Torr Argon Spectrum
6679-7350Å

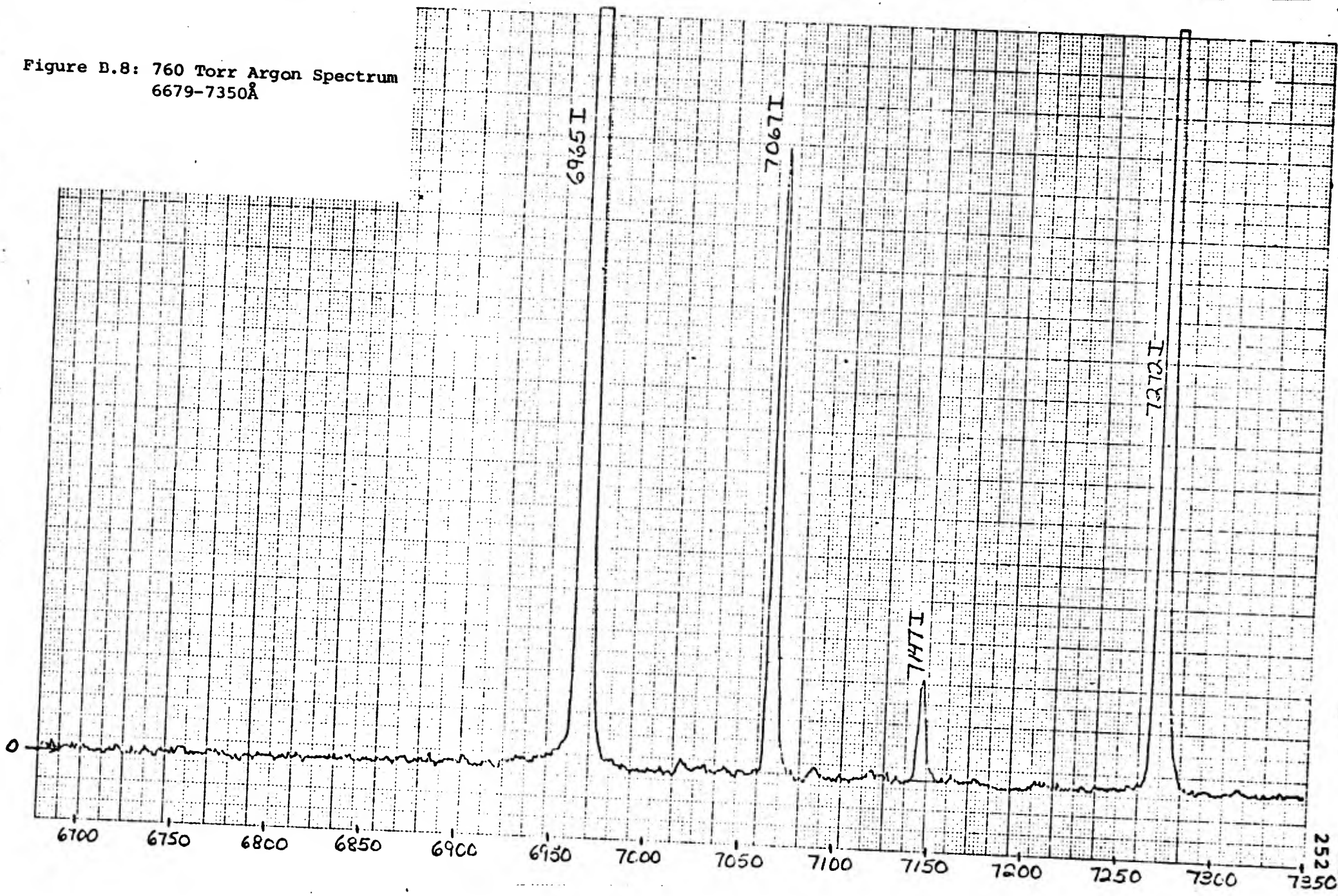

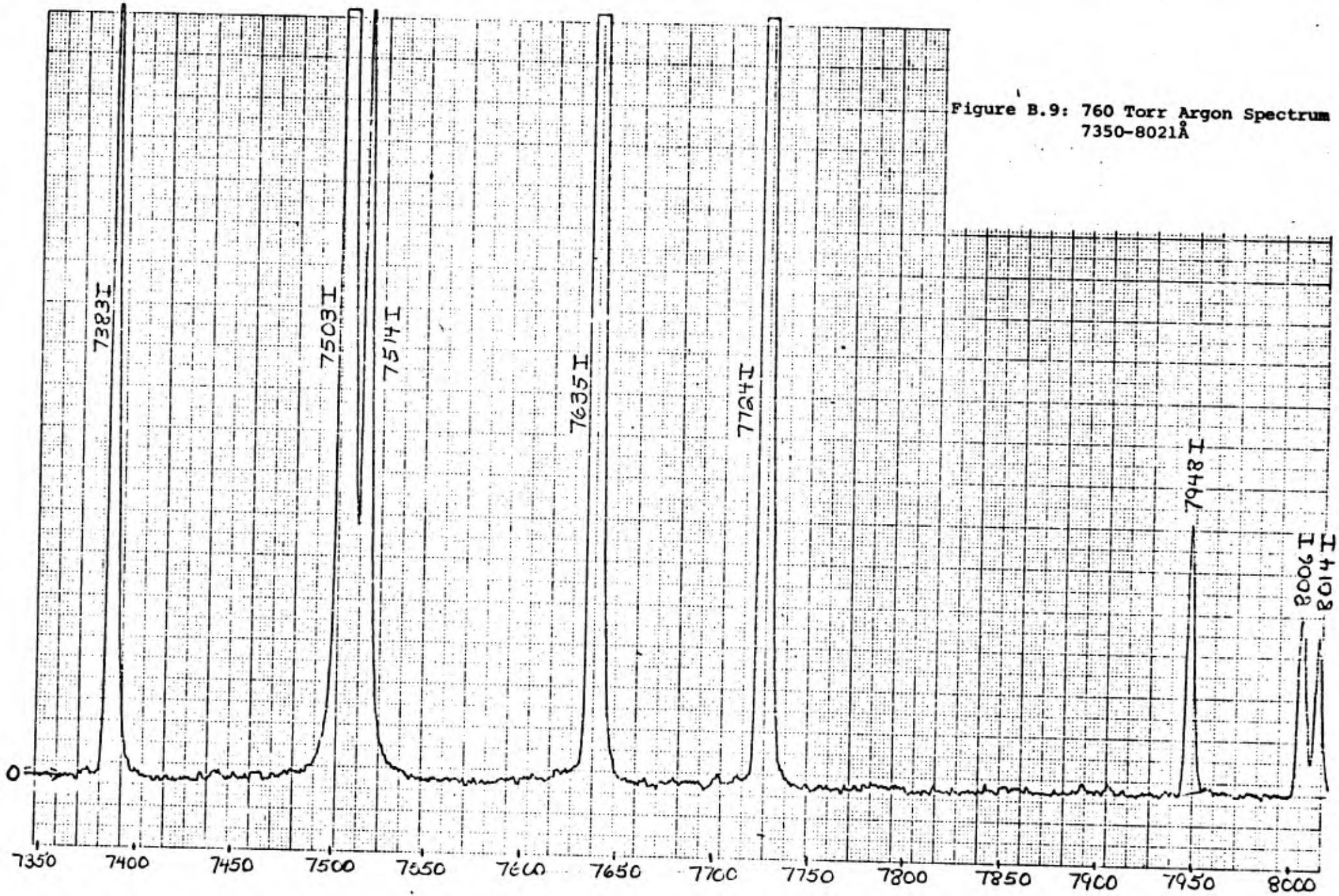

Figure B.9: 760 Torr Argon Spectrum
7350-8021Å

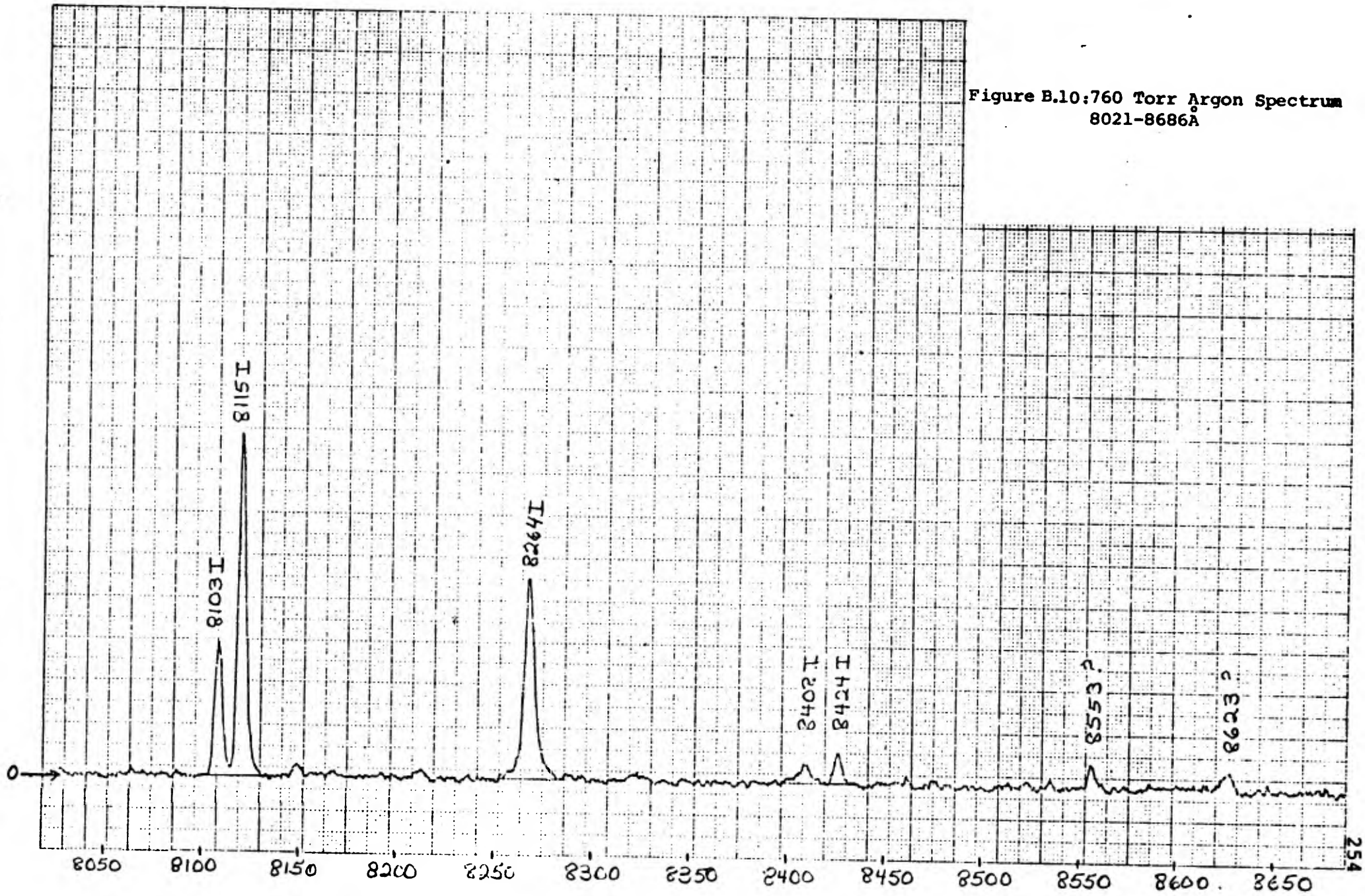

Figure B.10:760 Torr Argon Spectrum
8021-8686Å

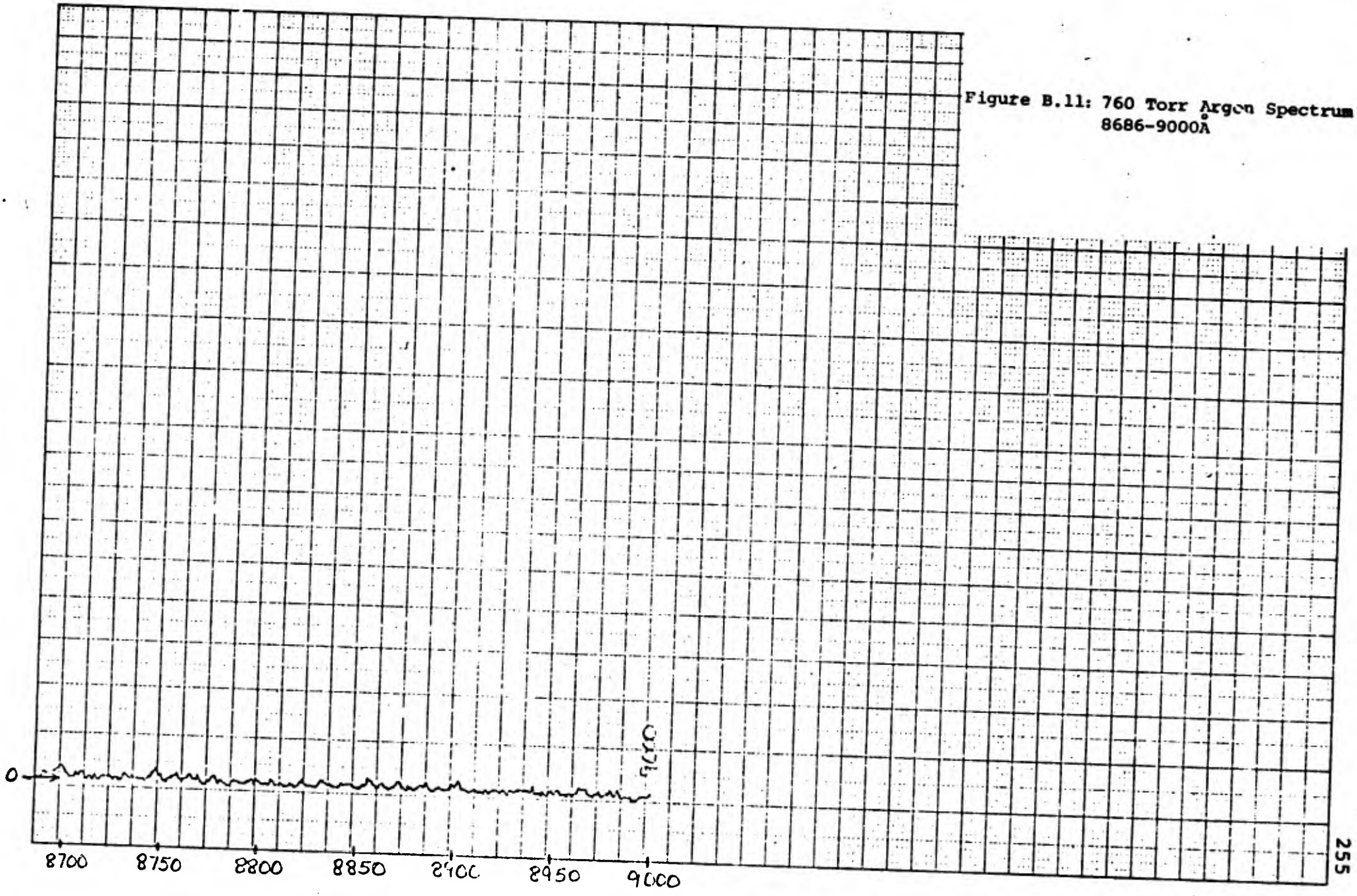

Figure B.11: 760 Torr Argon Spectrum
8686-9000Å

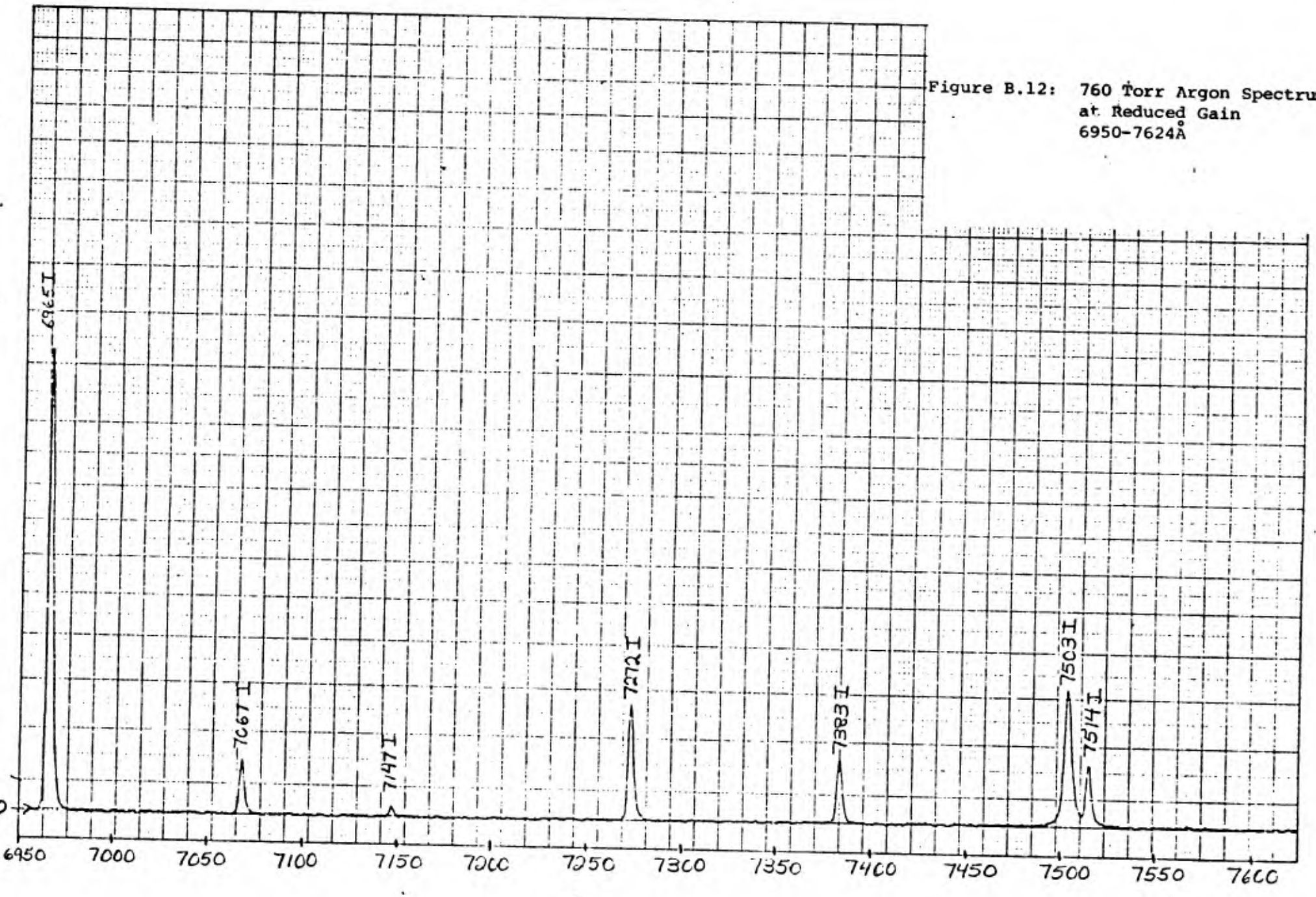

Figure B.12: 760 Torr Argon Spectrum at Reduced Gain 6950-7624Å

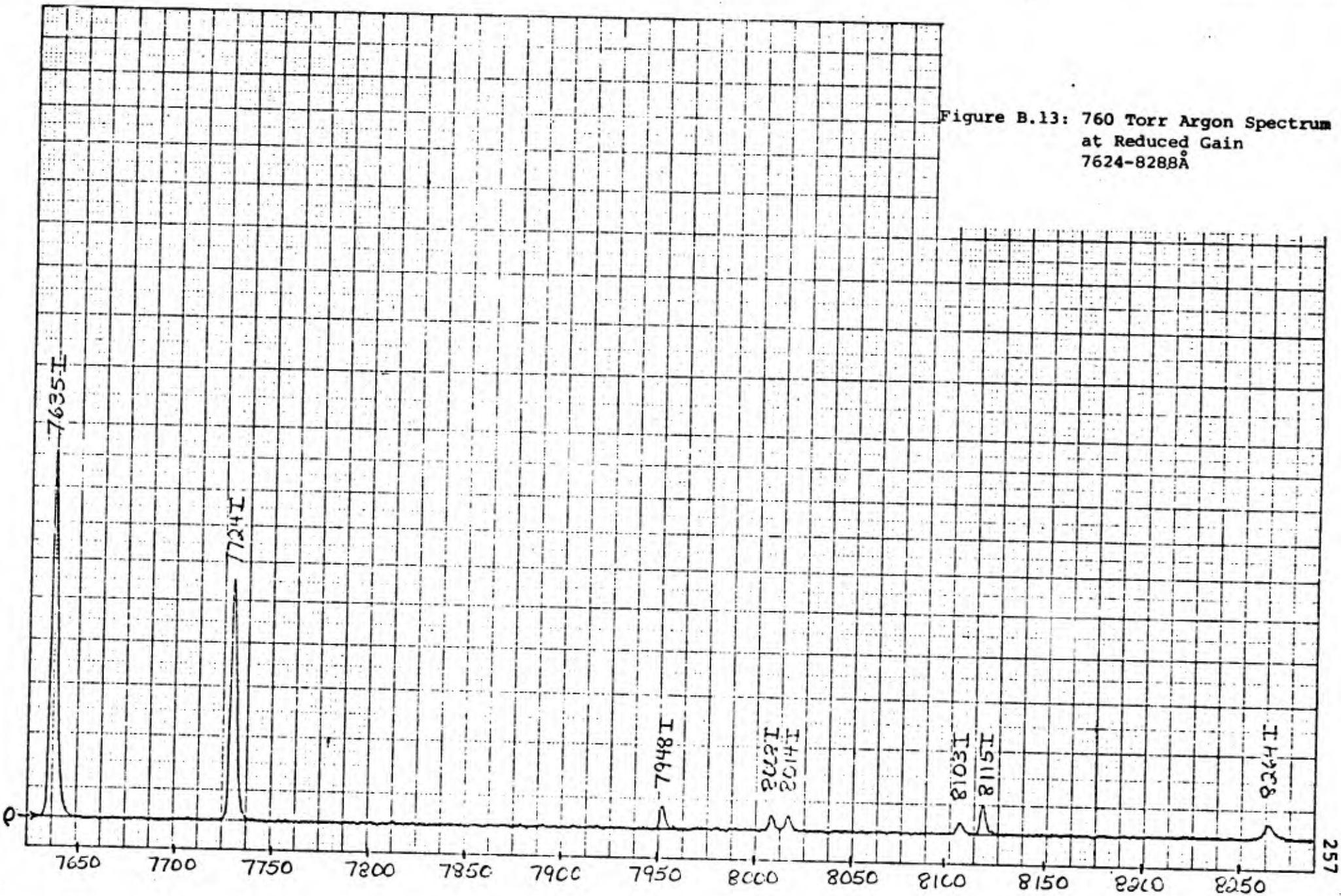

Figure B.13: 760 Torr Argon Spectrum at Reduced Gain 7624-8288Å

APPENDIX C

TABULAR SUMMARY OF WALTERS' DATA FOR ARGON

In Walters' dissertation [17] he only presents his data for Ar graphically. His analysis was strongly influenced by his efforts to characterize the plasma according to an LTE model and his excited state data are thus presented in terms of the log of relative populations. In addition, his data for different pressures are questionable at least as far as intensity versus pressure information is concerned. Because of these problems his data are presented again in this appendix in a normalized form such that one can see the variations in the relative spectral character as a function of pressure. It is hoped this will ease the task facing future researchers who need to use Walters' data. One note of caution, however, would seem in order. The line identifications made by Walters are not all in agreement with those this author would make, so as a further aid those lines which seem identified with high confidence are indicated by an asterisk. Also indicated in a column to the right of the tables are those data considered to be most reliable and used for comparison with the results of this study. Tables C.1 and C.2 list the data for ArI and ArII respectively. The data have been normalized such that the population of the $2p_3$ state as calculated from the 7383Å

line is unity. Thie choice was arbitrary. Only two significant figures are presented since the accuracy of the data can hardly be better than 10%, and this makes the tables easier to read. The data listed in the tables comes from the original computer output from the computer program run by Walters. Neither the computer code nor the input data was checked by this author for validity. Also indicated in the tables are the populations selected for analysis and use for comparison with the results of this study.

TABLE C.1: WALTERS' RELATIVE ArI POPULATIONS

Upper Level (Paschen)	Energy in cm^{-1} (eV)	Wavelength (Å)	Populations Pressure (torr) 25	75	150	284	450	600	760	Used in This Study
$3p_1$	118871 (14.75)	4259.36*	.26	.14	.10	.12	.084	.11	.11	
$3p_2$	118460 (14.70)	4181.88	1.5	.51	.43	.59	.45	.49	.60	
		3948.98	3.7	2.6	2.5	2.1	2.2	1.7	2.0	
$3p_8$	116999 (14.51)	4190.71	2.0	1.2	1.5	1.3	1.3	.53	1.3	
$3p_9$	116943 (14.51)	4200.67	1.6	.86	.71	.57	.58	.52	.75	
$2p_1$	108723 (13.49)	7503.87*	4.1	3.6	3.5	4.2	2.8	2.8	2.6	X
$2p_2$	107496 (13.34)	8264.52*	1.4	1.0	1.2	1.0	1.5	1.5	1.7	
		7272.93*	1.9	3.2	5.6	4.7	9.3	9.6	10.	
		7724.21*	1.0	1.5	2.6	2.3	4.4	4.5	4.8	
		6965.43*	1.7	2.6	4.4	5.1	7.7	7.9	9.7	X
$2p_3$	107290 (13.31)	7067.22*	.96	.92	.97	.93	1.0	.97	.95	
		7383.98*	1.0	1.0	1.0	1.0	1.0	1.0	1.0	X

TABLE C.1 (continued)

Upper Level (Paschen)	Energy in cm^{-1} (eV)	Wavelength (Å)	Populations Pressure (torr) 25	75	150	284	450	600	760	Used in This Study
$2p_4$	107132 (13.29)	7948.18*	.75	.84	.73	.79	.80	.74	.85	X
$2p_5$	107054 (13.28)	7514.65*	1.3	1.2	1.1	1.0	1.0	1.0	1.0	X
$2p_6$	106237 (13.18)	7635.11*	1.5	1.8	2.5	2.8	2.9	3.1	3.9	X
		8006.16*	1.1	1.3	2.7	1.4	2.0	1.6	1.5	
$2p_7$	106087 (13.16)	8103.69*	.43	.34	.40	.30	.33	.35	.46	X
		7723.76	2.3	3.4	5.7	5.1	9.8	10	10	
$2p_8$	105617 (13.10)	8014.79*	.79	.76	.69	.67	1.0	.79	.75	X
$2p_9$	105463 (13.08)	8115.31*	.39	.26	.33	.29	.31	.31	.40	X

TABLE C.2: WALTERS' RELATIVE ArII POPULATIONS

Upper Level	Energy in cm^{-1} (eV)	Wavelength (A)	Populations x 10^2 Pressure 25	75	150	284	450	600	760	Used in This Study
$(^3P)4p\ ^4P^0_{5/2}$	155043(19.23)	4400.99*	.37	.20	.15	.12	.12	.13	.--	
		4806.02*	.18	.094	.--	.070	.--	.073	.--	X
$(^3P)4p\ ^4P^0_{3/2}$	155351(19.27)	4371.3	1.5	.77	.51	.53	.23	.38	.--	
$(^3P)4p\ ^4D^0_{7/2}$	157234(19.51)	4013.86	.69	.26	.29	.14	.--	.--	.--	
		4348.06*	.19	.099	.060	.063	.037	.059	.056	X
$(^3P)4p\ ^4D^0_{5/2}$	157673(19.56)	4266.53	6.5	.38	.33	.23	.34	.34	.48	
		4426.01*	.30	.18	.10	.13	.12	.11	.11	X
$(^3P)4p\ ^4D^0_{3/2}$	158168(19.62)	4331.20	.41	.27	.24	.21	.12	.15	.16	
$(^3P)4p\ ^4D^0_{1/2}$	158428(19.65)	4379.67*	.47	.25	.19	.19	.20	.13	.13	X
$(^3P)4_p\ ^2D^0_{5/2}$	158730(19.69)	4879.86*	.35	.25	.18	.19	.12	.10	.14	X
		4228.16	1.4	.95	.84	.57	.55	.37	.69	
$(^3P)4p\ ^2D^0_{3/2}$	159393(19.77)	4965.07*	.49	.17	.27	.27	.--	.--	.--	
		4726.86*	.79	.35	.26	.26	.19	.25	.26	X

TABLE C.2 (continued)

Upper Level	Energy in cm^{-1} (eV)	Wavelength (Å)	Populations x 10^2 Pressure 25	75	150	284	450	600	760	Used in This Study
$(^3P)rp\ ^2P^0_{1/2}$	159706 (19.81)	4657.89*	1.0	.70	.48	.47	.32	.41	.39	X
$(^3P)4p\ ^2P^0_{3/2}$	160239 (19.88)	4545.04*	2.2	1.4	1.0	.96	.73	.77	.87	X
		4764.86*	1.6	.94	.68	.71	.61	.50	.52	X
$(^3P)4p\ ^4S^0_{3/2}$	161049 (19.98)	3729.31	.--	.22	.23	.13	.29	.--	.23	
		3850.58	.78	.70	.43	.44	.57	.52	.52	
		3928.63	1.0	.97	.73	.79	.61	.58	.68	
		4579.35	1.0	.79	.64	.58	.46	.53	.40	
$(^1D)4p\ ^2F^0_{5/2}$	170401 (21.14)	4589.90*	.36	.23	.14	.14	.13	.12	.13	X
$(^1D)4p\ ^2F^0_{7/2}$	170530 (21.16)	4609.56*	.38	.21	.14	.13	.13	.13	.15	X
$(^1D)4p\ ^2P^0_{3/2}$	172214 (21.36)	4237.22*	.96	.51	.51	.53	.35	.28	.39	
		4277.52*	1.2	.76	.54	.49	.38	.42	.33	X
$(^1D)4p\ ^2P^0_{1/2}$	172816 (21.44)	4131.73*	1.1	.62	.51	.47	.25	.33	.35	X

TABLE C.2 (continued)

Upper Level	Energy in cm^{-1} (eV)	Wavelength (Å)	Populations x 10^2 Pressure 25	75	150	284	450	600	760	Used in This Study
$(^1D)4p\ ^2D^0_{3/2}$	173343 (21.50)	4079.58	1.2	.93	.66	.62	.83	.35	.68	
		4042.90	.25	.12	.68	.86	.64	.74	.70	
$(^1D)4p\ ^2D^0_{5/2}$	173393 (21.51)	4035.46	2.8	1.5	.54	.82	1.8	1.0	.93	
		4072.01	.86	.57	.44	.38	.38	.36	.38	
		4481.81*	.40	.23	.15	.17	.15	.15	.16	X
		4300.65	1.6	1.0	.74	.67	.66	.--	.--	
$(^3P)5s\ ^4P_{5/2}$	181594 (22.53)	4103.91*	.10	.071	.056	.055	.058	.049	.059	X
$(^3P)5s\ ^4P_{3/2}$	182222 (22.61)	3770.52	.99	.86	.57	.52	.49	.45	.59	
		4156.09	1.0	.61	.54	.40	.27	.35	.45	
$(^3P)5s\ ^2P_{3/2}$	183091 (22.71)	4103.91	.14	.099	.077	.077	.082	.069	.082	
$(^3P)4d\ ^4D_{7/2}$	183676 (22.79)	3491.54*	.22	.16	.12	.12	.11	.12	.10	X
		3780.84*	.13	.12	.12	.086	.053	.093	.10	

TABLE C.2 (continued)

Upper Level	Energy in cm^{-1} (eV)	Wavelength (Å)	Populations x 10^2 Pressure 25	75	150	284	450	600	760	Used in This Study
$(^3P)4d\,^4D_{3/2}$	183986 (22.83)	3491.24	.48	.36	.26	.27	.25	.27	.22	
$(^3P)4d\,^4F_{9/2}$	185093 (22.96)	3588.45*	.15	.10	.098	.089	.066	.075	.076	X
$(^3P)4d\,^4F_{5/2}$	186074 (23.08)	3520.00	.59	.36	.30	.23	.40	.33	.35	
		3582.36*	.19	.10	.090	.091	.089	.082	.079	X
$(^3P)4d\,^4P_{1/2}$	186171 (23.10)	3979.36*	.34	.25	.19	.34	.25	.10	.23	X
$(^3P)4d\,^4P_{5/2}$	186891 (23.19)	3868.52*	.10	.097	.067	.074	.062	.032	.036	X
$(^1S)4p\,^2P^0_{3/2}$	191975 (23.82)	4052.92*	.21	.10	.13	.071	.034	.037	.073	X
$(^1S)4p\,^2P^0_{1/2}$	192333 (23.86)	3994.79	.29	.19	.12	.28	.18	.23	.18	
$(^1D)5s\,^2D_{5/2}$	195865 (24.30)	4448.88*	.10	.13	.093	.097	.095	.089	.072	X
$(^1D)4d\,^2F_{5/2}$	200235 (24.84)	372452	.81	.68	.57	.50	.56	.36	.46	

APPENDIX D

COMPLETE Xe SPECTRUM

Figures D.1 through D.13 were taken with a 300 μm slit setting. The data were used to obtain Figure 6.2 and to search for any continuum structure. Long wavelength pass filters as indicated were used in taking the data. The relative gain for each portion of the spectrum is also indicated. The data in Figures D.14 through D.17 cover the portions of the spectrum containing lines to be studied and were used to calculate excited state densities. The data were taken under the following conditions:

Slit setting: 150 μm
Monochromator scan rate: 20Å/min
Photomultiplier high voltage: -1250V
Picoampmeter full scale: 3×10^{-8} amp
Plotter sweep speed: 50 sec/cm
Plotter gain: .05V/cm

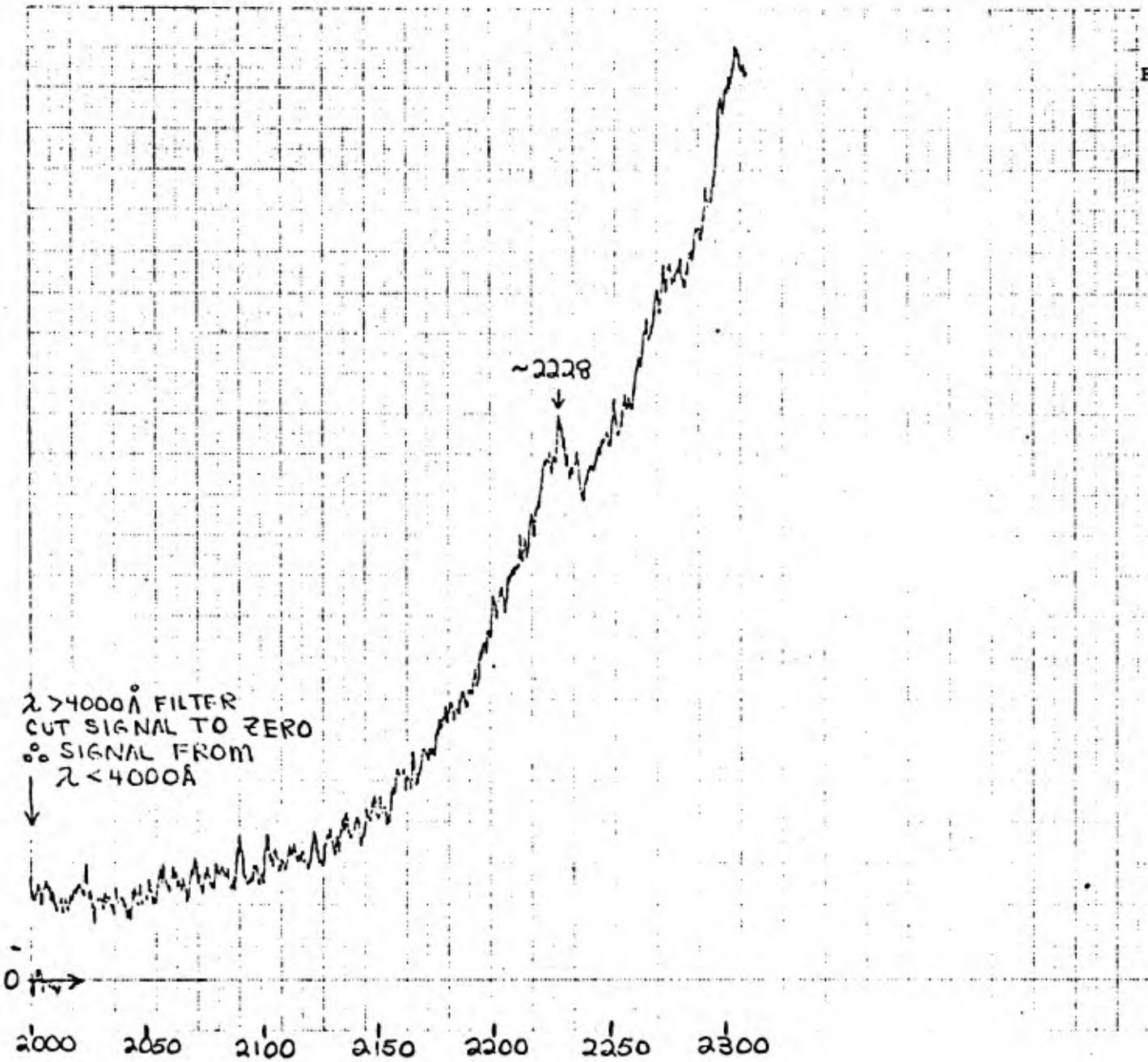

Figure D.1: 760 Torr Xenon Spectrum
(300 μm) 2000-2310Å
Gain: x30
Filter: none

18.08Å/cm

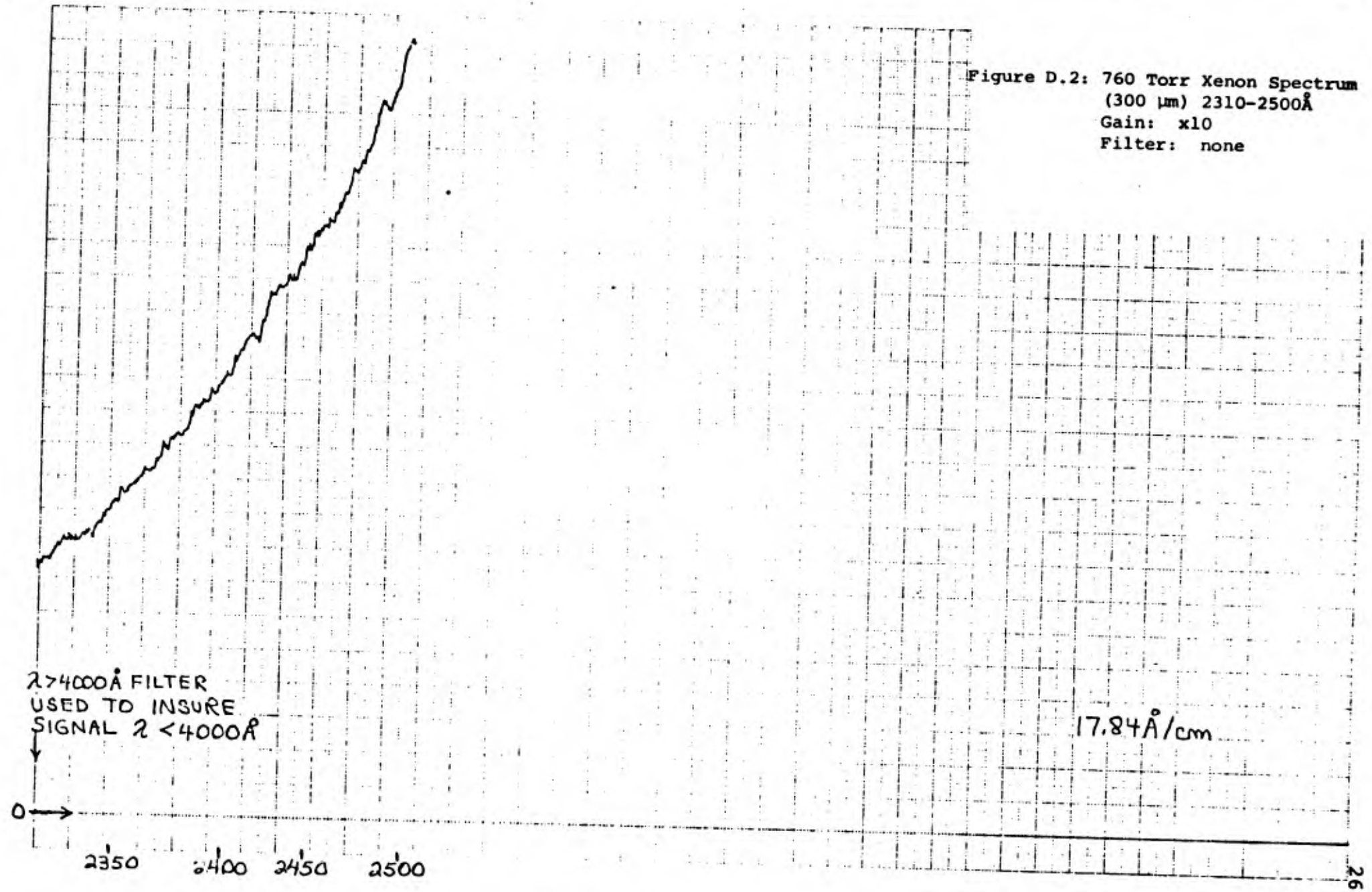

Figure D.2: 760 Torr Xenon Spectrum
(300 μm) 2310-2500Å
Gain: x10
Filter: none

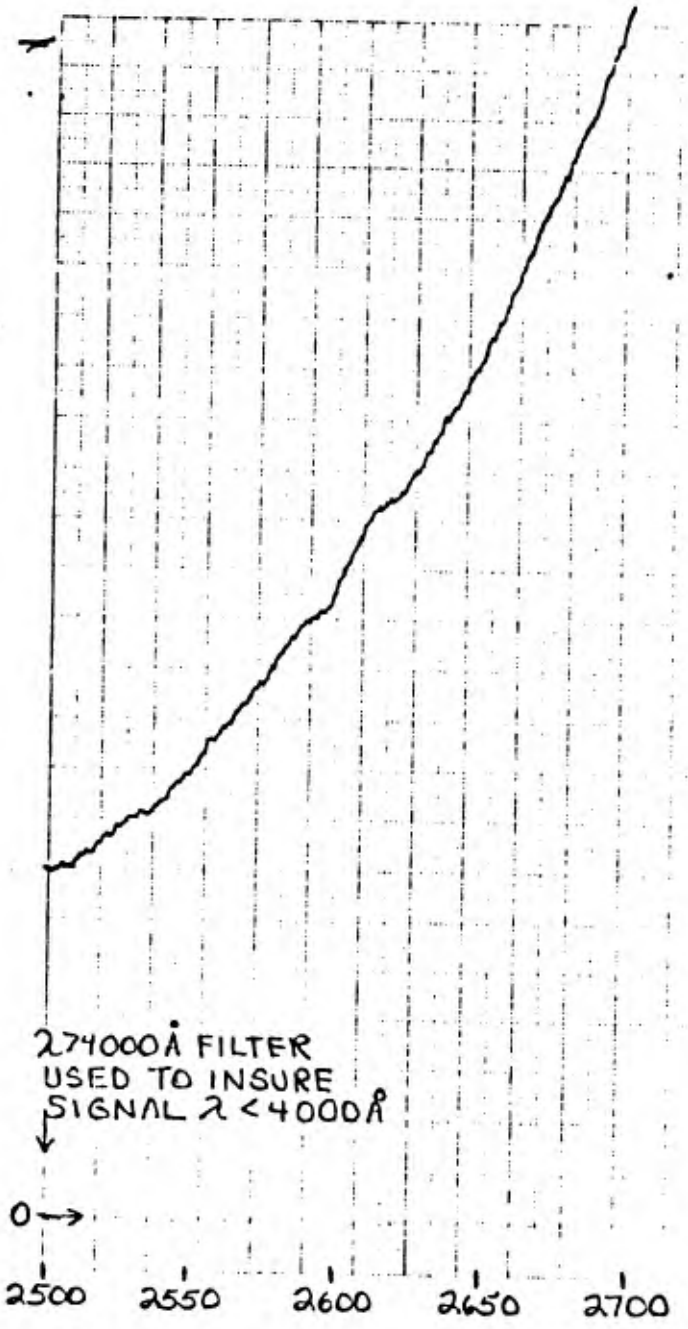

Figure D.3: 760 Torr Xenon Spectrum
(300 μm) 2500-2700Å
Gain: x3
Filter: none

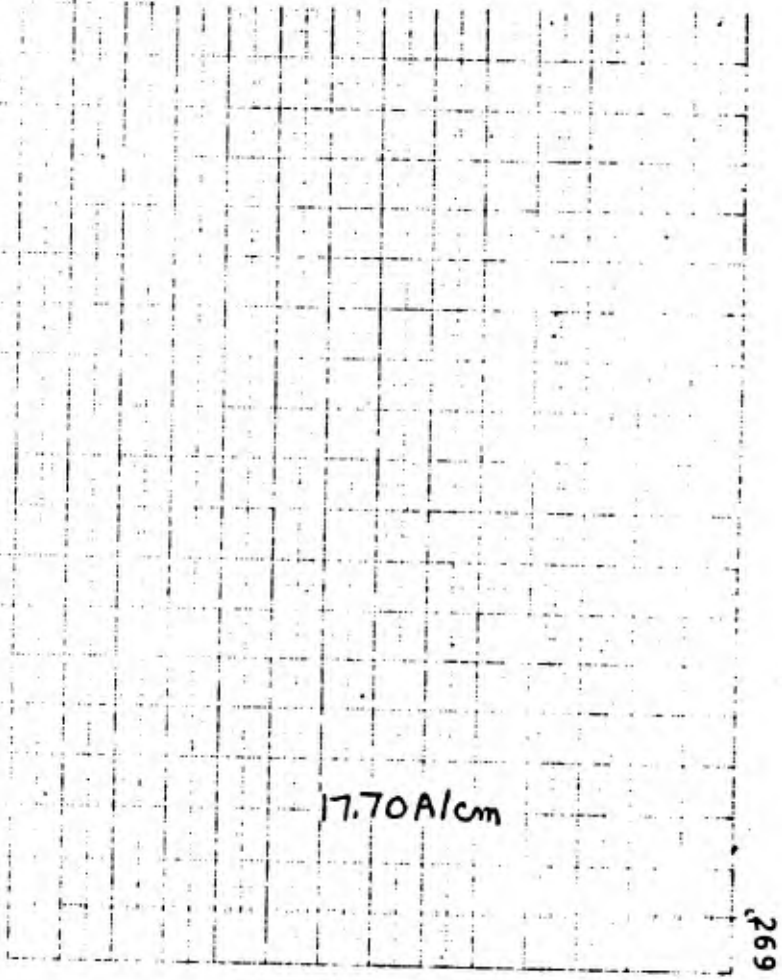

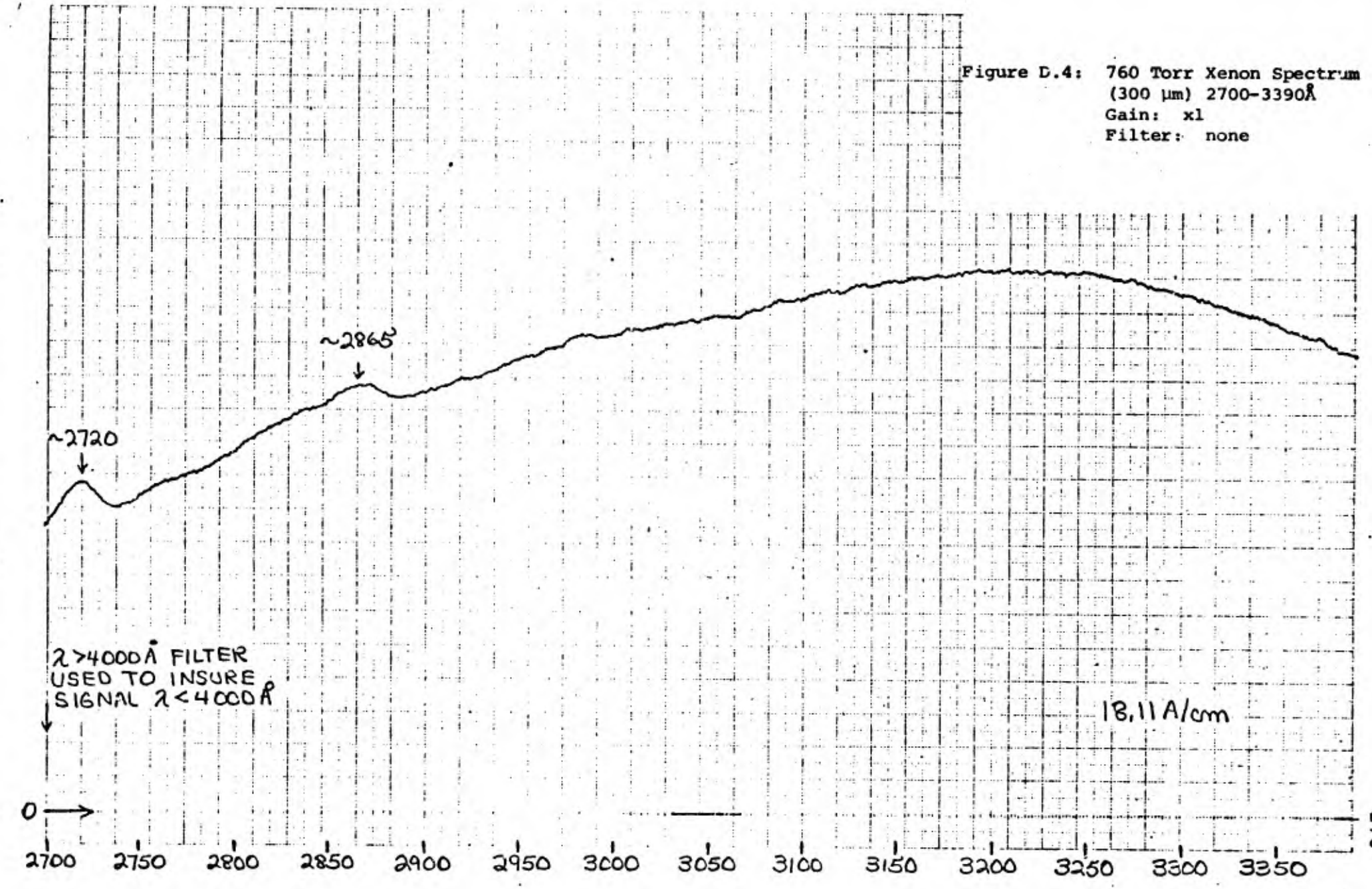

Figure D.4: 760 Torr Xenon Spectrum
(300 μm) 2700-3390Å
Gain: x1
Filter: none

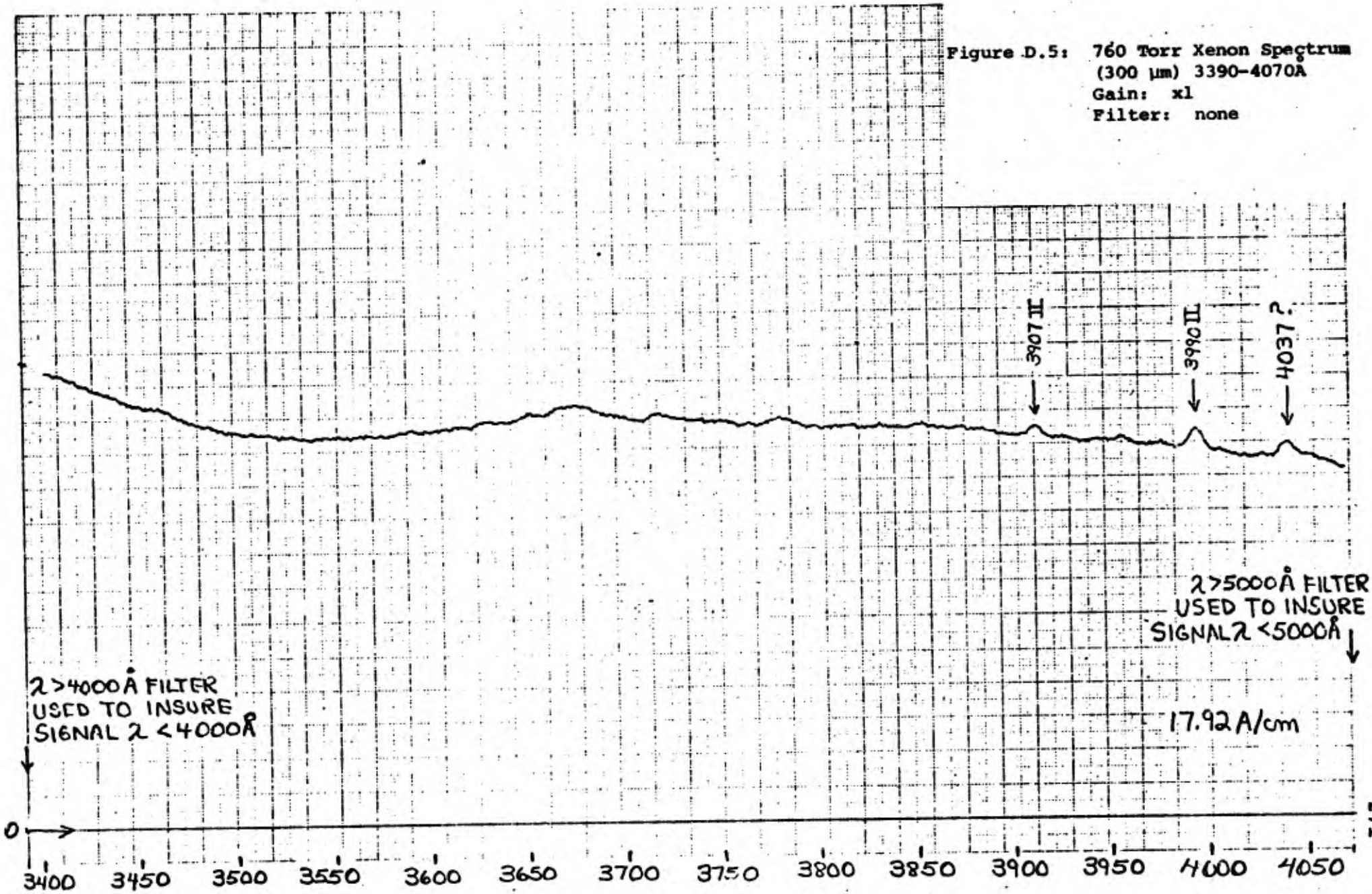

Figure D.5: 760 Torr Xenon Spectrum
(300 μm) 3390-4070Å
Gain: x1
Filter: none

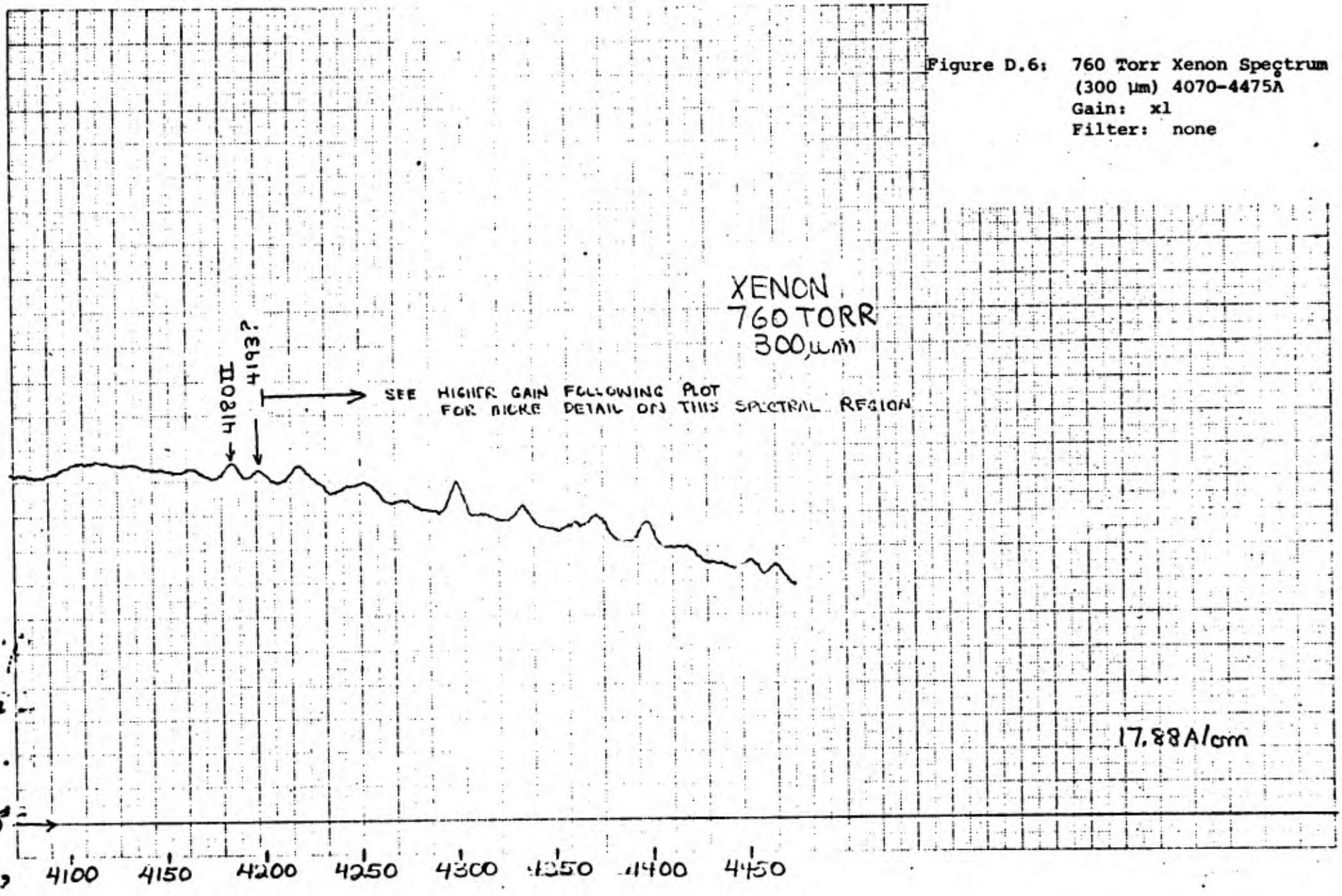

Figure D.6: 760 Torr Xenon Spectrum
(300 μm) 4070-4475Å
Gain: xl
Filter: none

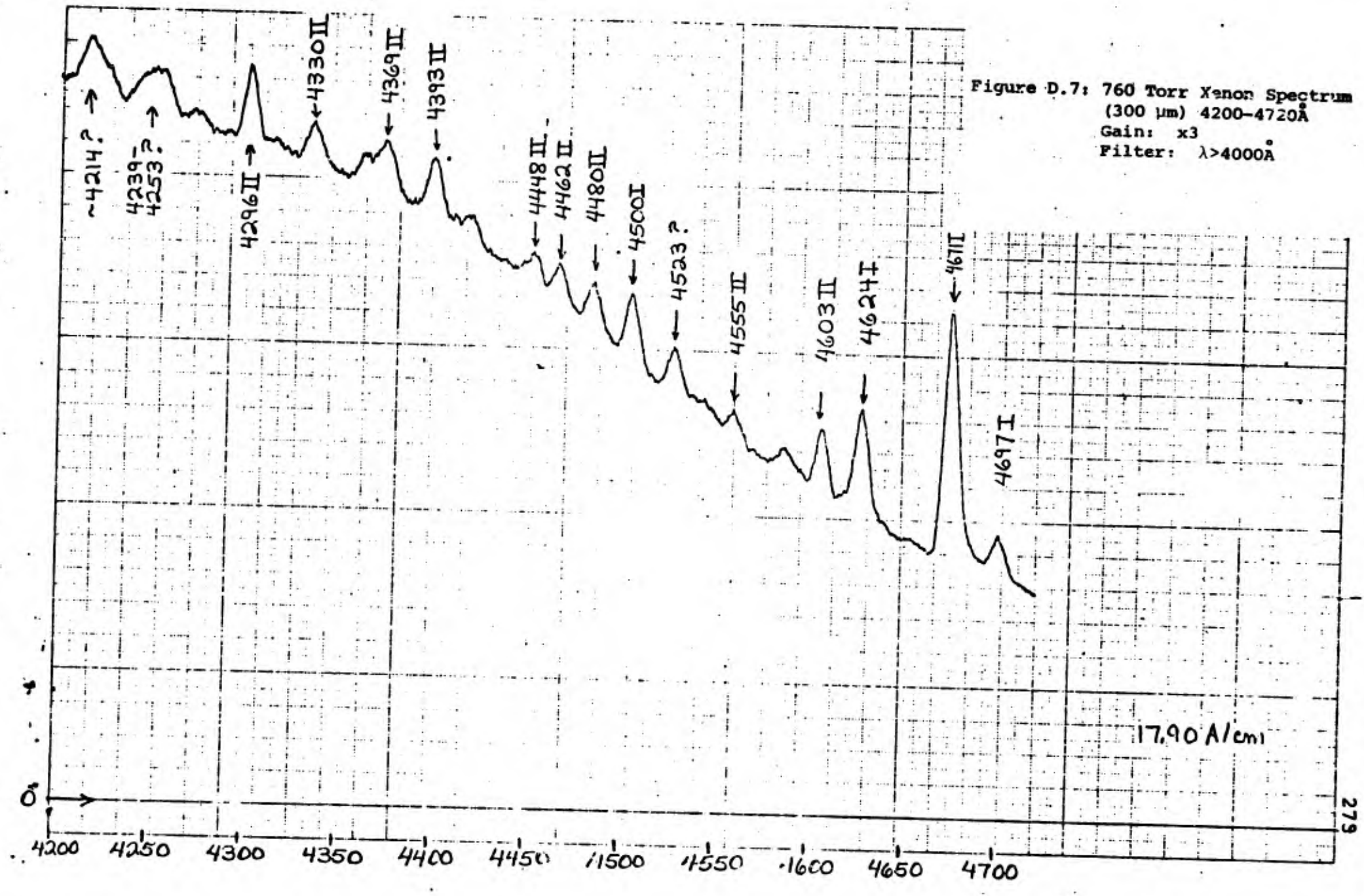

Figure D.7: 760 Torr Xenon Spectrum (300 μm) 4200-4720Å
Gain: x3
Filter: λ>4000Å

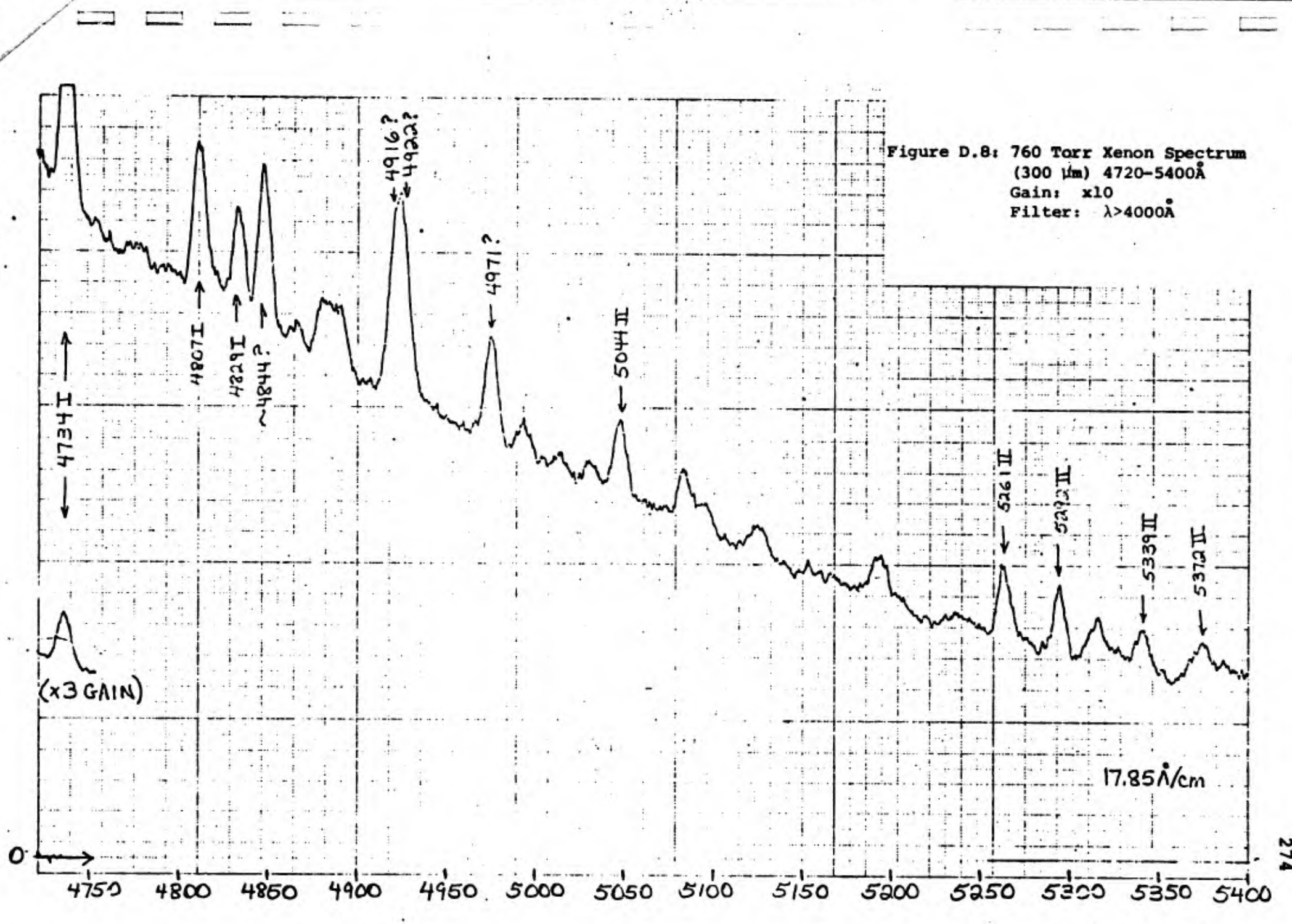

Figure D.8: 760 Torr Xenon Spectrum
(300 μm) 4720-5400Å
Gain: x10
Filter: λ>4000Å

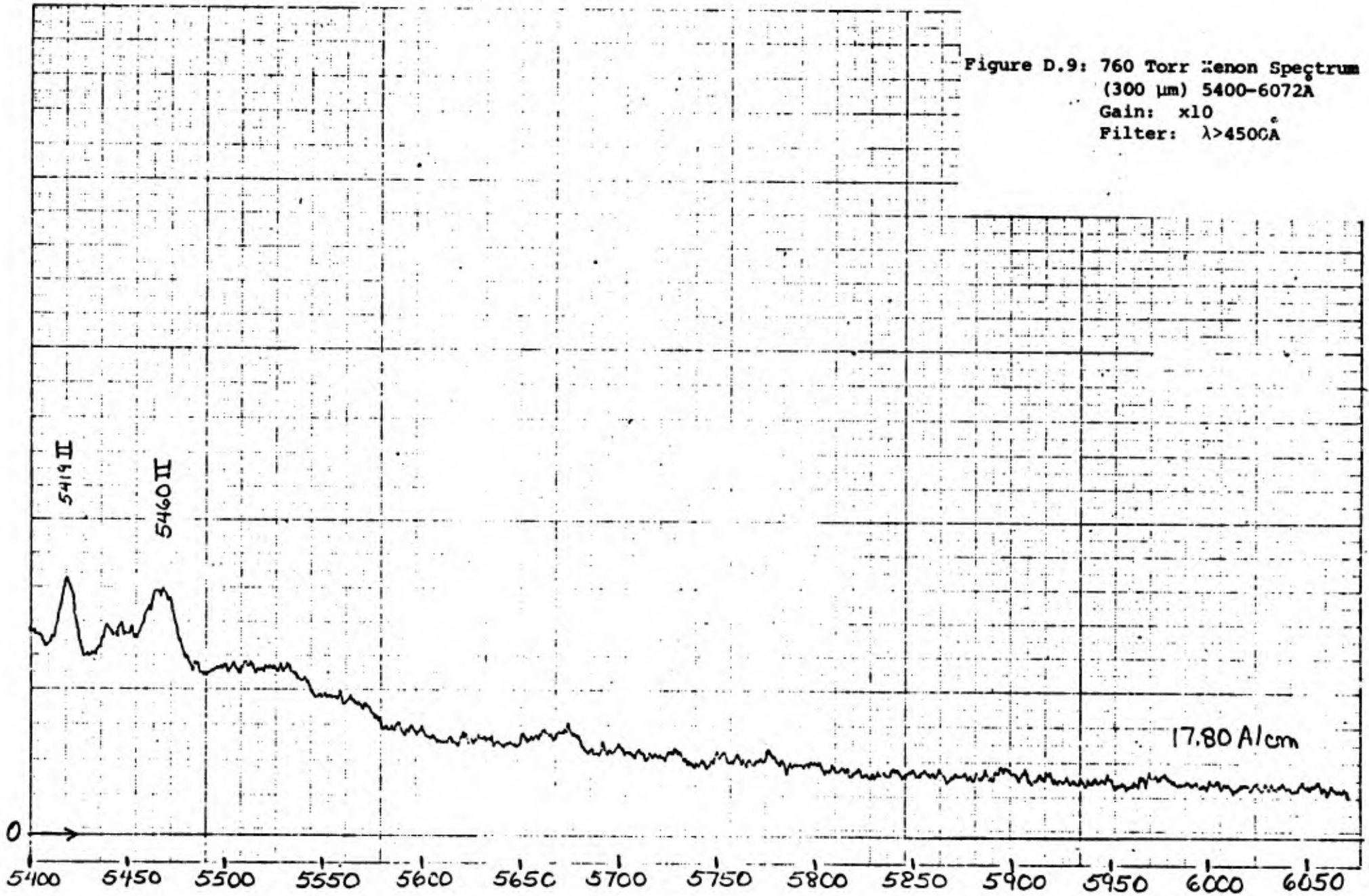

Figure D.9: 760 Torr Xenon Spectrum
(300 μm) 5400-6072Å
Gain: x10
Filter: λ>4500Å

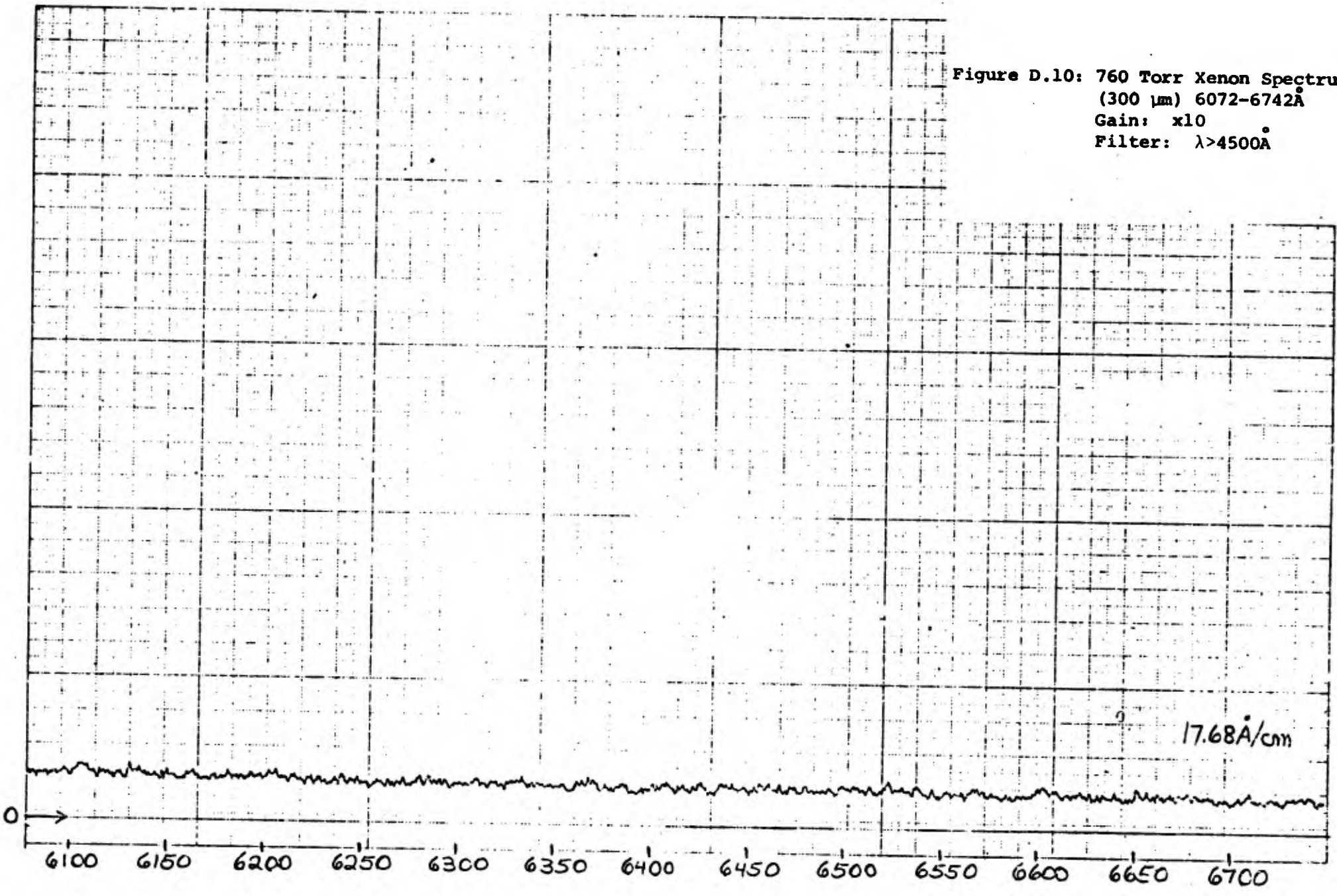

Figure D.10: 760 Torr Xenon Spectrum
(300 μm) 6072-6742Å
Gain: x10
Filter: λ>4500Å

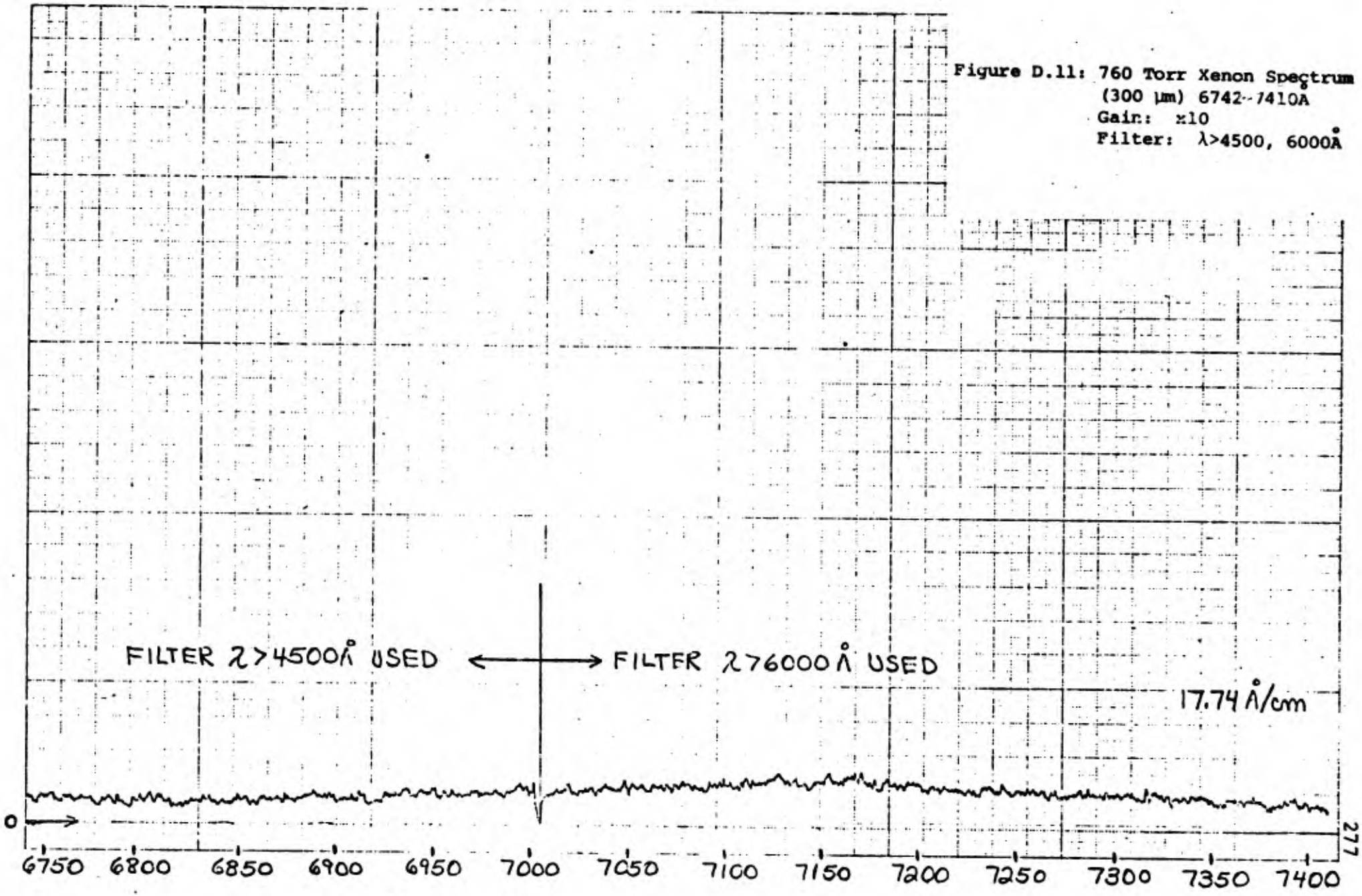

Figure D.11: 760 Torr Xenon Spectrum
(300 μm) 6742--7410Å
Gain: x10
Filter: λ>4500, 6000Å

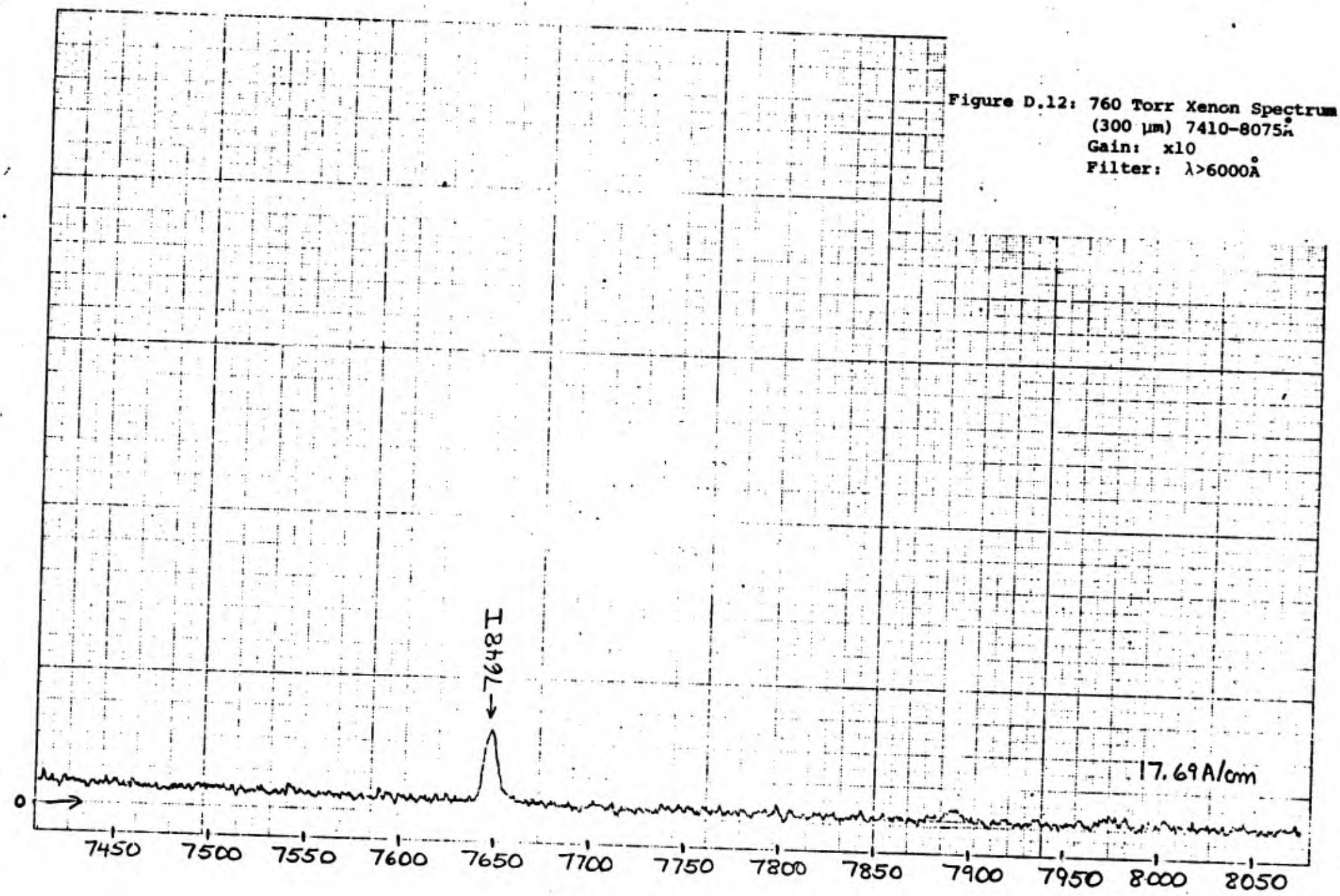

Figure D.12: 760 Torr Xenon Spectrum
(300 μm) 7410-8075Å
Gain: x10
Filter: λ>6000Å

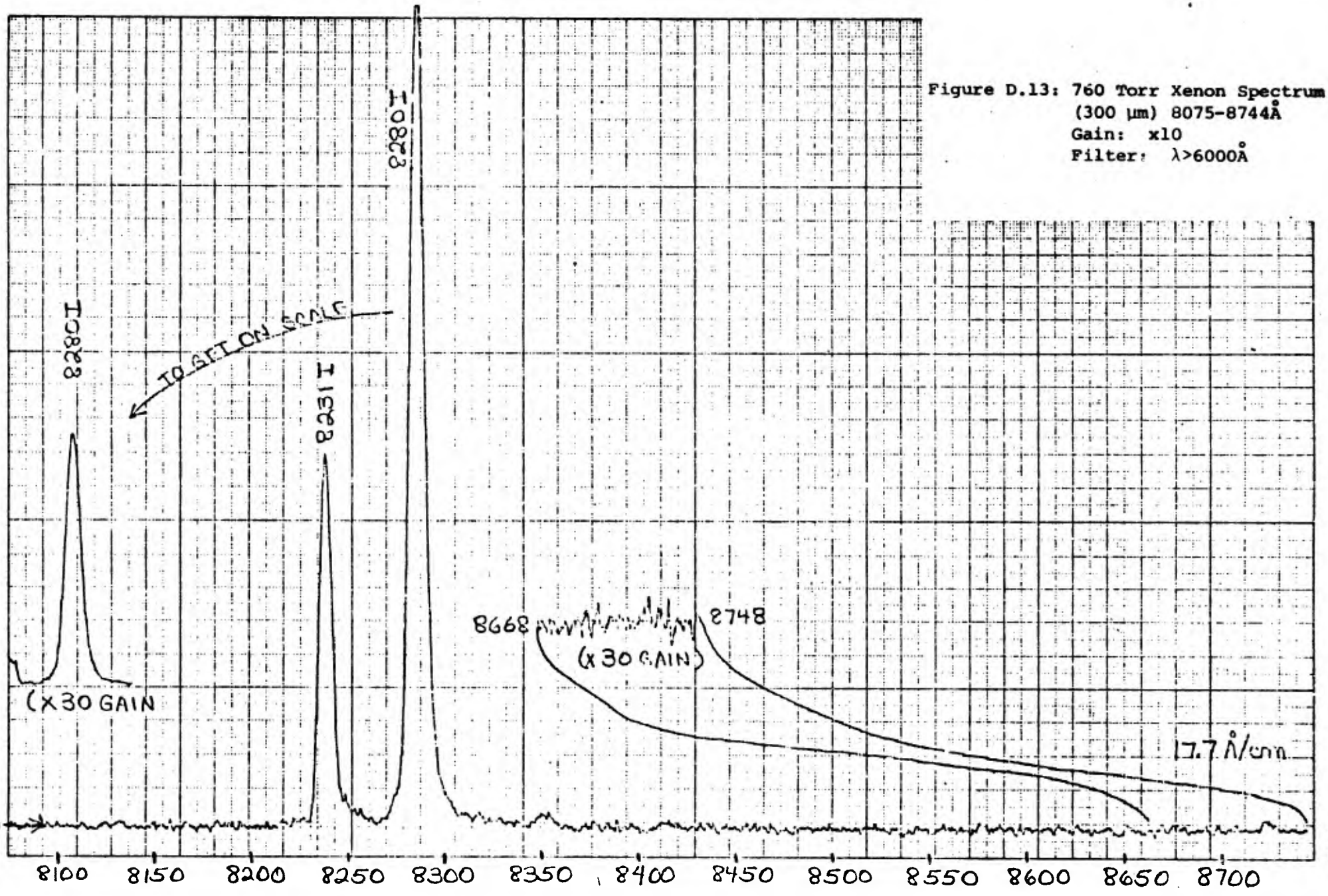

Figure D.13: 760 Torr Xenon Spectrum
(300 μm) 8075-8744Å
Gain: x10
Filter: λ>6000Å

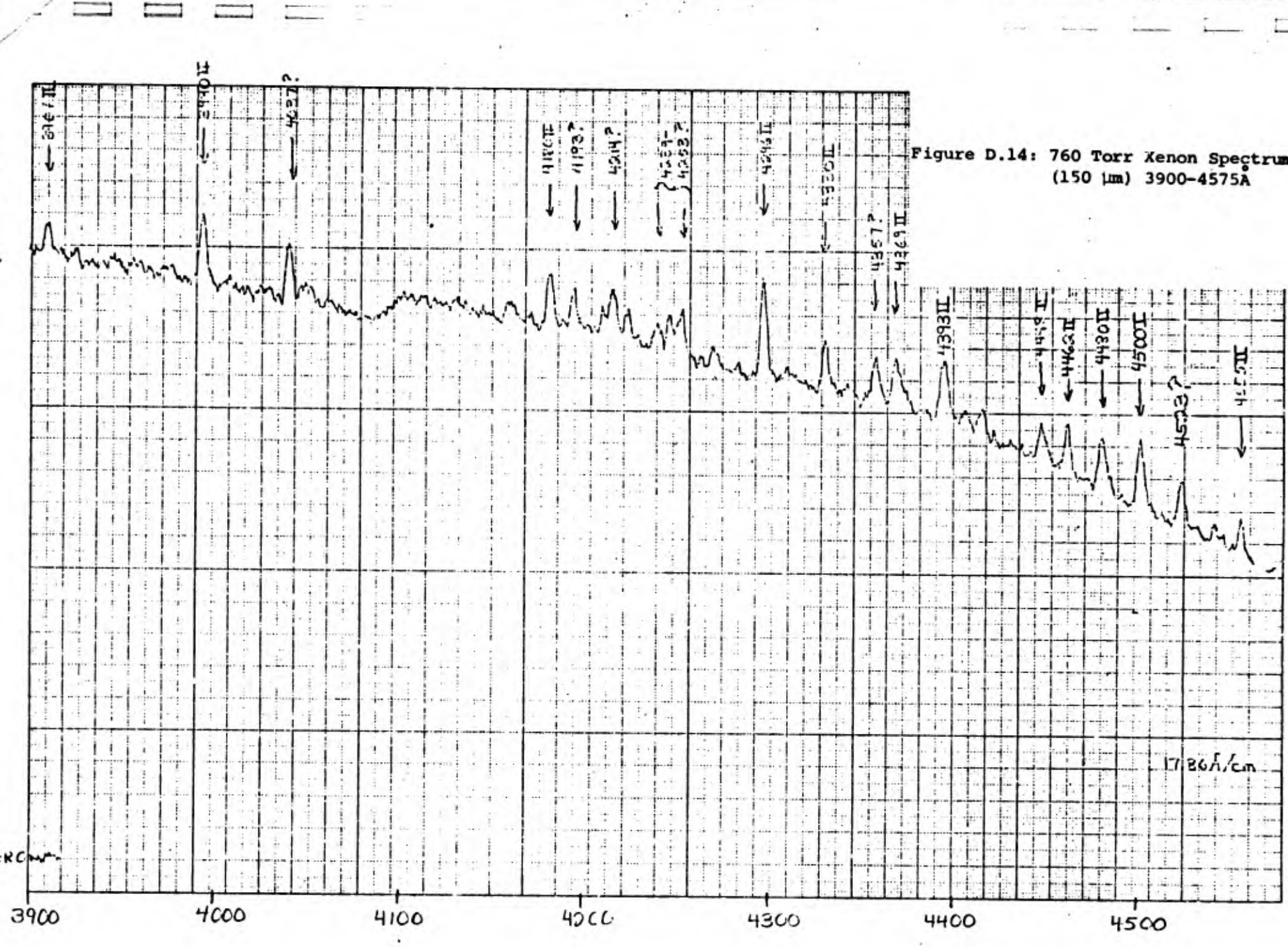

Figure D.14: 760 Torr Xenon Spectrum (150 µm) 3900-4575Å

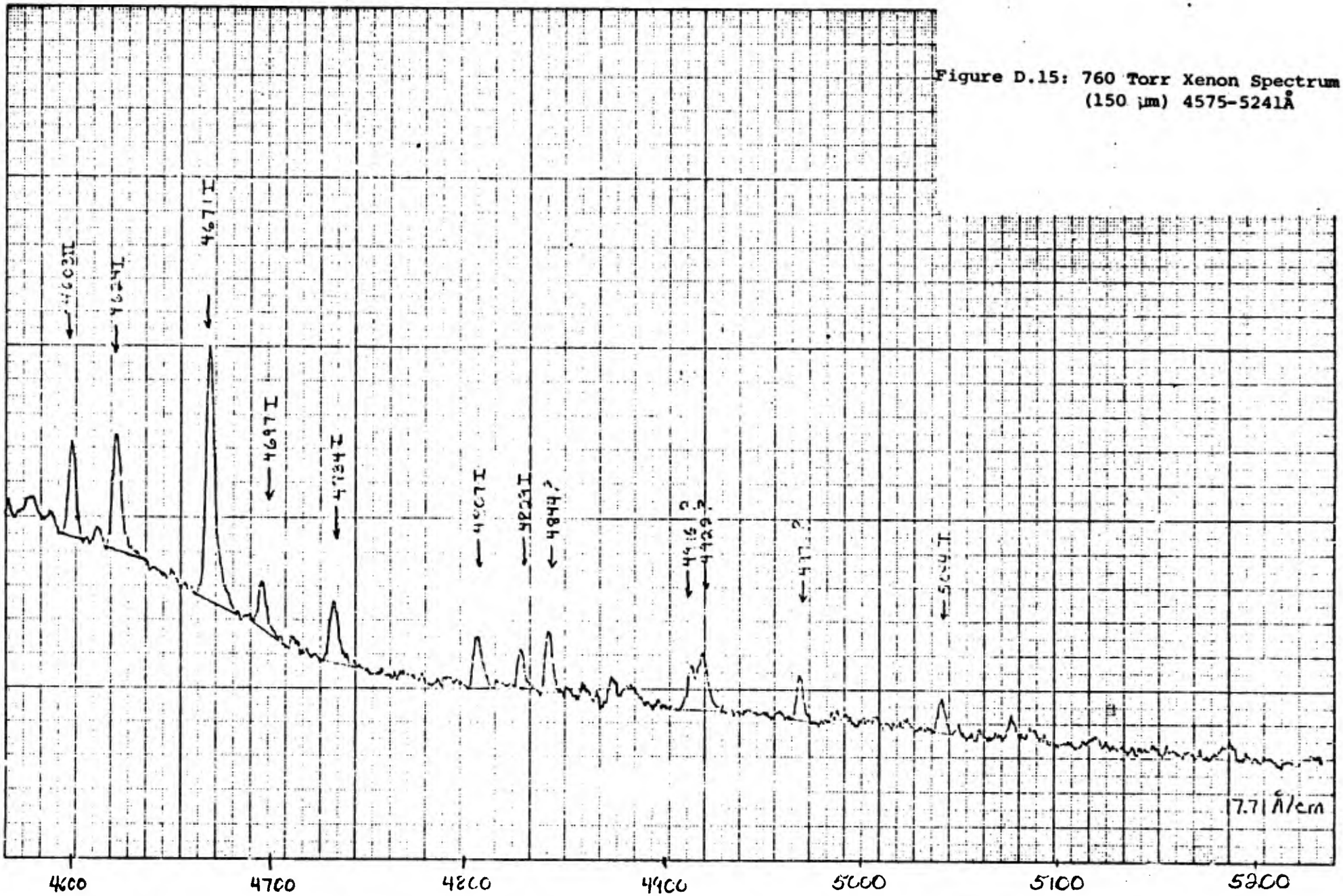

Figure D.15: 760 Torr Xenon Spectrum (150 μm) 4575-5241Å

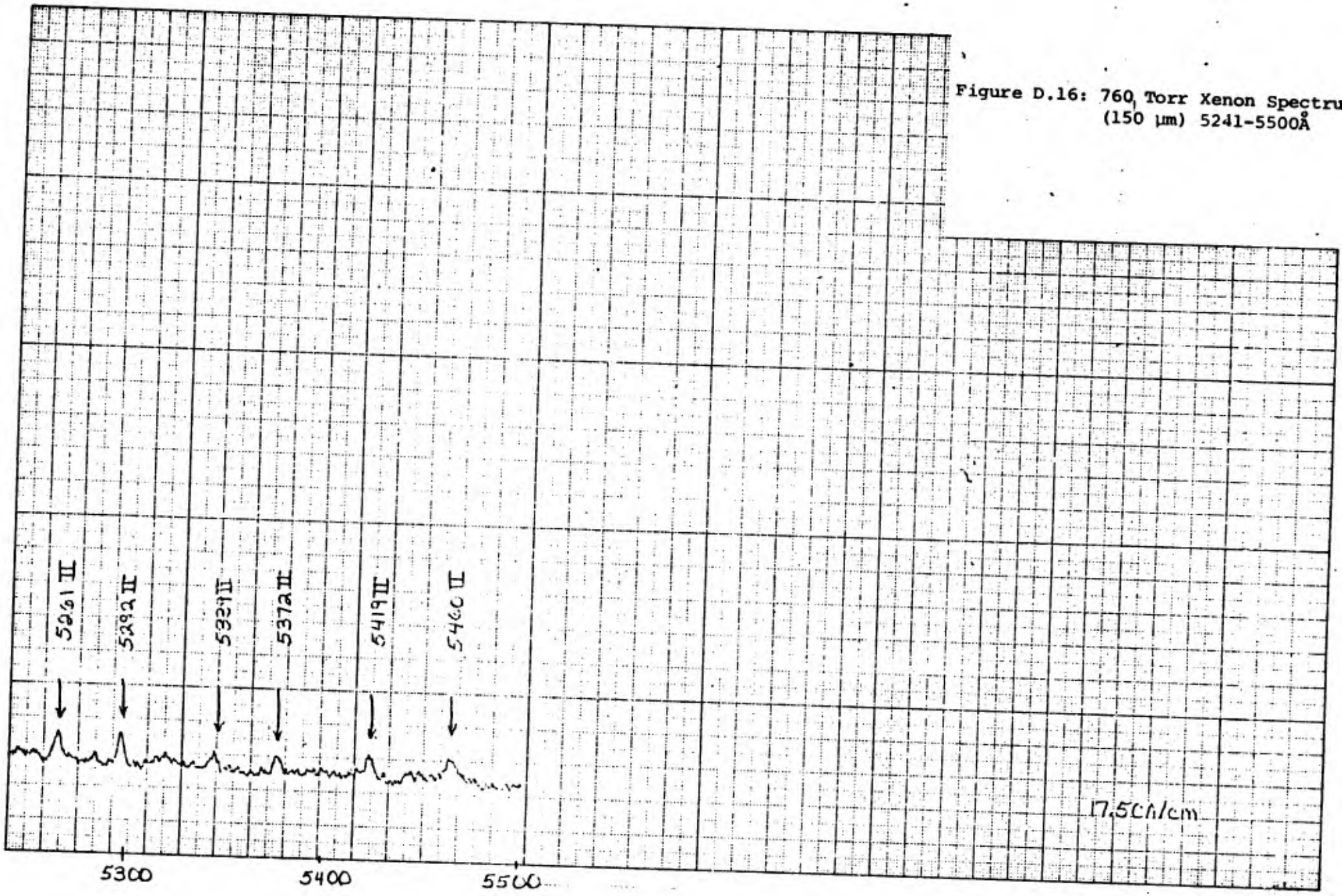

Figure D.16: 760 Torr Xenon Spectrum (150 μm) 5241-5500Å

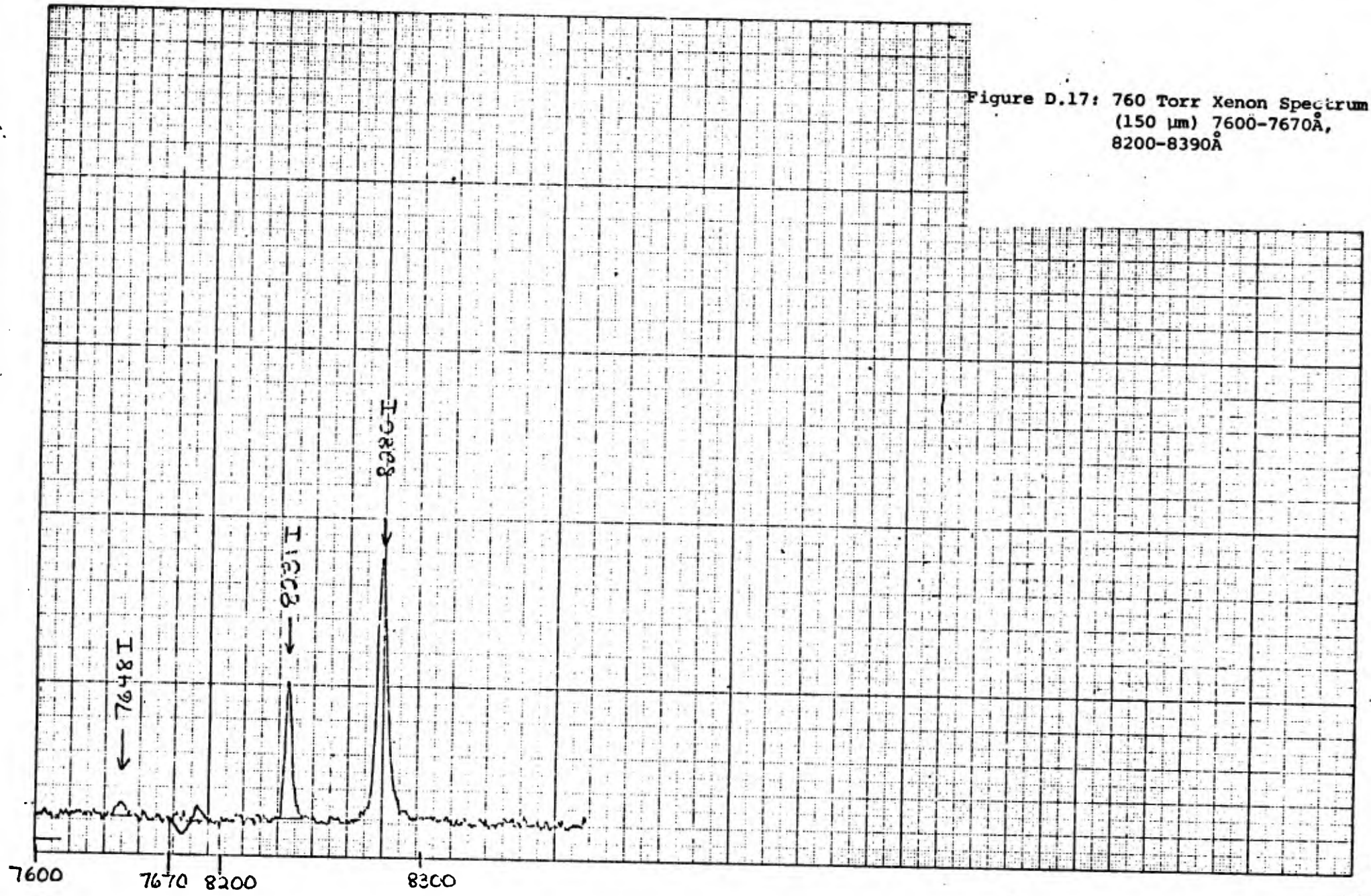

Figure D.17: 760 Torr Xenon Spectrum (150 μm) 7600-7670Å, 8200-8390Å

REFERENCES

1. Hyde, E.K.. The Nuclear Properties of the Heavy Elements, Volume III: Fission Phenomena, Englewood Cliffs: Prentice-Hall, 1964.

2. Evans, R.D., The Atomic Nucleus, New York: McGraw-Hill, 1955, p. 668.

3. Thom, K. and R.T. Schneider, "Nuclear Pumped Gas Lasers," AIAA Journal, 10, 400-406, 1972.

4. Walters, R.A., "Recent Experimental Results Concerning Nuclear Pumped Gas Lasers," Proceedings of the Society of Photo-Optical Instrumentation Engineers, 41, 79-87, 1973.

5. Schneider, R.T. and Thom, Karlheinz, "Fissioning Uranium Plasmas and Nuclear-Pumped Lasers," Nucl. Technol., 27, 34-50, 1975.

6. Fuller, J.L., Infrared Laser Emission from a Helium-Xenon Mixture Using Fission Fragment Interaction, Ph.D. Dissertation, University of Florida, 1975.

7. Helmick, H.H., Fuller, J.L. and Schneider, R.T., "Direct Nuclear Pumping of a Helium-Xenon Laser," Appl. Phys. Lett., 26, 327-328, 1975.

8. McArthur, D.A. and Tolleferud, P.B., "Observation of Laser Action in CO Gas Excited Only by Fission Fragments," Appl. Phys. Lett., 26, 187-190, 1975.

9. DeYoung, R.J., Wells, W.E., Verdeyen, J.T. and Miley, G.H., "A Direct Nuclear Pumped Ne-N_2 Laser," IEEE/OSA Conference on Laser Engineering and Applications, Washington, D.C., May 1975.

10. Stannett, V.T., "Large Scale Radiation Induced Chemical Processing," Ann. Rev. Nucl. Sci., 21, 397-416, 1971.

11. Thonnard, N. and Hurst, G.S., "Lime Dependent Study of Vacuum-Ultraviolet Emission in Argon," Phys. Rev., 5, 1110-1121, 1972.

12. Axtmann, R.C. and Sears, J.T., "Excitation of Nitrogen Gas by Alpha Particles and Fission Fragments," J. Chem. Phys., 44, 3279-3283, 1966.

13. Pagano, R., The Gas Scintillator as a Kinetic Energy Spectrometer for Fission Fragments, Ph.D. Dissertation, University of Florida, 1970.

14. Calo, J.M., "Electronic Energy Loss by Fission Fragments," Nucl. Sci. Eng., 42, 424-426, 1970.

15. Shipman, G.R., private communication, 1975.

16. Morse, F., Harteck, P. and Dondes, S., "Excited Species of Gases Produced in the Nuclear Reactor," Rad. Res., 29, 317-328, 1966.

17. Walters, R.A., Excitation and Ionization of Gases by Fission Fragments, Ph.D. Dissertation, University of Florida, 1973.

18. Walters, R.A. and Schneider, R.T., "Spectroscopic Analysis of Plasmas Produced by Fission Fragments," Trans. Amer. Nucl. Soc., 15, 634, 1972.

19. Miley, G.H. and Theiss, P.E., "A Unified Approach to Two-Region Ionization-Excitation Density Calculations," Nucl. Appl., 6, 434-351, 1969.

20. Theiss, P.E. and Miley G.H., "Calculations of Ionization-Excitation Source Rates in Gaseous Media Irradiated by Fission Fragments and Alpha Particles," Research on Uranium Plasmas and Their Technological Applications, NASA SP-236, 1971.

21. Guyot, J.C., Miley, G.H. and Verdeyen, J.T., "Application of a Two-Region Heavy Charged Particle Model to Noble-Gas Plasmas Induced by Nuclear Radiations," Nucl. Sci. Eng., 48, 373-386, 1972.

22. Walters, R.A. and Schneider, R.T., "Electron Energy Distribution Function of Fission Fragment Excited Gases," Trans. Amer. Nucl. Soc., 17, 1-2, 1973.

23. Lo, R. and Miley, G.H., "Calculation of Electron Energy Flux Distributions in Noble Gases," Trans. Amer. Nucl. Soc., 15, 581-582, 1972.

24. Wang, B.S. and Miley, G.H., "Monte Carlo Simulation of Radiation Induced Plasmas," Nucl. Sci. Eng., 52, 130-141, 1973.

25. Bennett, W.R., "Optical Spectra Excited in High Pressure Noble Gases by Alpha Impact," Annals of Physics, 18, 367-420, 1962.

26. Strickler, T.D. and Arakawa, E.T., "Optical Emission from Argon Excited by Alpha Particles: Quenching Studies," J. Chem. Phys., 41, 1783-1789, 1964.

27. Hanle, V.W., Kugler, E. and Schmillen, A., "Uber die Lumineszenz von Edelgasen bei Anregung mit Schnellen Elektronen," Ann. Physik., 60, 252-273, 1964.

28. Henck, R. and Coche, A., "Determination et Interpretation des Spectres de Florescence des gas Rares Excites par un Rayonnement ," J. de Physique, 26, 110-116, 1965.

29. Dondes, S., Harteck, P. and Kunz, C., "A Spectroscopic Study of Alpha-Ray-Induced Luminescence in Gases," Rad. Res., 27, 174-210, 1966.

30. Henck, R. and Voltz, R., "Etude Theorique et Experimentale de la Luminescence de L'Argon Induite par des Particles ," J. de Physique, 29, 149-158, 1968.

31. Hurst, G.S. and Bortner, T.E., "Proton Excitation of the Argon Atom," Phys. Rev., 178, 4-10, 1969.

32. Dolgov-Savelev, G.G., Knyazev, V.A. and Kuznetsov, V.V., "Excitation of Inert Gases by a Beam of Fast Electrons," Opt. Spectrosc., 27, 405-408, 1969.

33. Arai, S. and Firestone, R.F., "Evidence for the Formation of Neutral Rare-Gas Molecules by Electron-Beam Pulses," J. Chem. Phys., 50, 4575, 1969.

34. Thiess, P.E. and Miley, G.H., "Spectroscopic and Probe Measurements of Excited State and Electron Densities in Radiation Induced Plasmas," Proceedings of the 2nd Symposium on Uranium Plasmas, Georgia Institute of Technology, Nov. 1971.

35. Thiess, P.E. and Miley, G.H., "Studies of Excited States Formed in Neon and Argon by Ionizing Radiation," Trans. Am. Nucl. Soc., 18, 70-71, 1974.

36. Thiess, P.E. and Miley, G.H., "New Near-Infrared and Ultraviolet Gas-Proportional Scintillation Counters," Trans. IEEE Nucl. Sci., NS-21, 125-135, 1974.

37. Thiess, P.E. and Miley, G.H., "Optical Emission from Noble Gas Plasmas Created by Alpha Particles," Trans. Am. Nucl. Soc., 14, 134-135, 1971.

38. Carlson, G.A., "Spectroscopic Studies of the Emission from Plasmas Generated by an Intense Electron Beam," Record of the 11th Symposium on Electron, Ion, and Laser Beam Technology, 1974.

39. Davis, J.F., Ph.D. Dissertation, University of Florida (in preparation).

40. Northcliffe, L.C., "Passage of Heavy Ions Through Matter," Ann. Rev. Nucl. Sci., 13, 67-102, 1963.

41. Miley, G.H., Direct Conversion of Nuclear Radiation Energy, Hinsdale, Illinois: American Nuclear Society, 1971 (Chapter 3).

42. Knipp, J.K. and Ling, R.C., "On the Ionization Yields of Heavy Particles," Phys. Rev., 82, 30-35, 1951.

43. Platzman, R.L., "Total Ionization in Gases by High-Energy Particles: An Appraisal of Our Understanding," Int. J. Appl. Rad. and Isotopes, 10, 116-127, 1961.

44. Christophorou, L.G., Atomic and Molecular Radiation Physics, New York: Wiley Interscience, 1971.

45. Schmitt, H.W. and Leachman, R.B., "Ionization vs Energy Relation for Fission Fragments," Phys. Rev., 102, 183-185, 1956.

46. Orvis, D.D., Diffusion-Recombination Kinetics of Columnar Ionization in Gases, Ph.D. Dissertation, University of Florida, 1970.

47. Cooper, J., "Plasma Spectroscopy," Reports on Progress in Physics, 29, 35-130, 1966.

48. Bates, D.R., "Recombination," Case Studies in Atomic Physics, 4, 57-92, 1974.

49. Bardsley, J.N. and Biondi, M.A., "Dissociative Recombination," Advances in Atomic and Molecular Physics, 6, 1-57, 1970.

50. Connor, T.R. and Biondi, M.A., "Dissociative Recombination in Neon: Spectral Line-Shape Studies," Phys. Rev., 140, A778-791, 1965.

51. Frommhold, L. and Biondi, M.A., "Interferometric Study of Dissociative Recombination in Neon and Argon Afterglows," Phys. Rev., 185, 244-252, 1969.

52. Edwin, R.P. and Turner, R., "Interferometric Investigation of Line Shapes in the Spectra of Rare-Gas Afterglows," J. Chem. Phys., 50, 4388-4393, 1969.

53. Hughes, W.M., "126.1 nm Molecular Argon Laser," Appl. Phys. Lett., 24, 488-490, 1974.

54. Rhodes, C.K., "Review of Ultraviolet Laser Physics, IEEE J. Quant. Electronics, QE-10, 153-174, 1974.

55. Mehr, F.J. and Biondi, M.A., "Electron-Temperature Dependence of Electron-Ion Recombination in Argon," Phys. Rev., 176, 322-326, 1968.

56. O'Malley, T.F., Cunningham, A.J., and Hobson, R.M., "Dissociative Recombination at Elevated Temperatures II. Comparison Between Theory and Experiment in Neon and Argon Afterglows," J. Phys. B: Atom. molec. Phys., 5, 2126-2133, 1972.

57. Wilhelm, H.E., "Recombination in Columns," J. Chem. Phys., 47, 4356-4365, 1967.

58. Ellis, W.H. and Imani, K., "Kinetic Studies of Fission Fragment, $^{3}He(n,p)t$, and Gamma Ray Produced Plasmas," Proceedings of the 2nd Symposium on Uranium Plasmas, Georgia Institute of Technology, November 1971, 31-38.

59. McDaniel, E.W. and Mason, E.A., The Mobility and Diffusion of Ions in Gases, New York: John Wiley and Sons, 1973.

60. Oskam, H.J. and Mittelstadt, V.R., "Ion Mobilities in Helium, Neon and Argon," Phys. Rev., 132, 1435-1444, 1963.

61. McAfee, K.B., Sipler, J.D. and Edelson, D., "Mobilities and Reactions of Ions in Argon," Phys. Rev., 160, 130-135, 1967.

62. Biondi, M.A. and Chanin, L.M., "Mobilities of Atomic and Molecular Ions in the Noble Gases," Phys. Rev., 94, 910-916, 1954.

63. Kaiser, B.J., "Pulsed Ion Chamber Wide Range Radiation Field Monitor," M.S. Thesis, University of Florida, 1975.

64. Dolgov-Savelev, G.G., Knyazev, B.A., Koz'minykh, Y.L., and Kuznetsov, V.V., "An Investigation of Electron-Ion Recombination in Inert Gases," Sov. Phys. JETP, 30, 601-604, 1970.

65. Smith, D. and Cromey, P.R., "Conversion Rates and Ion Mobilities in Pure Ne and Ar Afterglow Plasmas," J. Phys. B: Atom. molec. Phys., 1, 638-649, 1968.

66. Smith, D., Dean, A.G. and Plumb, I.C., "Three Body Conversion Reactions in Pure Rare Gases," J. Phys. B: Atom. molec. Phys., 4, 2134-2142, 1972.

67. Huffman, R.E. and Katayama, D.H., "Photoionization Study of Diatomic-Ion Formation in Argon, Krypton, and Xenon," J. Chem. Phys., 45, 138-146, 1966.

68. Phelps, A.V., "Effect of the Imprisonment of Resonance Radiation on Excitation Experiments," Phys. Rev., 110, 1362-1368, 1958.

69. Redmond, R.F., Klingensmith, R.W. and Anno, J.N., "Energy Spectrum of Fission Fragments Emitted from Thin Layers of Uranium Dioxide," J. Appl. Phys., 33, 3393-3385, 1962.

70. Fulmer, C.B., "Density Effect on Energy versus Range of Fission Fragments in Gases," Phys. Rev., 139, B54-55, 1965.

71. Kahn, S., Harman, R. and Forgue. V., "Energy Distributions of Fission Fragments from Uranium Dioxide Films," Nucl. Sci. Eng., 23, 8-20, 1965.

72. Ogurtsov, G.N., "Energy Spectra of Electrons Ejected in Ion-Atom Collisions," Rev. Mod. Phys., 44, 1-17, 1972.

73. Berry, H.W., "Energy Distribution of Electrons from Ionizing Collisions of Atoms and Ions," Phys. Rev. 127, 1634-1637, 1962.

74. Anno, J.N., "Secondary Electron Production from Fission Fragments Emerging from Thin Layers of Uranium Dioxide," J. Appl. Phys., 33, 1678-1681, 1962.

75. Zuloaga, J.A., Operational Characteristics of the Modified UFTR, M.E Project Final Report, University of Florida, 1975.

76. Davie, R.N., Davis, J.F., Holtzclaw, E.T. and Schneider, R.T., A Safety Assessment of Proposed UFTR Gas Irradiation Studies Using the MCFIG System: A Report Prepared for UFTR Subcommittee Review, NES Dept., University of Florida, July, 1973.

77. Larrabee, R.D., "Spectral Emissivity of Tungsten," J. Opt. Soc. Am., 49, 619-625, 1959.

78. N.B.S. Publication entitled "Instruction for Using the NBS Standards of Spectral Radiance" supplied with the calibration data for lamp no. EPUV-1148.

79. Pressley, R.J., Handbook of Lasers with Selected Data on Optical Technology, Cleveland: The Chemical Rubber Co., 1971.

80. Wiese, W.L., Smith, M.W. and Miles, B.M., Atomic Transition Probabilities, Volume II, Sodium Through Calcium, National Bureau of Standards (NSRDS-NBS 22), October 1969.

81. Striganov, A.R. and Sventitskii, N.S., Tables of Spectral Lines of Neutral and Ionized Atoms, New York: Plenum, 1968.

82. Zapesochnyi, I.P. and Feltsan, P.V., "On the Excitation Cross Sections of 2p Levels of Argon, Krypton, and Xenon," Opt. Spectrosc., 20, 291, 1966.

83. Bridges, W.B. and Chester, A., "Spectroscopy of Ion Lasers," IEEE J. Quant. Electronics, QE-1, 66-84, 1965.

84. Sinclair, D.C., "Near Infrared Oscillation in Pulsed Noble Gas Ion Lasers," J. Opt. Soc. Am., 55, 571-572, 1965.

85. Horrigan, F.A., Koozekanani, S.H., and Paananen, R.A., "Infrared Laser Action and Lifetimes in ArII," Appl. Phys. Lett., 6, 41-43, 1965.

86. Rudko, R.I. and Tang, C.L., "Spectroscopic Studies of the Ar^+ Laser," J. Appl. Phys., 38, 4731-4739, 1967.

87. Feltsan, P.V. and Povich, M.M., "Excitation of Argon Ions by Electron-Atom Collisions," Opt. Spectroc., 28, 119-121, 1970.

88. Jortner, J., Meyer, L., Rice, S.A., and Wilson, E.G., "Localized Excitation in Condensed Ne, Ar, Kr and Xe," J. Chem. Phys., 42, 4250-4253, 1965.

89. Hill, R.M., private communication, 3 September 1975.

90. Herzberg, G., Spectra of Diatomic Molecules, 2nd ed., New York: D. Van Nostrand Company, Inc., 1950.

91. Tanaka, Y. and Yoshino, K., "Absorption Spectrum of the Argon Molecule in the Vacuum-UV Region," J. Chem. Phys. 53, 2012-2030, 1970.

92. Warren, R.W. and Parker, J.H., "Ratio of the Diffusion Coefficient to the Mobility Coefficient for Electrons in He, Ar, N_2, H_2, D_2, CO and CO_2 at low temperatures and low E/P," Phys. Rev., 128, 2661-2671, 1962.

93. McDaniel, E.W., Collision Phenomena in Ionized Gases, New York: John Wiley and Sons, 1964.

94. Huestis, D.L. and Hill, R.M., private communication, 2 September 1975.

95. Miller, M.H. and Roig, R.A., "Transition Probabilities of XeI and XeII," Phys. Rev. A, 8, 480-486, 1973.

96. Moore, C.E., Atomic Energy Levels, Volume III, N.B.S. Circular 467, 1958.

97. Prince, J.F. and Robertson, W.W., "Visible Continuua in Xenon, Krypton, and Neon," J. Chem. Phys., 46, 3309-3313, 1967.

98. Mulliken, R.S., "Potential Curves of Diatomic Rare-Gas Molecules and Their Ions, with Particular Reference to Xe_2^*," J. Chem. Phys., 52, 5170-5180, 1970.

99. Turner, R. and Riccius, H.D., "Visible Afterglow of Krypton," J. Chem. Phys., 48, 4351-4356, 1968.

100. Searles, S.K., "Superfluorescent Laser Emission from Electron-Beam-Pumped Ar-N_2 Mixtures," Appl. Phys. Litt., 25, 735-737, 1974.

101. Levy, P.W., "Color Centers and Radiation-Induced Defects in Al_2O_3," Phys. Rev., 123, 1226, 1961.

102. Rieke, J.K. and Daniels, F., "Thermoluminescence Studies in Aluminum Oxide," J. Phys. Chem., 61, 629, 1957.

103. Schulman, J.H., "Survey of Luminescence Dosimetry," Proc. Int. Conf. on Luminescence Dosimetry, Stanford, 1965. AEC Symp. Ser. Vol. 8, CONF-650637.

104. Gabrysh, A.F., Kennedy, J.M., Eyring, H. and Johnson, V.R., "Effects of High Pressure on the Thermoluminescence of Gamma Irradiated Alpha Al_2O_3 Single Crystals," Phys. Rev., 131, 1543, 1963.

105. Leverenz, H.W., An Introduction to Luminescence of Solids, New York: John Wiley & Sons, Inc., 1950.

106. Catalog 7009W, Ceramaseol, Inc., New Lebanon Center, N.Y. 12126, 1974.

107. Levy, P.W., Swyler, K.J. and Hardy, W.H. II., "Color Center Formation and Radioluminescence in NaCl, KCl, and LiF Measured During and After Electron Bombardment," Bull. Am. Phys. Soc., 20, 431, 1975.

BIOGRAPHICAL SKETCH

Robert N. Davie, Jr. [redacted] As the son of a military family his childhood was spent in numerous places which included three years in Japan and two years in Pakistan. In 1963 he graduated from W.P. Sprayberry High School in Marietta, Georgia, and entered the United States Military Academy at West Point. Upon graduation in 1967 he was commissioned a Second Lieutenant in the U.S. Air Force, married the former Janet Fay Sampson of Marietta, Georgia, and began graduate study in nuclear engineering at the Air Force Institute of Technology at Wright Patterson A.F.B., Ohio.

After receiving his Master of Science degree in 1969, Lt. Davie was assigned to the Air Force Weapons Laboratory (AFWL) at Kirtland A.F.B., New Mexico. During 1969-1970 he worked as a project officer in the Nuclear Safety Division examining advanced concept nuclear powered aircraft feasibility in terms of nuclear safety. In 1970 he was transferred to the Electromagnetic Pulse (EMP) Branch of the Electronics Division. He worked in the areas of advanced EMP simulator development, field testing as a consultant to

the U.S. Army for the Sprint and Spartan missile tests, Minuteman wartime reliability planning, and data reduction as technical director of AFWL EMP data reduction. From 1972 until his selection for and reassignment to graduate school in 1973 he served as test director of the B-1 Bomber EMP Scale Model Test Program. He presently holds the rank of Captain and upon graduation from the University of Florida will be assigned to the Air Force Technical Applications Center.

Captain Davie presently has two sons, Robert N. III and Christopher S. His hobbies include photography and numerous sports. He is a member of the American Nuclear Society, American Physical Society, Optical Society of America, Tau Beta Phi, and the National Society of Professional Engineers. He is a professional engineer registered in the state of Florida.